

MINISTRY OF EDUCATION AND RESEARCH



THE ANNALS OF “DUNAREA DE JOS” UNIVERSITY OF GALATI

**Fascicle IX
METALLURGY AND MATERIALS SCIENCE**

**YEAR XXV (XXX),
May 2007, no. 1**

ISSN 1453-083X



**2007
GALATI UNIVERSITY PRESS**



Table of Content

1.Elena DRUGESCU, Tiberiu POTECAȘU - Influence of the Furnace Temperature in Continuous Flux Quenching on the Characteristics of Low Carbon Steel Straps.....	5
2.Elisabeta VASILESCU, Marian NEACȘU, Ana DONIGA - Study of the ThermoMechanical Treatment Post-Deformation Maintaining Time Influence on the Mechanical Characteristics of the MicroAlloyed Steels.....	9
3.Nicoleta TORODOC, Ioan GIACOMELLI - Contribution of Heat and Thermo-Chemical Treatments to the Improvement of the Performances of High-Speed Steel Tools...	14
4.Maria BACIU, Teofana Emilia NECHITA - Implications of Thermal and Thermo Chemical Treatments in Electrolytic Plasma on the Phasic Composition of Steels 40Cr10 and OLC 55.....	17
5.Lidia BENEĂ, Viorel DRĂGAN - Study of Tribocorrosion Processes by Electrochemical Techniques.....	21
6.Ovidiu DIMA - Behaviour at Nitriding in Fluidized Layer of Austenitic Stainless Steels at the Temperature of 450°C.....	31
7.Maria VLAD - Researches on the Pollution of Underground Waters in a Certain Part of Galati District.....	37
8.Nicolae CANĂNĂU, Petrică ALEXANDRU, Gheorghe GURĂU - Experimental Researches on the Constitutive Equation of Concrete Steel With Superior Characteristics.....	46
9.Luminița MORARU - Grain Refinement in Aluminum Alloys by Acoustic Cavitation Phenomena.....	50
10.Viorel MUNTEANU - Steel Flow Control of Continuous Casted Slabs Using Submerged Entry Nozzle Exchange System for Tundish.....	55
11.V.G. GRECHANYUK, V.A. DENISENKO, L. ORAC - Structure and Corrosive Firmness of Composition Materials on the Basis of Copper and Molybdenum Got Method Electron-Beam Technology.....	60
12.Ion SANDU, Marta QUARANTA, Costică BEJINARIU, Ioan Gabriel SANDU, Dorin LUCA, Andrei Victor SANDU - Study on the Specific Effects of Corrosion Processes on Ancient Bronze Artefacts	64
13.Brândușa Ghiban, Sorin CIUCĂ - Austenitic Stainless Steels Corrosion Properties Modified by Silicon Alloying.....	74
14.Maria CIOROI, Licuța NISTOR - Recycling Possibilities of Metallurgical Slag.....	78
15.Liviu PALAGHIAN, Mioara THOMPSON, Svetlana BĂICEAN, Sorin BUCȘĂ - Modelling and Prediction in Failure Processes by Mechanical Stresses in Corrosive Environment.....	83
16.Victor STANCIU - Properties Corelation in Sintered Hard Alloys with High Toughness and Strenght.....	90
17.Carmela GURĂU, Gheorghe GURĂU, Petrică ALEXANDRU, Nicolae CANĂNĂU - Two-way Shape Memory Effect in a Cu-13wt. %Al-4 wt.%Ni Shape Memory Alloy by the Thermo - Mechanical Cycling Method	94
18.Gabriel ANDREI, Adrian CÎRCIUMARU, Iulian-Gabriel BÎRSAN, Dumitru DIMA - A Study of Electric Properties of Fiber Fabric Based Filled Epoxy Composites.....	97
19.Adrian CÎRCIUMARU, Gabriel ANDREI, Iulian-Gabriel BÎRSAN, Dumitru DIMA - Electric and Electromagnetic Properties of Fiber Fabric Based Filled Epoxy Composites.....	103
20.Ștefan DRAGOMIR, Silviu MACUȚĂ, Constantin SPÂNU - Vibration Diagnosis Systems for a Cold Rolling Mill Machine.....	109



21.Constantin GHEORGHIEȘ, Alina-Mihaela CANTARAGIU, Iuliana Valentina STASI - X-Ray Diffraction Residual Stress Measurements for Quality Control Testing.....	114
22.Bogdan GEORGESCU, Valeriu GEORGESCU - New Welding Technology – the Cold Welding on Cogged Surfaces.....	118
23.Alexander SAVAYDIS, Georgios TSAMASPHYROS, Dimitrios KARAGIANNIS, Georgios SAVAYDIS - Experimental and Theoretical Investigations on Mode I Crack Propagation in Notches under Cyclic Loading.....	123
24.Marian BORDEI, Aurel CIUREA, Ștefan DRAGOMIR - The Analysis of the Breaking Susceptibility of Some Feritic Stainless Steel	127
25.Leonard TEODORU, Valentin MIHAILESCU - Reduction Rate of Remanent Stress in Thermal Spraying Depositions by Shot Peening.....	132
26.Ioan MARGINEAN, Mihai TARCOLEA, Vasile MIREA, Sorin-Adrian COCOLAȘ - Granularly Unbind Materials for Casting Composite Moulds.....	136
27.Petre Stelian NITA – Values of Solutal Marangoni Number in Very Dilute Fe-C-O Solutions at 1873K.....	142



INFLUENCE OF THE FURNACE TEMPERATURE IN CONTINUOUS FLUX QUENCHING ON THE CHARACTERISTICS OF LOW CARBON STEEL STRAPS

Elena DRUGESCU, Tiberiu POTECAȘU

"Dunărea de Jos" University of Galati

email: tpotecasu@gmail.com

ABSTRACT

In this paper there are presented mechanical characteristics (resiliency, elongation) and structural characteristics resulted from quenching thermal treatment made on an experimental installation, in continuous flux, on low carbon steel straps ($C = 0,185\%$), cheap, elaborated without special purity prescriptions. The experiments were made varying the furnace temperature while keeping all the other technological parameters constant.

The straps' speed through the system was 2m/min and the cooling was made in water jet. Starting with heating temperatures of 900°C good mechanical characteristics are obtained: $R_m 1500 = \text{MPa}$ and $A_{80} = 4\%$.

KEYWORDS: low carbon steels quenching, continuous flux thermal treatment

1. Introduction

Low carbon steels, having low hardenability are not used in quenching thermal treatment consequently there is little study in this direction. In order to achieve high ultimate stress values higher carbon content steels are used or steels with alloying elements which increase their hardenability. Considering that these low carbon steels are easier and cheaper to produce, research towards broadening their domain of usage are opportune. Products with thin section areas are to be considered which should allow high cooling speeds hereby low hardenability

would no longer be a major impediment in obtaining high ultimate stress values.

2. Experimental results

An experimental installation was built for the research. Figure 1 presents a schematic representation of the installation. Furnace temperature and strap's speed logging and control were implemented. For continuous flux quenching several high speed cooling devices were designed and built trying to achieve stable robust high cooling speeds.

Table 1. The chemical composition of the analyzed steel

C	Mn	Si	P	S
[%]				
0.185	1.350	0.063	0.023	0.008

The studied steel is an ordinary elaborated steel as the microstructure on the polished and unetched sample shows in figure 2. – the inclusions' fiber-like texture resulted from rolling is present.

The studied samples presented in this paper were made from the following thermal treatment furnace temperatures: 850°C , 900°C , 950°C , 1000°C .

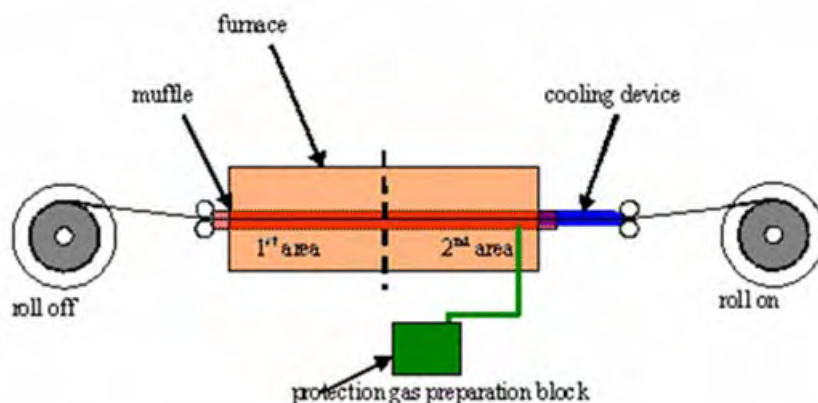


Fig. 1. Schematic representation of the continuous flux quenching installation.

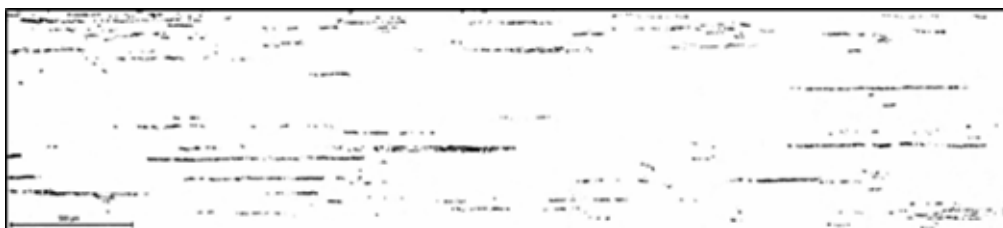


Fig. 2. Image realized on unetched sample showing the inclusions' fibrous structure

In fig. 3 the ultimate strength and elongation from the analyzed samples is presented in a graphical form and also a spline extrapolation was made to

point out the tendencies. As the results show very high ultimate stress values were obtained from an ordinary elaborated low carbon steel.

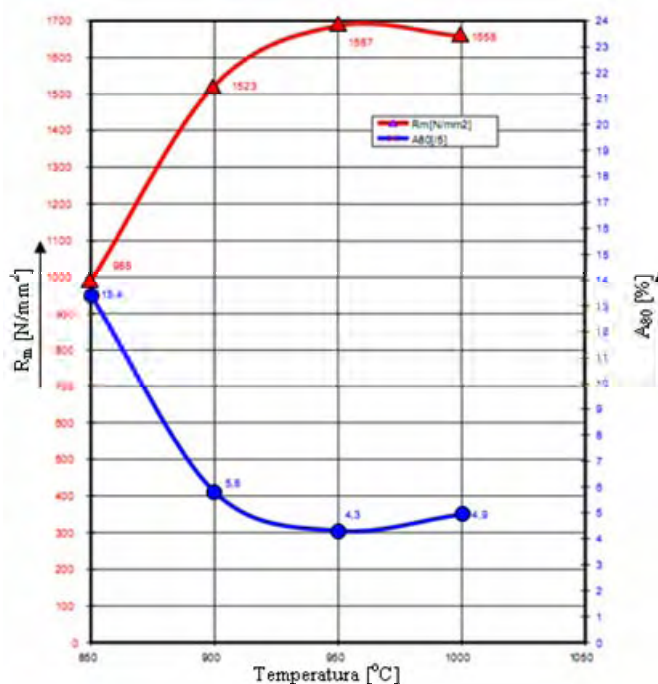


Fig. 3. The mechanical characteristics obtained at continuous flux quenching.

In figure 4 the microstructure of the sample quenched from 900°C is shown. The microstructure shows a typical quenching structure (martensitic

structure, acicular, very fine) in correlation with the spectacular increase in ultimate strength.

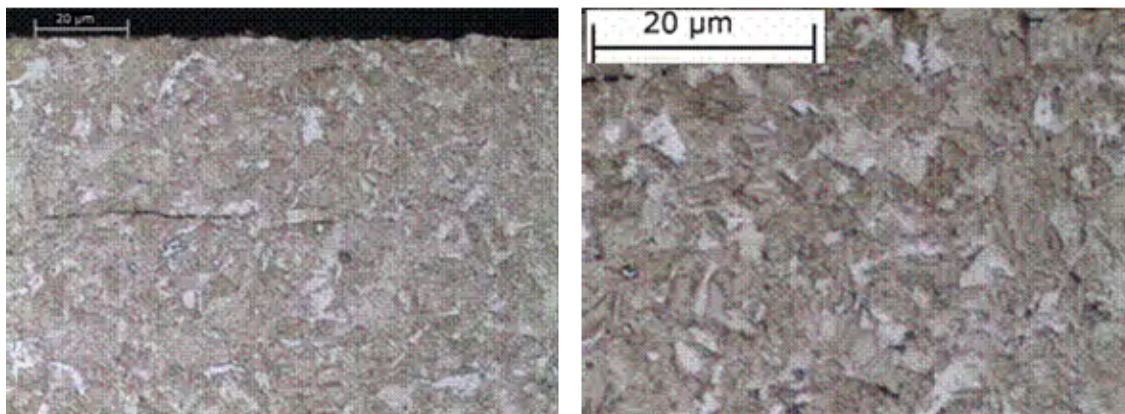


Fig.4. Quenched steel microstructure (etchant: nital 3%).

Both the mechanical ultimate strength value and the microstructural analysis show that for thin (0.8 mm) low carbon steel straps quenched in continuous flux, the austenite cooling transformation was without diffusion.

Although the microstructural analysis pointed out the presence of martensite grains, the XRD analysis showed only the ferrite specific peaks. The explanation is the low carbon content in the analyzed steel. It is known that in equilibrium cooling conditions ferrite can dissolve up to 0.002%C. The

analyzed steel had a carbon content of 0.185%, during the fast cooling of the austenite from furnace temperature (900°C) to water temperature (25°C) the carbon diffusion was virtually avoided hereby the oversaturated solid solution called martensite was obtained. The carbon over saturation degree that martensite can accommodate is practically much higher than the one resulted for this steel, hereby the tetragonality of the lattice is insignificant and unobservable by XRD (the martensite peaks overlap the ferrite peaks fig. 5).

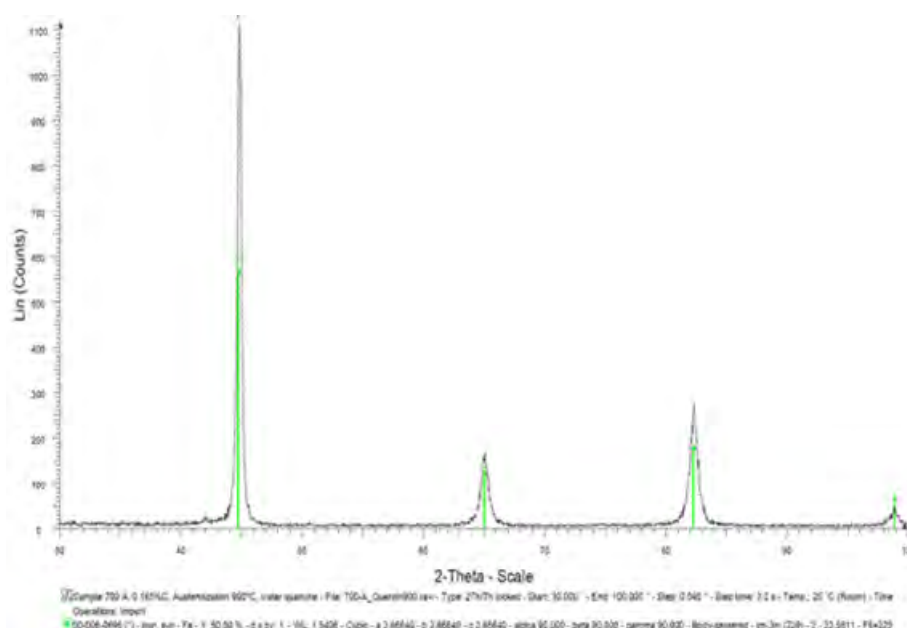


Fig. 5. XRD crystallographic structure.

X ray analysis showed that after the continuous flux thermal treatment the texture remains one

characteristic for cold rolled steel as shown in figure 6.

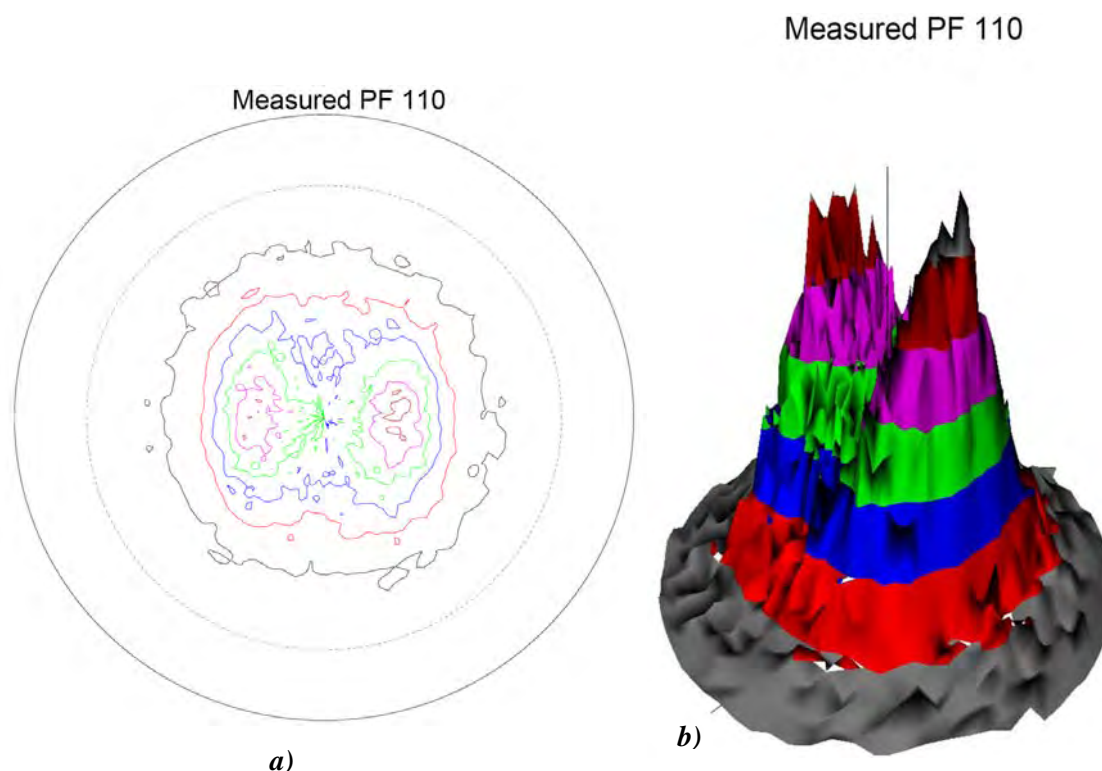


Fig. 6. XRD Pole Figure (110) – 2D (a) and 3D (b) representation.

3. Conclusions

By applying quenching thermal treatment on a continuous flux installation for a steel with 0.185%C high ultimate strengths can be obtained (1500 N/mm²) together with breaking elongations over 4%.

The research has shown that ordinary low carbon steels elaborated at convenient prices can enlarge their application area for products with thin sections (as packing steel straps) thereby hardenability can no longer be considered an obstacle in achieving high mechanical characteristics.

References

- [1]. ASM Handbook, Volume 1, Properties and Selection: Irons, Steels, and High Performance Alloys - Carbon and Low-Alloy Steels - Processing of Solid Steel – Annealing - Continuous Annealing
- [2]. ASM Handbook, Volume 4, Heat Treating - Heat Treating of Steel - Continuous Annealing of Steel
- [3]. ASM Handbook, Volume 4, Heat Treating - Heat Treating of

Steel - Quenching of Steel - Continuous Quenching

- [4]. ASM Handbook, Volume 4, Heat Treating - Heat Treating of Steel - Induction Heat
- [5]. ASM Handbook, Volume 4, Heat Treating - Section: Surface Hardening of Steel - Liquid Carburizing and Cyaniding of Steels - Furnaces and Equipment - Automatic and Semiautomatic Lines
- [6]. Cananau N., s.a. - Cercetări cu privire la călirea și revenirea tablei groase din oțel special cu limită de curgere ridicată. Analele Universității "Dunărea de Jos" Galați, fasc. 9, 1998 tom XVI(XXI), p. 302-306.
- [7]. Cananau, N. s.a. - Cercetări privind tratamentul termic de călire a tablelor groase din oțel A537. Analele Universității "Dunărea de Jos" Galați, fasc. 9, 1998 tom XVI(XXI), p. 307-312.
- [8]. Cananau, N. s.a. - Tratatamentul termic de revenire a tablelor groase din oțel A537. Analele Universității "Dunărea de Jos" Galați, fasc. 9, 1998 tom XVI(XXI), p. 313-318.
- [9]. F. Potecasu, O. Potecasu - The Temperature Influence on Mechanical Characteristics of Materials Hardened Through Deformation - Metalurgia International - ISSN 1582 – 2214, vol.XI, (2006) nr.8 - ISSN 1582 – 2214, pag.5-8
- [10]. F. Potecasu, O. Potecasu, P. Alexandru - Influence of the deformation degree on the structure and mechanical characteristics of steel sheets intended for producing car bodies - The 12th International Metallurgy & Materials Congress and Fair 28-30 sept 2005 Istambul, Turcia, e-book, ISBN 9944-89-073-1, 2005 p.89-95



STUDY OF THE THERMOMECHANICAL TREATMENT POST-DEFORMATION MAINTAINING TIME INFLUENCE ON THE MECHANICAL CHARACTERISTICS OF THE MICROALLOYED STEELS

**Elisabeta VASILESCU, Marian NEACȘU,
Ana DONIGA**

"Dunărea de Jos" University of Galati
email: elisabeta.vasilescu@yahoo.com

ABSTRACT

This paper-work shows the results of the laboratory researches of the post-deformation maintaining time influence on the physical-mechanical characteristics of the flat microalloyed steels, at high temperature thermomechanical treatments. The experiments have been made on the equipments of the Plastic Deformation and Thermal Treatments Laboratory from Faculty of Metallurgy and Materials Science using X60 steel – grade test specimen made at Mittal Steel Galati. The results of the laboratory experiments illustrated the importance of this technological parameter, which, together with temperature and deformation degree, decisively influences the structure and mechanical characteristics with a certain chemical composition of steel.

KEYWORDS: plastic deformation, thermomechanical treatment, post-deformation maintaining time.

1. Theoretical considerations

Combining the plastic deformation with thermal treatments is the most efficient way to put into operation all hardening mechanisms of steels (as hot or cold deformable ferro-alloys) this combination is the thermomechanical treatment essence.

The main part of the plastic deformation is due to the fact that, in this direct way, the crystallinity imperfections are created and, more than that, a certain oriented distribution of them is assured, which can be determinate by the used deformation diagram.

For a maximum hardening target, the light sliding plans of the structure are oriented to the external tangential tension direction, so that the metallic material plasticity is suddenly increased, even in hardened conditions.

To get to this basic target, the best way of the plastic deformation, the most efficient deformation degree, the best combination diagram of the thermal treatment with plastic deformation should be chosen and to correct, in an adequate way, the thermal treatment condition. When the deformation is made on the austenite at higher temperature than its simple

recrystallization temperature, the thermo mechanical treatment is considered of high temperature (TTMTI) (HTTMT)

High temperature thermo mechanical treatment (TTMTI) consists in an initial hot plastic deformation of the stable austenite and finally, under cooling and processing of the deformed austenite into martensite, pearlite or bainite. HTTMT I) results depend mainly on austenite condition during hot plastic deformation. The process of the hot plastic deformation could be controlled and analyzed by strain-deformation curve on which could be seen those four stages characteristics of the workable hardening (fig.1). The first stage is corresponding to a weak hardening by free and easy sliding of the grain dislocation and rotation. The second stage is characterized by an increased hardening, practically linear, determined by the multiple and broken dislocations, setting up obstacles in their movement (Cottrell-Lomer barriers, immobile steps in dislocations, dislocation agglomeration) the multiplication of the dislocation (the activation of the Frank-Read sources by the increase of the applied pressure). The dislocation density increases.

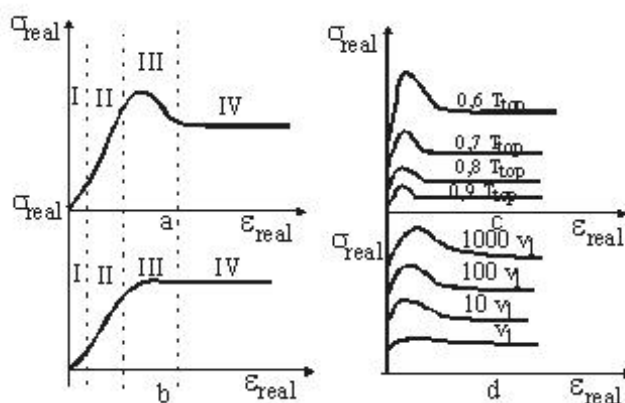


Fig.1. Deformation curve of the hot plastic deformation with hardening peak (point a) and without peak (b) and deformation temperature influence (c) and deformation speed (d) on the hardening curves.

The third stage is characterized by a slow down parabolic hardening determined by a plastic deformation and softening by the restoring and dynamic polygonizing. In this stage, up to the hardening peak, a polygonizing substructure is formed, with elongated subgrains, where a great density of free dislocations exists, unfixed in sub limits. After outrunning of the hardening maximum to the end of the third stage, the substructure is stable, polygonizing (getting a dynamic equilibrium condition) and subgrains become equiaxial, with more reduced density of the free dislocations. The second stage appears up to $\epsilon = 7...10\%$, when the hardening is increased and the third stage covers the deformation field from $\epsilon = 7...10\%$ up to ϵ_{max} . The fourth stage, established, is specific to hot plastic deformation. It is characterized by the deformation temperature and speed, i.e.: $T_{def} > 0,5 T_{top}$ and $\dot{\epsilon} > 10^{-4} s^{-1}$. In this stage, those two processes are balanced, softening determined by the restoring or dynamic recrystallization and hardening due to plastic deformation.

The development way of each of the mentioned stages depending on the internal parameters, material (chemical composition, atoms movability, energy of the packing defects) and external, technological parameters (deformation and temperature degree, post-deformation maintaining time, deformation speed).

Thus, according to the manufacturing conditions where the hot deformation is made, the metallic material might be in many various structural conditions, which go from the (hot) hardening condition up to that of static recrystallization (refining). This could be then fixed by quick later-on cooling, influencing the development of the subsequent transformation, final structure and metallic material characteristics.

Post-deformation maintaining time is a parameter for thermo mechanical treatment. The higher its value, the more favored are its polygonization and static recrystallization in detriment to the hot hardening structure, particularly the ratio of polygonized volume and hardened volume increases, though the volume of the polygonized austenite might increase or decrease according to the recrystallization process. Simultaneously, the density of dislocation in hardened and polygonized volumes decreases, as well as the global density (volume) of dislocations (which reaches values of $1,2 \cdot 10^9 - 2 \cdot 10^9 cm^{-2}$).

Experimental conditions

For experiments, test specimen of X60 steel grade has been used having chemical composition and mechanical characteristics mentioned in **Table no.1**, and size of 5x10x70 mm.

Table 1 Chemical composition and mechanical characteristics of test specimen X60 steel grade

C	Mn	Si	V	Al	Nb	Ti	Rm	Rp _{0,2}	A
[%]							[MPa]		[%]
0,09... 0,12	1,30... 1,60	0,17... 0,30	0,03... 0,08	0,015... 0,05	0,03... 0,05	max. 0,02	min 413	min 331	min. 22

Test specimen heating was made in the electrical furnace with sillite bars, at 900°C temperature of all experimented ranges. The maintaining time in the furnace, calculated according to the specimen thickness, was 15 minutes for all conditions.

The rolling was made in the laboratory rolling mill with rolls diameter $D = 129\text{mm}$.

More thermo mechanical treatment conditions have been experimented, such as:

- one pass rolling with deformation degree $\varepsilon_1 = 15\%$; $\varepsilon_2 = 30\%$

- air still maintaining time after deformation 5, 10, 20, 40 seconds, and then water cooling. The first test specimen has been cooled directly in water (maintaining time: 0 seconds) without air maintaining, and the last one was cooled in air only.

Experiments results

a) The first series of the test specimen has been rolled with $\varepsilon_1 = 15\%$. After thermo mechanical treatment, the test specimen has been processed and then submitted to the mechanical tests. The results are mentioned in **Table 2** and diagrams fig.2.

Table 2. Mechanical characteristics of the test specimen rolled with $\varepsilon_1 = 15\%$

Test specimen number	Post-deformation maintaining time	Mechanical characteristics			
		Rm	Rc	A	Hardness
$\varepsilon_1 = 15\%$	(seconds)	[MPa]		[%]	[HB]
1	0	775	630	19	286
2	5	760	622	20	268
3	10	703	590	21	255
4	20	678	599	22	252
5	40	671	555	23	250
6	60	576	432	33	190

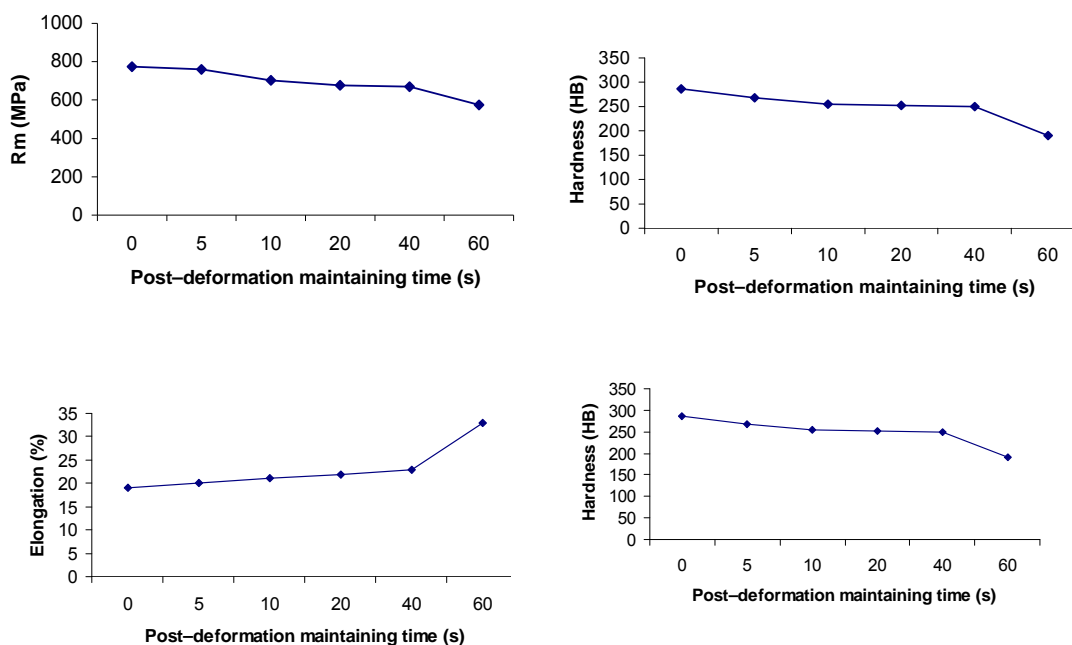


Fig.2 The influence of the post-deformation maintaining on the test specimen mechanical characteristics rolled with $\varepsilon_1 = 15\%$.

b) The second series of the test specimen has been rolled with $\varepsilon_2 = 30\%$. After thermo mechanical treatment conditions, the mechanical characteristics

have been determined. The results are mentioned in Table 3, and diagrams fig.3



Table 3. Mechanical characteristics of the test specimen rolled with $\varepsilon_2 = 30\%$

Test specimen number	Post-deformation maintaining time (seconds)	Mechanical characteristics			
		Rm	Rc	A	Hardness
$\varepsilon_1 = 30\%$		[MPa]		[%]	[HB]
7	10	726	619	23	261
8	20	686	514	27	230
9	40	637	487	29	225
10	60	580	423	30	193

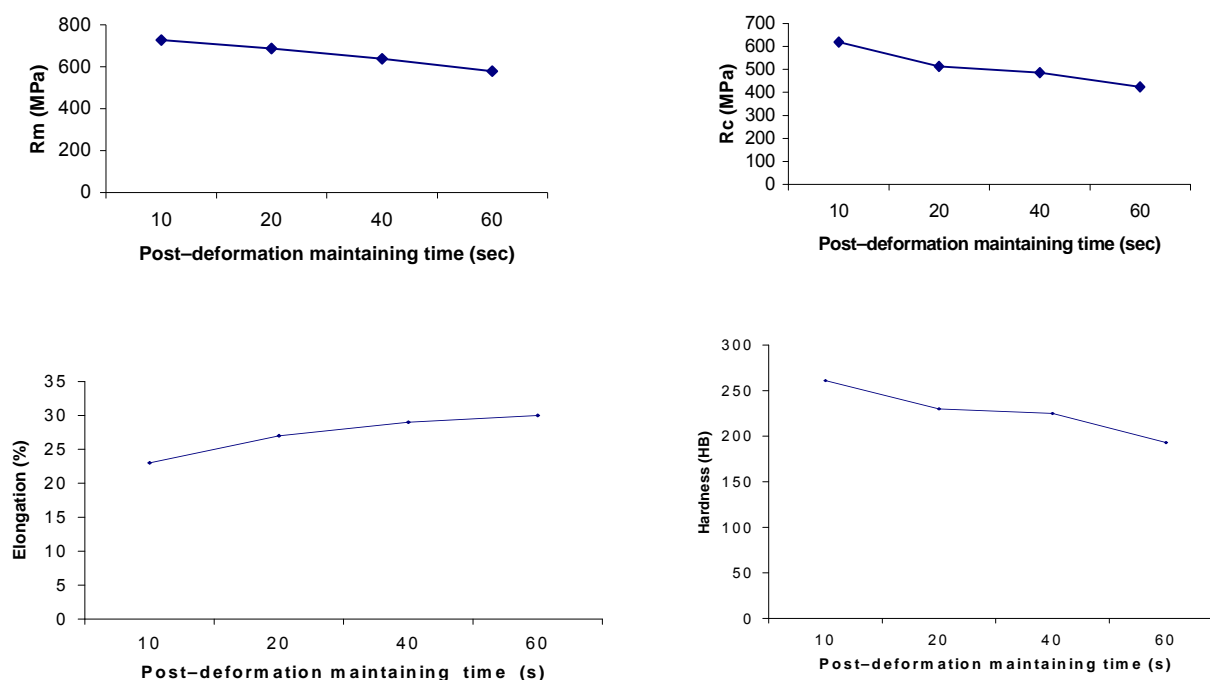


Fig.3 The influence of the post-deformation maintaining time on the test specimen mechanical characteristics rolled with $\varepsilon_2 = 30\%$.

Table 4 show the mechanical characteristics values comparatively, R_m and R_c , to the post-deformation maintaining time for the two test specimen groups (rolled with $\varepsilon_1 = 15\%$ and $\varepsilon_2 = 30\%$).

Table 4. Mechanical characteristics of the test specimen rolled with $\varepsilon_1 = 15\%$ and $\varepsilon_2 = 30\%$

Post-deformation maintaining time	$\varepsilon_1 = 15\%$		$\varepsilon_2 = 30\%$	
	Rm	Rc	Rm	Rc
	[MPa]			
0	775	630		
5	760	622		
10	703	590	726	619
20	678	599	686	514
40	671	555	637	487
air	576	432	580	423

As it could be seen from these experiments, the post-deformation maintaining time influences appreciably the mechanical characteristics of both deformation degrees. Generally, strength characteristics decrease with post-deformation maintaining time increase and elongation increases.



The low values of the maintaining time (0-10 seconds) approach the cooling to the hardening of the plastic deformed austenite. The maintaining time increase determines an increase of the recrystallized austenite volume, even a slight increase of the grains, determining a decrease of the strength characteristics, R_m and R_c , and elongation increase, too (**Tables 2 and 3**). The mechanical characteristics values (R_m and R_c) are comparable for the two deformation degrees, as it can be seen in fig.3, for the same post-deformation maintaining time. As regarding the deformation degree, it is ascertained that for $\epsilon_2 = 30\%$, the elongation values begin to exceed the minimum limit specified by standards, the strength characteristics being kept at high enough values. As usually, for TTMTI it is recommended a deformation degree of 25-30% according to the real possibilities of the equipment used.

Conclusions

In case of thermo mechanical treatments, the post-deformation maintaining time is an important technological parameter because it influences,

together with the deformation degree and final rolling temperature, the processing way of the austenite static recrystallization, which, finally, leads to achieving certain mechanical characteristics. This is the reason why, in the rolling mills where these technologies can be applied, the distance between the finishing stand of the mill and the accelerated cooling installation of the heavy plates is extremely important.

References

- [1]. Doniga A, Vasilescu E, Udvuleanu A. - *Bazele teoretice ale tratamentelor termomecanice* E.D.P. 2004
- [2]. Popescu, N. - *Tratamente termice neconvenționale* Editura Tehnică București, 1990
- [3].**** *Fundamentals of the Controlled Rolling Processes*, Niobium Information nr.2/1994
- [4].**** *Thermomechanically Rolled Flat Products*, Niobium Information nr.5/1995
- [5].**** *Normalized HSLA Steels* - Niobium Information nr.8/1995
- [6].**** *Ferroniobiu Alloying Technologies* - Niobium Information nr.6/1994
- [7]. Taloi, D. Florian, E. - *Optimizarea proceselor metalurgice* Editura didactică și pedagogică, București, 1983.



CONTRIBUTION OF HEAT AND THERMOCHEMICAL TREATMENTS TO THE IMPROVEMENT OF THE PERFORMANCES OF HIGH-SPEED STEEL TOOLS

Nicoleta TORODOC, Ioan GIACOMELLI

"Transilvania" University of Brasov
email: nicotorodoc@yahoo.co.uk

ABSTRACT

The In this paper the influence of non-conventional heat and thermo chemical treatments upon the structure of tool steels and implicitly, upon the performances that are derived from applying such treatments, is presented. Reference is made to the conditions in which the heat and thermo chemical treatments in vacuum and in electrolyte baths are carried out. The advantages of these procedures are evidenced both from a technical as well as an economic standpoint.

The experiments have been carried out on Rp3 and Rp5 steels, with application of vacuum at the final heat treatments.

KEYWORDS: cyanurated layer, electrically activated salts

1. Introduction

In the modern industry which uses more and more materials with superior quality properties, the usual thermal treatments start to be replaced with new technology.

The most important reason for the introduction of new technologies is the necessity to comply with the requirements of the quality standard ISO 9000.

The important steps of this standard are connected to the flow of raw materials, as well statistic control and TQM-receptions services.

An essential step was the appearance of the concept of a "clean product" that has determined direct actions of modification of high technologies, that are friendly to the environment.

The introduction on a large scale of the automation of technological processes for metalworking, of the use of high speed turning is accompanied by the increase of demands on the metalworking tools.

The characterization of the diverse types of tool steels can be effected on the basis of the newest technologies and from the experience of the tool producing factories.

Thermal treatments in vacuum

The principal purpose of thermal treatments in vacuum is to protect products surface against physico-chemical actions of environments of usual heating.

This way thermal treatments in vacuum can be a good solution from many points of view, in comparison with usual thermal treatments in protective atmospheres or salt baths. Because the heating ovens in the vacuum heat treatment procedure can function over a wide interval of temperature, but in special at high temperature (over 700°C), this procedure allows treatment of almost all metallic materials used now in industry. The first types of ovens for vacuum heat treatment consisted of a room that could be voided, mounted in an oven heatable with electrical resistances, with walls consisting of refractory bricks kept warm. With time these ovens have been optimized regarding heat utilization yields.

The construction of new types of vacuum ovens has increased the use of vacuum heat treatments. A new type of heat treatment oven has been designed that is used at temperatures of 1300 °C, at an advanced vacuum, at high thermal yield. Heat treatments in vacuum can be of the type: degassing, annealing, quenching and thermo chemical treatments.

In *table 1* the main parameters of heat treatment for the Rp5 high-speed steel samples are indicated.

Table 1. The main parameters of heat treatment for the Rp5 high-speed steel samples

Nº.	Type of heat treatment	Heating parameters			Cooling conditions			Hardness
		Pressure	Temperature	Time	Parameters		Medium	
					v	T _{final}		[HRC]
		[torr]	[°C]	[min]	[°C/h]	[°C]		
1.	Annealing for globulizing	10 ⁻³	760	120	35	590	N ₂ recycled	32-34
2.	Quenching	10 ⁻²	870	40	30	65	N ₂ purified	60-61
		0.2-0.3	1220	7-10				
3.	Tempering	400	560-570	2x 90		65	N ₂ purified	62-63

3. Thermo chemical treatment in electrically activated salt baths

The favorable effect of electrolysis being known upon the diffusion processes at low temperature thermo chemical treatments, the stimulation of this process at the cyanuration of high-speed steels has been undertaken.

Samples of Rp5 high speed steel, after oil quenching from 1290 °C and a tempering of 1.5 hours at 560°C, have been cyanurated at the same temperature in a salt bath containing 23% sodium cyanate. Also, an electrical tension has been applied between the interior wall of the vessel and the device containing the samples.

At the electrolysis in stationary electric current, the anodic dissolving process takes place; this process has been evidenced also at lower temperatures (180-200°C) at anodic sulphurization.

The increase of the bath temperature has as an effect the increase of the metal losses from the work pieces. In order to avoid this process, alternative electrical current has been used, at the industrial frequency of 50 Hz.

The measurements carried out in this case revealed that under such conditions the losses by dissolving are negligible. In table 2 and fig 1 the results obtained in these experiments are presented.

Table 2. Results obtained at thermo chemical treatment for Rp5 steel

N ^o	Current density [A/dm ²]	Layer thickness		
		10 min	15 min	20 min
		[mm]		
1.	0	0.008	0.137	0.0160
2.	1.02	0.0173	0.0195	0.0250
3.	2.05	0.0180	0.0233	0.0273
4.	3.5	0.0187	0.0296	0.031

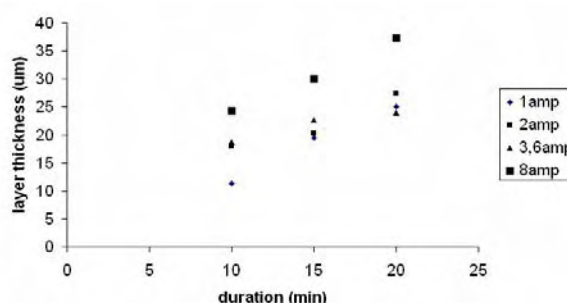


Fig. 1. Influence of current intensity and duration upon the cyanurated layer thicknesses

In fig. 2 the variation of the current density on the thickness of the cyanurated layer is shown.

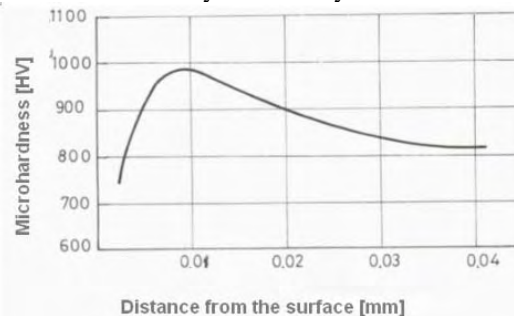


Fig. 2. Variation of the microhardness of the cyanurated layer $t=20$ min at $d=3,5A/dm^2$

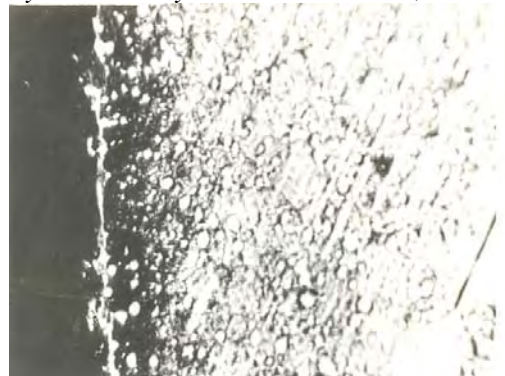


Fig 3. Rp5 steel cyanurated 20 min at $d=0 A/m^2$. Nitral attack, magnify: 750:1.

A positive influence of electrical stimulation has been noticed, at applying electric current the increase of diffusion speed is significant. The stepwise increase of current density has a favorable effect, but not directly proportional. The explanation can be the increase (sometimes minor) of the rate of the dissolving process, that is manifesting in some measure under these conditions.



Fig. 4. Rp5 steel cyanurated 20 min at $d=3,5A/m^2$, Nital attack, magnify: 700:1.

The structure of the basis material is composed from martensite of tempering origin, carbides and residual austenite. The superficial diffusion layer, of white color, contains nitrous martensite, carbides and nitrides. In the superficial layer of white color, in larger amounts, nitrides and special carbides are present.

4. Conclusions

The modern heat treatment and thermo chemical treatment procedures have an increasing spread in the industry due to the advantages which these have, such

as:

For heat treatments in vacuum:

- higher values of the hardness
- work conditions that are more hygienically,
- more advanced protection of the environment
- the elimination of supplementary operations

For thermo chemical treatment under electrical stimulation:

- the significant increase of the diffusion rate
- the realization of diffusion layers with high performance properties
- the possibility of remaking the thermo chemically treated layer, after wear of the active part of the cutting tool etc.

Even if one works with salt mixtures that contain toxic components, the procedure can be successfully used with special tools and high-precision tools, that need special qualities.

References

- [1] Giacomelli, I., Druga L., Samoila C., Bot D. - *Tehnologii neconventionale cu transformari de faza*- Editura Lux-Libris, Brasov 2200
- [2] Dulamita T. - *Oteluri de scule-proprietati, tratamente termice, utilizari*.- Editura Tehnica-Bucuresti 1990.
- [3] V.I. Popescu, C. Chiriac - *Oteluri rapide*- Editura Agir 2002
- [4] Krauss G. - *Principles of Heat Treatment of Steel*- Metallurgy and Technology by, ISBN- 13:978-087170108
- [5] Henley W. - *Hardening, tempering, annealing and forging of steel: Including heat treatment of modern alloy steels: a complete treatise on the practical treatment and working of high and low grade steel* by ASIN: B 00086U8F8
- [6] *Heat Treatment of High-Speed Steels*, <http://www.key-to-steel.com/Articles/Art57.htm>
- [7] *Effects of heat treating high-speed, steel-cutting tools*, *American Machinist Journal*, findarticles.com/p/articles/mi_hb008/is_199806/ai_hibm1P129025 259.



IMPLICATIONS OF THERMAL AND THERMO CHEMICAL TREATMENTS IN ELECTROLYTIC PLASMA ON THE PHASIC COMPOSITION OF STEELS 40Cr10 and OLC 55

Maria BACIU, Teofana Emilia NECHITA

Technical University "Gh. Asachi" Iași
email: maria_baciu2004@yahoo.co.uk

ABSTRACT

The X-ray diffraction researches allowed the identification of the phases present in the structure of steels 40Cr10 and OLC 55, treated thermally and thermal-chemically in electrolytic plasma and the calculation of concentration of the structural phases identified. .

KEYWORDS: electrolytic plasma, steels, nitration, X-ray diffraction

1. Introduction

The analysis of the phase composition of the steels 40Cr10 and OLC 55, treated thermally and thermal-chemically in electrolytic plasma allows the establishing of a correlation between the technological parameters of the processing methods and the physical-mechanical properties obtained in the end.

The experimental determinations were effectuated by X-ray diffraction, the analysis of diffraction diagrams allowing the identification of phases present in the structure of each sample and the

calculation of the plane spacing d_{hkl} and the phase concentration.

2. Experimental procedure

The experimental researches were effectuated by cylindrical samples $\phi 15 \times 50$ mm, from the steels 40Cr10 and OLC 55, processed thermally by anodic heating in watery electrolytes according to the conditions presented in table 1. The diffraction diagrams were obtained by the device DRON 2, using radiations MoK_{α} and FeK_{α} . The interval analysed is comprised between: $2\theta = 15^{\circ} \dots 40^{\circ}$

Table 1. Technological parameters of thermal and thermal-chemical treatment in electrolytic plasma

No. crt.	Steel type	Sample	Thermal and thermal-chemical treatment applied	Technological parameters of thermal processing
1	40Cr10	3B	nitration + tempering + bluing	$T_{inc} = 650^{\circ}C$; $t_{inc} = 6$ min $T_{rev} = 350^{\circ}C$; $t_{rev} = 1$ h
2		3D	nitration + tempering	$T_{inc} = 700^{\circ}C$; $t_{inc} = 6$ min
3		3HH	nitration + tempering + bluing	$T_{inc} = 750^{\circ}C$; $t_{inc} = 6$ min $T_{rev} = 350^{\circ}C$; $t_{rev} = 1$ h
4		3A	nitration + tempering	$T_{inc} = 650^{\circ}C$; $t_{inc} = 6$ min $T_{aust} = 750^{\circ}C$
5	OLC 55	4V	nitration + tempering + bluing	$T_{inc} = 650^{\circ}C$; $t_{inc} = 6$ min $T_{rev} = 350^{\circ}C$; $t_{rev} = 1$ h
6		4DD	nitration + tempering	$T_{inc} = 700^{\circ}C$; $t_{inc} = 6$ min
7		4MM	nitration + tempering + bluing	$T_{inc} = 750^{\circ}C$; $t_{inc} = 6$ min $T_{rev} = 350^{\circ}C$; $t_{rev} = 1$ h
8		4Y	nitration + tempering	$T_{inc} = 650^{\circ}C$; $t_{inc} = 6$ min $T_{aust} = 750^{\circ}C$

3. Experimental results

In figures 1...8 we present the diffraction diagrams obtained.

On the diffraction diagrams we identify the peaks of high intensity specific to phases and diffraction planes:

- austenite: (111); (200); (220); (311);
- martensite: (110); (200); (211);
- nitrides: Fe₃N.

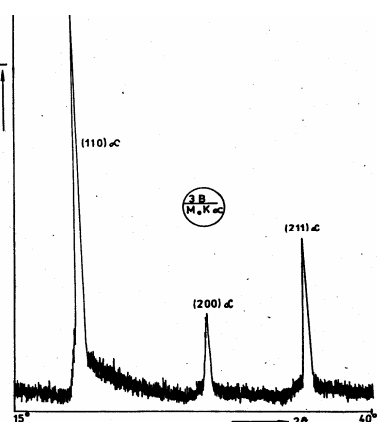


Figure 1. Diffraction diagram of steel 40Cr10 nitrated and tempered in electrolytic plasma and subsequently blued at 350°C in oven – sample 3B.

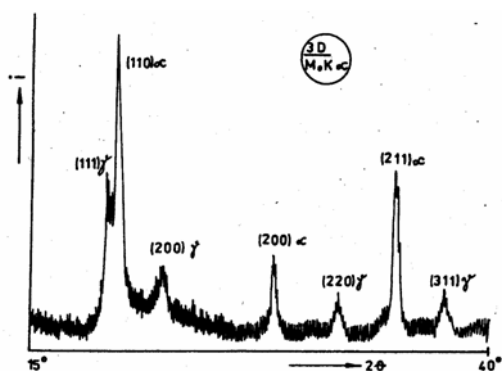


Figure 2. Diffraction diagram of steel 40Cr10 nitrated and tempered in electrolytic plasma – sample 3D.

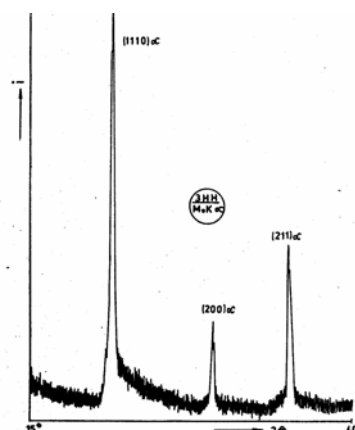


Figure 3. Diffraction diagram of steel 40Cr10 nitrated and tempered in electrolytic plasma and subsequently blued at 350°C in oven – sample 3HH.

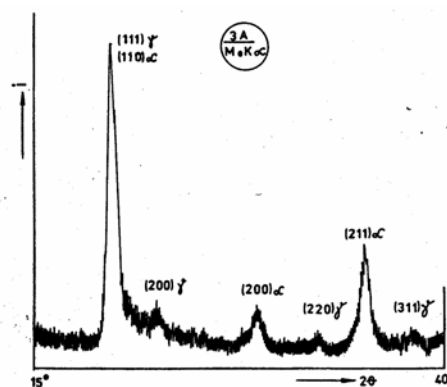


Figure 4. Diffraction diagram of steel 40Cr10 nitrated and tempered in electrolytic plasma – sample 3A.

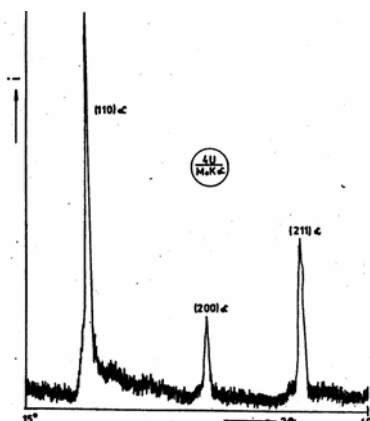


Figure 5. Diffraction diagram of steel OLC 55 nitrated and tempered in electrolytic plasma and subsequently blued at 350°C in oven – sample 4V.

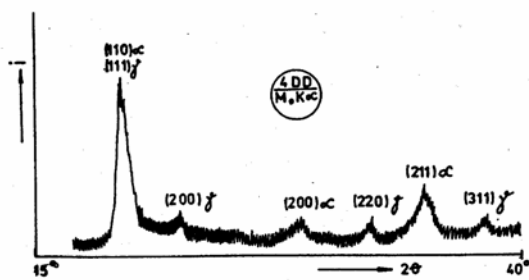


Figure 6. Diffraction diagram of steel OLC 55 nitrated and tempered in electrolytic plasma – sample 4DD.

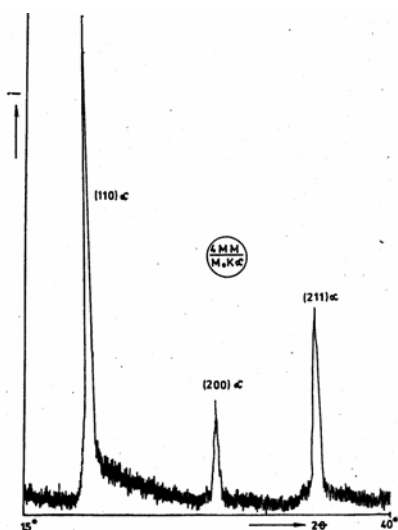


Figure 7. Diffraction diagram of steel OLC 55 nitrated and tempered in electrolytic plasma and subsequently blued at 350°C in oven – sample 4MM.

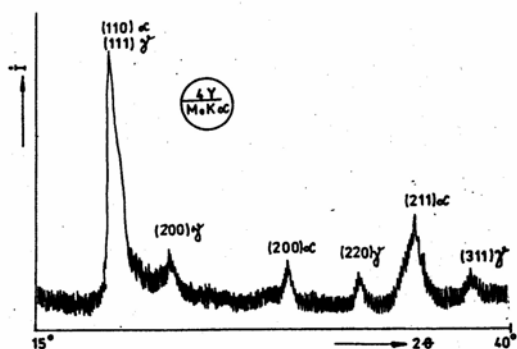


Figure 8. Diffraction diagram of steel OLC 55 nitrated and tempered in electrolytic plasma – sample 4Y.

Table 2. Plane spacing and phase nature presented in the structure of steel 40Cr10 nitrated and tempered in electrolytic plasma and subsequently blued at 350°C in oven – sample 3B

d_{hkl}	Phase	(h k l)
2,053	α	110
1,4378	α	200
1,1646	α	211

Table 3. Plane spacing and phase nature presented in the structure of steel 40Cr10 nitrated and tempered in electrolytic plasma – sample 3D

d_{hkl}	Phase	(h k l)
2,076	γ	111
2,024	α	110
1,8161	γ	200
1,4364	α	200
1,2857	γ	220
1,1763	α	211
1,0929	γ	311

Table 4. Plane spacing and phase nature presented in the structure of steel 40Cr10 nitrated and tempered in electrolytic plasma and subsequently blued at 350°C in oven – sample 3HH

d_{hkl}	Phase	(h k l)
2,024	α	110
1,4328	α	200
1,1692	α	211

Table 5. Plane spacing and phase nature presented in the structure of steel 40Cr10 nitrated and tempered in electrolytic plasma – sample 3A

d_{hkl}	Phase	(h k l)
2,076	α+γ	110 _α +111 _γ
2,024	α	110
1,8161	γ	200
1,4364	α	200
1,2857	γ	220
1,1763	α	211
1,0929	γ	311



Table 6. Plane spacing and phase nature presented in the structure of steel OLC 55 nitrated and tempered in electrolytic plasma and subsequently blued at 350°C in oven – sample 4V

d_{hkl}	Phase	(h k l)
2,0510	α	110
1,4369	α	200
1,1716	α	211

Table 7. Plane spacing and phase nature presented in the structure of steel OLC 55 nitrated and tempered in electrolytic plasma – sample 4DD

d_{hkl}	Phase	(h k l)
2,0680	$\alpha+\gamma$	$110_{\alpha}+111_{\gamma}$
1,8161	α	200
1,4364	α	200
1,2800	γ	220
1,1777	α	211
1,0908	γ	311

Table 8. Plane spacing and phase nature presented in the structure of steel OLC 55 nitrated and tempered in electrolytic plasma and subsequently blued at 350°C in oven – sample 4MM

d_{hkl}	Phase	(h k l)
2,0580	α	110
1,4443	α	200
1,1739	α	211

Table 9. Plane spacing and phase nature presented in the structure of steel OLC 55 nitrated and tempered in electrolytic plasma – sample 4Y

d_{hkl}	Phase	(h k l)
2,0686	$\alpha+\gamma$	$110_{\alpha}+111_{\gamma}$
1,8278	α	200
1,4400	α	200
1,2800	γ	220
1,1787	α	211
1,0904	γ	311

As for the concentration of the phases present in the structure of the samples investigated, we determined the values presented below table 10.

Table 10. Technological parameters for thermal and thermal-chemical treatment in electrolytic plasma

Sample	v_{α} , [%]	v_{γ} , [%]	v_N , [%]
3B	100	-	-
3D	78,30	21,70	-
3HH	100	-	-
3A	65,80	8,30	25,90
4V	100	-	-
4DD	70,30	12,40	17,40
4MM	100	-	-
4Y	64,70	14,10	21,20

4. Conclusions

1. The Roentgen structural investigations effectuated pointed out the nature of phases present in the structure of the two steels processed thermally in electrolytic plasma: nitrogen-based martensite (nitromartensite); residual austenite and chemical compounds (nitrites).

2. The structural phases identified correspond to the thermal-chemical treatment applied, their concentration being dependent on the two main technological parameters: temperature and diffusion time.

Thus, in the improving steels 40Cr10 and OLC 55 nitrated, we notice a reduction of the nitride quantity once with the increase of the diffusion temperature.

3. The application of bluing in oven after nitration and tempering in electrolytic plasma has as effect the complete transformation of the residual austenite in cubic martensite.

References

- [1]. Baci, Maria, Contributions on the structural and property changes of thermally and thermochemically treated steels in electrolytic plasma (in Romanian), PhD thesis, „Gh.Asachi” Technical University from Iași, 1999.
- [2]. Belkin, P.N., Ignat'kov, D.A., Pasinkovskij, E.A., Azotirovanie v elektrolitnoj plazme, Kolloquium Eigenspannungen und Oberflächen-verfestigung, p.265, 1982.
- [3]. Belkin, P.N., Pasinkovskij, E.A. Termičeskaâ i himiko - termičeskaâ obrabotka stalej pri nagreve v rastvorah elektrolitov, Metallovedenie i termičeskaâ obrabotka metallov, nr.5, pag.12-17, 1989.
- [4]. Duradži, V.N., Parsadanian, A.S., Nagrev, metallov v elektrolitnoi plazme (lb. rusă), Ed. Stiinca, Kișinev, 1988.



STUDY OF TRIBOCORROSION PROCESSES BY ELECTROCHEMICAL TECHNIQUES

Lidia BENEĂ, Viorel DRĂGAN

"Dunărea de Jos" University of Galati

Competences Center Interfaces – Tribocorrosion and Electrochemical Systems (CC-ITES)

email: Lidia.Benea@ugal.ro

ABSTRACT

Tribocorrosion is defined as the chemical-electrochemical-mechanical process leading to a degradation of materials in sliding, rolling or erosion contacts immersed in a corrosive environment. That degradation results from the combined action of corrosion and wear. The mechanism of tribocorrosion is not yet fully understood due to the complexity of the chemical, electrochemical, physical, and mechanical processes involved. Examples of the occurrence of tribocorrosion in service are the accelerated corrosion of steel conveyors exposed to ambient air of high relative humidity, the fall out of electrical connectors in the automotive industry, the degradation of hip prosthesis and dental fillers, the erosion wear of turbine blades, etc. The combined corrosion-wear degradation of materials in sliding contacts immersed in electrically conductive solutions is investigated in-situ by electrochemical techniques. Such techniques are the open circuit potential measurements, E_{OC} , the potentiodynamic polarization measurements, PD and the electrochemical impedance. Capabilities and present limitations of these techniques are discussed based on a tribocorrosion study of a cobalt chromium alloy hard coating (Stellite6) and stainless steel (304L) immersed in water-based electrolytes, namely aerated 0.5 M sulphuric acid, Ringer solution or cooling water reactor (12 ppm Li as LiOH+1000 ppm Boric Acid) and sliding against a corundum counterbody. Some novel insights into the tribocorrosion mechanism of active and passive materials are discussed. These in-situ electrochemical data provide insights into a possible synergism between corrosion and wear processes in sliding contacts. This paper concludes on the benefit of using different electrochemical analyzing techniques when investigating the behaviour of materials under corrosion-wear test conditions.

KEYWORDS: tribocorrosion, active, passive, cobalt-chromium alloy, stainless steel 304L, electrochemical techniques.

1. Introduction

In industry corrosion and wear are responsible for maintenance expenses and loss of productivity resulted from the shortened life of components and catastrophic failure leading to massive costs of the replacement and litigation [1, 2].

Tribocorrosion is defined as the chemical-electrochemical-mechanical process leading to a degradation of materials in sliding, rolling or erosion contacts immersed in a corrosive environment. That degradation results from the combined action of corrosion and wear. The mechanism of tribocorrosion

is not yet fully understood due to the complexity of the chemical, electrochemical, physical, and mechanical processes involved. Examples of the occurrence of tribocorrosion in service are the accelerated corrosion of steel conveyors exposed to ambient air of high relative humidity, the fall out of electrical connectors in the automotive industry, the degradation of hip prosthesis and dental fillers, the erosion wear of turbine blades, etc. The evidence of tribocorrosion wear in pressurized water reactors was reported recently by Lemaire and Le Calvar [3]. Some authors have reported on a modification of the surface state of materials in sliding contacts, which results from mechanical, chemical and



electrochemical processes [4-6]. That interaction is of increasing interest since it may result in a new concept of operating materials under lubrication-free sliding or rolling conditions. Indeed, such tribo-reactive surface layers may modify the corrosion process on contacting materials that in turn may modify friction and wear of materials.

Recently, there has been an increase in the interest on the investigation of the combined corrosion-wear degradation of materials by electrochemical methods. The influence of passivity on the tribocorrosion of carbon steel and TiN coatings in aqueous solutions was investigated by Mischler et al. [7, 8]. They used potentiodynamic polarization measurements and performed tests under electrochemical control at different potentials. They concluded that the potential dependence of corrosion-wear is most likely due to the potential dependent lubricating properties of the thin surface films formed in the passivation region. Takadom [9] investigated the influence of potential on the tribocorrosion of nickel and iron in sulfuric acid solutions. He concluded also that potential affects greatly friction and wear processes. Depending on the applied potential, either corrosion, wear or a conjoint action between them leads to a material loss. Mischler and Ponthiaux [10] reported on a round robin action related to the combined electrochemical and sliding tests on corundum/stainless steel contacts immersed in diluted sulfuric acid. The reproducibility and scattering of their results appeared not to be significantly affected by sliding, and thus they conclude that electrochemical experiments can be correctly carried out in sliding corrosion-wear tests. Watson et al. [11] reported on methods for measuring the corrosion-wear synergism. They proposed penetration rate equations to quantify the wear and corrosion processes as well as the corrosion-wear synergism based on experimentally determined polarization resistance and Tafel slopes. A microelectrochemical technique, in which the current of a metal probe in an electrolyte under rubbing conditions is measured, was proposed by Assi and Böhni [12] to study the corrosion-wear synergy. Their technique allows the study of the repassivation kinetics of surface areas activated by tribocorrosion processes. Ponthiaux et al. [13] used electrochemical noise measurements for the determination of the depassivated area in sliding contacts. They found an interesting correlation between the electrochemical noise and the mechanical processes occurring in sliding contacts. From these investigations it can be concluded that some electrochemical techniques do provide interesting information on the surface state of materials in sliding contacts, but the unravelling of these experimental data towards modelling of tribocorrosion processes, is still very limited.

That modeling of tribocorrosion is indeed rather limited in literature, and the modeling done does not yet allow a correlation between electrochemical data and material losses in corrosion-wear sliding contacts or a predictive approach of the corrosion-wear synergism. Jemmely et al. [14] proposed an electrochemical modeling of the passivation phenomena in tribocorrosion. That model was developed taking into account the film growth kinetics and the ohmic drop in the electrolyte between wear scar and reference electrode. The model could simulate the general trends observed in current transients but the agreement with experimental data was only fair. Reasons put forward by them are an insufficient insight in the electrochemical conditions in the contact zone and the role of the third body particles. Garcia et al. [15] analysed the corrosion-wear of passive materials in sliding contacts based on a concept of active wear track area in combination with Quinn's mild-oxidation model. Polarization curves were determined under mechanically unloaded and loaded conditions. From that active wear track area and by using repassivation kinetics of bare metals, the material loss in corrosion-wear sliding tests was analysed. Mischler et al. [16] proposed a model that describes the effect of mechanical and materials parameters on the wear-assisted corrosion rate of passive metals under sliding wear conditions. They concluded that to understand the mutual interaction between mechanical and electrochemical parameters affecting wear-accelerated corrosion it is necessary to look at the tribocorrosion system as a whole.

In this paper, an overview of electrochemical and surface analysis techniques of interest for studying specifically the in-situ tribocorrosion process is presented. Experimental data obtained by these electrochemical analysis techniques on the tribocorrosion behaviour of a cobalt chromium alloy hard coating (Stellite6) and stainless steel (304L) immersed in water-based electrolytes, namely aerated 0.5 M sulfuric acid, Ringer solution or cooling water reactor (12 ppm Li as LiOH+1000 ppm Boric Acid) are reported. These two materials are representative for respectively passive and active materials at open circuit potential [17, 18]. The aim is to demonstrate capabilities and present limitations of these techniques for studying the degradation processes of materials in sliding contacts immersed in an electrolyte. Although, attempts are not yet been made to correlate these electrochemical data with material losses in sliding contacts, the in-situ information gathered in this way on the surface state of materials in sliding contacts is expected to support further modelling work.

In many tribocorrosion systems the passivable materials are used. The passive properties of Stellite6

are of great importance in PWR environments, because the nature of the oxide films governs the corrosion release rate and the oxides are involved in plant dosimetry. Chromium enhances passivation of the cobalt alloys and stainless steel, in the presence of oxygen, and is the key ingredient with regard to corrosion resistance in oxidising media.

2. Experimental

Both uni-directional pin-on-disk and ball-on-disk contact geometry have been used in this investigation. Schematic diagrams of the setups are given in Fig. 1. Pin-on-disk and ball-on-disk materials were immersed in the electrolyte and placed in an electrochemical cell containing a counter electrode and a reference electrode. The disks were made of either cobalt chromium alloy (Stellite6) and stainless steel (304L). Stainless steel and cobalt chromium alloy were selected for their good corrosion resistance that results from the formation of a nanometer thick protective oxide layer (passive film) at its surface in contact with air and or with many oxidizing electrolytes in open circuit potential conditions.

Just before immersion in the electrolyte, the disks were degreased by dipping in alcohol. The pins made of corundum (Al_2O_3), an electrically non-conductive material, were degreased in alcohol and loaded on the disk. All sliding tests were carried out at a constant rotation speed between 30 and 120 rpm. Depending on the tribometer used, friction was generated by applying a load on the rotating disk facing downwards, against the fixed corundum ball (Fig. 1 a), or by rotating the corundum pin against the fixed disk facing upwards (Fig. 1 b).

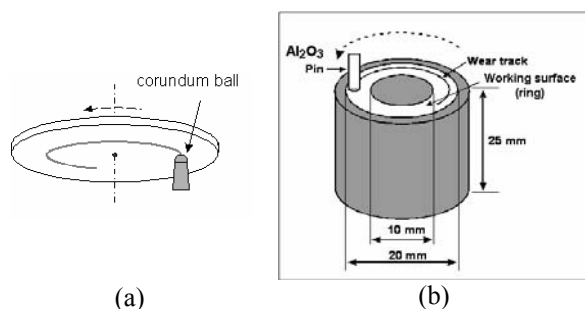


Fig. 1. Schematic description of the ball-on-disk (a) and pin-on-disk (b) se-tups used to study Stellite6 and stainless steel respectively

Despite these differences, the results of the tribocorrosion tests carried out on both tribometers were found to be in very good agreement for the same tribocorrosion conditions (sliding speed or contact frequency, normal load, electrochemical conditions).

Such uni-directional sliding conditions lead, in contrast to alternating (bi-directional) contact conditions like fretting [18], to a steady electrochemical condition all over the wear track area on the disk material [4, 17]. That steady state is however quite complex since between the successive passes of the pin or ball, each point on the wear track reacts with the surrounding liquid. Notwithstanding that time-related evolution of the material in the wear track, the achievement of a steady state is revealed by the fact that, if a constant potential value is applied to the metal under friction in the potential range where passivation or dissolution occurs, a steady-state current is obtained. Such a condition is required for the implementation of electrochemical techniques (polarization curves, impedance measurements, etc.).

Corundum as a counter body material in electrochemical tests has a number of advantages. A negligible mechanical deformation of this material takes place on loading onto stainless steel or cobalt – chromium alloy. A negligible wear of the pins or balls occurs, and neither general corrosion of corundum nor galvanic coupling with the counterbody material (in this case the disk material) can take place.

3. Open circuit potential measurements

This method gives information on the electrochemical state of a material, for example active or passive state in the case of stainless steels. However, open circuit potential measurements provide limited information on the kinetics of surface reactions. The open circuit potential recorded during uni-directional pin-on-disk sliding tests, in which the disk is the material under investigation, is a mixed potential reflecting the combined state of the unworn disk material and the material in the wear track. One must be aware that a galvanic coupling between worn and unworn parts on the disk surface may take place [19]. Consequently, the open circuit potential depends on the following parameters:

*The respective intrinsic open circuit potentials of the materials in worn and unworn areas. These open circuit potentials are different because the electrochemical state of the metal is disturbed by the removal of the surface films that may consist of adsorbed species, passive films, or corrosion products, in the sliding contact, and by a mechanical straining of the metal.

*The ratio of worn to unworn areas. In particular, if the extent of the worn area increases, the open circuit potential of the disk will shift depending on the controlling electrochemical processes, being either the anodic (e.g., the dissolution of the metal) or the cathodic reaction (e.g., the reduction of hydrogen or dissolved oxygen).

*The relative position of worn and unworn areas. As a result of the galvanic coupling, a current is flowing between anodic and cathodic areas. The ohmic drop may induce a non-uniform distribution of potential and current density over the disk surface. The measured open circuit potential is thus an average value depending on that distribution.

*The mechanism and kinetics of the anodic and cathodic reactions in worn and unworn areas.

The evolution of the open circuit potential is shown in Fig. 2 for Stellite6 in 0.5 M H₂SO₄ solution at intermittent friction (200 s latency time) with 15N normal force load (F_N) and 120 rpm. The evolution of the open circuit potential was measured under unloaded and mechanically loaded conditions.

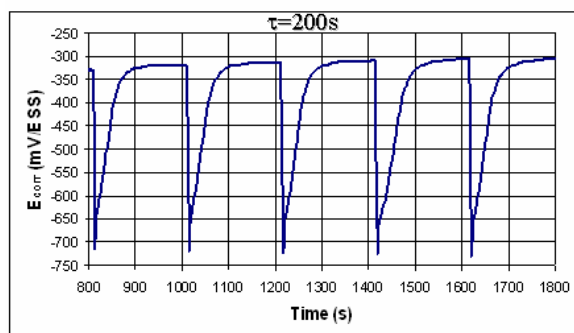


Fig. 2. Electrochemical measurements of open circuit potential (E_{corr}) recorded, during, an unidirectional friction test on Stellite6 with a corundum counterbody in 0.5 M H₂SO₄ solution at intermittent friction (200 s latency time) with 15N normal force load (F_N) and 120 rpm.

A normal load of 120MPa was applied for 2 s, followed by a latency time (rotation stopped) of 200 s, and this cycle was repeated 2500 times. On immersion, the Stellite6 disk stabilizes at an open circuit potential of -0.32V versus SSE. At the start of the first loading step, a large drop of the potential down to -0.76V versus SSE is noticed. On unloading, the potential increases steeply at first and then at a lower rate, reaching a value of about -0.48V versus SSE after 200 s. This case corresponds to Fig. 2 and an anodic dissolution of the Stellite6 material in the wear track can be expected. The potential of -0.76V versus SSE is re-established during the successive loading steps. Before starting the corrosion-wear sliding tests, the freshly ground and thus active cobalt chromium alloy stainless disk material was immersed for 10⁴ sec. In that time interval, a large increase of the open circuit potential of the alloy is noticed. That increase indicates that a stable passive surface state is achieved. At the time the corundum ball is loaded on the rotating alloy disk, a sudden decrease of the open circuit potential takes place (see cathodic shift during

friction). The open circuit potential during the corrosion-wear test is quite close to the open circuit potential of the active base material noticed on immersion of the sample in the electrolyte. Finally on unloading of the ball from the disk, the open circuit potential of the stainless steel disk starts to increase (anodic shift) and reaches after some time the initial open circuit potential back. This indicates the re-establishment of a passive state on the surface of the stainless steel material in the wear track area. It should be noticed that the rate at which the open circuit potential decreases on loading and increases on unloading is totally different. The underlying processes are thus different in both cases and have different kinetics. Indeed on loading, a sudden mechanical destruction of the passive surface film is taking place, while on unloading repassivation takes place at a rather limited oxidation rate. It is also interesting to note that the time for initial passivation of the freshly ground surface at the beginning of the test is much longer than the time for repassivation after unloading. At the beginning of the test, the whole surface is in an active state, and a long time is required for passivation in the open circuit potential conditions. On the contrary, after unloading, only a small part of the disk surface in the wear track is active, and a galvanic coupling takes place between this small active area and the rest of the disk surface in a passive state. This coupling induces an anodic polarization of the active area, resulting in an increase of the passivation rate, and a smaller passivation time constant. The typical potential-current response recorded before, during, and after fretting tests performed on AISI 304L stainless steel sliding against corundum in a Ringer solution is shown in Fig. 3.

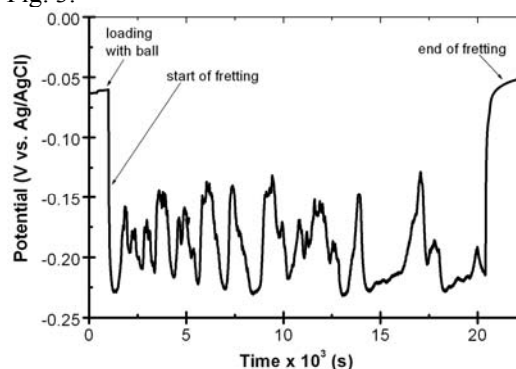


Fig. 3. Electrochemical measurements recorded before, during, and after a fretting test on AISI 304L stainless steel sliding against corundum in Ringer solution at 1 N, 1 Hz, displacement amplitude of 200 μ m, and for 20 000 cycles.

Under unloaded conditions, the potential variations are quite small and stable. When the ball is loaded on top of the sample, a small decrease in

potential was noticed. At the start of the fretting-corrosion test, the potential of the stainless steel sample undergoes a significant negative shift of about 16 mV. After a running-in phase, the potential fluctuates as long as the fretting-corrosion test was going on. When fretting was ended and the corundum ball was lifted away from the worn surface, the potential of the working electrode returned progressively to the value recorded before the start of the fretting test. Accordingly, the potential and current variations in Figure 3 suggest that the tested stainless steel sliding against corundum under the considered test conditions; mainly undergo a removal of their passive surface film at the start of fretting. They remain partly active during the sliding test, and finally progressively repassivate on unloading. In the case of passivating materials like stainless steel, the potential drop on loading/sliding can be a few hundred millivolts large as it is illustrated in Fig. 3. From Fig. 2 and 3 it can be seen that the open circuit potential of Stellite6 and stainless steel immersed in aqueous solutions decreases on loading and subsequently at the start of a bi-directional sliding test (fretting). That potential drop should not be solely related to a change in free energy, but one should also consider the possible effect of a mechanical degradation of the surface oxide on loading and under sliding. In any case, since loaded and unloaded materials are physically and electrically connected, a mixed potential, E_{mix} is induced. At that mixed potential, anodic and cathodic currents are equal but of opposite sign. Considering that the only possible anodic and cathodic reactions are represented by Eq. (1), an electrochemically induced material transfer takes place between loaded and unloaded areas, consisting of an anodic dissolution and a subsequent cathodic re-deposition.



The result is that a net weight loss will thus not be measured although a height difference between loaded and unloaded areas will appear.

From this analysis of the electrochemical behaviour of materials in partially mechanically loaded conditions, some reflections on synergism in tribocorrosion can be formulated. The definition of synergism in corrosion-wear, W_{synerg} as proposed by Stack and Pungwiwat [xx 9] is:

$$W = W_{mech} + W_{corr} + W_{synerg} \quad (2)$$

Where W is the weight loss in tribocorrosion tests, W_{mech} the weight loss in absence of corrosion and W_{corr} is the weight loss in the absence of wear.

The open circuit potential of passive materials in sliding contacts is quite sensitive to the loading conditions and type of test aqueous solution. The open circuit potential of AISI 304L stainless steel disks immersed in Ringer solution varies largely with

normal force and contact frequency (Fig. 4). In unloaded conditions and without any rotation of the disk, the open circuit potential after an initial delay of 6 000s, corresponds to that of disk material in passive state. Once a mechanical contact is established and the disk is rotating, friction occurs and a shift of the open circuit potential towards lower potentials (cathodic shift) is observed. The amplitude of that shift increases with increasing normal force and/or increasing sliding speed or contact frequency.

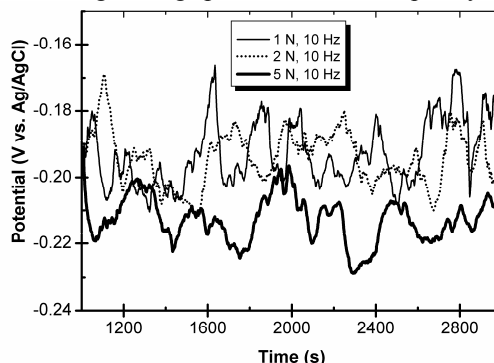


Fig. 4. Potential variation recorded on AISI 304L stainless steel during fretting-corrosion against corundum in a Ringer solution at 10 Hz, 200 μ m, 20000 fretting cycles under different applied normal forces.

The open circuit potential of cobalt chromium alloy (Stellite6) immersed in 0.5M sulphuric acid is shifted down during fretting with a contact pressure of 120 MPa and 200 s latency time with about 350 mV at room temperature (Fig. 2). For cobalt chromium alloy, immersed in cooling water reactor at 85 °C and the same fretting conditions, the open circuit potential is shifting down during fretting with only 200 mV, see Fig. 5 [20].

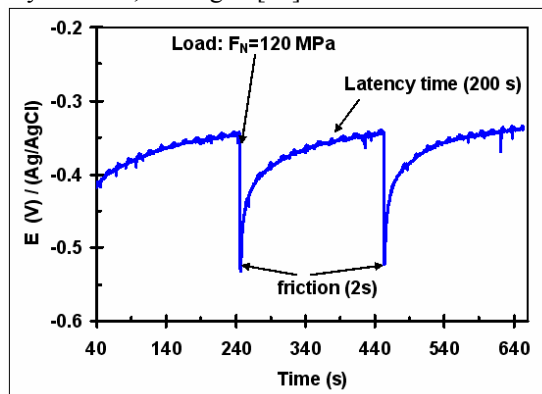


Fig. 5. Electrochemical measurements of open circuit potential (E) recorded, during, an unidirectional intermittent friction test on Stellite6 with a corundum counterbody in water cooling reactor solution at 85 °C (200 s latency time) with 15N (120 MPa) normal loading force

Such a shift in the open circuit potential can be explained as follows:

*The passive film can be partly destroyed (cracking, partial removal) in the contact area under sliding conditions where friction occurs. This may initiate a galvanic coupling between the passive surface layer and the bare base material, with a local dissolution of the base material as a consequence. Since the open circuit potential of active material is cathodic compared to passive material, the open circuit potential of partially depassivated materials shifts towards the active region.

*The contact area (Hertzian contact area) between the first bodies increases at increasing normal load. The increase of the normal load generates a larger wear track area and a larger active area. The lowering of the open circuit potential can be explained by the increase of the active-to-passive area ratio.

*The variation of the open circuit potential with contact frequency is linked to the time interval between two successive contact events during which material in the wear track may repassivate. At higher contact frequency, the amount of active material in the wear track area thus increases. This results in a cathodic shift of the open circuit potential due to an increased ratio of active-to-passive area.

Variations of the open circuit potential of materials subjected to sliding conditions can thus be correlated with variations in the surface conditions of the material under investigation. However, a detailed interpretation of open circuit potential measurements is difficult. Indeed, the open circuit potential is an average value determined by factors as the ratio active-to-passive material in the wear track, the repassivation kinetics of the base material, the contact frequency, and the normal load. As a consequence, the local surface conditions of the material in and outside the wear track cannot be precisely derived from open circuit measurements unless more detailed electrochemical data on passive and active material become available. Such information on the local tribological and electrochemical conditions across a partly worn surface could be gained from a precise knowledge on the potential distribution over that surface.

Microelectrodes could be helpful in that respect. Some reviews are available showing the use of such microelectrodes to investigate localized corrosion [12] and corrosion-wear [18]. However, the interpretation of the variation of open circuit potential and potential distribution requires kinetic data to characterize the electrochemical reactions occurring on active and passive materials. Such kinetic data can be acquired by electrochemical techniques such as potentiodynamic polarization and electrochemical impedance measurements.

4. Potentiodynamic polarisation measurements

Potentiodynamic polarization measurements can be used to derive the dependence of anodic or cathodic current, I , on the electrode potential, V , measured vs. a reference electrode. This method is useful in determining the active/passive behaviour of materials at different potentials.

Such potentiodynamic polarization curves obtained at increasing potential dV/dt (direct scan) on cobalt chromium alloy (Stellite6) immersed in 0.5 M sulfuric acid is shown in Fig. 6. Two cases are shown, namely one (1) without any external loading and one (2) in contact with a sliding corundum ball loaded at 15 N. Both curves were recorded after the open circuit potential of the alloy has reached the passive value [17, 20].

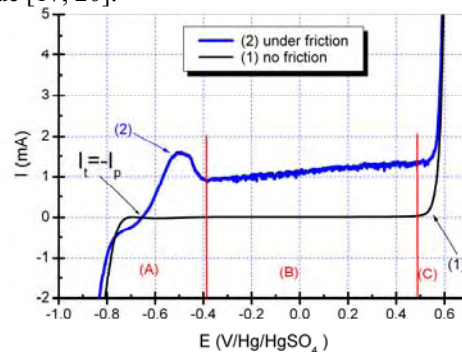


Fig. 6. Potentiodynamic polarization curves of Stellite6 in H₂SO₄ 0.5M recorded by direct potential scan, from -1.0 to $+0.6$ V/SSE, at 0.1 V/min. Curve (1): no friction applied. Curve (2): continuous friction (10 N; 120 rpm).

If the stellite surface of the specimen is not subjected to rubbing (curve 1), hydrogen evolution and oxygen reduction are the only reactions detected in the potential domain A. In domain B, the alloy was passivated, and the current remained very small ($<10\mu\text{A}$). The zero-current potential lay between -0.3 and -0.5 V/SSE. In domain C (potential >0.4 V/SSE), the anodic current increases with the applied potential, revealing the dissolution of the alloy, induced by oxidation of the Cr^{3+} cations of the passive film, giving soluble Cr^{6+} . When friction is applied (curve 2), the shape of the polarization curve changes: hydrogen evolution on Stellite6 is not modified in domain A, but an anodic current of about $0.5\text{--}1.0\text{mA}$ appears in the potential range from $[-0.75; +0.5]$ V/SSE, indicating dissolution of the alloy. A first approach for interpreting the polarisation curve under friction can be developed from the following considerations, based on a concept of "active wear track" [15]:

-The measured current, I can be considered as the sum of two partial currents I_t and I_p :

$$(I = I_t + I_p) \quad (3)$$

Where: I_t is the current originated from the wear track areas where the passive film is destroyed and metal is active, and I_p the current linked to the surface not subjected to friction and that remains in passive state.

-At the zero-current potential (-0.75 V/SSE) where $I = 0$, a galvanic coupling is established. I_t and I_p are different from zero, and $I_p = -I_t$. These partial currents flow between the active wear track areas and the rest of the surface. On the wear track, where dissolution of the material and the formation of a new passive film occur, I_t is anodic. On the remaining surface, I_p is cathodic and is related to reactions such as dissolved oxygen or hydrogen reduction.

-When the potential increases, the galvanic coupling is broken and I_t is no longer equal to $-I_p$. Both I_t and I_p increase. As a result, the measured current I , flowing between the specimen and the counter electrode increases.

On the surface not subjected to friction and in passive state, I_p cannot exceed the value of the current measured at the same potential on the unrubbed specimen. By comparing the values of I in both conditions (see Fig. 6), it can be deduced that, under friction, $I = I_t$ (from -0.7 to 0.5 V/SSE). The total current measured under friction and its evolution with applied potential, are characteristic of the behaviour of material in the wear track. The steep increase of the current with potential around the zero-current potential indicates that a rapid dissolution occurs in the wear track.

The further decrease of the dissolution current above -0.6 V/SSE reveals the effect of repassivation in the active wear track.

The rate of this reaction, occurring in the areas where the passive film is removed, increases with potential. This induces a lowering of the total depassivated area, and thus a decrease of the dissolution current.

The same potentiodynamic curves recorded for Stellite6 in cooling water reactor (12 ppm Li as LiOH+1000 ppm Boric Acid) at 85°C reveals a different behaviour see Fig. 7.

For the curve (1) recorded without fretting we can see the passivation domain. When friction is applied (curve 2 at 30 MPa) and curve (3 at 120 MPa), the shape of the polarization curve changes. In the passive domain we observe that a continuous dissolution of alloy occurs instead of a passivation, even if we have the same parameters of sliding (Contact pressure and rotation speed of counter body).

Thus, polarization curves reveal the occurrence of depassivation and dissolution of the alloy induced by friction in the wear track, and give the opportunity

of quantitative measurements concerning the variation of the active wear track area with tribological parameters (normal load, sliding speed, etc.) [20, 21].

Both effects can be explained by an increase of the area depassivated by friction. At increasing sliding speed, the area depassivated per unit of time increases whereas the restoration rate of the passive film remains constant. On the other hand, at increasing normal loads the contact area where destruction of the passive film occurs, increases, and as a result the total active area also increases.

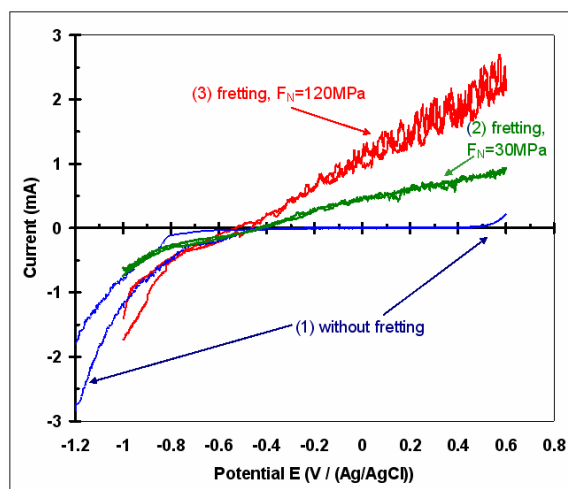


Fig. 7. Potentiodynamic polarization curves of Stellite6 in cooling water reactor, recorded by direct potential scan, from -1.0 to $+0.6$ V/SSE, at 0.1 V/min. Curve (1): no friction applied. Curve (2): continuous friction at 30 Mpa; Curve (3) Continuous friction at 120 Mpa
Rotation speed 120 rpm

Potentiodynamic current potential curves recorded on Stellite6 allow the prediction of the huge influence of friction on the total wear rate in tribocorrosion conditions. One possible synergy between the processes governing wear and corrosion can be pointed out, namely the local destruction of the passive film in the contact area that increases the corrosion rate of the material by several orders of magnitude. Consequently, when a metal is "active" in a corrosive medium, the influence of friction on its electrochemical behaviour can not be neglected. Synergy between friction and corrosion must be considered.

Polarization curves are thus useful in tribocorrosion studies in so far as they give information on changes in electrochemical reaction kinetics induced by sliding, and also on the influence of the surface reactions on the sliding conditions in the contact. The interpretation of polarization curves

has similar limitations as those encountered in the interpretation of open circuit potential measurements, namely due to the coexistence of galvanic coupling of worn and unworn areas. However, by considering carefully the heterogeneous state of tribological surfaces, polarization curves in tribocorrosion studies can yield detailed quantitative information on aspects as mechanical depassivation of worn surfaces, local and overall corrosive wear rates, and the mechanism of mechanical wear under various tribological conditions [17, 18].

Nevertheless, tribocorrosion in field conditions essentially occurs at open circuit potential. However, in most laboratories electrochemical tests are performed under polarization and not at open circuit potential. One possible solution is to use electrochemical impedance spectroscopy (E.I.S.). That method allows a thorough investigation of the corrosion mechanism and the kinetics under open circuit conditions. The measurement of the electrochemical impedance is made by using a sinusoidal voltage signal with small amplitude (5 to 10 mV). This has the advantage of generating only a negligible perturbation on the open circuit potential of the material tested.

5. Electrochemical Impedance Measurements

It is interesting to compare the impedance diagrams corresponding to a totally active surface (diagram 1) and to a totally passive surface (diagram 2). The size of the impedance diagrams differs by several orders of magnitude, particularly in the "low frequency range" (typically < 0.1 Hz). A classical interpretation of impedance diagrams consists in relating the corrosion current, I_c , on a given area, A , to the charge transfer resistance, R_{ct} [22, 23], which is a parameter of the electrochemical impedance that can be deduced from the experimental diagrams:

$$I_c = \frac{B}{R_{ct}} \quad (4)$$

B is a constant factor related to the corrosion or passivation mechanism (value between 25 and 50 mV) [23]. In the case of diagrams consisting of a single arc of circle, the charge transfer resistance R_{ct} is also the polarization resistance, R_p ($R_{ct} = R_p$), defined as the limit of the impedance Z_i of metal-electrolyte system when the frequency tends to zero:

$$R_{pol} = \lim_{\omega \rightarrow 0} Z_i \quad (5)$$

In the case of diagrams as in Fig. 8, the polarization resistance is directly related to the size of the semi-circle. The polarization resistance corresponds to the value of the impedance at very low frequencies.

Impedance diagram from Fig 8, recorded before passivation of the Stellite6 alloy at active potential value $E = -700$ mV vs. Ag/AgCl, corresponds to a totally active surface. The electrical equivalent circuit describing the surface in active state is presented in Fig. 9. By simulating the experimental data with this equivalent circuit we calculated the charge transfer resistance corresponding to active state of the alloy surface, $R_{ct} = 4.48$ k Ω cm². $R_e = 1.48$ k Ω is the electrolyte resistance, and CPE is the capacitive element depending on frequency.

According to equation (4), the corrosion current I_c is 1.42×10^{-9} A (with $B = 25$ mV). Considering the total area of the specimen (4.9 cm²), the corrosion current density i_c is 0.28×10^{-9} Acm⁻².

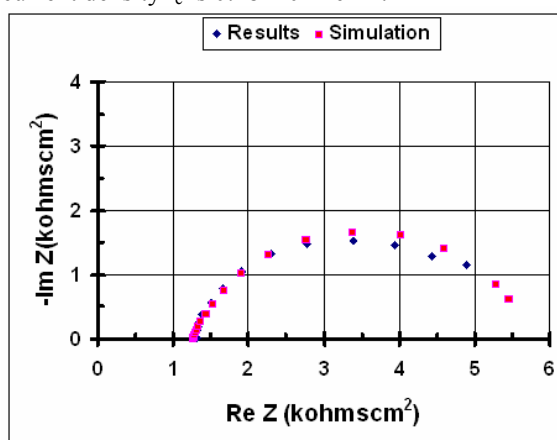


Fig 8. Nyquist representation of impedance measurements of Stellite6 alloy in water cooling reactor at 85 °C, recorded at active potential value $E = -700$ mV vs Ag/AgCl, in active state of the surface: (▲) experimental data; (■) fitting diagram

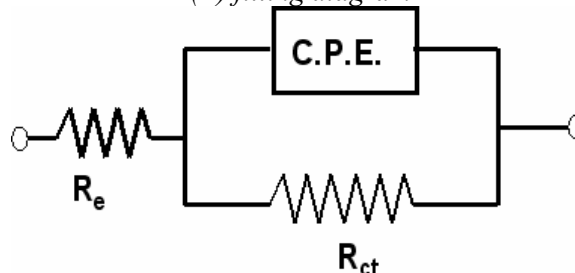


Fig. 9. Equivalent electrical circuit representing the impedance of the Stellite6 alloy in the active state, immersed in cooling water reactor at 85°C, at potential value $E = -700$ (mV/Ag/AgCl)

Impedance diagram from Fig. 10 have been recorded after passivation and before applying the friction, corresponds to a totally passivated surface of Stellite6 alloy in cooling water reactor at 85°C, recorded at passive potential $E = 0.00$ V(Ag/AgCl).

The electrical equivalent circuit describing the alloy surface in the passive state is similar with those presented in Fig. 9. Instead of a charge transfer resistance, R_{ct} , we have now the polarisation resistance, R_p . By simulating the experimental data with this equivalent circuit we calculated the polarisation resistance corresponding to passive state of the alloy surface, $R_p=264.9 \text{ k}\Omega\text{cm}^2$. $R_e=1.3 \text{ k}\Omega$ is the electrolyte resistance, and CPE is the capacitive element depending on frequency.

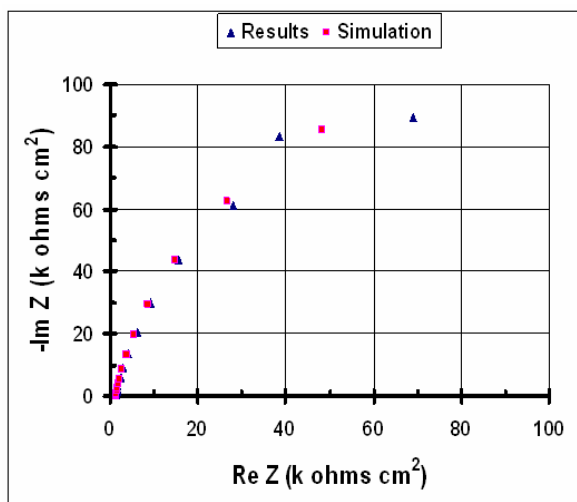


Fig 10. Nyquist representation of impedance measurements of Stellite6 alloy in water cooling reactor at 85 °C, recorded at passive potential value $E=-700\text{mV}$ vs Ag/AgCl , in passive state of the surface: (\blacktriangle) experimental data; (\blacksquare) fitting diagram

The residual corrosion current (passivation current) can be assessed by equation (4) from the value of R_p determined on the diagram from Fig 10 after simulation and fitting ($R_p = 264.9 \times 10 \text{ ohms}$) so that $I_c=8.42 \times 10^{-10} \text{ A}$ (with $B=25\text{mV}$) corresponding to a corrosion current density $i_c=1.71 \times 10^{-10} \text{ Acm}^{-2}$.

In the case of friction tests we have on the surface both areas: active area corresponding to the wear track and the remaining passive area. This aspect can be interpreted by a simple model based on an equivalent electrical circuit of the impedance of the sample undergoing the tribocorrosion test (Fig. 11).

In a first approach, the global impedance of the sample is considered as a parallel connection of impedances Z_a (corresponding to the active surface) and Z_p (corresponding to the passive surface). Z_a represents the impedance of the material in an active electrochemical state (where the passive film was destroyed by friction, for example), and Z_p the impedance of the surface still covered by a passive film.

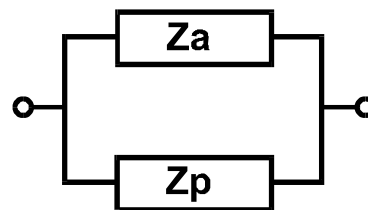


Fig. 11: Equivalent electrical circuit representing the impedance of the sample surface by a parallel combination of the impedance of the active and passive areas (Z_a and Z_p respectively).

For such a model, the global impedance is given by:

$$\frac{1}{Z} = \frac{1}{Z_a} + \frac{1}{Z_p} \quad (6)$$

It must be noticed that this relation is valid over the whole frequency range, and in particular at very low frequencies where $Z \cong Z_i = R_p$. Consequently, a relation similar to equation (5) can be derived for the polarization resistance R_{pol} , $R_{pol/active}$, and $R_{pol/passive}$ being the polarization resistances relative to the total area, the active area and the passive area respectively.

If one assumes that the electrochemical activity of the area depassivated by friction is the same as the one of the active surface before friction, the value of the current density i_c can be used to evaluate the active area A_a . The impedance measurements carried out during tribocorrosion tests illustrate the usefulness of this method to study the mechanism of electrochemical reactions involved in tribocorrosion processes, and the interaction between corrosion and friction. More detailed information on tribocorrosion processes are expected from a systematic study of impedance diagrams recorded at varying tribological test conditions (variation of the normal force, sliding speed, rotation frequency, etc.). The interpretation of impedance measurements recorded during sliding tests is difficult due to the heterogeneous state of the surface, as in the case of polarization measurements. In fact, a non-uniform distribution of the electrochemical impedance over the disk surface must be considered. The action of friction can be thoroughly analyzed, only if this distribution is known. In tribocorrosion experiments, a local analysis of the electrochemical state is thus necessary to interpret impedance measurements. Research work on electrochemical systems with a non uniform distribution of the electrochemical impedance is available now [24]. Such measurements and models can be adapted to tribocorrosion conditions. In that field, microelectrodes could help to map the electrochemical impedance on disk surfaces. Electrical equivalent circuit models or finite element



models could be used to get distributions of impedance, and to calculate the overall impedance.

6. Conclusions

This overview points out the capabilities of electrochemical methods like open circuit potential measurements, polarization curves, and EIS measurements, for the *in situ* investigation of materials used under tribocorrosive conditions in sliding contacts.

They can provide not only essential information on the surface conditions of materials in sliding contacts, but also on the kinetics of reactions that control the corrosion component in the material loss during tribocorrosion tests.

Aspects of the tribocorrosion mechanism that can be clarified in this way are the nature of electrochemical reactions, the formation of protective passive surface films, the interactions between electrochemical reactions and friction. Information can also be gained on kinetics such as corrosion rate, rate of depassivation by mechanical action in the contact area, and rate of repassivation.

Electrochemical methods in tribocorrosion are still facing a few limitations related to the particular conditions of tribocorrosion tests, mainly the heterogeneous state of the surface subjected to sliding, and the time evolution of the wear track area.

In most tribocorrosion tests, in particular sliding tests, only a fraction of the disk is undergoing sliding. The risk of a galvanic cell (corrosion cell) between the wear track area and the rest of the disk surface must be considered. That galvanic cell may induce an electrochemical potential distribution over the disk affecting the rate of electrochemical reactions in the wear track and on the rest of the disk.

This can even destabilize a protective passive film. In such an extreme case, friction applied on a limited fraction of the surface of a passive material may induce a general corrosion over the entire surface.

The time evolution of the wear track material is determined by the contact conditions (unidirectional, bi-directional, intermittent, continuous, etc.).

Notwithstanding the fact that steady state conditions can be obtained during a limited time, it must be considered that at the local scale on every point of the wear track, transient electrochemical

conditions are encountered. Measurement procedures, data analysis and modeling must take into account such local transient and periodic aspects. A full understanding of the tribocorrosion mechanisms requires thus a in-depth analysis of and correlation between electrochemical data, surface analyses, and material degradation.

References

- [1] A. V. Levy, Surf.Coat. Technol. 36 (1988) 387.
- [2] A. J. Ninkam, A. V. Levy, Wear 121 (1988) 347.
- [3] E. Lemaire and M. Le Calvar, Wear, 249 (2001) 338.
- [4] B. W. Madsen, Wear, 171 (1993) 271.
- [5] X. X. Jiang, S. Z. Li, D. D. Tao, J. X. Yang, Corrosion, 49 n 10 (1993) 836.
- [6] T. C. Zhang, X. X. Jiang, S. Z. Li, X. C. Lu, Corrosion Science 36 n°12 (1994) 1953.
- [7] S. Mischler, A. Spiegel, M. Stemp and D. Landolt, Wear, 251 (2001) 1295.
- [8] S. Barril, S. Mischler and D. Landolt, Tribology International, 34 (2001) 599.
- [9] J. Takadoum, Corrosion Science, 38 (1996) 643.
- [10] S. Mischler and P. Ponthiaux, Wear 248 (2001) 211.
- [11] S.W. Watson, F.J. Friedersdorf, B.W. Madsen and S.D. Cramer, Wear, 181-183 (1995) 476.
- [12] F. Assi and H. Böhni, Tribotest Journal 6 (1999) 17.
- [13] P. Ponthiaux, F. Wenger, J. Galland, G. Lederer and N. Celati, Matériaux & Techniques, Numéro hors série, Juillet 1997, p 43.
- [14] P. Jemmely, S. Mischler and D. Landolt, Wear 237 (2000) 63.
- [15] I. Garcia, D. Drees and J.P. Celis, Wear 249 (2001) 452.
- [16] S. Mischler, S. Debaud and D. Landolt, J. Electrochem. Soc. 145 (3) (1998) 750.
- [17] L. Benea, P. Ponthiaux, F. Wenger, J. Galland, D. Hertz, J. Y. Malo, Wear, Wear Modelling, 256, 9-10, (2004) 948-953.
- [18] A. Berradja, F. Bratu, L. Benea, G. Willems and J.-P. Celis, Wear, Volume 261, Issue 9, 20 November 2006, Pages 987-993.
- [19] R. Oltra, in "Wear-Corrosion Interactions in Liquid Media" edited by A. A. Sagües and E. I. Meletis, Minerals, Metals and Materials Soc. (1991) 3.
- [20] Lidia Benea, François Wenger, Pierre Ponthiaux; CD ROM Proceeding of EMCR 2006 - Electrochemical Methods in Corrosion Research 18 Jun 2006 - 23 Jun 2006 Dourdan, France.
- [21] Benea L., Iordache V. E., Wenger F., Ponthiaux P., Peybernes J., Vallory J.; The Annals University of Galati, Fascicle VIII Tribology, pp. 5-10; 2005, ISSN 1221-4590.
- [22] M. Keddad, O. R. Mattos, H. Takenouti, J. Electrochem. Soc. 128 n 2 (1981) 257.
- [23] I. Epelboin, C. Gabrielli, M. Keddad, H. Takenouti, in "Electrochemical Corrosion Testing", ASTM Special Technical Publications n 727 (1981) 150.
- [24] F. Wenger and J. Galland, Electrochimica Acta 35 n 10 (1990) 1573.



BEHAVIOUR AT NITRIDING IN FLUIDIZED LAYER OF AUSTENITIC STAINLESS STEELS AT THE TEMPERATURE OF 450°C

Ovidiu DIMA

"Dunarea de Jos" University of Galati
e-mail: ovidiu.dima@ugal.ro

ABSTRACT

Stainless austenitic steels have a good corrosion resistance but reduced abrasion strength due to low strength below 200HV₅. By nitriding one may ensure the obtaining of a superficial layer with increased strength that should maintain unaltered the corrosion resistance. The nitriding in fluidized layer applied at 450 °C allowed the obtaining of diffusion layers formed of nitrogen enriched austenite with certain nitride separations. For the CrNi, CrNiMo usual steels, the obtained strengths have been higher than 1000 HV₀₀₅. In the case of steel X1CrNiMoCu20.18.7 with more than 50% of alloying elements, the strengths did not exceed 500 HV₀₀₅ due to the low nitrogen concentration, much below the saturation limit determined by the reduced diffusion speed. The corrosion test in saline mist indicates the maintaining of corrosion resistance, the materials ranging in the group of Perfectly resistant. Also, the abrasion strength increased 2-3 times due to the limited diffusion speed at low temperature. The favourable property assembly allows the usage of the treatment for some practical applications.

KEYWORDS: austenite, nitriding, corrosion, abrasion

1. Introduction

By nitriding we want to improve the strength properties, mainly the superficial strength in order to ensure an abrasion resistance of the austenitic stainless steels. Such steels are characterized by a good corrosion resistance but the strength during solution tempering, the usual delivery and usage condition is low, below 200 HV₅. Nitriding must ensure the formation of an improved strength

superficial layer but also of a structure that should ensure the conservation of the corrosion resistance properties. For the performance of the treatment we used the method of nitriding in fluidized layer in quartz sand, washed and dried, and as fluidizing agent and treatment atmosphere a mix of nitrogen and 30% ammoniac. For the research we used samples of 6 austenitic stainless steel CrNi and CrNiMo whose chemistry is presented in Table 1.

Table 1

Steel code	Related mark SR:EN 10283-98	C	Mn	Si	Cu	Cr	Ni	Mo	Ti	V
		[%]								
1	X2CrNi18.8	0,12	1,24	1,64	0,06	23,2	9,8	0,11	0,01	0,02
2	X6CrNi18.10	0,06	1,55	0,65	0,08	17,1	9,3	0,05	0,60	
3	X2CrNi18.9	0,03	1,27	0,42	0,19	18,9	8,95	0,15	0,01	0,02
4	X2CrNiMo17.11.2	0,02	2,06	0,78	0,27	20,0	8,8	2,7	0,03	0,03
5	X6CrNiMoTi17.12.2	0,045	0,96	0,54	0,16	18,1	11,6	2,04	0,32	
6	X1CrNiMoCu20.18.7	0,02	1,12	0,41	0,70	20,1	18,1	6,1		0,2

The parameters of the nitriding process have been established on the basis of the experience obtained in the previous research. The 450 °C nitriding temperature has been chosen, inferior to the

interval of rendering sensitive the austenitic stainless steels, for the reduction of the risk of separating the chromium nitrides. The duration of the nitriding treatment has been established at 3 hours.

2. Analysis of the samples nitrided at 450 °C

For the measuring of strength and its variation in the nitrided layer Vickers trial with small HV₀₀₅ load trial at pressure load of 0.50N has been used. The nitrided samples have been transversally cut, perpendicularly on the nitrided layer, with abundant cooling abrasive disk, grinded on metallographic paper and polished with diamond paste. The results of the strength trials are presented in fig. 1. Based on the strength trials and its variation curves in the superficial layer we could precisely estimate the

depth of the nitrided layer. The estimated values are presented in table 2.

Table 2. Values of the layer depth
nitrided at 450 °C.

Steel code	Layer depth [μm]
1-X2CrNi18.8	14
2-X6CrNi18.10	20
3-X2CrNi18.9	20
4-X2CrNiMo17.11.2	17
5-X6CrNiMoTi17.12.2	16
6-X1CrNiMoCu20.18.7	19*

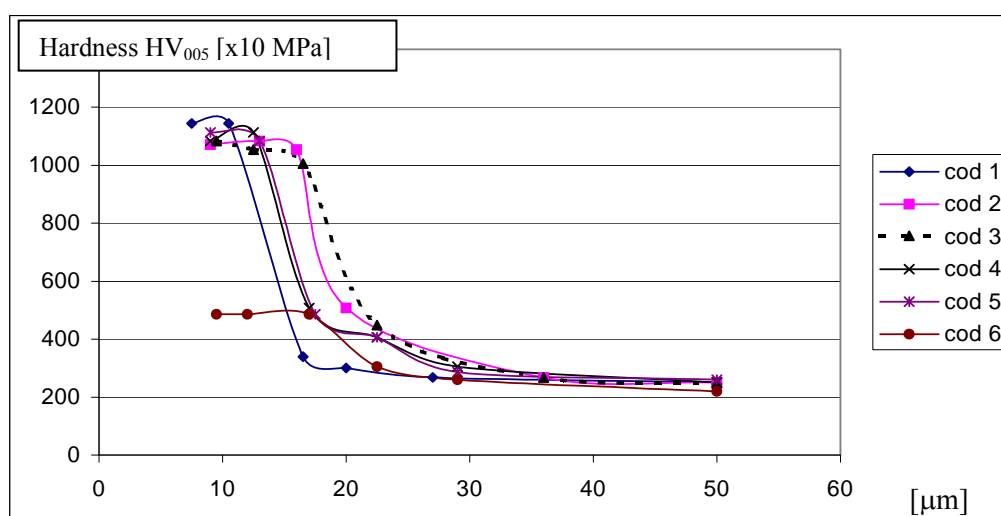


Fig. 1. Strength variation in the nitrided layer at 450 °C.

The analysis of the strength trials results show the presence of the nitrided layer and important increase of strength at the steels code 1, 2, 3, 4, 5 of about 1000-1100 HV₀₀₅ and lower increase at the steel code 6 of maximum 486 HV₀₀₅. The values of the lower strengths on the case of nitriding code 6 steel X1CrNiMoCu20.18.7 shows that in the layer the nitrogen concentration is lower, which is justified by the high concentration of the alloying elements over 50% and especially of the 18% Ni and cca 1% Cu concentration which amplify the austenizing effect of Ni and reduces the speed of the diffusion processes. The diffusion speed is also limited by the reduced temperature of the process which leads to the reduced concentration of the nitrogen and also to the reduced depth of 20 μm.

3. Analysis of the samples nitrided at 450 °C

The analysis of the samples nitrided at 450 °C does not show the presence of any distinct presence superficial layer. This proves that the layer is obtained by diffusion, being formed of austenite

alloyed with nitrogen, the phase noted by most authors with. The large strength difference between the first five usual steels and high alloyed steel code 6 is caused by the different nitrogen concentration in the layer. In figure 2 is presented the microstructure of the steel code 4 X2CrNiMo17.11.2 nitrided at 450°C. X-ray analysis of the layer nitrided at 450 °C confirms the results of the microstructure analysis.

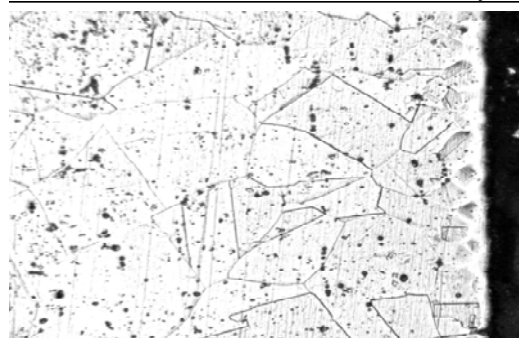


Fig. 2 Microstructure of the steel code 4
X2CrNiMo17.11.2 nitrided at 450°C, x400

In figure 3, there are presented comparatively the diffractograms for the samples of the steel code 4 X2CrNiMo17.11.2 in the initial state and nitrided at 450 °C and for the high alloyed nitrided steel code 6 X1CrNiMoCu20.18.7. In the diffractograms of sample having code 4, initial steel, there are droplets corresponding to the diffraction angles of the γ_{Fe}

phase, initial austenite. In the diffractogram of sample having the code 4 nitrided at 450 °C there are droplets of high amplitude corresponding to the diffraction angles of the γ_N phase, nitrogen enriched austenite and droplets of lower amplitude for the diffraction angles corresponding to the CrN phase.

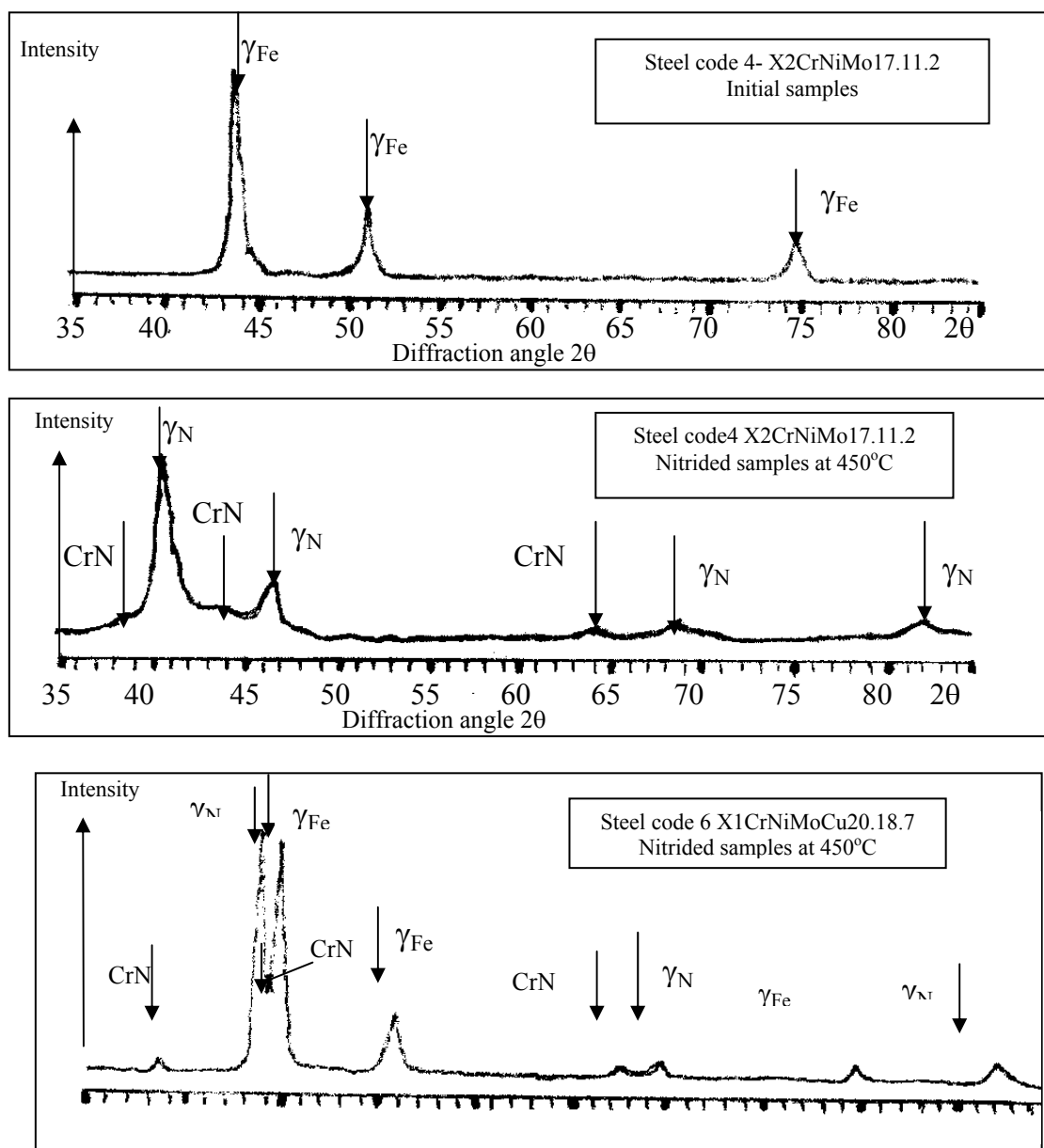


Fig. 3. Diffractograms of the initial samples and those nitrided at 450°C steel code 4 X2CrNiMo17.11.2 and code 6 X1CrNiMoCu20.18.7.

It results that in the structure there are small quantities of chromium nitrates along with the high alloyed gamma solution enriched with nitrogen in high concentration, close to the saturation limit. The presence of the two phases justifies the increase in strength recorded in the layer nitrided at 450 °C. On the diffractogram of code 6 sample nitrided at 450 °C there are droplets of high amplitude corresponding to the diffraction angles of the γ_{Fe} phase, initial austenite and γ_N nitrogen enriched austenite. The distinct prominence of the two austenite types is caused by the fact that the interstitial penetration of the nitrogen in the austenite determines a dilation of the network and thus, a modification of the network parameter. There are also much lower amplitude droplets for the diffraction angles corresponding to the CrN phase. The presence of these phases lead to the increase of strength, its lower value being determined by the lower concentration of nitrogen in the austenite and small quantities of punctiform nitrates separated in the austenite.

4. The analysis of corrosion behaviour in saline mist of the steels nitrided at 450 °C

For the estimation of the corrosion resistance of the samples the accelerated corrosion test in saline mist STAS 9229-95 has been used. The estimation of the corrosion behaviour has been done comparatively between the original samples with austenitic structure for the tempering for dipping in solution and nitrided samples. The composition of the solution for the obtaining of the saline mist has had a salt concentration of 35 g/liter as follows: 27 g/l NaCl, 6 g/l MgCl₂, 1 g/l CaCl₂, 1 g/l KCl with addition of boron acid for the adjustment of the pH in solution. The corrosion in saline mist is accelerated and this is explained by the high contribution of oxygen and the temperature of 35 °C in the enclosure. In figure 4 there are presented comparatively the average corrosion speeds in saline mist STAS 9229-95 for the initial trials and those nitrided at 450 °C. The test took place over 300 hours with weighing every 100 hours.

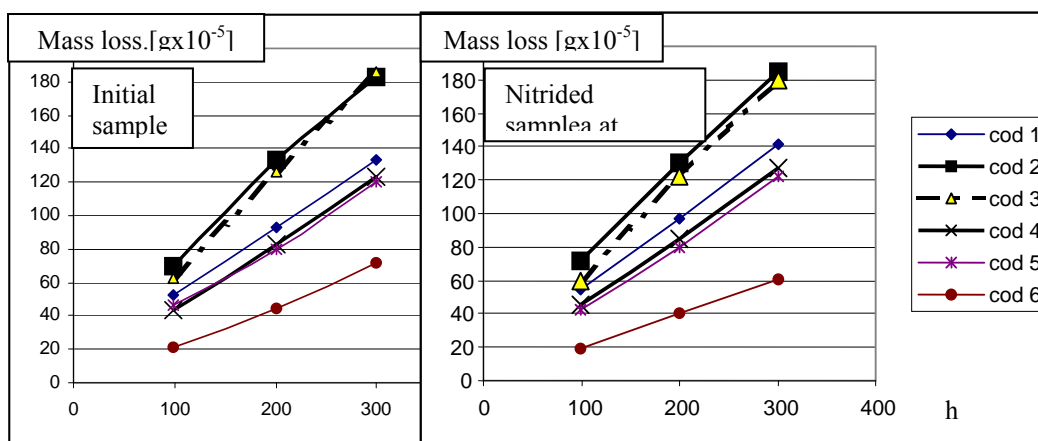


Fig. 4 Time variation of mass losses for initial and nitrided materials.

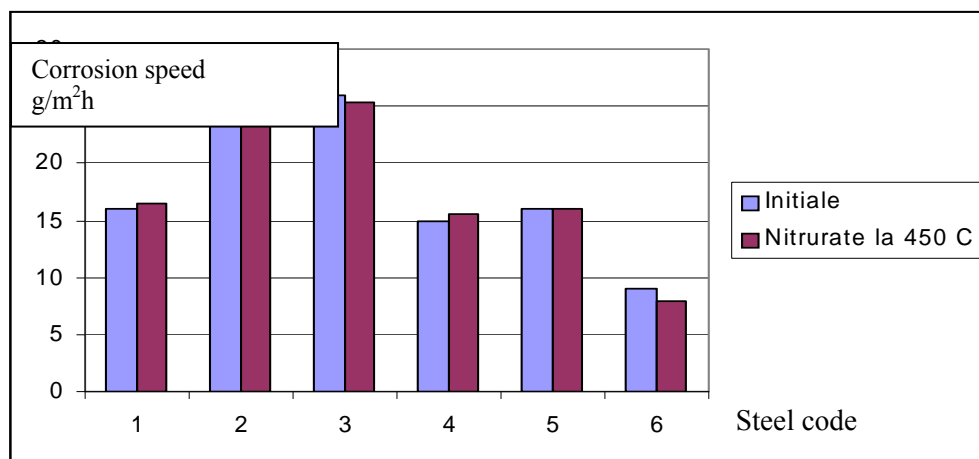


Fig. 5. Average corrosion speeds in saline mist for the initial and nitrided materials at 450°C

The analysis of the results show a similar behaviour of the original samples and of those nitrided at 450 °C at the corrosion test in saline mist, the mass losses and determined corrosion speeds are very close values, figure 5. According to the determined values, the steels nitrided at 450 °C range within the same corrosion resistance classes as the initial steels, the measured values indicating slight increases or decreases determined by other factors.

Thus, steels code 1, 2, 3, 4, 5, both original and nitrided at 450 °C range within the *Perfectly resistant* material group with merit note 1.2 and steel code 6, both initial and nitrided at 450 °C ranges within the *Perfectly resistant* material group with merit note 1.1. These results are also confirmed by the traced potential curves. In figure 6 there are presented comparatively, the potential dynamic curves traced for the initial materials and those nitrided at 450°C of steel code 4 –X2CrNiMo17.11.2.

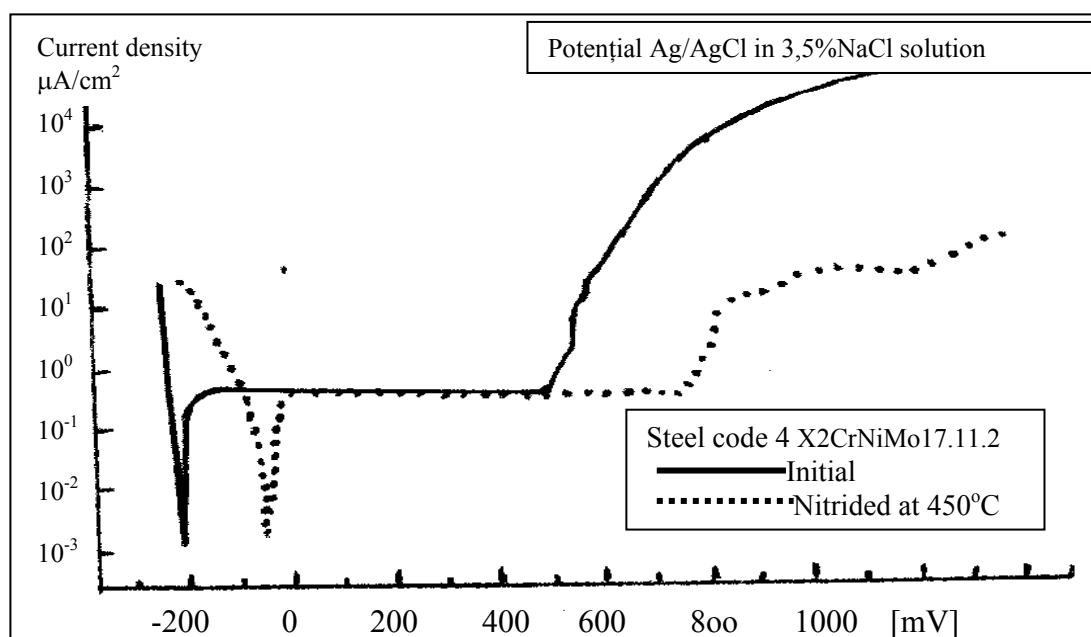


Fig. 6. The potential dynamic curves traced for the original materials and those

5. Analysis of the abrasive wearing strength of the steels nitrided at 450 °C

From the analysis of the potential curves results that in the case of the samples nitrided at 450 °C in comparison with the initial samples, the passive domain is enlarged and shifts to more electropositive values and the current density in the passive domain is maintained even manifesting a downward tendency.

The shape of the polarization curves indicates a good corrosion behaviour of the steel nitrided at 450 °C, justified by the fact that the structure of the steel is mono phase, formed of solid γ_N austenite solution enriched with nitrogen.

Nitrogen proves to have a beneficial effect over the corrosion resistance and corrosive behaviour in general.

The abrasive wearing test was performed according to STAS 9639-81, using a friction coupling abrasive disk-pin. The conditions of the trial were: sample section 50 mm², granulation pointage of the abrasive disk-800, disk speed 25 rpm, radial sample advance 0.5 mm/rotation, pressure on sample 10 MPa, average sliding speed 10 m/min, length of the travel space 25 m. The results of the abrasion test, namely the mass losses by wearing for the samples nitrided at 450 °C as compared to the original samples are presented in table 3 namely figure 7. The analysis of the results indicate an increase of the abrasive wearing strength of the samples nitrided at 450 °C, 2,5-3 times comparatively with initial steel code 1,2,3,4,5 and 2 times for the steel code 6. The increases to wearing strength depends also on the thickness of the layer and hardness variation in the nitrided layer.

Table 3. Abrasion test results

Steel code	Initial materials		Nitrided materials at 450°C		
	Hardnes HV ₀₀₅	Abrasive wear	Layer depth	Hardnes HV ₀₀₅	Abrasive wear
	[x10 MPa]	[g]	[μm]	[x10 MPa]	[g]
1-X2CrNi18.8	198	0,0066	14	1144-500	0,0024
2-X6CrNi18.10	202	0,0065	20	1084-500	0,0026
3-X2CrNi18.9	188	0,0065	20	1084-500	0,0026
4-X2CrNiMo17.11.2	180	0,0069	17	1114-500	0,0024
5-X6CrNiMoTi17.12.2	204	0,0064	16	1114-500	0,0022
6 X1CrNiMoCu20.18.7	182	0,0071	19*	486	0,0037

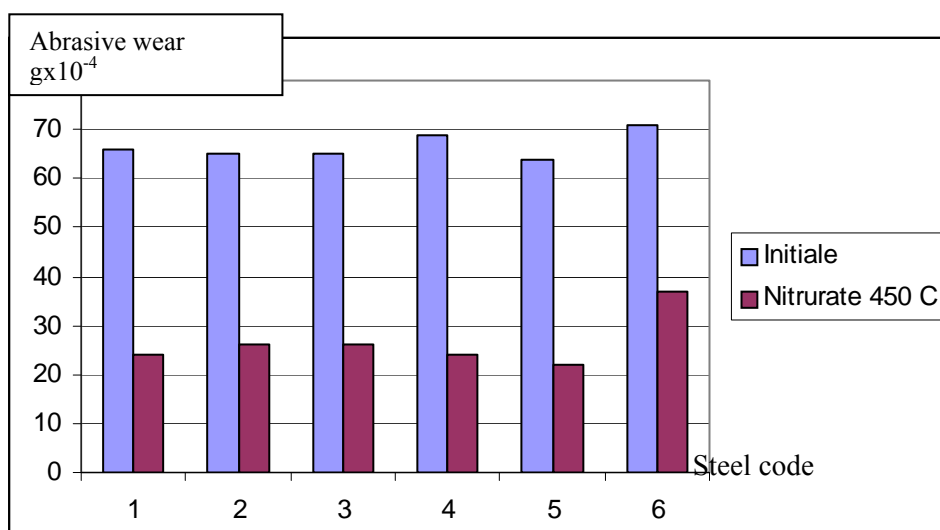


Fig.7 Behavior of initial and nitrided samples at 450°C to abrasive wear

6. Conclusions

Anssamby of corrosion resistance properties for nitrided samples show for 450 °C especially favourable situation. The corrosion resistance of the nitrided materials or even better wearing strength has increased 2.5-3 times.

High alloyed code 6 steel with Cr, Ni, Mo with over 50% alloying elements has a more special behaviour due to the lower nitrogen diffusion speed caused by the high concentration of the alloying elements, especially Nichel.

The diffusion speed is also reduced due to the low temperature which makes the depth of the nitrided layer not to exceed 20 μm, yet sufficient for some practical applications.

References

[1] Berns H. "Case hardening of stainless steel using nitrogen". Ruhr University, Bochum, Germany 2002.

[2] Bard A.J., Faulkner L.R. "Electrochemical methods, Fundamentals and aplications" Wiley Science Publication 2000.

[3] Dima O. Cazacu N. "Surface hardening by nitration for some stainless austenite steel types." Lucrarile simpozionului international "Turnatoria de la rigoarea tehnica la arta" Ed. ACADEMICA Galati 2006

[4] Dima O. Levcovici S. Georghies C. "Aspects of nitrided layer structure for some types of austenite stainless steel" Lucrarile simpozionului international "Turnatoria de la rigoarea tehnica la arta" Ed. ACADEMICA Galati 2006

[5] Dima O. Mitoseriu O. "Behavior of some stainless nitrided austenite steel types to corrosion and abrasion". Lucrarile simpozionului international "Turnatoria de la rigoarea tehnica la arta" Ed. ACADEMICA Galati 2006

[6] Fossati A., Borgioli F, Galvanetto E, Bacci T. "Corrosion resistance properties of glow-discharge nitrided AISI316L austenitic stainless steel in NaCl solution" Corrosion Science, Vol.48, Issues 6, June 2006, pag. 1513-1527.

[7] Gheorghies C. s.a. "Incerarea materialelor Vol.III" Ed. Tehnica Buc. 1994.

[8] Levcovici S.M. s.a. "Ingineria suprafețelor " EDP, RA București 2003

[9] Mirkin L.I. "Controlul cu raze X a structurii materialelor" Moscova 1979

[10] STAS 9229 -1995 "Incerarea rezistenței la coroziune in ceata salina".



RESEARCHES ON THE POLLUTION OF UNDERGROUND WATERS IN A CERTAIN PART OF GALATI DISTRICT

Maria VLAD

"Dunărea de Jos" University of Galați
e-mail: mvlad@ugal.ro

ABSTRACT

The paper underlines the importance of monitoring the quality of the underground waters and presents the experimental results as regards the pollution of underground waters in a certain part of Galati district. The final target of underground waters quality monitoring is to design quality and quantitative prediction models and provide monitoring and optimization programs for environment investigations. Much interest is currently attached to the rehabilitation of aquifer.

KEYWORDS: contaminants, underground waters, monitorisation, quality

1. Introduction

Since water quality is a world wide priority and the only pollution -free water source is the underground reservoir, avoiding its contamination is crucial for mankind. The underground water contamination is associated with a multitude of unpleasant aspects such as taste, smell, colour, hardness, existence of microroganisms and toxic, flammable or explosive matter. Underground water contamination may render impossible the use of, aquifer for longer periods of time, such as decades or even centuries. This is mainly due to the very low velocity of the underground waters. Due to the underground and surface waters inter-influence there is a strong interdependence between their qualities as well. The surface waters represent boundary

conditions for the underground range, both from the hydraulic and contaminant concentration viewpoints.

Hydrologic cycle

Water features higher mobility than lithosphere but lower than the atmosphere. Such mobility implies physical and even chemical transformations and is easy to take place according to certain physical laws. At planet scale, the hydrosphere is a functional system where sun and/or earth energy penetrates into. Said energy generates a continuous movement of waters, thus forming certain regular or periodic circuits. It is common knowledge the saying „water natural circuits”. In more general terms, this means that water on ocean and continent surfaces evaporates, gets higher and precipitates as rain and snow thus coming back to the ocean either directly or through running waters and iceberg.

Subprocesses specific to the hydrologic cycle

Precipitations
Dams
Surface drainage
Infiltrations

Flowing into unsaturated soils
Flowing of underground waters through saturated soils
River flowing
Evaporation

The basic pollution sources for the underground waters [1, 2] are:

1. Excessive extraction from deep wells (more than the underground water supply)
2. Contaminants penetration into underground water through surface waters:
 - a) from house basements or disposal of waters;
 - b) from industry effluents (waste water, insufficiently filtered);
 - c) from solid garbage mixed with water;

d) from excessive use of pesticide and fodders in agriculture ;

e) from accidental leakages.

3. excessive salinity. This is caused by low precipitations unable to feed the underground water supply.

4. Pollution caused by insufficient drainage systems.

5. Pollution caused by filtering plants, unsuitably operated.

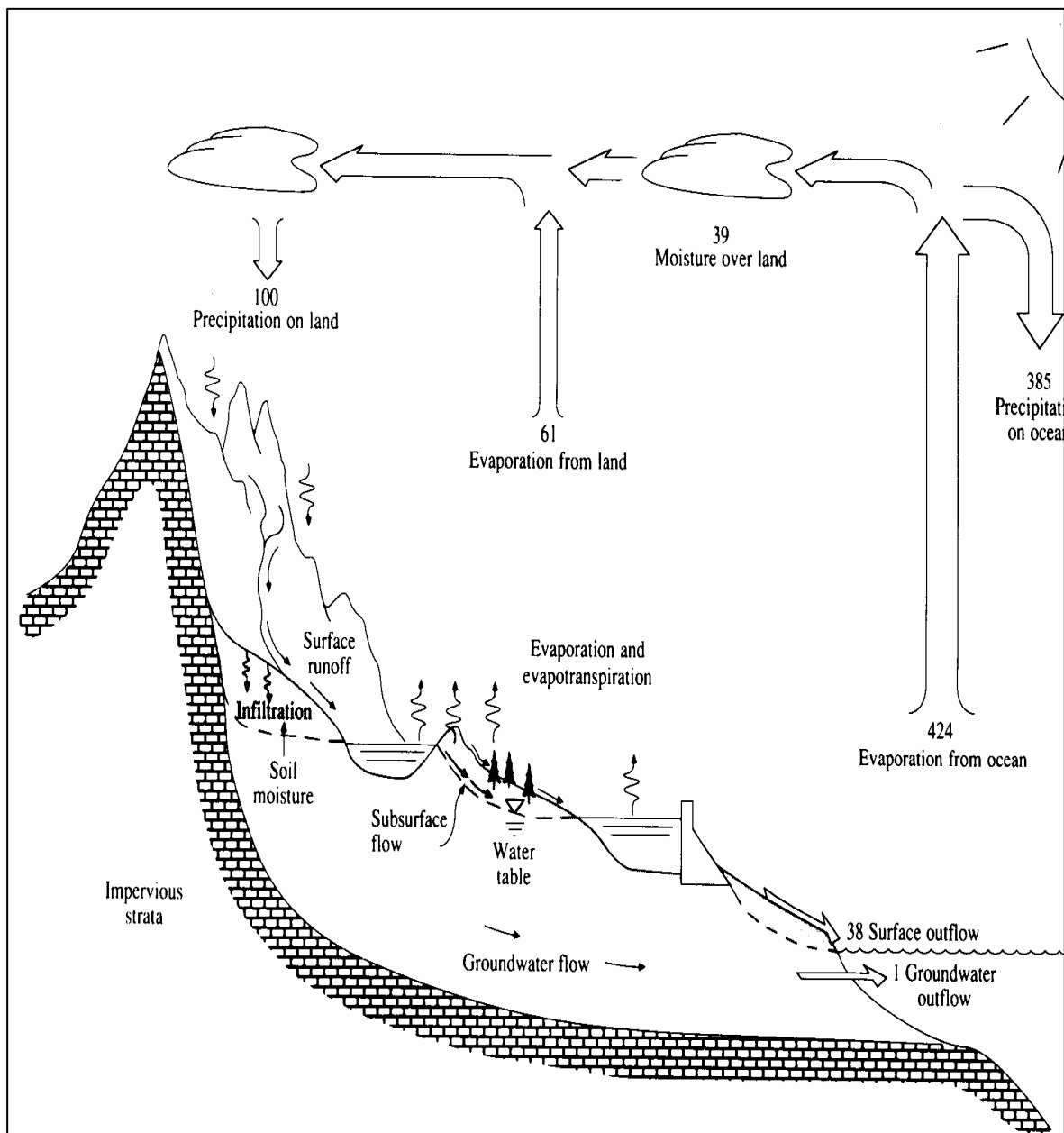


Fig.1. Hydrodynamic cycle acc. to Chow et al., 1988, Water circuit on Terra.

Pollution sources

They can be localized: on the terrain surface or underground; above the underground water level; under the underground water level.

2. Evaluation methods

An adequate approach to a pollution problem implies:

- 1) data acquisition and processing;
- 2) conceive and use the prediction models
- 3) check how prediction functions.

The Romania's total water resources are about 40 billions m³/year, out of which, under the present hydrographic arrangement, approx 13 milliards m³/year. The water resources from inland rivers amount to only 5 billions m³ / year under natural environment and almost double under various arrangements; it should also be added 3 billions m³/year of underground water and about 10 billions m³/year supplied by the Danube. In general, the pollution sources and main contaminants are the same for both surface and underground waters; also similar are the impact and measures taken to improve water quality.

2.1. Characteristics of water monitoring systems

The water monitoring systems aims at controlling the quality of the hydrographic basin waters (including rivers, lakes, gulfs), in seas and oceans along with underground, thermal and mineral waters [4].

Water monitoring involves various types of measurements:

- chemical measurements to determine the dissolved oxygen, suspension matters, nutrients, oils, metals, pesticides, etc.;
- physical measurements to determine temperature, flow rates, colour, turbidity;
- biological measurements to estimate the variety and abundance of aquatic plants and animals, and also the testing organisms capacity of surviving in certain water samples.

As regards the time taken to monitor water quality, there is:

- permanent intensive monitoring performed in plants (waste water filtering, drinking water treatment);
- temporary or seasonal monitoring – beach survey in summer, for example;
- emergency monitoring – accidental contaminants leaks.

The most important objectives of a water monitoring system are:

- Determining water general features and identification of its modifications and tendencies in time;
- Identification of specific problems or emergency cases likely to affect water quality;
- Collect information (providing data bases) in order to further develop contamination prevention and fighting programs;
- evaluate whether the target of some programs (eg implementation of pollution control systems) has been reached;
- to promptly cope (by warning systems) with accidents/natural calamities, leakage, heavy rains, floods.

Some monitoring systems can achieve simultaneously part of these objectives, others are designed for a particular task/target. As a principle, national entities for environment protection and pollution prevention submit the pollution management and control programs to the local agencies and support them in developing said programs and reporting the results.

2.2. Methodology of water quality control

Water quality research involves several aspects [5]:

a) establishing the research objectives.

The objective of the research may be monitoring the drinking water quality, the factors influencing the water quality and removal of those elements likely to harm people's health.

b) establishing the main indicators or parameters being monitored;

Two elements are taken into account: types of indicators and their level. The former is usually established depending on the nature of the water being investigated (drinking, surface waste waters). The number of indicators should not be too large so as to make results interpretations easier.

c) establishing the analysis methods

All qualitative and quantitative methods of the analytical chemistry can be applied taking into account the following criteria:

- an as small as possible detection limit (this is the min. concentration detectable by 95% probability);
- high sensitivity to allow for the deceleration of the smallest variation, inside the sample, of the substance concentration (sensitivity is estimated by the measurable distance from the parameter being measured);
- high selectivity, which means to avoid interference of other substances;
- accuracy (the values obtained should be as close as possible to the actual concentrations in the sample);
- fastness (to allow for the determination of the substance in the shortest period of time).

One element that should be taken into account is the degree of difficulty of the method especially when analysis is very frequently performed. Both manual and instrumental methods can be used. The composition of the water sample should reflect the composition of the water being sampled. The sampling place may differ according to the use and objective pursued: water distribution network- in the case of drinking water; inlet and outlet of the water filtering plant to monitor its efficiency etc. Moment and frequency of sampling depend on various parameters such as: water quality, distribution regime, source flow rate, etc.

There are:

- instantaneous samplings (single samples), when parameter variations are low and measurement is performed manually;
- permanent samplings (average samples), when parameters variations are high and instruments are used for the purpose of measurement.

Establishing unitary systems of terms to express results. This should be unitary so that the results may be correlated for a further relevant conclusion. In short, the general characterisation of waters and water quality control enable an overview estimation and



determination of certain physical, chemical, bacterial and biological features.

2.3. Water sampling

Sampling is an extremely important stage in the water physical-chemical analysis process because sampling can affect the analysis results. Therefore the samples should be relevant and sampling should not cause alterations of water compositions and quality because of improper techniques or inaccurate conditions for material preparation.

Sampling vessels must be cleaned to remove organic matter or other impurities likely to alter the sample composition.

Upon sampling, the bottle is rinsed 2-3 times in the water to be sampled, then is completely filled with this water and sealed off so that no bubbles should remain inside the bottle.

Sampling procedures depends on the water source, namely:

- water is collected from the water supply network after the tap has been cleaned inside and outside with a clean buffer and the stagnant water flows freely through the pipeline for about 5 min.;

- in the case of intermittent supply, one sample is collected from the first jet so as to have the first water passing through the tap and another sample is taken after two hours' continuous flowing;

- in case of storage reservoirs, sampling is performed at the reservoir outlets;

- in pumped-water fountains, water sampling is performed after 10 minutes' pumping;

- in bucket fountains, water sampling is carried out by immersing the bucket 10-30 cm deep under the water surface and then water is poured into the sampling bottle;

- in case of surface waters, sampling is performed by fastening the bottle into a special holder which provides the necessary weight to the bottle to easily go down under the water level. These sampling devices allows bottle opening only when it has reached the required depth. Sampling is carried out along the water stream where depth is maximum, upstream from any affecting effluent and downstream where there is a total blending of the receiver and the effluent ;

- in case of waste waters, single/unique, average and proportional average samples are taken.

As regards the unique samples, they are sampled once, either from the general effluent, from the distinct sectorial effluents (eg. industrial waters), or from the partial effluents of a certain sector or a certain institution (in case of sewage and households wastes). The average samples are taken at 30-60 minutes intervals in preset amounts and stirred together in a common bottle.

For average proportional samples, water is also sampled at 30-60 minutes intervals but in various amounts proportional to the effluent flow rate and subsequently stirred together into a common bottle.

Each sample should be accompanied by a sheet containing the most important data: date and place of sampling, water depth and temperature, the analysis objective, etc.

Three systems can be used:

- water sampling device for volatile substances, associated with a closed-loop stripping device ;

- adsorption system based on macroporous resins;

- liquid-liquid extractor.

The last two devices can operate at various pH values. An extraction cell is less sensitive to the presence of solid suspensions than resins; on the other hand, resins allow for the recovery of a large number of compounds (eg. Humic acids).

2.4. Water samples preservation

Since water can change its chemical composition due to oxidation-reduction processes, microorganism operation and ion exchange between water and vessel walls, it is recommended to have an as short as possible interval between sampling and analysis (max. 4 hrs).

Temperature and pressure changes may result in loss of gaseous substances (O_2 , CO_2 , H_2S , Cl_2 , CH_4), this is the reason why it is recommended that gas measurements be performed at the sampling site or the water samples be treated with various reactants for preservation purpose.

Thus, to prevent metal ion deposition (Al^{3+} , Fe^{3+} , Cd^{2+} , Mn^{2+}) by hydrolysis, mineral acids are added.

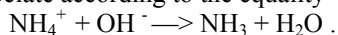
The pH or hydrogen exponent (Sorensen) is understood as decimal logarithm of the hydrogen ion activity with changed signed:

$$pH = -\lg a_H$$

The water pH plays an important role in the vital processes of vegetal and animal organisms, human body and industrial processes.

2.5. Toxicity of substances

The toxic substances are „ exogenous or endogenous substances which act chemically upon organisms, in small quantities, causing vital malfunctions”. The ammonia reaches the rivers through waste waters containing ammonia and ammonia salts discharged from coke factories, chemistry and food industries. The aqueous ammonia solution features basic reaction, while ammonia salts dissociate according to the equality :



With higher values of the pH the amount of free

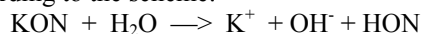


ammonia increases and with low pH values, there is an increase in the amount of ammonia ions. Wuhrmann and Woker's researches have shown that the ammonia ions are not toxic for fish and ammonia salt toxicity is given by the ammonia molecules (Liebmann, 1960) Toxicity also depends on the amount of free CO₂ in water due to its influence on pH; an increase in CO₂ leads to lower ammonia toxicity.

B) Cyanides have a very harmful influence on aquatic organisms. When discharged into water, soluble cyanides are hydrolyzed forming the cyanhydric acid, which penetrates the breathing apparatus of underwater organism, having a harmful to lethal effect on the breathing enzymes.

The toxicity of the cyanhydric acid solutions and soluble cyanides is accounted for by the action of nondissociated cyanhydric acid molecules which have a higher capacity of penetrating the tissues than ions.

The soluble cyanides hydrolyzes in water according to the scheme:



The intensity of dissociation, implicitly the toxicity, are influenced by the pH of the solution. As the pH increases, the dissociation is higher and consequently the toxicity decreases.

Cyanides of heavy metals, together with alkaline cyanides form cyanidic complexes which also have a toxic action on hydro-organisms.

The cyanhydric acid and its salts have a harmful effect on the biological processes in the surface waters, causing inhibition of their self-filtering capacity; also, they cause inhibition of the biochemical processes in the biological systems in the wastes waters (Liebmann).

C) the phenols, hydrolixic derivatives of the aromatic hydrocarbons, fall into two categories: monophenols and polyphenols.

Phenols have a harmful effect on aquatic basins, implicitly on aquatic organisms, by:

- Consuming the oxygen dissolved into water;
- Giving water specific unpleasant taste and odour;

Affecting aquatic flora and fauna even down to decay. The degree of phenol toxicity vary much a major role being played by hydroquinone and least harmful being fluoroglucine. An increase in temperature makes phenols even more toxic.

Phenols combined with one another or with other chemical substances have higher cumulative toxic action.

D) Oil products are the most widely spread dirty agents of both surface and underground waters, giving water an unpleasant taste and odour. Water contaminated with such substances cannot be used as drinking water or food industry, irrigations, nautical sports. Directly, oil products act either mechanically

preventing breathing and other physiological processes, or attacking cell membrane due to their toxicity of lipoids nature. Naphtenic acids are also toxic and affect the nervous systems and the skin irrigation net.

E) Heavy metals. The salts of heavy metals represent a very serious contamination source for the surface waters, because of their toxicity and stability, causing disturbances of the biological balance with negative effects on the self-filtering process, fish stock and various usage of water.

In the heavy metal contaminated rivers it has been found a decrease in the number of species and individuals, along with a certain gradation in the different groups and species of organisms in terms of their resistance to a certain metal ion.

2.6. Analysis of the indicator „suspension”

Suspension matter represents substances which are insoluble in water, can be separated by filtering, centrifugation or settling (max 2 mm diameter) According to density, suspension matter can be settled and unsettled (including floating matter). The method basically consists in separating suspensions by filtering and centrifugation, followed by drying and weighting the residues down to their constant mass. The precipitable suspension matters can be determined by two methods: volumetrically; gravimetrically.

The principle of the volumetric method:

The precipitable suspended matters are determined by free precipitation within a given time interval in a graded cylinder or in Imhoff cone. Devices/instruments required: glass Imhoff cone, 1000 cm³, of 1 cm³ divisions, graded glass cylinder, de 1000 cm³, han-holder rod, and disk for stirring purpose. The principle of the gravimetric method: precipitable suspended matters are determined by the difference between the total suspended matters in the sample and the unsettled suspended matters, after free settling/precipitation, during a given time.

2.7. Analysis of indicator „CBO5”

The biochemical oxygen consumption after n days (CBO_n) is the massive concentration of dissolved oxygen under specific conditions by biochemical oxidation of the organic and/or inorganic substances in water. „n” is the incubation period, this being equal to 5 or 7. The working sequence is as follows: the sample being analyzed is brought to 20 grades Celsius and aerated if necessary. If aerated, the sample is left to rest for about 15 min. The air bubbles and possible supersaturation in oxygen are eliminated. Determination by measuring the dissolved oxygen – iodometric method:

After incubation the concentration of oxygen dissolved in each bottle of the first series is measured.

The bio-chemical oxygen consumption after n days, expressed in milligrams per litre, is calculated by the equation :

$$CBO_n = (C1 - C2),$$

where: C1-concentration of dissolved oxygen in the sample being analyzed at the initial moment in milligrams per litre; C2-concentration of oxygen dissolved in the sample being analyzed after n days, in milligrams per litre.

2.8 .Analysis of indicator „CCOCr”

The chemical consumption of oxygen is the oxygen concentration equivalent to the amount of potassium dichromate consumed by the matter dissolved and in suspension, when a water sample is

treated with this oxidant. The chemical consumption of oxygen in water, determined by the potassium dichromate, may be regarded as an approximate method of the theoretical oxygen consumption, which represents the amount of oxygen consumed by total chemical oxidation of the organic compounds to inorganic ones.

3. Experimental results

Considering the particulars of the water quality monitoring and the associated research methods, the experimental results as regards the underground waters contamination in Chiajna, Galati district, have been obtained and interpreted from three stations, figures 2 ÷ 10.

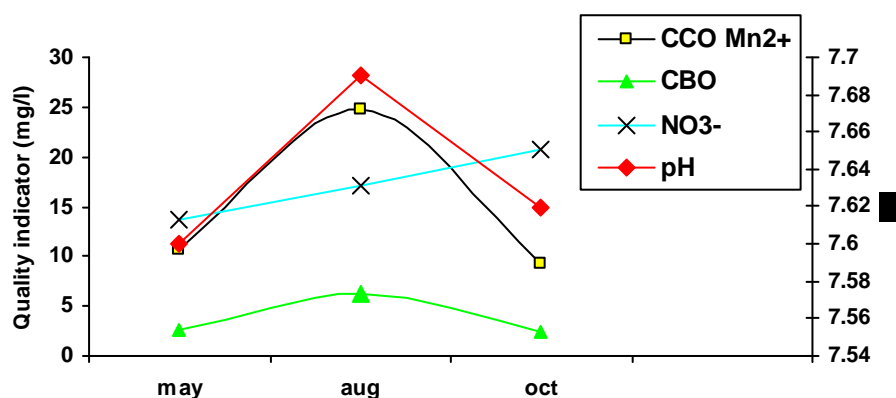


Fig.2. Values of pH, CCOMn²⁺, CBO₅, NO₃⁻ of underground waters, station 1.

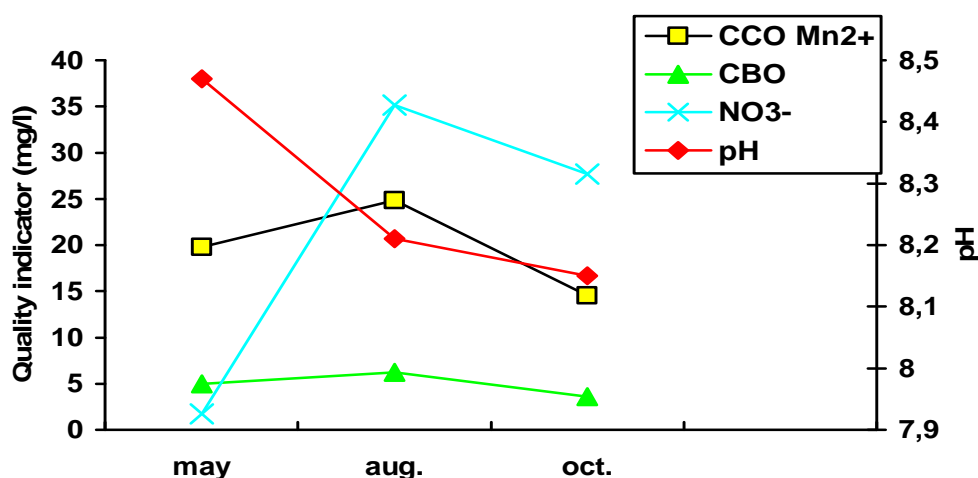


Fig.3. Values of pH, CCOMn²⁺, CBO₅, NO₃⁻ of underground waters, station 2.

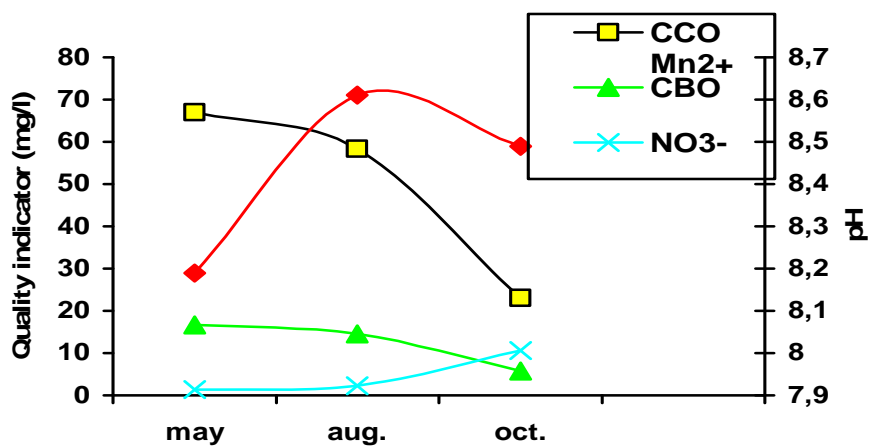


Fig.4. Values of pH, CCO, Mn²⁺, CBO, NO₃⁻ of underground waters, station 8.

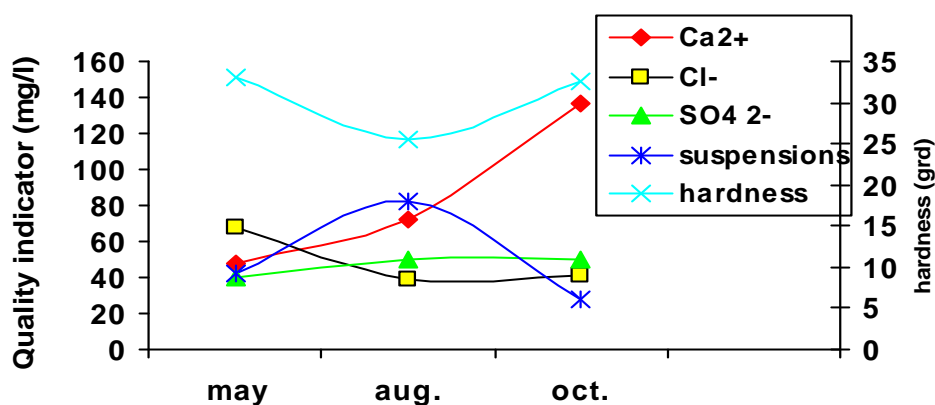


Fig.5. Values of Ca²⁺, Cl⁻, SO₄²⁻, water hardness, suspensions of underground waters, station 1.

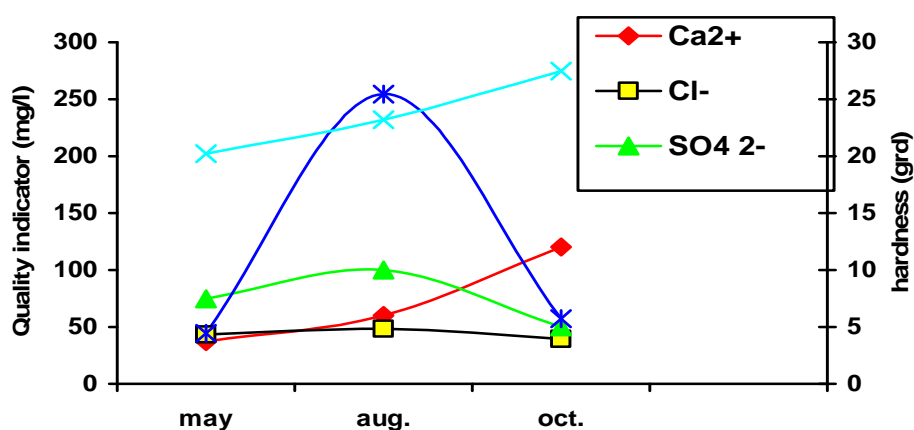


Fig.6. Values of Ca²⁺, Cl⁻, SO₄²⁻, water hardness, suspensions of underground waters, station 2.

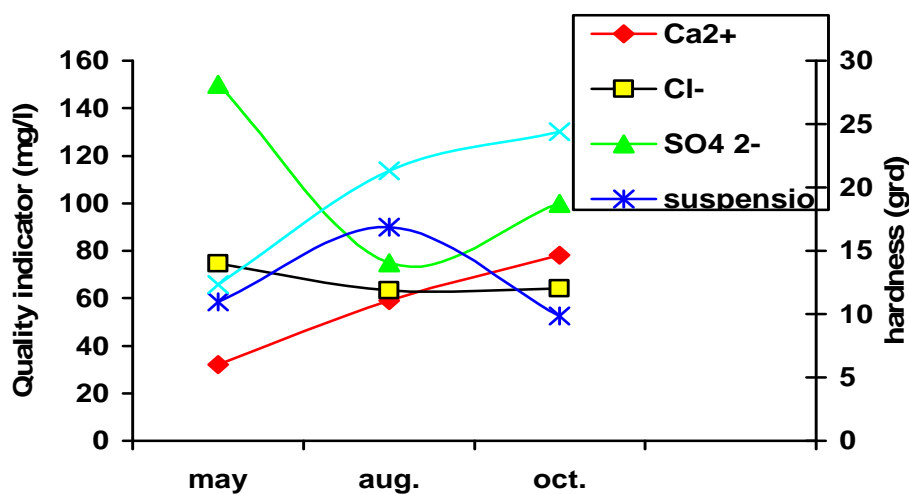


Fig.7. Values of Ca^{2+} , Cl^- , SO_4^{2-} , water hardness, suspensions of underground waters, station 8.

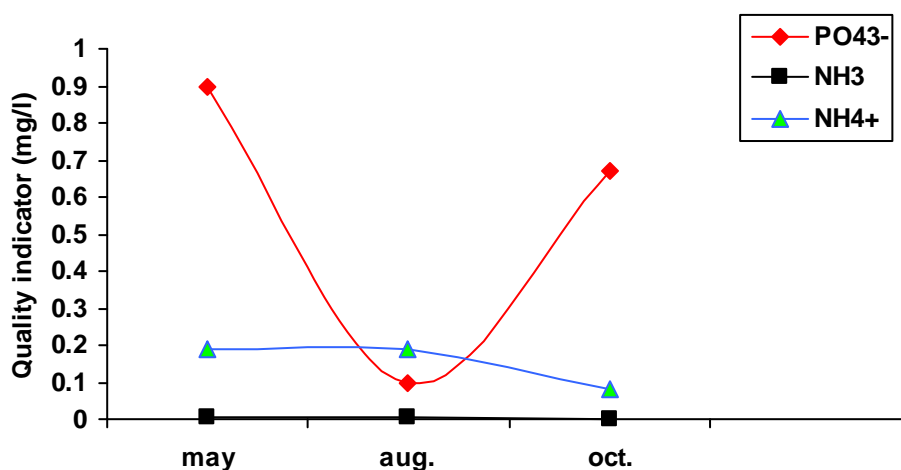


Fig.8. Values of PO_4^{3-} , NH_3 , NH_4^+ , of underground waters, station 1.

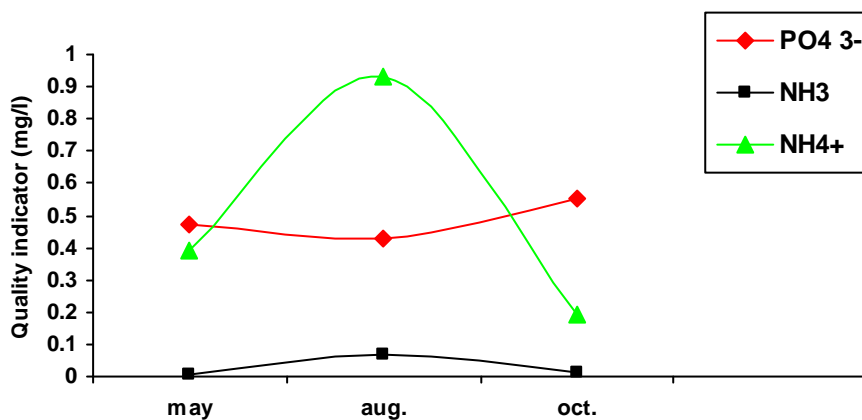


Fig.9. Values of PO_4^{3-} , NH_3 , NH_4^+ , of underground waters, station 2.

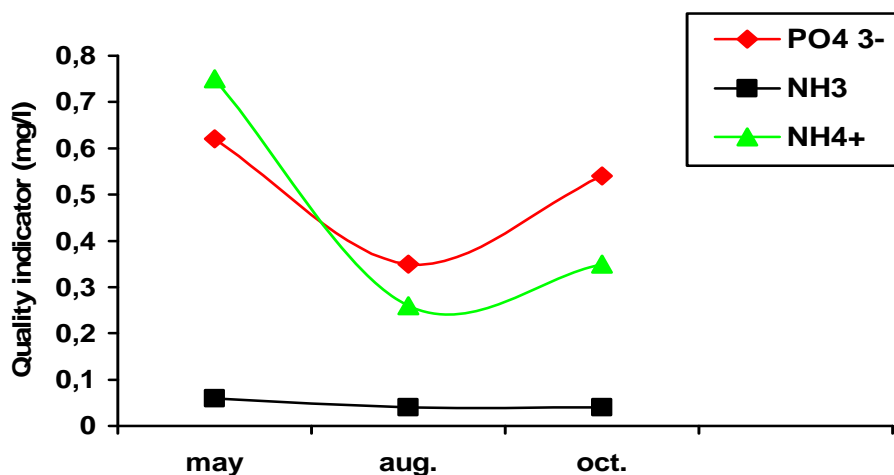


Fig.10. Values of PO_4^{3-} , NH_3 , NH_4^+ , of underground waters, station 8.

4. Conclusions

Underground water quality indicators vary depending on the moment when and the site where the related measurements are made;

The content of NO_3^- increases in time, the largest amounts being reported in the month of October;

The content of calcium ions in the underground water reaches a peak in October, increases in time and depends on the site of measurement;

The values of PO_4^{3-} are high at all measuring stations and they fail to meet a certain rule; therefore, one of the main sources of the underground water contamination in these areas is represented by the chemical fodders used in agriculture;

In all waters analyzed large amounts of chlorides and anions of SO_4^{2-} along with large amounts of suspension matters have been found.

References

- [1] Wilbert, M.C., J. Pellegrino, J. Scott and Q. Zhang. - *Water Treatment Estimation Routine (WATER) User Manual* Water Desalination Research and Development Programme Report No. 43. Washington, D.C.: United States Department of the Interior, Bureau of Reclamation, August 1999.
- [2]. Abdul-Malik, Q.Y. - *Yemen's Water Resources and Treated Wastewater*. at: <http://www.idrc.ca/waterdemand/docs/english/yemenenglish.doc>.
- [3]. Giurma Ion, *Sisteme de gospodaria apelor*. Partea I, Ed. CERMI Iasi, 2000, 221p.
- [4]. Varduca Aurel, *Protectia calitatii apelor*. Ed. H.G.A., Bucuresti, 2000, 417p.
- [5]. Varduca Aurel, *Monitoringul integrat al calitatii apelor*, Ed. H.G.A., Bucuresti, 1999, 355p.
- [6]. Drobot Radu, Serban Petru, *Aplicatii de hidrologie si gospodaria apelor*. Ed. H.G.A., Bucuresti, 1999, 375p.

EXPERIMENTAL RESEARCHES ON THE CONSTITUTIVE EQUATION OF CONCRETE STEEL WITH SUPERIOR CHARACTERISITICS

Nicolae CĂNĂNĂU, Petrică ALEXANDRU,
Gheorghe GURĂU, Ionel PETREA

"Dunărea de Jos" University of Galati

email: nicolae.cananau@ugal.ro

ABSTRACT

The plastic deformation behavior is defined by the function of the deformation strength according to the strain, strain rate and temperature as the factor of the deformation process. The behavior law establishes by the experimental way, using the torsion test method. The paper shows the results of the researches for establishing of the equation of deformation behavior of steel destined of rolled wires for reinforced concrete.

KEYWORDS: constitutive equation, torsion test, stress intensity, strain intensity

1. Introduction

The plastic deformation of a metallic material is described by the equation [1]:

$$\sigma = \sigma(\varepsilon, \dot{\varepsilon}, T) \quad (1)$$

in this equation σ is the stress intensity in the really deformation conditions, ε - strain intensity, $\dot{\varepsilon}$ - strain rate intensity, T - temperature.

The knowledge of this equation of plastic deformation behavior is necessary for the evaluation, programming, modeling, simulation and optimization of the plastic deformation processes, by applying in the calculus program of the constitutive equation [1,2].

$$\dot{\varepsilon}_{ij} = \frac{2}{3} \cdot \frac{\dot{\varepsilon}_0}{\sigma_0} \cdot S_{ij} \quad (2)$$

in this equation $\dot{\varepsilon}_{ij}$ - is the component ij of the strain rate tensor, $\dot{\varepsilon}_0$ - is the strain rate intensity in the really deformation conditions, σ_0 - the stress intensity, S_{ij} - the component ij of the deviator tensor of stress state. This equation is defined by:

$$S_{ij} = \sigma_{ij} - \delta_{ij} \cdot \sigma_m \quad (3)$$

in equation σ_{ij} is the component ij of the stress tensor, δ_{ij} - Kronecker's symbol, σ_m - mean normal stress of the stress tensor.

In this paper it presents the results of researches effectuated for establishing of the equation of plastic deformation behavior of steel for wires destined to reinforced concrete.

2. Experimental conditions

The constitutive equation is established through experimental way using a torsion testing machine.

The researched material has the chemical composition rendered in table 1.

Table 1. Chemical composition of steel, [%]

C	Mn	Si	P	S	Cr	Ni
0.18	1.23	0.35	0.37	0.035	0.21	0.15

The form of active zone of the sample is cylindrical and has the dimensions $(\phi 6 \pm 0.02) \times (36 \pm 0.1)$ mm.

The torsion testing installation is equipped with: electro-hydraulic system for action of sample with the power of 5kW, the revolution is 1-2000 rpm, data acquisition system type Spider 8, heating system, maximum temperature of 1100°C and precision ± 5 °C [3,4]. The research program must cover a temperature area, according to the researched material and a domain of the strain rate values. A test corresponds at a certain strain rate value and certain temperature according to the established research program. In the aim of the testing we must regulation the revolution of

hydraulic system, then it mounts the sample in the action device and we put in the function the heating system. Also it is put in the function the data acquisition system.

When the temperature of the sample becomes equal at the programmed temperature, the action system is coupled and the deforming process it is made until the tearing of the sample.

As result of the torsion test we obtain the torque diagram $M(t)_{\dot{\epsilon},T}$ where t is the time, which may be transformed in strain. Thus we obtain the $M(\epsilon)_{\dot{\epsilon},T}$ diagram.

3. Experimental results

The research program consists in: research temperatures of 1023K, 1073K, 1123K, 1173K and the revolution of 25, 107, 400 rpm.

The torsion moment diagrams are rendered in the figure 1, 2, 3.

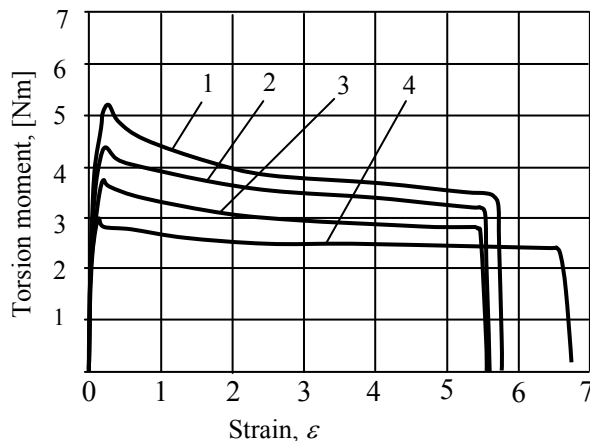


Fig. 1. The torsion moment diagram – strain for the revolution of 25rpm: 1-1023K, 2-1073K, 3-1123K, 4-1173K

The analysis of the diagram shows that at the increasing of the strain rate the deformation resistance of material increases and its deformability decreases. At the increasing of the temperature the deformation resistance decreases and the deformability increases. At the temperature of 1073K it is manifest a trend of decreasing of the plasticity.

The function of the torsion moment is depended of the deformation degree (ϵ), strain rate ($\dot{\epsilon}$) and the temperature (T). The mathematical expression of the torque is:

$$dM = \frac{\partial M}{\partial \epsilon} \cdot d\epsilon + \frac{\partial M}{\partial \dot{\epsilon}} \cdot d\dot{\epsilon} + \frac{\partial M}{\partial T} \cdot dT \quad (4)$$

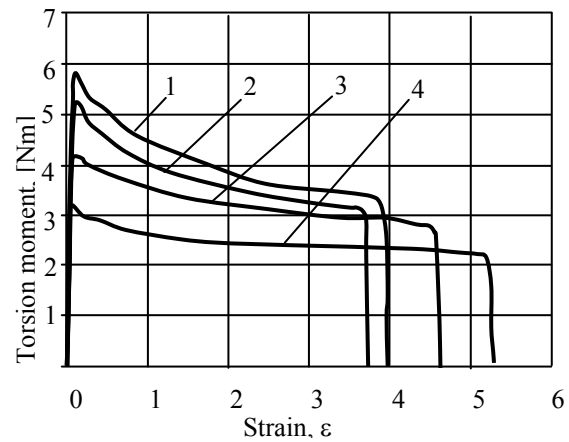


Fig. 2. The torsion moment diagram – strain for the revolution of 107rpm: 1-1023K, 2-1073K, 3-1123K, 4-1173K

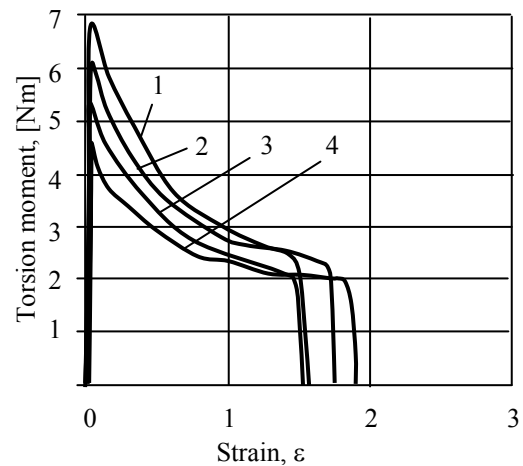


Fig. 3. The torsion moment diagram – strain for the revolution of 400rpm: 1-1023K, 2-1073K, 3-1123K, 4-1173K

For the maximum values of the torque the expression (4) becomes:

$$dM_{max} = \frac{\partial M_{max}}{\partial \dot{\epsilon}} \cdot d\dot{\epsilon} + \frac{\partial M_{max}}{\partial T} \cdot dT \quad (5)$$

Selecting the maximum values of the torque, which correspond at the research tests, according to the strain rate and temperatures values we obtain the diagrams rendered in figure 4.

The deformation strength of the metallic materials varies with the strain ϵ by a hardening law (power or exponential law), with the strain rate $\dot{\epsilon}$ by a power law and in function of temperature through an exponential law.

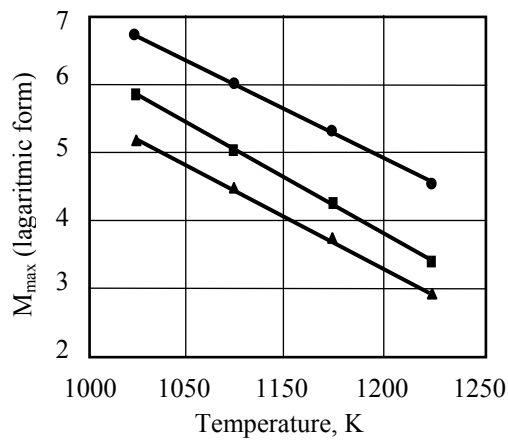


Fig.4. Torsion moment diagram in logarithmic coordinates: 1-25rpm, 2-107rpm, 3-400rpm

The general mathematical expression of the torsion moment, frequently used for description of the function of the torsion moment has the following expression [2,4,5]:

$$M_{max} = A_2 \cdot \dot{\epsilon}^m \cdot \exp\left(\frac{m \cdot Q}{RT}\right) \quad (6)$$

In (5) m is the coefficient of the sensibility of deformation strength at the strain rate, Q is named the activation energy of deformation process, R – the ideal gas constant, T – temperature, in Kelvin, A – experimental constant.

We transformed the relation (6) in the linear form (we applied the logarithmic coordinates) and applied a regression calculus program with two independent variables and one dependent variable and we obtained the results rendered in table 2.

Table 2. Regression data at the equation (5)

Standard Error of the Estimate = 6,56297855244627E-02				
Coefficient of Multiple Determination (R^2) = 0,9415813889				
Regression Variable Results				
Variable	Value	Standard Error	t-ratio	Prob(t)
a	-2,299048475	0,405759417	-5,666038497	0,00031
b	0,119960921	0,016731242	7,16987528	0,00005
c	4687,084251	484,3296201	9,677467692	0,0

The constants which are included in the expression (6) have the values:

$$\begin{aligned} A_2 &= 9,964 ; \\ m &= 0,119961 ; \\ Q &= 325,858 \text{ kJ/mol} \end{aligned}$$

The mathematical expression of the maximum torsion moment is the following:

$$M_{max} = 9,964 \cdot \dot{\epsilon}^{0,119961} \cdot \exp\left(\frac{4687,08}{T}\right) \quad (7)$$

The determination of the function of the stress intensity is possible using the expression:

$$\sigma = \frac{\sqrt{3}}{2\pi R^3} \left(3M + \dot{\epsilon} \frac{\partial M}{\partial \dot{\epsilon}} + \epsilon \frac{\partial M}{\partial \epsilon} \right)$$

We admit a composed function for the hardening factor. The equivalent stress may be defined by equation [2,5]:

$$\bar{\sigma} = \begin{cases} A \cdot a \cdot \left(\frac{\epsilon}{\epsilon + \epsilon_0} \right)^p \cdot \left(\dot{\epsilon} \right)^m \cdot \exp\left(\frac{mQ}{RT}\right) & \text{for } \epsilon \leq \epsilon_0 \\ \sigma^* \cdot \exp(-n(\epsilon - \epsilon_0)) \left(\dot{\epsilon} \right)^m \cdot \exp\left(\frac{mQ}{RT}\right) & \text{for } \epsilon > \epsilon_0 \end{cases} \quad (8)$$

In this expression ϵ_0 is the value of the strain which corresponds at the maximum value of the torsion moment. This factor is, also, a function of the strain rate and temperature. The exponent p has the order 2.

The values of the constants end exponents of the relation (8) will be established using a calculus program for experimental data.

The experimental data for the strain ϵ_0 that corresponds at the maximum torque are rendered graphic in the figure 5.

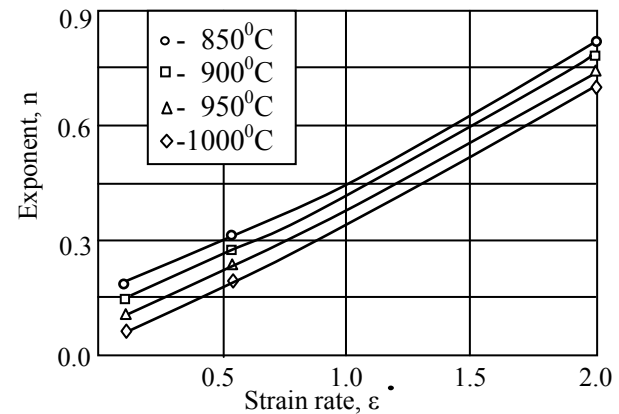


Fig.5. Values of the factor ϵ_0

The formula of the factor ε_0 has the expression:

$$\varepsilon_0 = a_\varepsilon \cdot T^{b_\varepsilon} \cdot (c_\varepsilon)^{\dot{\varepsilon}} \quad (9)$$

Constants have the values:

$$a_\varepsilon = 3712423635$$

$$b_\varepsilon = -3.445121355$$

$$c_\varepsilon = 0.4117625738$$

The coefficients of quality of statistic evaluation

are:

Standard Error of the Estimate =

$$= 1.73577573415809E-02$$

Coefficient of Multiple Determination

$$(R^2) = 0.9583618773$$

Proportion of Variance Explained =

$$= 95.83618773\%$$

The experimental data for the exponent n are rendered graphic in the figure 6.

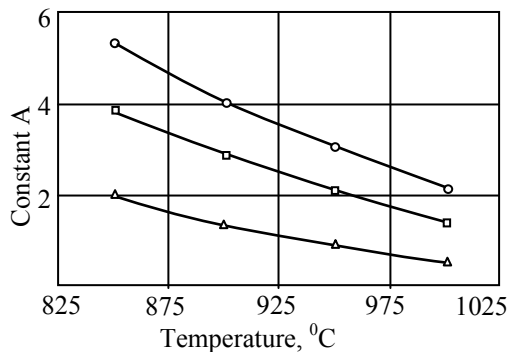


Fig.6. Values of the exponent n

The formula of the factor ε_0 has the expression:

$$n = a_n \cdot T^{b_n} \cdot (c_n)^{\dot{\varepsilon}} \quad (10)$$

Constants have the values:

$$a_n = 1063.736881$$

$$b_n = -1.255542663$$

$$c_n = 1.990376716$$

The coefficient of quality of statistic evaluation

are:

Standard Error of the Estimate =

$$= 0.031135955009085$$

Coefficient of Multiple Determination

$$(R^2) = 0.9899384287$$

Proportion of Variance Explained =

$$= 98.99384287\%$$

The experimental data for the constant A are rendered graphic in the figure 7.

The formula of the factor ε_0 has the expression:

$$A = a_A \cdot T^{b_A} \cdot (c_A)^{\dot{\varepsilon}} \quad (11)$$

Constants have the values:

$$a_A = 1.106688815E+020$$

$$b_A = -6.575749697$$

$$c_A = 0.5306206519$$

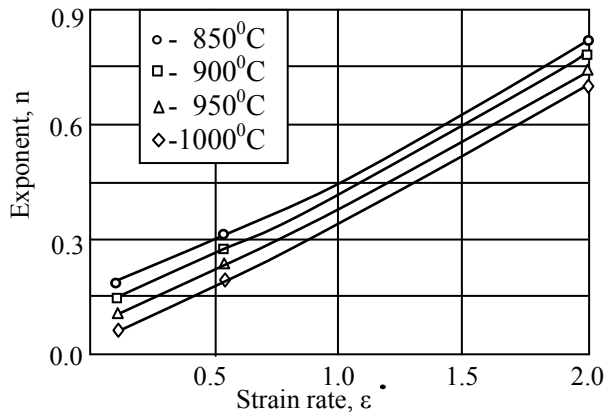


Fig.7. Values of the constant A .

The coefficients of quality of statistic evaluation

are:

Standard Error of the Estimate =

$$= 0.289355804175773$$

Coefficient of Multiple Determination

$$(R^2) = 0.9687668616$$

Proportion of Variance Explained =

$$= 96.87668616\%$$

The factor a from the equation (8) has the value:

$$a = 30,645$$

4. Conclusions

The knowledge of the constitutive equation of the material is necessary form the modeling, simulation and optimization of the plastic deformation process. The best method for establishing of constitutive equation is the torsion testing. Applying a research program at the torsion testing machine in the Plastic deformation laboratory at the Faculty of Metallurgy and materials science from *Dunarea de Jos* University of Galati it established the constitutive equation of steel for wires destined at the reinforcing of the concrete. The constitutive equation shows that the influence of strain rate is described of the power mathematical relation, the influence of the temperature is described by an exponential function. The strain has a complex influence described by a compose function.

References

- [1]. Cănanău N., *Teoria deformării plastice*, Universitatea Dunarea de Jos din Galați, 1994.
- [2] Dumitrescu A.T.- *Contribuții la modelarea laminarii in calibre*. Teza de doctorat, Institutul Politehnic București, 1986.
- [3] Corobete, G. -*Contribuții la cercetarea procesului de laminare a sârmelor din otel cu caracteristici mecanice superioare*. Teza de doctorat, Universitatea Dunărea de Jos din Galați, 2006.
- [4] Moussy F., Franciosi P.- *Physique et mecanique de la mise en forme des metaux*. Presses du CNRS, Paris, 1990, ISBN 2-87682-023-4
- [5] Cananau N., Petrea I, Corobete G. - *Modelling of the flow and deformation fields at the profiles rolling by field lines method*, The Annals of "Dunarea de Jos" University of Galati, Fascicle IX, Nov. 2005.



GRAIN REFINEMENT IN ALUMINUM ALLOYS BY ACOUSTIC CAVITATION PHENOMENA

Luminita MORARU

Physics Department, Faculty of Sciences, University of Galati
email: Luminita.Moraru@ugal.ro

ABSTRACT

In this article, ultrasonic method of transmitting forced vibrations to solidifying aluminum-alloy melts is presented. In the presence of well developed cavitation situations, a fine and homogeneous microstructure has been observed throughout the irradiated ingots. The effects produced when high-intensity sonic or ultrasonic waves are propagated through molten metals can be listed under three main categories: grain refinement, dispersive effects, and degassing resulting in reduced porosity. It has been found that vibrations of a mechanical origin are effective in increasing fluidity by as much as a factor of three and consequently, favorably influence the mold-filling ability of aluminum alloys. There appear to be two distinct views regarding the mechanism, which may be explained by the cavitation effects and the influence of the fluid-flow phenomena.

KEYWORDS: solidification, grain size, ultrasonic field, acoustic streaming, cavitation

1. Introduction

Owing to their impact on industrial casting processes, increasing interest has been shown in fundamental and applied investigations on metal solidification, either in the presence of free convection or when various dynamic treatments generating forced convection are applied in the melt during freezing. A number of examples can be found in the literature where external forces have been applied to induce fluid flow during solidification in order to refine grain size. These methods include rotation of the mold, mechanical or electromagnetic stirring of the melt, and rheocasting [1-6]. Under these conditions, grain structures of castings and ingots change from columnar-dendritic to equiaxed dendritic or globular when they are solidified in the presence of a sufficiently intense forced convection, which generally promotes both the evacuation of superheat and the homogenization of the melt temperature. The phenomena occurring during these various treatments are currently well understood. Several investigators have found that mechanical vibrations of both sonic and ultrasonic character, when applied during the solidification of metals and alloys, modify conventionally obtained macrostructures and microstructures [7,8]. The most commonly observed effect is the suppression of

undesirable dendritic and columnar zones and the development of a fine-grained equiaxed structure. In fact, the effects produced when high-intensity sonic or ultrasonic waves are propagated through molten metals can be listed under three main categories: grain refinement, dispersive effects, and degassing resulting in reduced porosity. In addition, it has been found that vibrations of a mechanical origin are effective in increasing fluidity by as much as a factor of three and consequently, favorably influence the mold-filling ability of aluminum alloys. There appear to be two distinct views regarding the mechanism, which may be explained by the cavitation effects and the influence of the fluid-flow phenomena.

Cavitation is the term used to describe the formation of bubbles, or cavities, in liquid. These cavities may be filled with air or vapor or may be almost empty; they can be produced in liquids by the passage of sonic or ultrasonic waves, provided they are of suitable frequency and intensity. Due to the oscillation of the medium, regions of compression and rarefaction are formed. In the rarefaction regions, a negative pressure (tension) may exist and air or vapor bubbles can form. In most liquid metals, a considerable amount of gas is present in the form of very small bubbles, which are, in most circumstances, seeded from pre-existing gas pockets [8,9]. Liquid vapor may also evaporate into the partial void

produced by the sudden expansion of the undissolved gas bubbles. The usefulness of cavitation in processes such as cleaning, dispersion, and grain refinement is largely due to the very high pressure produced locally on the collapse of the cavities. During this collapse time, the walls of the bubble are forced inward until they impinge on the small nuclei of gas or vapor contained in the cavity, which is severely compressed at the time. It has been demonstrated that the pressure in the bubbles immediately prior to their final collapse can reach several thousand atmospheres [8-10]. Thus, when the bubbles finally disappear, extremely powerful shock waves occur, which are responsible for most of the phenomena brought about by cavitation. In particular, during metals and alloys solidification, the forces associated with cavitation result in the dislocation of growing crystals. This splitting up of crystals effectively produces many more nuclei around which new crystals can form. Thus, in this manner, the crystals never grow beyond a certain size.

The other view is that vibrations also give rise to considerable agitation of the melt and result in the newly formed nuclei being distributed throughout the solidifying pool, so that crystallization takes place uniformly inside the entire volume. Moreover, the vibrations have much the same effect as turbulence, dispersing small crystals so that more of them grow, resulting in reduced grain size.

2. Experimental setup

The sonic or ultrasonic irradiation of molten metals is mainly carried out with magnetostrictive, or piezoelectric, transducers. Coupling rods made of quartz, graphite, and various ceramic materials have been used to communicate vibrations to a molten metal, and these materials are attached to the transducer by special cements. However, such a technique presents several disadvantages. The oscillating rods are very rapidly dissolved when they are immersed into molten aluminum alloys, and this circumstance provokes an undesirable contamination of the metal. Moreover, the intensity of cavitation is greatest near the transducer or the coupling rod face; thus, the use of such a system is principally justified for the treatment of metal mixtures on a small scale.

In our experiment, the ultrasonic field was generated using a magnetostrictive transducer and an ultrasound generator. We preferred to introduce the ultrasound continuous longitudinal waves through the bottom of the crucible.

In this arrangement, there is no barrier between the ultrasound source and the melted metal. The stepped stainless steel horn was used to transmit the ultrasound to the molten and it is completely resistant to ultrasonic erosion.

Typical operating parameters were frequency of 20.338 kHz and the nominal input power of 600 W. The acoustic power dissipated by ultrasonic probe in

1000ml-deionized water at ambient temperature and pressure as a function of electrical input power was determined by calorimetry.

These data were used to allow selection of the appropriate input power to give constant transmitted power. After the completion of measurements, the ultrasonic horn was examined microscopically. No attack of the stainless steel by liquid metal samples was observed in either case, so there was no evidence of contamination of the liquid metal by alloying.

We used samples solidified in presence and in absence of ultrasonic field.

The metallography results are obtained by means of TEM (Transmission Electron Microscopy) and EDX (X-ray Photoelectron Diffraction) techniques. The TEM technique is used in the analysis of thin foils of aluminum alloys and allows obtaining important information about the substructure. The measurements were done in Physical Laboratory of **Alcan Děčín** Extrusions s.r.o., The Czech Republic.

3. Results and discussions

From the hydrodynamic standpoint, the melt flow may be considered as the superposition of three motions: two alternating flows of N and $2N$ frequency, respectively, and an unstable recirculating flow that may be resolved into a steady component and a random component.

In these experiments, the pressure in the solidifying liquid metal is the sum of static and oscillating terms (Figure 1). Actually, the metalostatic pressure $p g h'$ at depth h' and the fluctuating dynamic pressure $\rho u^2/2$ can be neglected here. Accordingly, if the ultrasonic pressure amplitude is greater than the atmospheric pressure, then the pressure in the liquid will be negative (tension) for part of each period (Figure 1-b).

Cavitation takes place with full efficiency during the negative pressure part of a cycle or a series of cycles (Figure 1-b), and nucleation follows either as a result of the modification in equilibrium temperature, caused by the pressure change during the collapse of the cavitation bubbles, or as a result of cooling the surface of the bubbles by evaporation during its growth. Under this circumstance, cavitation may occur at several points inside the liquid and on the wall mould.

On the other hand, velocity measurements [11] showed that the fluctuating flow is relatively intense. When the ultrasound pressure is optimal, the shear rate reaches a value comparable to the magnitude order obtained in the rheocasting operation. It appears that during the irradiation of the semisolid alloy, the apparent viscosity remains practically unchanged up to a solid fraction on the order of 0.5, whereas the velocity decreases dramatically when the solid fraction exceeds 0.55.

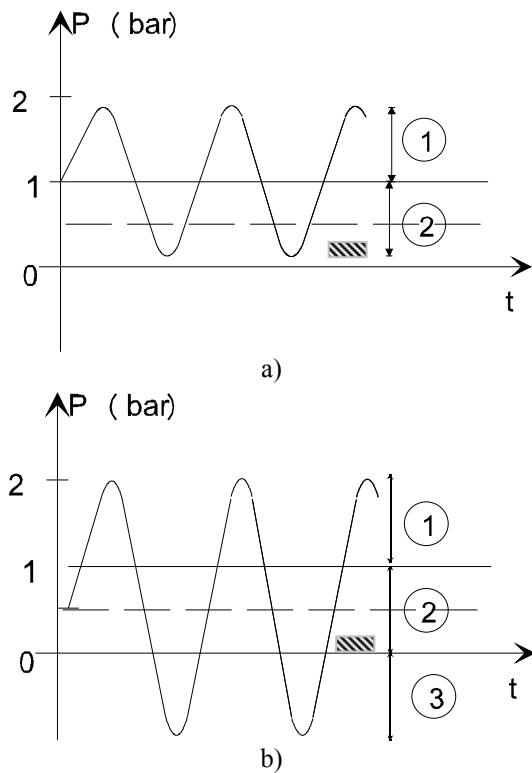


Fig. 1. The influence of the ultrasonic pressure amplitude on the grain refinement at (a) the simultaneous influence of shear rate and cavitation and (b) the predominance of cavitation effects, producing a fine microstructure. 1-ultrasonic pressure amplitude, 2-static pressure, and 3-tension generated in liquid (negative pressure). The dotted line corresponds to the onset of a significant grain refinement provoked by the oscillating flow, and the hachured area corresponds to the critical threshold zone of cavitation.

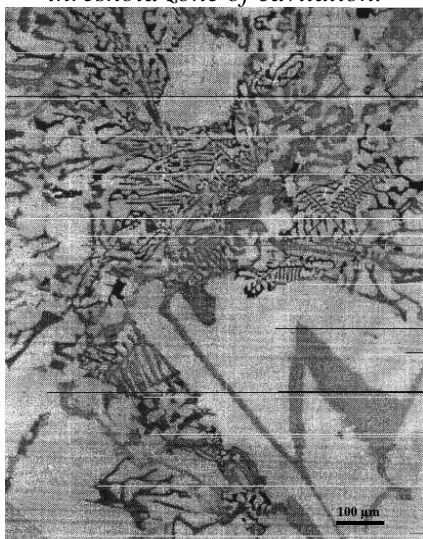


Fig.2. Optical micrographs of the cast structure of aluminum alloy exhibits a typical dendritic structure.

The production of cavitation in liquid metals strongly depends on the most volatile undissolved gas content of the liquid, and it has been established that in the case of aluminum melts, the hydrogen content is the controlling factor [8,12]. The solubility of hydrogen in aluminum is dependent on both the partial pressure of gas and the melt temperature. At a constant temperature, the equilibrium concentration of gas in solution is proportional to the square root of the partial pressure [13,14].

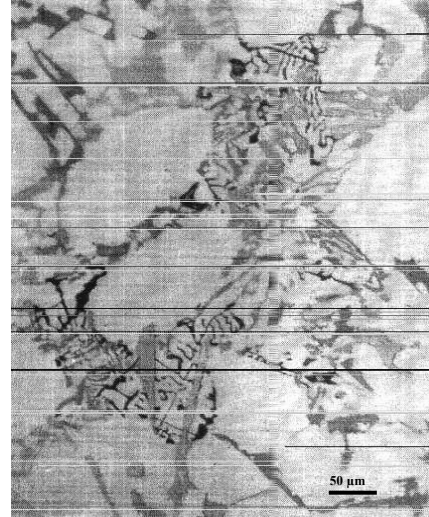


Fig.3. The micrograph exhibits a typical nondendritic crystals (with smaller size) due to cavitation conditions.

Figure 3 relates to the following test: an ultrasonic pressure field was applied to the solidifying alloy for five minutes from the liquidus temperature, with a cooling rate of 6°C /min. In this experiment, the operation corresponds to grain refinement, consisting mainly of the presence of an agglomeration of nondendritic crystals (with smaller size) due to cavitation conditions. This observation is understood by the disintegration of a cluster, probably under the action of a single cavitation event producing impressive mechanical damage over a microscopic region. Identical repetitive tests have confirmed this observation. In such a case, cavitation in the solidifying two-phase mixture does not take place uniformly, and systematic trials showed that the regions of intense cavitation are quite random from one experimental run to the next.

Examination of Figure 3 reveals that the grains are much finer and globular than those produced by the hydrodynamic effect in the absence of cavitation (Figure 2). Moreover, it is seen that the cavitation effects result in the total disappearance of the numerous large clusters.

It appears that contrary to the case of natural cooling melts, the ultrasonic irradiated semisolid alloy samples exhibit uniform grain refinement across the entire section. This is due to the fact that in this experiment, the ultrasonic forces that induce acoustic

flow motion act uniformly throughout the semisolid melt. Moreover, it should be noted that the cavitation causes efficient degassing, resulting in tremendously reduced shrinkage and porosity [12]. Consequently, the compactness of the irradiated material is considerably improved. Under ultrasonic conditions, the acoustic flow takes place in the liquid metal. It is clearly demonstrated that the acoustic flows are associated with the ultrasound absorption, whatever its nature. However, the absorption coefficient is quite small for the liquid metals, so the increase in the temperature of the melt caused by absorption process has been eliminated. In these conditions, the reason for this prominent change in solidification kinetic is assumed to be large-scale acoustic streaming. Its effect is a permanent stirring of the melt so the effects of thermal and mass homogeneity of the melt are quite obvious. The increasing in the intensity of fluid flow can give rise to grain multiplication, which can be attributed to the increased effective nucleation rate caused by the extremely uniform temperature and composition fields in the bulk liquid at early stages of solidification. Also, the forced convection increases the growth rate. The solidification starts by heterogeneous nucleation at the crucible wall through the so-called "big-bang" mechanism. Only a fraction of the nuclei formed at this stage contributed to the formation of the chilled zone and the majority of the nuclei are transferred into the hotter bulk liquid and remelted. The final solidified microstructure depends largely on the amount of nuclei surviving after the big-bang nucleation. Under the ultrasound action both the temperature and composition fields of the liquid metal are extremely uniform. The nuclei formed will survive due to the uniform temperature field, resulting in an increased effective nucleation rate. In addition, the intensive stirring may also disperse the cluster of potential nucleation agents, giving rise to an increased number of potential nucleation sites. Also, under forced convection, the nucleation and the growth at the chilled wall were suppressed, while the nucleation and growth in the bulk liquid were enhanced [15].

It has been suggested that the forced convective fluid flow induced by ultrasound may be sufficient to break small dendrite arms and distribute them throughout the melt. If a high energy boundary is formed in a metal in contact with its liquid then the condition indicates that the grain boundary will be wetted by the liquid phase, i.e. replaced by a thin layer of liquid and thus the dendrites break appear. Further these broken dendrites act as nucleants and grow as globular nondendrite structures.

The acoustic streaming produced the change in possibility that hydrodynamic force to cause breakage of dendritic arms under the solidification conditions. In the same time, due to supplementary energy contribution, the ultrasonic field presence hinders the long-range ordering processes of atoms. At this moment, they act as nuclei for the growth of more

particles and the relatively small dendrite spacing are created.

The possibility that fluid flow could disrupt the crystal bonding is also considered [16,17]. The shear forces resulting from natural convection flow of the melt are too weak to disrupt the crystal bonding during solidification. However under ultrasonic field, these forces are dramatically increasing. The accuracy of sonic measurements is reasonable taking into account the difficulties associated with getting the ultrasound into the melted metal.

The ultrasonic field presence into a liquid causes cavitation phenomenon [15]. This imposes a sinusoidal variation in pressure on a steady state ambient pressure. One new question of this study is the problem of cavitation and its microstreaming effect. The effect of ultrasound increases with increasing power, but not indefinitely since there is an optimum value beyond which the effect diminishes. When 20.338 kHz high-intensity ultrasound was applied to the molten system, a mixing of the melted metal close to the solid-liquid interface and the crucible wall due to cavitation was produced. Near the solid surface, cumulative jets can be generated and the diffusion layer is thinned due to enhanced mass transport resulting from microstreaming. In our experiment, these optimum conditions in cavitation were studied in deionized water at ambient temperature. The ultrasonic treatment of liquid metals differed essentially from that of aqueous solutions and organic liquids. This is due to the different nature of cavitation nuclei and, hence different conditions required for the initiation and development of acoustic cavitation. Only fine solid particles (mainly oxides, e.g. Al_2O_3 in aluminium melt) can act as cavitation nuclei in metallic melts. At the same time, because the molten metals feature light opacity, the cavitation cannot be studied directly.

4. Conclusion

The paper presents the way how mechanical vibrations of ultrasonic character applied during the solidification of metals and alloys, modify conventionally obtained macrostructures and microstructures. The most commonly observed effect is the suppression of undesirable dendritic and columnar zones and the development of a fine-grained equiaxed structure.

Also, the ultrasonic field presence into a liquid causes cavitation phenomenon. The usefulness of cavitation in grain refinement is largely due to the very high pressure produced locally on the collapse of the cavities. When an ultrasonic pressure field was applied to the solidifying alloy the grain refinement, consisting mainly of the presence of an agglomeration of nondendritic crystals (with smaller size) due to cavitation conditions, appears. This observation is understood by the disintegration of a cluster, probably under the action of a single cavitation event

producing impressive mechanical damage over a microscopic region. Identical repetitive tests have confirmed this observation.

This process presents a serious drawback for very important potential industrial applications (which consist of alloy-grain refinement), since, for the large-scale ingot castings, substantial energy consumption is required to reach the cavitation threshold.

Another technique consisting of the continuous maintenance of the melt at resonance can be considered. Under this condition, the ultrasonic power would be markedly lowered, and, consequently, the facility cost and energy expense would be decidedly reduced.

References

- [1]. C. Vivès and C. Perry, 1986, Grain Refinement in Aluminium Alloys by Means of Electromagnetic Vibrations Including Cavitation Phenomena, *Int. J. Heat Mass Transfer*, 1, p. 21.
- [2]. C. Vivès, 1989, Grain Refinement in Aluminium Alloys by Means of Electromagnetic Vibrations Including Cavitation Phenomena, *Metall. Trans. B*, 20B, p. 623.
- [3]. C. Vivès, *Metall. Trans. B*, 20B (1989), p. 631.
- [4]. M.C. Flemings, 1991, *Metall. Trans. B*, 22B, p. 269.
- [5]. C. Vivès, 1992, Effect of low frequency electromagnetic field on microstructures and macrosegregation of horizontal direct chill casting aluminium alloy, *Metall. Trans. B*, 23B, p. 189.
- [6]. C. Vivès, 1993, Grain refinement induced by electromagnetic stirring: A dendrite fragmentation criterion, *Metall. Trans. B*, 24B, p. 493.
- [7]. J.-P. Gabathuler et al., 1992, *Processing of Semi-Solid Alloys and Composites*, ed. S.B. Brown and M.C. Flemings (Cambridge, MA: MIT, p. 33.
- [8]. O. Abramov, 1994, *Ultrasound in Liquid and Solid Metals* Boca Raton, FL: CRC Press, p. 289.
- [9]. T. Leighton, 1994, *The Acoustic Bubble*, London: Academic Press Ltd, p. 531.
- [10]. J. Szekely, 1979, *Fluid Flow Phenomena in Metals Processing*, New York: Academic Press Ltd, p. 305.
- [11]. C. Vivès, (1990) *Int. J. Heat Mass Transfer*, 33, p. 2585.
- [12]. L. Moraru, S Macuta, 2006, Acoustical degassing of molten aluminium, SISOM 2006 (Annual Symposium of the Institute of Solid Mechanics), Bucuresti, 17-20 Mai, CD-ROM publication
- [13]. C. Vivès, 1996, Effects of Forced Electromagnetic Vibrations during the Solidification of Aluminium Alloys: Part I. Solidification in the Presence of Crossed Alternating Electric Fields and Stationary Magnetic Fields, *Metall. Trans. B*, 27B, p. 445.
- [14]. C. Vivès, 1996, Effects of Forced Electromagnetic Vibrations during the Solidification of Aluminium Alloys: Part II. Solidification in the Presence of Colinear Variable and Stationary Magnetic Fields, *Metall. Trans. B*, 27B, p. 456.
- [15]. Abramov O.V., 1993, *Ultrasound in liquid and solid metals*, Russian Academy of Sciences, Moscow, (in English).
- [16]. Moraru L. 2005, The effect of fluid flow on solidification of light metal alloy, *Transaction of the University of Kosice*, Vol 5, pp70-75.
- [17]. Moraru L., Tudose C., 2004, Analytic model of bonding forces in liquid metals and ultrasound influence, *Proc 2nd Int Conf Romanian Acoustical Society*, Impuls Publishing House Ed., București, pp 75-80.

STEEL FLOW CONTROL OF CONTINUOUS CASTED SLABS USING SUBMERGED ENTRY NOZZLE EXCHANGE SYSTEM FOR TUNDISH

Viorel MUNTEANU

"Dunărea de Jos" University of Galati
email: viorel.munteanu@ugal.ro

ABSTRACT

In the steel making process, the continuous casting of molten steel is a very important step which involves hi-tech facilities. The flow control is a very important issue that influences the quality of the final products. The parameters of flow control from the tundish into the mold are achieved by means of stopper, taking into account the casting speed, tundish weight, mould and a new generation of submerged nozzle exchange mechanism developed by Vesuvius – SEM 2085 – along with the chemical behaviour refractory component during steel casting.

KEYWORDS: continuous casting, steel, tube changer, tundish, mould, steel flow control

1. The new generation of tube changers

Development of a new generation of tube changers

In order to develop a new generation of tube changer, it took into consideration new requirements such as robust and simple mechanism (less parts) easy to install, handle and maintain, with air tightness improvement, operating in full automatic mode for casting longer sequences of very high quality steel grades including stainless steel, etc. The introduction of tube changer has an impact on productivity (improving by over 2% as the proportion of time for re-stranding is reduced), yield (primary yield can be improved by 0.85% through the elimination of 1.5 meter crop required to remove the scar on a flying tundish), steel quality, safety and operational conditions.[1]

The tube changer cassette

The core of the system is the „cassette” that holds the refractory and the pressure loading device. (see figures 1 and 2).

There is a cassette for normal size refractory (tube changer bore size $\leq 85\text{mm}$) and a cassette for extra-large refractory (tube changer bore size $>85\text{mm}$).[2]

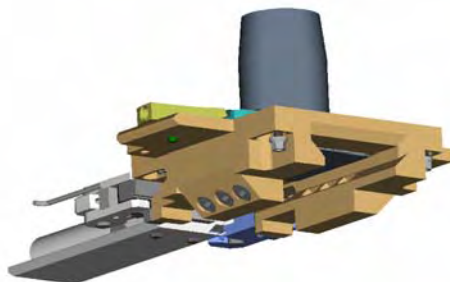


Fig. 1. Tube changer cassette without submerged entry nozzle plate.

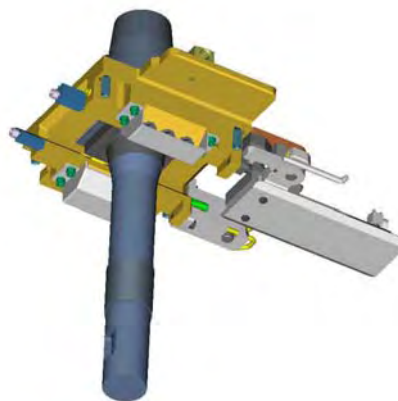


Fig. 2. Tube changer cassette with submerged entry nozzle plate.

Monobloc inner nozzle plate clamping device

In order to reach an improved air-tight system, it is important to have a sturdy monobloc inner nozzle plate that can be strongly fixed in the mechanism and reliably connected to the argon supply network. In this regard, a completely new design of canned nozzle plate has been designed with a parallelepipedic flange provided with two 45° tapered faces. (see figure 3 and 6).

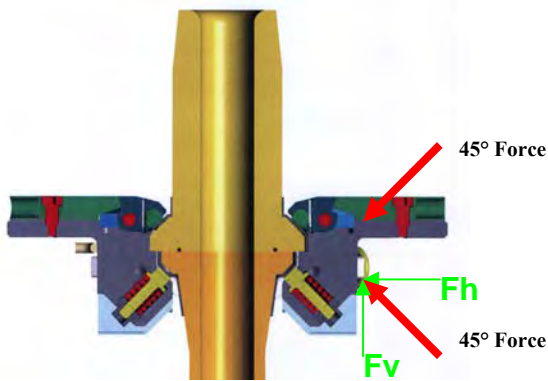


Fig. 3. Cassette – Monobloc inner nozzle support and submerged entry nozzle-plate spring-pushers device

This design is very strong. It also allows to precisely position the refractory in the cassette and to firmly lock the piece by means of 2 rotary wedges pressing 2 rockers. (see figures 4 and 5)

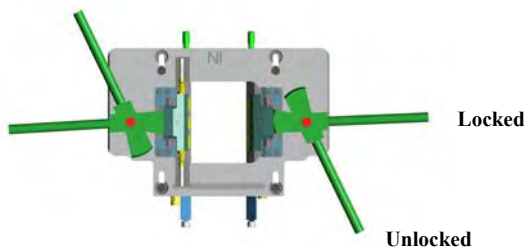


Fig. 4. Inner nozzle clamping device rotary wedges pressing rockers in locked and unlocked positions

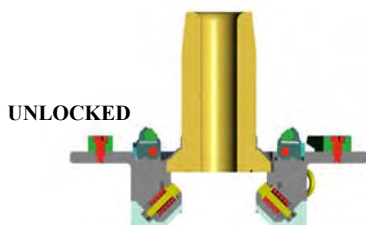


Fig. 5a. Inner nozzle clamping device in unlocked position

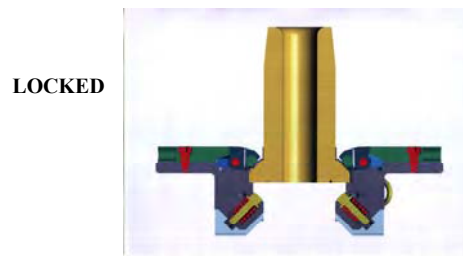


Fig. 5b. Inner nozzle clamping device in locked position

The clamping forces are directed in 45° angle towards the center. This unique clamping concept reduces stress peaks and also causes horizontal compression forces acting at the plate sector of the refractory elements. (see figure 3)

Monobloc submerged entry shroud design and support

The new monobloc submerged shroud also has now a flange that looks similar the inner nozzle plate, for the same reasons. (see figure 3 and 6).

It is supported by means of 6 direct acting pushers and 6 high temperature resistant springs. (see figure 3) The direction of the force is 45° inclined towards the center, similar to the inner nozzle. This also generates a combination of vertical and horizontal forces on the flange of the tube leading to reduced stress in the piece.

Inert gas supply

The argon connection is “automatic” when the inner nozzle plate is installed. (see figures 7 and 9) Some of the pushing rockers are provided with argon injection tuyeres. When the rockers are in the pushing position, they provide a reliable argon-tight connection with the argon input holes (with graphite gasket) that are located on one of the tapered faces of the nozzle plate flange.

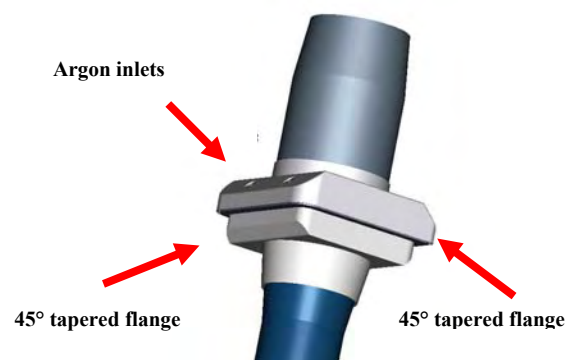


Fig. 6. Monobloc inner nozzle plate and monobloc submerged entry nozzle design

Two independent networks can fill argon in the nozzle plate itself (purging) and in a sealing groove located in its sliding surface. It allows a very accurate tuning of the argon flow/pressure in each zone, which is critical for clogging avoidance and steel quality.

Automation

The process can be automated in order to link the casting speed, the mould level and the stopper rod positions for a one-button operation.[4]



Fig. 7. Tube changer in operation on the slab caster no.1 in Mittal Steel Galati [3]

Modular concept

Targeting a flexible “Modular Design”, the two kinds of cassettes can be combined with different driving mechanisms such as:

a) Pneumatic shifting drive with push-bar and side mounted cylinder: (see figure 8)

It does not need any hydraulic supply. The cylinder is directly attached to the tube changer cassette. It is a simple control system, which allows automated tube change.

b) Hydraulic shifting drive with push-bar and side mounted cylinder: (see figure 9)

The drive is attached to the tube changer cassette but the hydraulic cylinder is detachable. It remains on the tundish car or it remains on the mechanism and is connected with quick couplings. It allows automated tube change.

c) Manual swing arm mounted hydraulic direct shifting drive: (see figure 10)

This is a pivot mounted direct acting hydraulic cylinder with self locking device.

The cylinder is easy to detach and remains on the tundish car.

It is the most simple configuration, but it is not capable of automated tube change

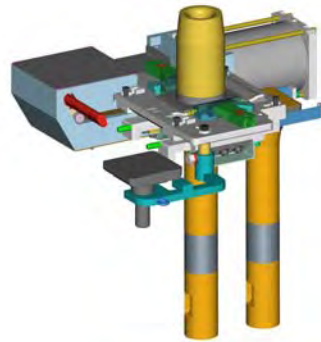


Fig. 8. Push-bar with Pneumatic Drive = "PP" version

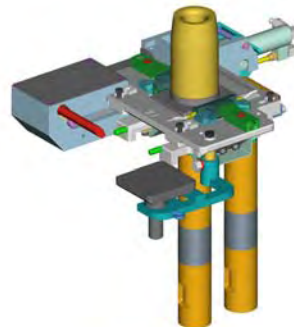


Fig. 9. Push-bar with Hydraulic Drive = "HP" version

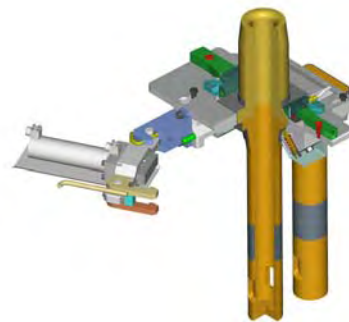


Fig. 10. Manual Swing Arm with Hydraulic Drive = "HM" version

2. Chemical behavior refractory component during steel casting

The classical experimental evaluation of steel corrosion is not enough to determine refractory component. Standard experimentation are conducted with limited amount of steel, while in reality steel is continuously renewed at refractory interface.

The second limitation faced today is that refractory interface is, in reality, controlled by variables like steel dissolved elements and steel inclusions. For instance, the volume of inclusion during continuous casting is comparable to the volume of refractory components used so they have a strong influence on steel refractory reactivity.

So the only possible approach to corrosion is to determine experimentally mass transfer from refractory to steel and to extrapolate to continuous casting conditions.

2.1 Steel and refractory interaction model

To precise the nature of chemical reactions, specific experiments have been conducted:

For the first type of experiment, pure iron is melted in an induction furnace with tailored alloys addition. A rotating refractory sample is placed in the melt and steel chemical composition change are determined by steel sampling during the experiment.

A second set of experiment consist to degassing evaluation on refractory samples using a mass spectrometer at increasing temperature.

For the different type of refractory composition used in steel casting the following major reaction have been determined and quantified:

- Carbon dissolution $C \rightarrow \underline{C}$
- Silica reduction $SiO_2 + C \rightarrow SiO(g) + CO(g)$
- Magnesia reduction $MgO + C \rightarrow Mg(g) + CO(g)$
- Zirconia reduction $ZrO_2 + 3C \rightarrow ZrC + 2CO(g)$
- Oxides dissolution $MxOy \rightarrow x\underline{M} + y\underline{O}$

The different reaction kinetics have been determined depending on steel grade, refractory composition, microstructure and physical parameters at refractory interface (pressure, temperature)

For example the model for Carbon dissolution is show in Fig 11.

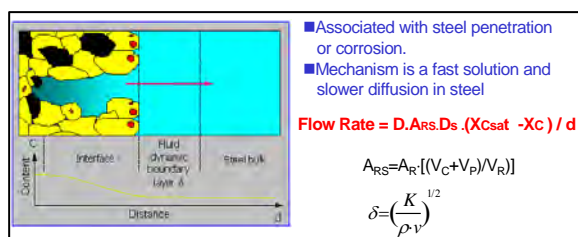


Fig 11. Carbon dissolution: carbon flow rate as a function of reactive surface (A_{rs}), carbon content (X) and steel flow.

The global result is a mathematical program which calculate the flow rate of species passing from the refractory interface to the steel.

3. Steel flow control optimization

In order to better understand steel flow characteristics during casting and steel flow consequences on refractory components, specific fluidodynamic models have been developed.[5]

The main features investigated are for example:

- Specific meshing refinement at refractory interface to capture physical parameters at refractory interface.
- Thermal exchange between refractory and steel to better evaluate temperature loss in steel as well as thermal gradient in refractory
- Chemical interaction with refractory interface and contamination diffusion in steel flow.

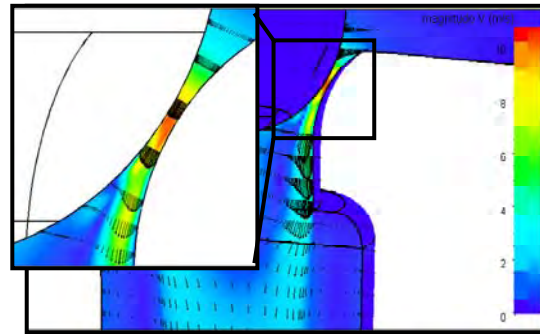


Fig. 12. Calculated steel flow at stopper regulation point

The mesh refinement capability is illustrated in figure 12 representing the steel flow regulation between a tundish stopper and a submerged nozzle.

The noticeable high speed at the regulation area justify the occurrence of severe corrosion phenomena at this location.

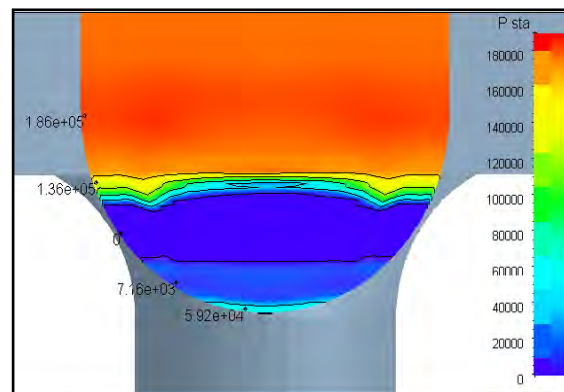


Fig 13. Pressure at refractory surface on tundish stopper

Secondly the extraction from the steel flow results of the pressure at refractory surface (figure 13) explain the strong degassing of refractory observed in this area.

The casting rate is controlled by a stopper or a slide gate, but depends on the ferrostatic head in the tundish and the bore size only. The withdrawal speed of the caster can be adjusted to cope with the flow

rate from the tundish and maintain a satisfactory steel level in the mold. (fig.14).[1]

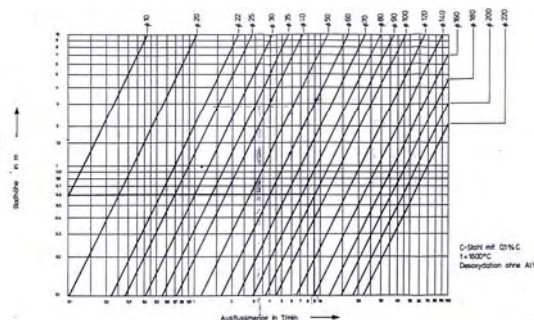


Fig. 14. Flow Rate Calculation

4. Conclusions

The continuous casting process of slabs can be automated using submerged nozzle exchange mechanism, flow control of which is achieved by means of a stopper. The tube changer offers :

improved caster scheduling, increased caster productivity, increased prime grade slabs, increased yield and reduced operating cost.

In addition to the extension of the tundish service life, there are advantages on improvement of the operation flexibility and security.

References

- [1] **Munteanu, V.** – *Contributii la dinamica mecanismului de inchidere cu sertar pentru recipientii de turnare ai otelului*. Teza de doctorat-1984, Universitatea „Dunarea de Jos”, Galati
- [2] **V. Boisdequin, S. Gangai** - “*Submerged entry nozzle exchange system for tundish*”, Vesuvius Systems Ghlin, pag. 25-32, 2006
- [3] **Munteanu, V., Zorlescu, D., Deac, F.** – *Modernization of continuous casting slab machine no.1 from Ispat Sidex, Galati* – 5-th European Continuous Casting Conference Proceedings, Nice, 2005, pp.165-172
- [4] **Munteanu, V.** – *Instalatie de autoreglare a nivelului otelului lichid in distribuitorul masinilor de turnare continua*. Brevet de inventie nr.78734 - Romania
- [5] **J. Cesar, H. Plostajner**, “*Automatic Mould Level Control*”, Store, 12.12.2002.

STRUCTURE AND CORROSIVE FIRMNESS OF COMPOSITION MATERIALS ON THE BASIS OF COPPER AND MOLYBDENUM GOT METHOD ELEKTRON-BEAM TECHNOLOGY

V.G. GRECHANYUK¹, V.A. DENISENKO¹, L.ORAC²

¹ Kiev National University of Building and Architecture Ukraine, Kiev,

² "Dunarea de Jos" University of Galati

e-mail: gekont@ukr.net

ABSTRACT

The article describe the study of corrosive firmness of composition materials on the basis of copper, obtained by EB-PVD method. Corrosive firmness of condensates was explored by gravimetric method. The especially decreasing of the corrosive stability is definite during concentration of molybdenum about 12 % . Chemical composition of condensates showed that in the stationary terms of receipt of materials, their chemical composition is heterogeneous on a thickness. The structure of condensate has the expressly expressed macro-laminated character, the size of layers hesitates from a few ten microns of the to several hundred.

KEYWORDS: composite materials, EB-PVD, corrosive stability.

1. Introduction

Lately wide application for making of electric contacts was found by the condensed from a steam phase composition materials Cu-Mo-Zr-Y.

The indicated materials with concentration of molybdenum to 12 % mass. are used in the contacts of alternating and permanent currents by force to 1000 A. Attempts to get similar materials with greater concentration of molybdenum on revolved at a speed of 38 turns in a minute on substrate at the temperature of besieging 700 ± 30 °C success was not had.

In such condensates there was friable destruction in the process of deposition.

In also time the receipt of the condensed materials is of interest on the basis of copper and molybdenum with greater concentration of molybdenum and expansion of possibilities of application of these compositions in the range of currents over 1000A.

2. Experimental

The composition materials Cu-Mo were got on stationary substrate made from carbon steel, measuring 250x220x10 mm at the temperature 900 ± 30 °C method of electron-beam evaporation and subsequent condensation in a vacuum on a technological scheme, presented on the fig. 1.

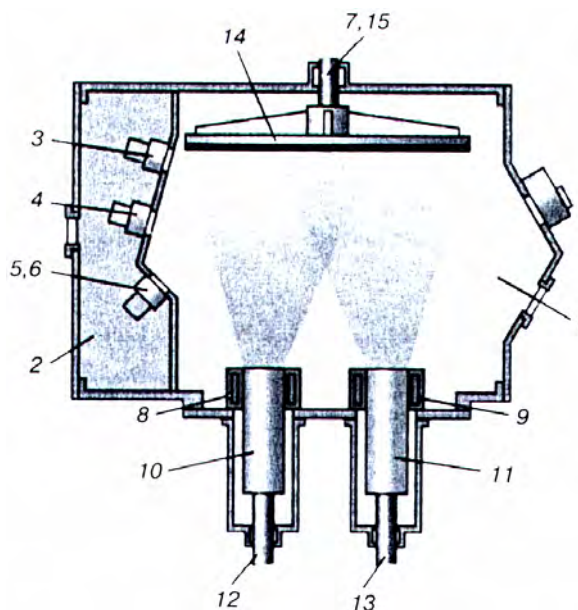
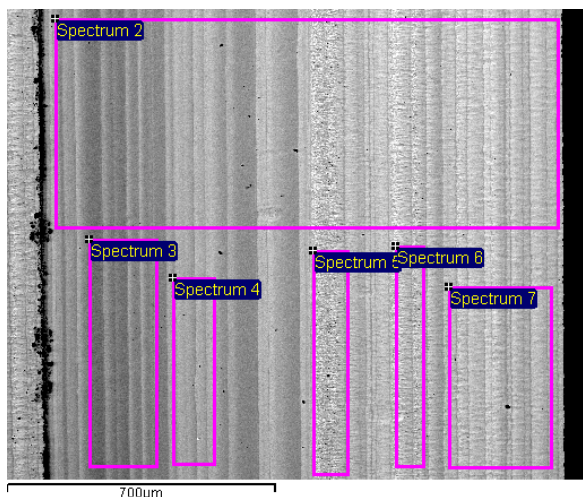


Fig. 1. Scheme of receipt of the composition materials Cu-Mo: 1 – working chamber; 2 – gun chamber; 3 - 6 – EB heaters; 7 – substrate rotation rod; 8, 9 – crucibles for evaporation of copper and molybdenum, respectively; 10, 11 – ingots for evaporation; 12, 13 – mechanisms for feeding ingots into evaporation zone; 14 – disc-substrate; 15 – substrate rotation mechanism.

The presented technological scheme allowed to form the condensed compositions with a gradient for concentrations of molybdenum from 0 to 32.5% mass. (basis copper).

The study of chemical composition of condensates showed that in the stationary terms of receipt of materials, their chemical composition is heterogeneous on a thickness (fig.2).



Spectrum	Cu	Mo	Total
Spectrum 2	87,57	12,43	100
Spectrum 3	96,19	3,81	100
Spectrum 4	86,96	13,04	100
Spectrum 5	79,76	20,24	100
Spectrum 6	81,82	18,18	100
Spectrum 7	84,02	15,98	100

Fig.2. Chemical composition on the thickness of condensate

Neutralized chemical composition on the thickness of condensate shows concentration of molybdenum 12.43% mass. In also time, distribution of components on separate areas on the thickness of

condensate has a heterogeneous character and hesitates from 3.81 to 20.24 % mass. The data resulted on fig.3 testify to heterogeneity of distributing of components.

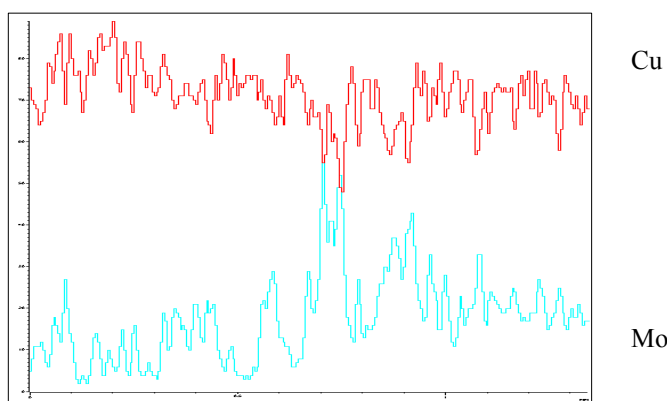


Fig. 3. Distribution of components on the thickness of condensate

3. Results and discussions

The analysis of distributing of components in area of minimum maintenance of molybdenum shows that there is heterogeneity on a molybdenum even in a relatively narrow region, so on a depth a 50 µm heterogeneity hesitates from 0.11 to 3.89 % mass. Molybdenum.

The structure of condensate has the expressly expressed macro-laminated character. The size of layers hesitates from a few ten microns of the to

several hundred. Interface of macro-layers clear without the visible distortion conditioned by the roughness of substrate (fig.2). In also time of micro-lamination, discovered before in the condensed materials got on revolved substrate, is not exposed.

Increase of concentration of molybdenum on the neutralized chemical analysis from 12.43 to 40.36 % mass. direct substantial change of macrostructure of condensate (fig.4).

Interface between macro-layers has a wavy character.

The level of heterogeneity of distribution of molybdenum and copper in macro-layers is increased.

The character of distribution of components is presented on the fig. 5.

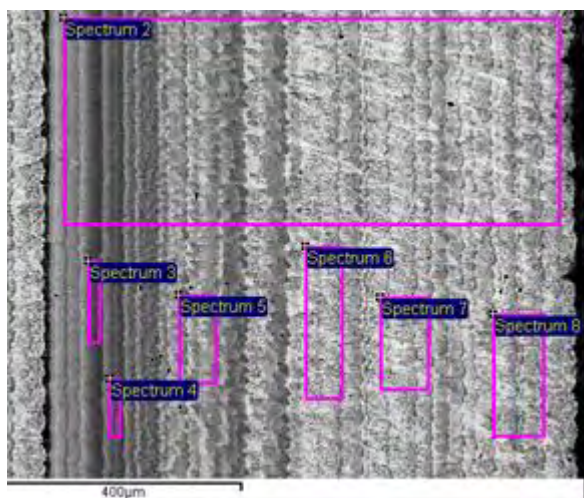


Fig.4. Structure of condensate with the raised content of molybdenum

For regions with the maximal content Mo (fig.6) the unclear expressed columnar with predominating content of molybdenum (the light field) and promoted concentration of copper (the dark field).

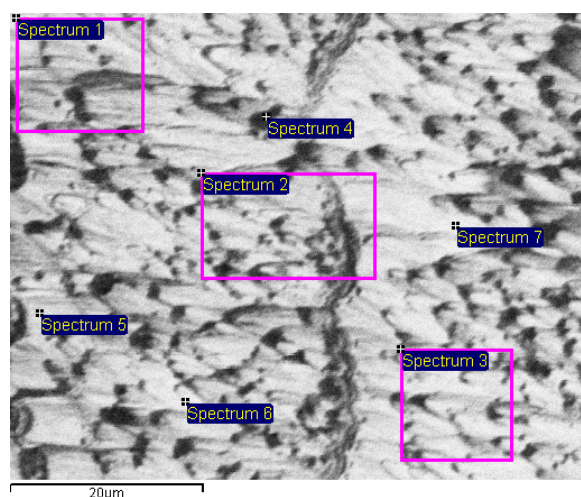


Fig.6. Distribution of components in a region with maximum content of molybdenum

Corrosive firmness of condensates was explored by gravimetric method. Samples by an area 100 mm² after preliminary treatment placed on corrosive agent (water) on 100 hours. The control after the change of mass of samples was carried out in every 20 hours. Researches were conducted in the static mode in the distilled water. Gravimetric researches complemented by determination of

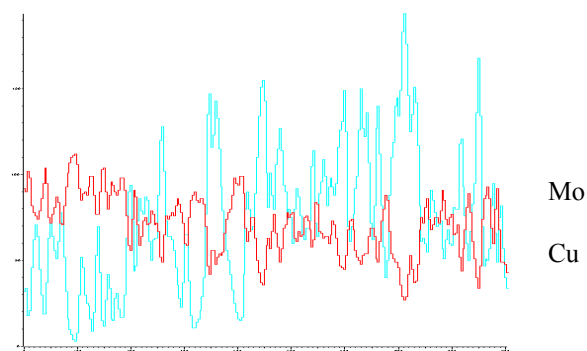
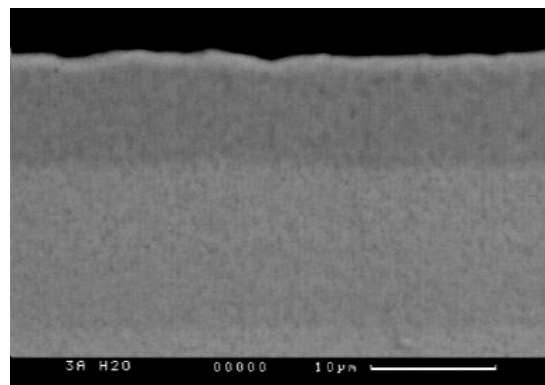
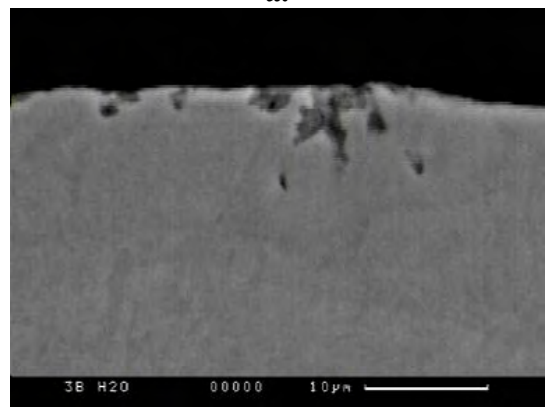


Fig.5. Distribution of components on the thickness of condensate

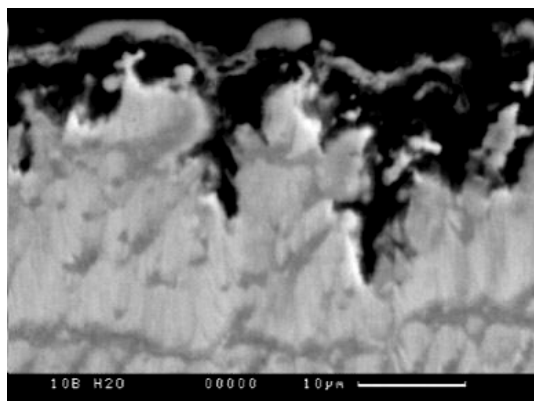
composition of corrosive environment before and after conducting of corrosive tests, and also electronic-microscopic researches.



a.



b.



c.

Fig.7. *The electronic-microscopic researches of condensate after the corrosive testing*

The electronic-microscopic researches of condensate, conducted after the corrosive testing, showed that at small concentrations of molybdenum destruction of surface of samples is practically absent (fig.7, *a*), and is observed only on areas, on which are present the defects of structure (fig.7 *b, c*), caused by a technological process.

At the increase of concentration of molybdenum destruction of surface is increased and on separate areas can achieve at 20 µm (fig.7, *c*).

4. Conclusions

1. The rise of temperature of substrate with 700 °C to 900 °C during joint condensation of copper and molybdenum on stationary substrate allows to get the condensed material on the basis of copper and molybdenum with the promoted content of molybdenum.
2. For condensates of got in stationary terms the macro-layers with chaotic their distribution on the thickness are characteristic.
3. Corrosive destructions are observed on areas on which are present defects of structure.

References

- [1]. M.I. Grechanyuk, V.O. Osokin, I.B. Afanasiev, I.M. Grechanyuk - *Pat. 34875* Ukraina. MPK C23C/20. Compozitionnai material dlia electriceskih contactov i sposob ih proizvodstva, Opubl. 30.12.2002; Bul. Nr.12.
- [2]. N.I. Grechanyuk, V.A. Osokin, I.B. Afanasiev, I.N. Grechanyuk - *Electronno-lucevaia tehnologhia polucenia materialov dlia electriceskih contactov*, Electriceskie contacta i electrode: Sb. Tr. – Kiev: IMP NANU, 1998. – S. 51-66.
- [3]. TU U 201/3410.001-98. Materiala dispersno-uprocinennae dlia electriceskih contactov. – Vved. 01.05.98.
- [4]. B.A. Movcian, V.A. Osokin, L.V. Puscinicova, N.I. Grechanyuk - *Electronno-lucevoe isparenje i condensatia medi cerez vannu-posrednic*, Probl. spet. electrometallurghii. – 1991. – Nr. 3 – S. 58-61.
- [5]. Nesmeianov A.N.- *Davlenie para himiceskih elementov*. – M.: Izd-vo AN SSSR, 1961. – 396 s.



STUDY ON THE SPECIFIC EFFECTS OF CORROSION PROCESSES ON ANCIENT BRONZE ARTEFACTS

Ion SANDU¹, Marta QUARANTA², Costică BEJINARIU³
Ioan Gabriel SANDU³, Dorin LUCA³, Andrei Victor SANDU⁴

¹ "Al.I.Cuza" University of Iasi, Arheoinvest Platform, Laboratory of Scientific Investigation
and Cultural Heritage Conservation

² Università degli Studi di Bologna;

³ "Gh. Asachi" Technical University of Iasi

⁴ Romanian Inventors Forum, RDI Department

email: ion.sandu@mail.dntis.ro

ABSTRACT

The paper presents the cases of the corrosion processes which take place on starting from the usage period when the primary patina is being formed and when the secondary patina starts, than continuing with the archaeological site where the contamination patina is obtained under the influence of the pedological processes. The paper is a review from the specialised literature and from the contributions of the authors. There has been used the direct analysis with optical instruments, electron microscopy and EDX.

KEYWORDS: corrosion products; primary, secondary and contamination patina; ancient bronze artefacts; Liesegang effect; perturbed and non-perturbed archaeological sites.

1. Introduction

Metals, as compared to other materials, have a unique behaviour after the creation of artefacts, such as *high resistance* to exogenous factors, *returning to the primitive state of mineral* through the processes of corrosion and erosion [1-4].

Among the Cultural Heritage assets, the *coins* and other metallic numismatic pieces offer many *case studies of the conservation state* and, in the research field, they can be adequate samples to be used for experiments, but except for the *treasures*, the coins are not always easily discovered by excavation if dispersed in the archaeological sites [2].

Except for the *treasures* made of noble metals, the pieces made of other metals have the disadvantage of a precarious conservation state, in the worst case of *pre-collapse* – as the pieces with a very thin metallic bulk that merely preserve their shape – or of *collapse* – when the metallic bulk is completely absent and the shape cannot be recognized, their authentication being almost impossible [1-6]. Among these, the pieces made of *ancient bronze* have a *very complex composition* of the corrosion products, resulted from the reactions with the *corrosion agents* (of chemical, electrochemical or microbiological natures,

respectively), or by *contamination*, during the various *pedological processes* (*segregations, cementations - monolithisations, re-crystallizations*, etc.). The most important problems arise for the *pieces without metallic bulk*, pieces which during the *preliminary classification* in the yard (excavation place) have been destined to the "*grey fund*", abandoned in the most cases.

These pieces are a very important source of information, mainly about the basic mineral, often being the unique proofs of a technique or metallurgical tradition/period [7-11].

Thick corrosion crusts on artefacts fabricated from copper, bronze or other copper alloy may display complex structures. Some of these structural details may be dependent on the microstructure of the metal, which is attacked by corrosive agents during burial. Their formation may also be influenced by a variety of growth mechanisms relating to the development and morphology of the corrosion products themselves [12].

Some papers of interest concerning this subject have been published: unusual phenomena in the corrosion of ancient bronzes are reported [13]. The particular observations of interest here are those concerning the periodic or banded layers of corrosion

which are sometimes observed in the polished cross-sections of ancient copper alloys [14].

The origin of the banding which is observed in some archaeological material may be the result of the slow diffusion of metallic constituents and of the salts present in soil groundwaters. So there are a series of reactions that produce precipitation of relatively insoluble corrosion products, such as: cuprite, malachite, atacamite and paratacamite, tin and lead oxide and also other products, which may be present in segregated or banded layers.

Some of the segregation effects which are observed are due directly or indirectly to microstructure-related segregation, such as are observed in dendritic castings, or in multi-phase alloys. Rhythmic banding, however, is not normally explicable as a consequence of the initial metallographic structure of the artefact concerned.

The formation of these periodic structures are based on Belousov-Zhabotkinskii type oscillant reactions of precipitation in heterogeneous phase, which holds the name of Liesegang phenomena or effect [14]. Many studies of this intriguing phenomenon have been made and a number of different mathematical models advanced to explain the precipitation processes [15 - 17]. The stratification of corrosion products, which is formed during burial, it is based on complex processes with cumulative effects, as are: electrochemical processes, template/coordination processes, microbiological processes, fossilisation (mineralisation), segregations, diffusions, etc.

Bronze and brass artefacts present specific cases of the conservation state resulted both from the usage period and after abandon.

These specific effects have interested many researchers during the years. These effects have been studied in order to determinate the formation mechanism or the archaeometric characteristics.

In general, the specific effects are based on complex corrosion processes of old bronzes and brasses which take place inside or at the surface.

This paper reviews some of already published specialized literature on these phenomena, with some notes regarding to the contribution of the authors.

2. Surface Effects

According to the previous studies [1-6], ancient bronze objects, both the ones with metallic bulk and the ones without it, coming or not from perturbed sites, three types of products can be differentiated in the structure of the *archaeological patina*: the first ones resulted from the corrosion processes, the second ones from the acid-base processes, mainly through hydrolysis and ionic exchange, and the third ones

from the processes of contamination (diffusion, segregation, deposition, etc.). These products are formed in different stages, being characteristic to certain types of patina.

The oxides and sulphides, formed since the usage period, constitute the *primary patina*; the hydroxyhalogenides, oxyhydroxides, carbonates, sulphates, phosphates, etc., resulted in the last period of utilization (before abandon) and in the first step of the pedological period, define the *secondary patina*; finally, those resulted from the physical processes of diffusion-segregation-recrystallization-deposition-monolithisation-mineralisation are forming the *contamination patina* [3, 4].

The study of these products allows not only the explanation of the inner mechanisms of formation but also the evaluation of some archaeometric parameters which can point out some elements useful for authentication, such as the nature of the alloy, the type of the mineral, the technology (the elaboration of the alloy and of the coin), the provenience of the coin (the period and place of creation), the way and the period of utilization and some other data concerning the "time imprint" [4, 7].

The continuous stratigraphical depth of the site in time, from the surface where the action of the climatic, microbiological and anthropological agents is strong and cyclic, towards the internal zones where the aerobical or anaerobical conditions of the soil alternate and the oxygen and water in soil have oscillations in time creating another different system of cyclic variation, has a very important role in structuring the corrosion products, the ionic exchange or the contamination products.

The last cyclic processes, although occur with a very slow rate during the centuries, produce important structural modification of the ancient patina of an object, creating a stratigraphical distribution of the three groups of products. The cyclic properties of the pedological processes determine the specific stratification of the three patinas which can be easily rendered evident by means of the known stratigraphical methods.

If we compare the micro-stratigraphies of the archeological patinas of two coins coming from different sites - one non-disturbed and with low and almost constant humidity, the other one situated in an area with a great mobility of subterranean water and a complex chemistry - we notice the stratigraphical distribution under the form of deposits of products specific to the three types of patina: primary, secondary and of contamination, Fig. 1a [7], for the first coin and a deposition of micro-crystals, not uniform in the volume phase of the archaeological patina for the second coin, Fig. 1b [3, 4].

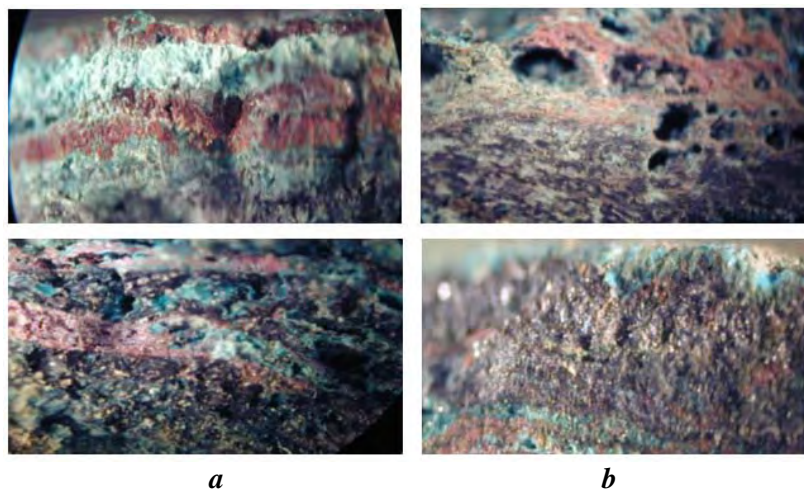


Fig. 1. Micro-stratigraphical structure of the archaeological patina [3, 4]:
a – patina for coin coming from archaeological non-disturbed (non-perturbed) site and with low Humidity, b – patina for coin coming from archaeological site with a fluctuant chemistry produced by the abundant subterranean water.

If in the case of a non-disturbed site, we can easily draw up the structural phenomenological correlations for the chronological valuations, for the second one, the study of the parameters implied in such correlations requires either some complex analyses with the help of the co-assisting systems or the corroboration of new methods and techniques of high resolution.

So, the stratigraphical morphology of the most archaeological patinas of the ancient bronze pieces has a *sandwich* structure, characteristic to the *Liesegang effect*, [7] in which the layers of primary patina are overlapped or partially interposed with the ones of the secondary patina. The layers of contamination products, formed during the chemical chronological processes that occur in the heterogeneous liquid-solid systems, with a sequential formation of products with characteristic morphology, are also named the "*Liesegang rings*". In the case of the bronze coins, the primary patina contains layers of *oxydes* and *sulphides* (*cuprite* or *cuprite/tenorite*), the secondary patina of *malachite/azurite*, overlapped or alternated with layers of *atacamite/paratacamite* and of contamination products such as the *ankerite*, *gypsum*, *silicates* and *caolinite* interposed with *cassiterite*, resulted from the segregation and the diffusion processes in the inferior layers [3, 4, 8-11].

If the inner effects are well determined by cross-section analyses, the surface ones can be observed

directly or through optical devices as microscopes and stereomicroscopes.

Some authors [18] studied the of surface of archaeological artefacts and effects and grouped them in the following groups: the "even" surfaces, pits or crevices and "coarse" surfaces (Fig. 2).

The "even" surfaces can have extended monochrome areas, easy to identify by mineralogical analysis, but also small areas polychrome and non-uniform.

These surfaces can have dominant colours specific to primary patina compounds (red, brown and green-grey) and few from secondary patina (blue, green, brown, grey bright to dark), with even and bright aspect.

Pits or crevices have as cause the stress from physical and mechanical effects on cracks produced by inter-crystalline corrosion and some inclusions from casting.

The "Coarse" surfaces could have different types of representation: lamellar plates; limpets or buboes (nodules) effect (mono- or polychrome); crust (thick or thin); cracks;

From the study of some ancient bronze coins, made by our collective, some surface effects were identified, not enough studied till now (Fig. 3).

Among the buboes and limpets effects, we discovered dislocation effect through dissolution of the buboes or nodules braking, resulting large round holes.

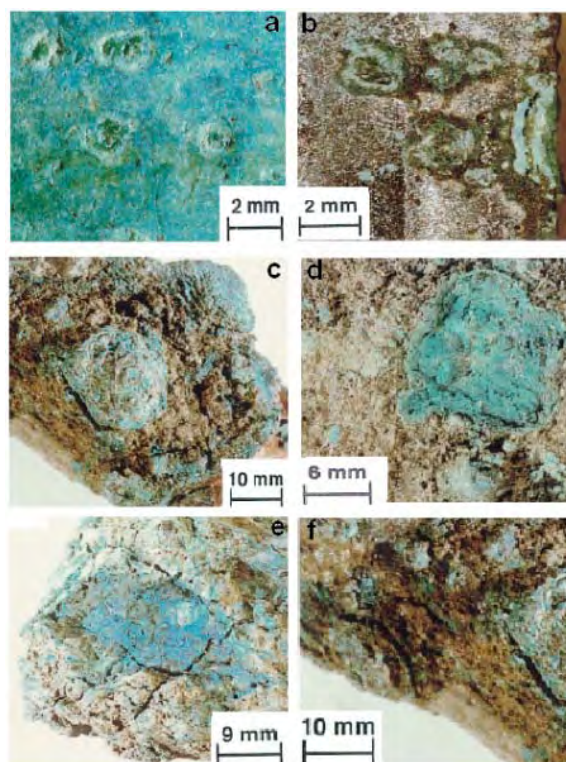


Fig.2. Macroscopic views of archaeological bronzes dating from the Bronze Age (1500-750 BC) [18]:
a – pits and pitting caps; b – lamellar plates; c - buboes (nodules); d – thin crusts; e – cracks; f – crevices.

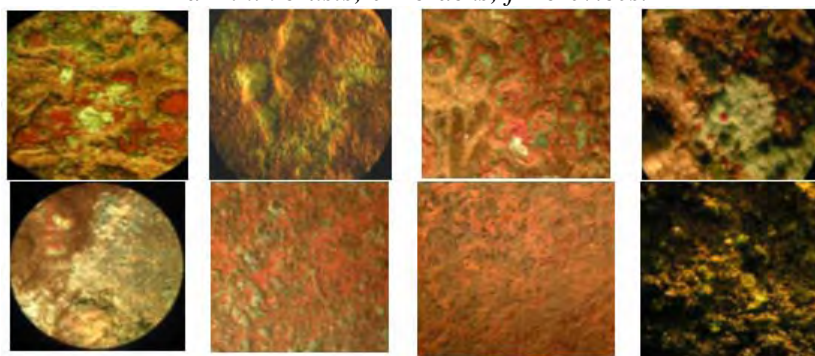


Fig. 3. Microscopic view of some bronze Austrian and Romanian coins (1880-1888 AC) [3, 4]

Copper products can form deposits according to the corrosive context:

- hydroxychlorides in seawater;
- hydroxysulphates in the outside environment;
- phosphates, sulphides and silicates from soil;
- hydroxycarbonates elsewhere.

They are described in the literature as corrosion or barrier layers, films and crusts.

They could be formed at any time in the life of the object, so they may possibly carry imprints of its earlier life. For example, it has been noticed that some copper deposits have maintained vegetal or animal

fibre structures. Even insects have been noticed and described. This last point is of primary importance and remains to be developed; meanwhile, it is important to continue to look for such traces. The archaeology of the corroded surface could prove to be a source of new criteria for classifying and estimation of the mechanisms.

The formation of the secondary patina has as a first step the transformation of cuprite and chalcokite in malachite, azurite, atacamite, paratacamite, antlerite, brochantite and nantokite (Fig. 4). There have also been identified macrocrystalline surface formations with different arrangements (Fig. 5).

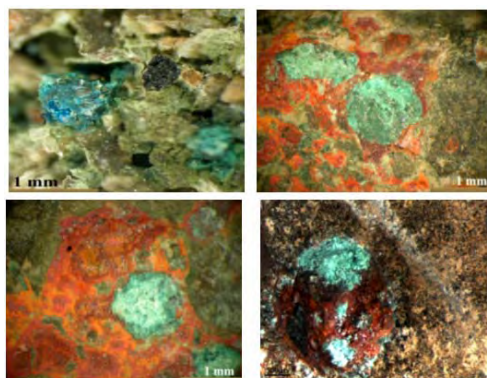


Fig.4. Optical images that show the first stages of the bronze disease occurrence that seems to start from cuprite nodules and layers [21].

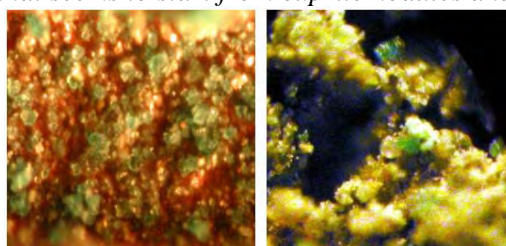


Fig. 5. Malachite and azurite structures on bronze surface [3, 4]

3. Inner Effects

Consequently soil elements incorporation is of major importance in the achievement of the final colour of the surface, whereas the dissolved amount of copper due to the selective dissolution is not characteristic of a given aspect of the patina. Robbiola [18] describes two types of deviations from the basic structure. **Type I** has other three kinds of deviations. The first is characterized by the presence of a porous external crust or deposit (often several hundred of μm thick) covering the outer layer, the latter sometimes being less developed than in the case when no crust is present. Analysis of such deposits revealed mainly

copper corrosion products, such as cuprous oxide (cuprite) and/or cupric compounds, such as hydroxycarbonates or hydroxysilicates and even including sand.

The two zones - top layer (crust) and outer layer - are usually easy to distinguish. For example, on the left of Figure 6-a, the green and brown deposit hugs the concave curve of the engraved decoration, revealed here by the blue-green outer layer.

The interface between this kind of crust and the underlying layer corresponds to the original surface. The external porous deposit is clearly linked with the precipitation of dissolved copper cations onto the surface.

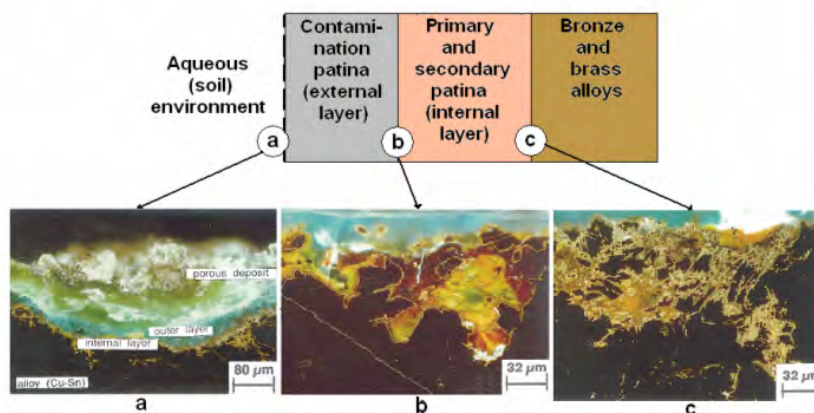


Fig.6. Type I corrosion structures the three kinds of structural deviations from the basic structure (optical microscopy in dark field: the alloy appears in black) [18]: a – deposit of copper compounds on the outer layer; b – localised attack or crack within the basic structure; c – internal attack of the corrosion/alloy interface.

The second kind of deviation Figure 6-b corresponds to modifications of the structure due to either localized extension of the inner layer into the alloy or internal cracking. The extension of the internal layer is accompanied by the incorporation of corrosive species, such as chloride anion, which plays a prominent part in localized corrosion (orange zone in Figure 5-b) Cracking can be attributed to many causes, such as internal stresses inside the corrosion layers or ageing of the corrosion products.

The third kind of deviation (Fig. 6-c) corresponds to inter- or transgranular attacks at the layer/alloy interface, ascribable to internal oxidation processes along diffusion short-circuits (possibly due to the presence of defects in the grain boundaries or even to the metallurgical structure itself, as it could be the case for hammered metals).

Type II corresponding to coarse surfaces, results from localized corrosion phenomena, but also from generalized attacks due to a high dissolution rate. In both cases, paradoxically, they show a similar structure and the same distribution of the chemical elements into the corrosive structure. The main characteristic is the presence of high chloride amounts at the internal layer/alloy interface. It appears already that, in contrast with Type I structure, the formation of the internal corroded layer is linked to an enrichment of the corrosion products in chloride anions issued from the soil.

Type II surfaces are rough and their colour may be red, brown or more often green. They fall into two different classes for which, contrary to the structure of Type I, the original surface is not left untouched:

- areas on which corrosion deposits – buboes (Fig 2-c), crusts (Fig 2-d) hide the original surfaces;
- zones on which the original surface of the artefact is clearly destroyed, with loss of matter - pits (Fig. 2-a), crevices (Fig. 2-f) or lamellar plates (Fig. 2-b).

Examination of cross-sections of artefacts shows that all types of Type II corrosion patterns are very close from a structural and chemical point of view. The alterations are often well developed and they are typically 200 μm to several μm thick, depending on the severeness of the attack.

The microstructures displayed in Fig. 9-b and c show that such deposits, whatever their shape, are constituted by a superposition of three layers schematically represented in Figure 7-a.

- an external altered zone of green Cu(II) compounds;
- a red layer of cuprous oxide, often disrupted or fragmented;
- an internal layer, with different possible colours (yellow, orange, brown) characterized by lower copper amounts and relatively higher tin contents than in the alloy, associated with soil elements (mainly O and Cl).

The second kind of deviation results from intensified localized attacks, leading to zoning inside very thick internal layers as in Figure 7-d or to highly developed inter- or transgranular corrosion (Fig 7-e).

The formation of complex stratified corrosion layers has sometimes a periodicity, leading to a complete mineralized structure, such a phenomenon has already been observed, as described by Scott [10,12] for Egyptian artefacts, or by Robbiola [20] for Bronze Age artefacts. The interest for the complex structure of bronze corrosion products led to a European Partnership [21]. They have studied the ancient bronzes from the Mediterranean Area. In Fig. 8 – 15 are presented some cross-section with uncommon and commonly observed cases of corrosion of Cu-base archaeological artefacts.

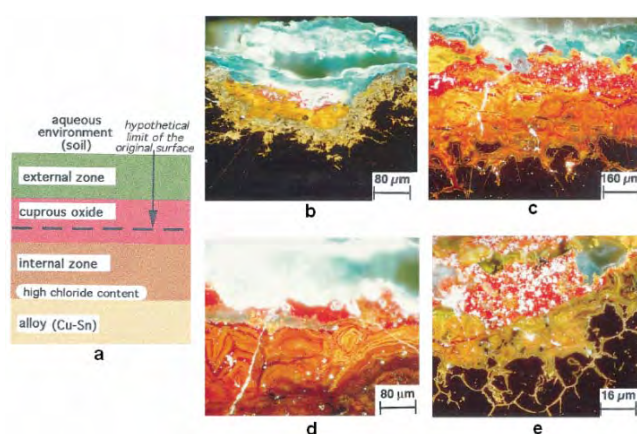


Fig. 7. Type II corrosion structures (coarse surfaces) characterized by the loss of the limit of the original surface (optical microscopy in dark field: the alloy appears in black) [18]: a – schematic representation of the structure; b - transversal section of a pit; c - transversal section of a thick crust, d and e - details of the internal altered zone under the red cuprous oxide layer; d - is a detail of b showing a thin disrupted cuprous chloride layer up to the internal zone where „ghost” structures of the alloy are still observed; e - shows a pit with intergranular corrosion - the blacks spots in the internal zone in yellow-brown are „ghost” sulphide inclusions remnants of the initial alloy.

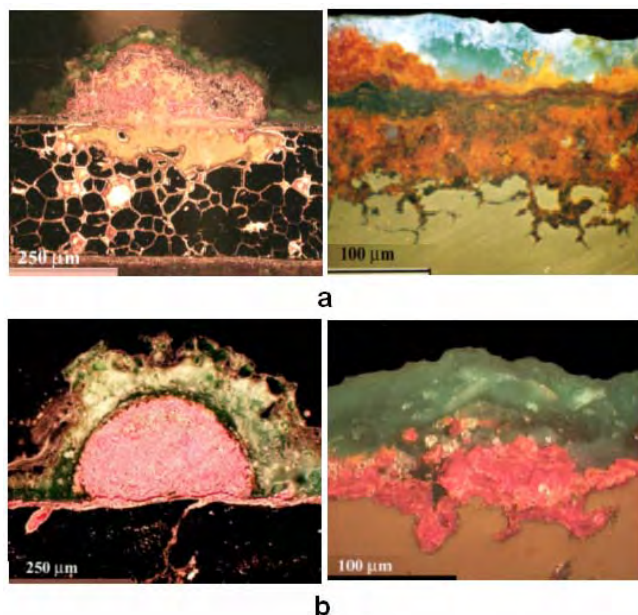


Fig.8. Optical images of cross sectioned ancient patinas grown on archaeological artefacts during the long-term burial (a) and the artificial corrosion products layers grown on the reference Cu-based alloys by using the CuCl_2 method and subjected also to a burial (b). It is possible to identify distinctly different layers in the corrosion products whose location, structure, nature and composition are similar to those observed for archaeological artefacts [21].

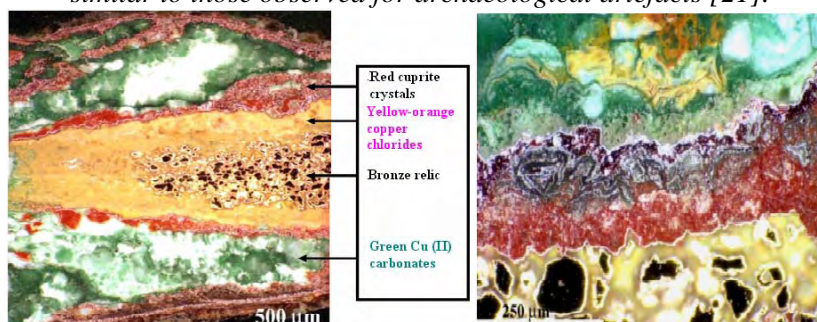


Fig.9. Optical images that show the complex nature of the stratified corrosion products. The dark spheroidal areas are constituted by the surviving metal (dark field observation) [21].

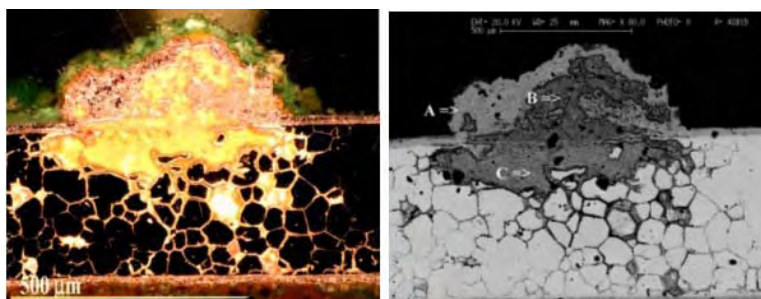


Fig.10. Typical aspect of cross sectioned archaeological artefacts where erupting cuprite nodules are present. The images show that cuprous chloride (yellow-orange layer) is present at the interface between external corrosion products and metal relic and where also bronze disease is occurring as shown by optical (dark field) and electron images: A – SnCl_2 ; B – Cu; C – CuCl_2 [21]

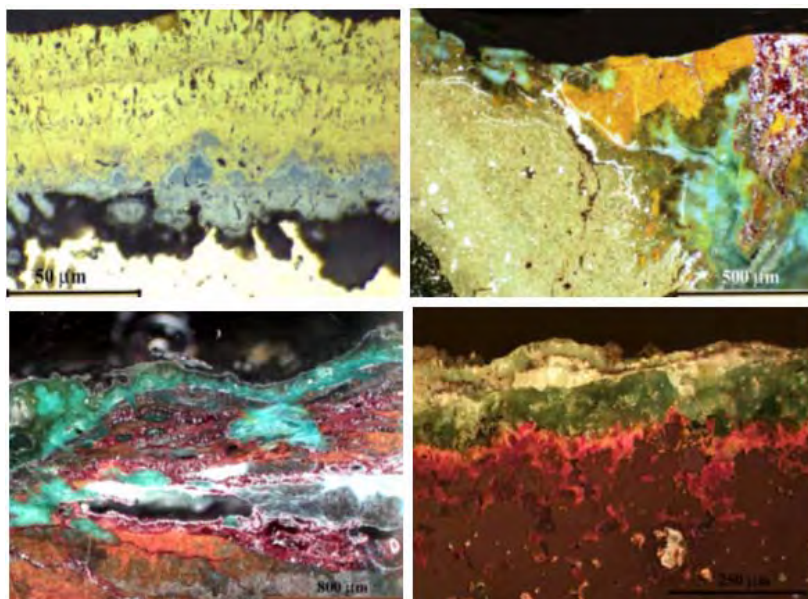


Fig.11. Uncommon and commonly observed cases of corrosion of Cu-base archaeological artefacts that have induced the formation of complex compounds. The patinas are composed by copper-iron sulphides, pyromorfite, cerussite, azurite, malachite, leadhillite, cassiterite, cuprite and copper chlorides [21]

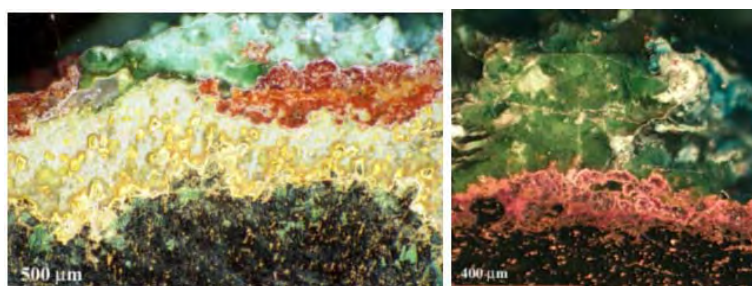


Fig.12 Optical images obtained from two different areas of the Roman coin. The image on the left discloses the first stages of the so-called bronze disease and the second column evidence the protective role of the copper (II) compounds and of the cuprite that impede the occurrence of the bronze disease. This information demonstrates that the conservation materials and methods must locally inhibit chlorine [21]

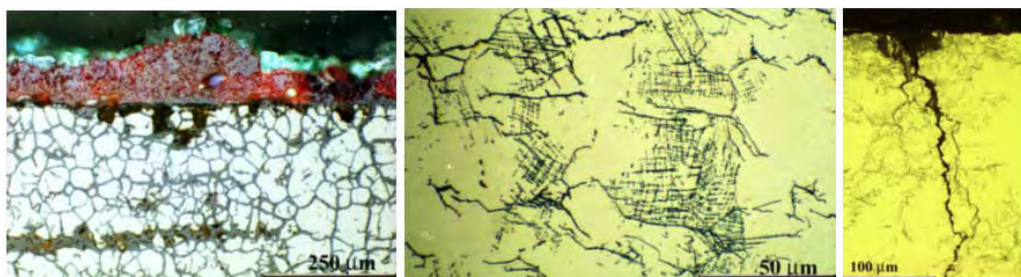


Fig.13 Examples of selective inter-granular corrosion that preferentially attack grain boundaries and slip lines [21]

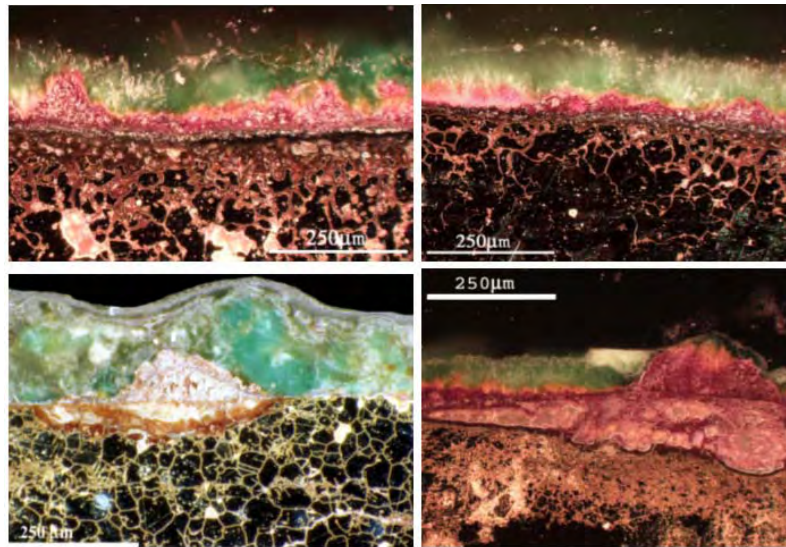


Fig.14 Optical images for some selected Cu-base artefacts that disclose [21]

- the first stages of the bronze disease induced by the cyclic reaction between uncoated copper chlorides, oxygen and humidity (first row);
- the presence of thick layer of cuprite or of Cu (II) compounds that protect the surface thus inhibiting the occurrence of the cyclic reaction.

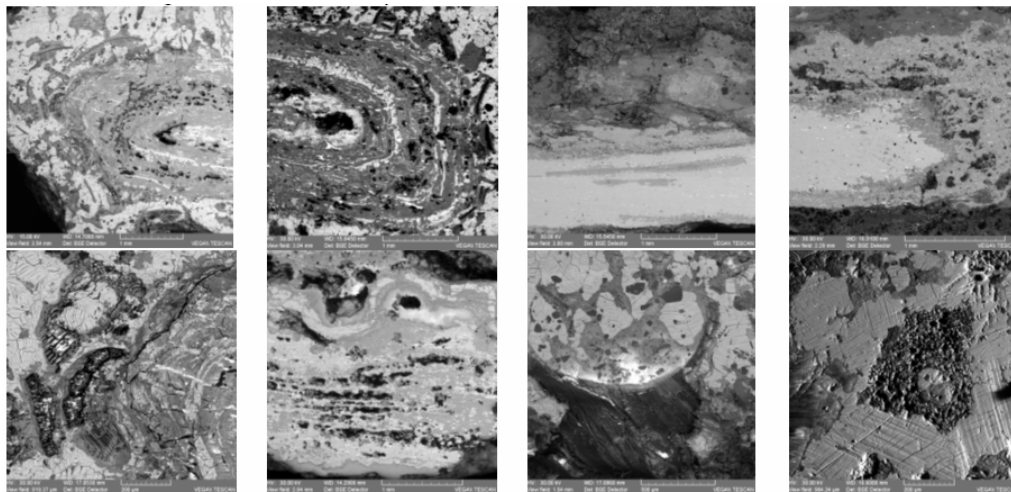


Fig. 15 SEM images of some bronze coins (Xth Century) in cross-section: on first line is visible the Liesegang Effect in a non-disturbed archaeological site; on the second line are complex monolith structures with silicates, calionite, sulphides films, wood, micro-fossils.

There also exist other effects such as:

- Diffusion and segregation effects, with the copper extraction and (the reduction of the copper concentration) or the reduction of the concentration in the active metals (see brasses) with the refining process (spongy structures)
- Fossilization and mineralization effects;
- Monolithisation effects and embedding effects of the mineral, vegetal or animal formations

- Effect of the lenses made up of lead, tin or other non-corroded metal in the case of the pieces with or without strongly brittle metallic cores, respectively

- Effect of the deep cracks which pass through the corrosion products up to both the metallic intercrystalline or transcrystalline cores (inter- or trans-granular) and the closed inner cracks, respectively



- Effect of the segregation of the compounds and their unidirectional crystallization.

4. Effects from Stress

Metallic pieces are subjected to the following stress groups:

- **Erosion Mechanical Stress (EMS)** – abrasion from the period when the object is used or from the archaeological site under the influence of the tectonic movements and groundwaters dynamics;
- **Stress Corrosion Cracking (SCC)**, mechanism consists in the simultaneous action of a corrosive environment and mechanical load;
- **Corrosion and Irradiative Stress (CIS)** is due to the continuous corrosion of the environment and to the thermal or irradiative fluctuation from the environment;
- **Electrochemical and Erosion Stress (EES)**, erosion and contact with metal of different chemical nature.

5. Conclusions

The paper, as a review, presents the different cases of the conservation state of the bronze artefacts. The multitude and complexity of the cases reveal some problems in their classifying and in the establishing of the forming mechanisms of these corrosion products.

Thus, there has been established three main groups which determine the forming mechanisms of the corrosion products, namely, the environment aggressivity, the nature and the complex structure of the alloy, the obtaining alloy technology, the technology of the artefact manufacturing and the shape, the complexity and chemical reactivity of the corrosion products. As far as the corrosion products are concerned, a main role in the establishing of the forming mechanism of the archaeological patina is being played by the primary patina, especially by the products with high chemical inertia and with a protecting role by the surface passivation (e.g. phosphates, chalcokites, cuprites and silicates). Therefore, the protection role provided by the soils with phosphates and sulphides which form continuous passivant films.

This paper succeeds in rendering evident the role of these films in the accomplishing of the morphology and structure of the archaeological patina.

The forming of the secondary patina by the acid-base and hydrous processes above the primary patina (resulted from the redox processes) starts from the pre-abandon period and strongly goes on into the archaeological site under the influence of the pedological factors (chemical aggressivity, groundwater dynamics, soil tectonics, other physical and mechanical processes which perturb the archaeological site).

References

1. **I. Sandu, A. Dima, I.G. Sandu**, *Conservation and Restoration of Metallic Artifacts*, Ed. Corson, Iasi, 2002.
2. **I. Sandu, C. Marutoiu, I.G. Sandu, A. Alexandru, A.V. Sandu**, *Acta Universitatis Cibiensis - Chemia*, 9, (2006), 39-53.
3. **I.G. Sandu, S. Stoleriu, I. Sandu, M. Brebu A.V. Sandu**, *Revista de Chimie, Bucharest*, 56, (2005), 981-994.
4. **I. Sandu, N. Ursulescu, I.G. Sandu, O. Bounegru, I.C.A. Sandu, A. Alexandru**, *Corrosion Engineering, Science and Technology*, 42, 3, (2007), p. 312;
5. **W. Mourey**, *Conservation of Metallic Antiquities – from Archaeological Site to Museum*, Ed. Tehnica, Bucharest, 1998.
6. **I.G. Sandu, I. Sandu, A. Dima**, *Modern Aspects Concerning the Conservation of Works of Art. Vol. III. Authentication and Restoration of Artifacts from Inorganic Materials*, Ed. Performantica, Iași, 2006.
7. **R. Mazzeo**, *Kermesquaderni*, Ed. Nardini, Firenze, 2005, 29-43.
8. **C.V. Horie and J.A. Vint**, *Studies in Conservation*, 27, (1982), 185.
9. **J.D. Meakin, L.D. Ames, D.A. Dolske**, *Atmospheric Environment*, 26B, (1992), 207.
10. **D.A. Scott**, *Copper and Bronze in Art. Corrosion, Colorants, Conservation*, The Getty Conservation Institute, Los Angeles, 2002.
11. **I. Constantinides, A. Adriaens and F. Adams**, *Applied Surface Science*, 189, (2002), 90-102.
12. **D.A. Scott**, *Studies in Conservation*, 30, (1985), 49-57.
13. **W.A. Oddy, N.D. Meeks**, *Science and Technology in the Service of Conservation, IIC*, London, 1982, 119-124.
14. **R.E. Liesegang**, *Naturwissenschaftliche Wochenschrift*, 11, (1896), 353-362;
15. **R. Feeney, S.L. Schmidt, P. Strickholm, J. Chadam, P. Ortoleva**, *Journal of Chemical Physics*, 78, (1983), 1293-1311;
16. **J.B. Keller, S.I. Rubinow**, *Journal of Chemical Physics*, 74, (1981), 5000-5007;
17. **M. Flicker, J. Ross**, *Journal of Chemical Physics*, 60, (1974), 3458-3465;
18. **L. Robbiola, J.M. Blengino, C. Fiaud**, *Corrosion Science*, 40, 12, (1998), 2083-2111;
19. **T.H. Merkel, S.O. Pehkonen**, *Corrosion Engineering, Science and Technology*, 41, 1, (2006), p. 21-37;
20. **L. Robbiola, I. Queixalos, L.P. Hurtel, M. Pernot, C. Volfovsky**, *Studies in Conservation*, 33, (1988), p. 205-214;
21. EFESTUS Project, INCO-MED Contract No. ICA3-CT-2002-10030 (www.efestus.just.edu.jo/index.jsp);



AUSTENITIC STAINLESS STEELS CORROSION PROPERTIES MODIFIED BY SILICON ALLOYING

Brândușa GHIBAN, Sorin CIUCĂ

University POLITEHNICA of Bucharest

email: brandusa@sim.pub.ro

ABSTRACT

In the present paper there are presented results concerning comparative corrosion resistance of some austenitic stainless steels, with or without silicon content. The silicon content is varying in the range of 1-5 %, in a matrix of alloyed austenite, containing 20% Cr and 15-18%Ni and with very low carbon contents (lower than 0,03% C). There are investigated different types of corrosion resistance: intergranular corrosion in nitrogen media, stress corrosion resistance in chloride media, and transpassive behaviour in sulphuric media. The tested media contained nitrogen, as it follows: Huey test (65% HNO₃, at boiling temperature, 244 hours maintain), and 5N HNO₃ + 1g/l Cr⁶⁺ (144 h, b.t.). The media contained chloride is 45% MgCl₂ at boiling temperature, with a period of 1000 hours. The transpassive behaviour is tested in 10% HSO₄. The investigations were made by optic and electronic microscope, and the corroded surfaces were examined by scanning electron microscopy.

KEYWORDS: corrosion resistance, austenitic stainless steels

Introduction

In nitric acid environments austenitic stainless steels have been used only in low concentrated media due to the breakdown of the corrosion resistance which can take place at great concentrated media. Several works ([1] ÷ [6]) have previous shown that silicon addition in 18Cr-15Ni matrix has a pronounced beneficial effect on different types of corrosion resistance: intergranular corrosion resistance, stress corrosion resistance and having a good transpassive behavior.. The aim of present paper is to put in

evidence the influence of silicon alloying on different type of corrosion behavior of the austenitic stainless steels. There are used several aggressive media containing nitrogen, chloride and sulfuric acid.

Experimental procedure and materials

Experimental silicon alloyed stainless steels were produced in a vacuum furnace, in charges of about 50 kg. The chemical composition of the experimental steels is presented in table 1.

Table 1. Chemical composition of the experimental steels

Steel	C	Mn	S	P	Si	Cr	Ni
[%]							
A	0.020	0.87	0.007	0.017	0,94	18,62	15.6
B	0.015	1.48	0.008	0.011	3.39	18.7	15.2
C	0.022	1.23	0,006	0.011	3.B3	18.3	15.1
D	0.012	1.42	0.007	0.015	5.12	17.92	15,2

Ingots were hot rolled to 5 mm (hick strip, which were solution annealed at 110G°C, 1/2 hour

by water quenched. Corrosion test coupons (25x50x5 mm) were sheared from the annealed

strip. Half of the test coupons were sensitized at 650°C/1 h and were air cooled and the other half were tested in the annealed state. The heat treated samples were surface polished and then were decreased.

Corrosion tests were conducted in both states in boiling reagents, in the following conditions: a) nitric acid (Huey test, in 65% HNO₃ vol.) in five periods of 48 h at boil period; b) nitric acid media with hexagonal chromium ions (5N HNO₃ +1g/lss Cr⁶⁺), in three 48 h boiling period.

Each steel sample was remote of each period, washed with distilled water, hot air dried, weighted and re-immersed for further test period. Corrosion was calculated for each boiling period in terms of the corrosion rate (g/m² .h) and the surfaces were investigated in both optic and scanning electronic microscopy, for characterizing the morphology of the corroded surfaces.

In order to determine stress corrosion behavior of the experimental steels it was used a solution in accordance with ASTM 3079, respectively 45% MgCl₂ at boiling temperature.

The experimental method use samples for DISTINGTON device, equipped wit thermostats glass cell. The appreciation of the stress corrosion cracking resistance was made depending on the fracture time of the sample. The maximum value of test time was 1000 hours. The values of the selected stresses were in different proportion from the yielding strength of the considered steel.

Results and Interpretations

Sample of each experimental stainless steels were X-ray diffraction examined and were found to contain full austenite, with no grain boundaries precipitated particles, in according with calculations based on Schaeffler diagram. No sigma phase was found. Experimental corrosion intergranular results are presented in terms of binary diagrams (figure 1), in two states: quenched and sensitized and also by scanning electron microscopy, which are presented in figure 2 and figure 3.

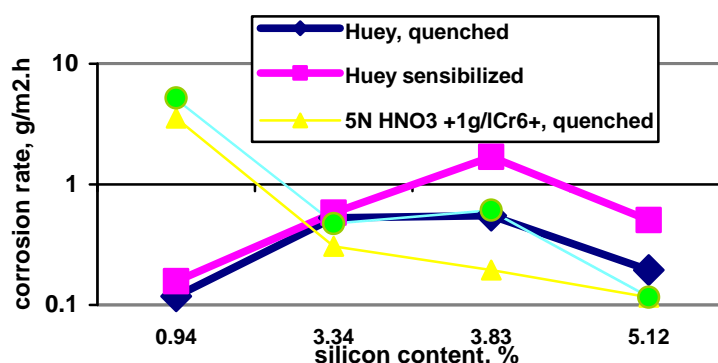


Fig. 1. Silicon influence on the corrosion resistance of the experimental steels in nitric media

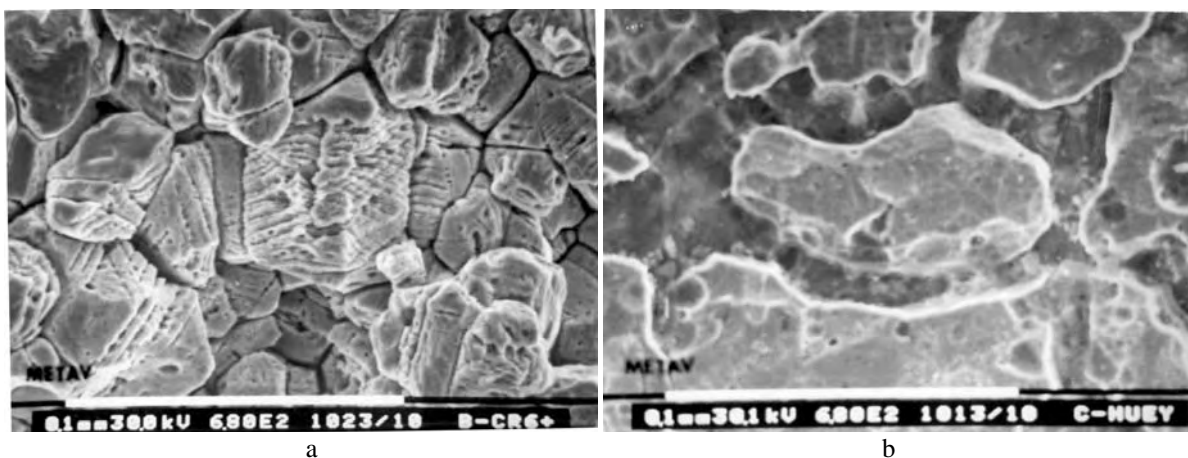


Fig 2. Scanning electron microscopy of the corroded surfaces of the silicon austenitic stainless steels after Huey test: steel B, b- steel C

It may remark the following aspects:

- silicon do not improve the intergranular corrosion resistance of the stainless steels in Huey test (the corrosion rate are higher than $0.5 \text{ g/m}^2 \cdot \text{h}$ and the intergranular attacks are about $30\text{-}50 \mu\text{m}$);
- silicon may roughly increase the intergranular corrosion resistance in highly oxidant medium (in nitric acid with hexagonal chromium ions); so, in steel A it can be seen the most intensive intergranular attack, and in steel D (with the highest silicon and nitrogen content. there is no attack, field

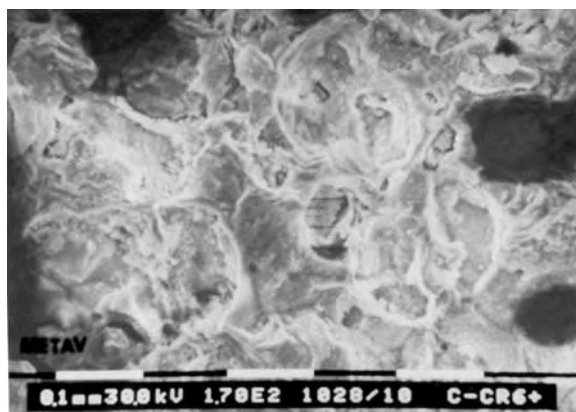


Figure 3. Scanning electron microscopy of the corroded surfaces of steel C after testing in $5\text{N HNO}_3 + 1\text{g/l Cr}^{6+}$, b.t.

- scanning electron microscopy reflects very well the intergranular corrosion resistance: as it is shown in fig.2, and 3 the intergranular attack is proportionally with the general corrosion rates in similar conditions. In non-resisted steel (like steel A in $5\text{N HNO}_3 + 1\text{g/l Cr}^{6+}$) the attack is so severe, not only at grain boundaries but also inside the grains at twin boundaries or high density atoms lines. In resistant steel there is no intergranular attack or there is an incipient intergranular attack (like steel B or C in $5\text{N HNO}_3 + 1\text{g/l Cr}^{6+}$).

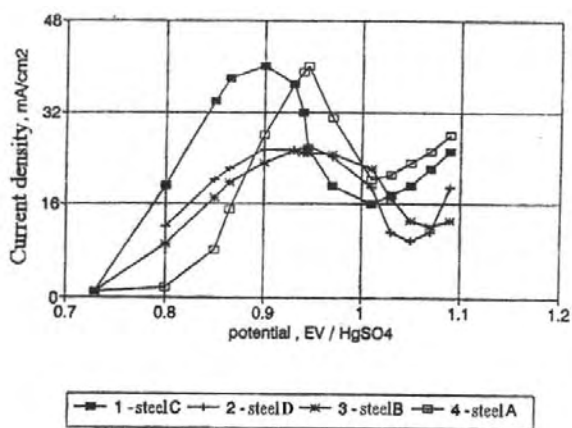


Figure 4. Anodic polarization curves of the silicon experimental steels in $2\text{N H}_2\text{SO}_4$, 20°C in transpassive

The beneficial influence of silicon considering transpassive field of corrosion is illustrated in figure 4. Silicon do not influence the extension of passive field, but in an aggressive media such as $2\text{N H}_2\text{SO}_4$ silicon may diminish the potential in secondary passivity. If steel A presents a secondary passivity field at a high value of current ($i_{ps} \approx 18\text{mA/cm}^2$), for a potential about 1.02V (ESC) at steels with silicon

alloying a diminishing value of the current is observed in secondary passivity field and an increasing of the corresponded potential, i_{ps} , of steel D decrease from 10mA/cm^2 for a potential of 1.05 V (ESC). Experimental results concerning stress corrosion resistance of the silicon alloyed stainless steels are given in table 2. Microstructural features of the stress corrosion surfaces are illustrated in figure 5.

Table 2. Stress corrosion Behavior in $45\% \text{ MgCl}_2$, b.t., of the silicon austenitic stainless steels

Steel	Yielding strength, MPa	Applied stress		Fracture time, hours
		% $R_{p0.2}$	MPa	
A	145	125	181.25	2
		100	145	2.75
		50	72.5	10
		25	36.25	100
B	214	125	267.5	No fracture
		110	235.4	No fracture
		100	214	No fracture
C	258	125	322.5	No fracture
		110	283.8	No fracture
		100	258	No fracture
D	274	125	342.5	No fracture
		100	274	No fracture

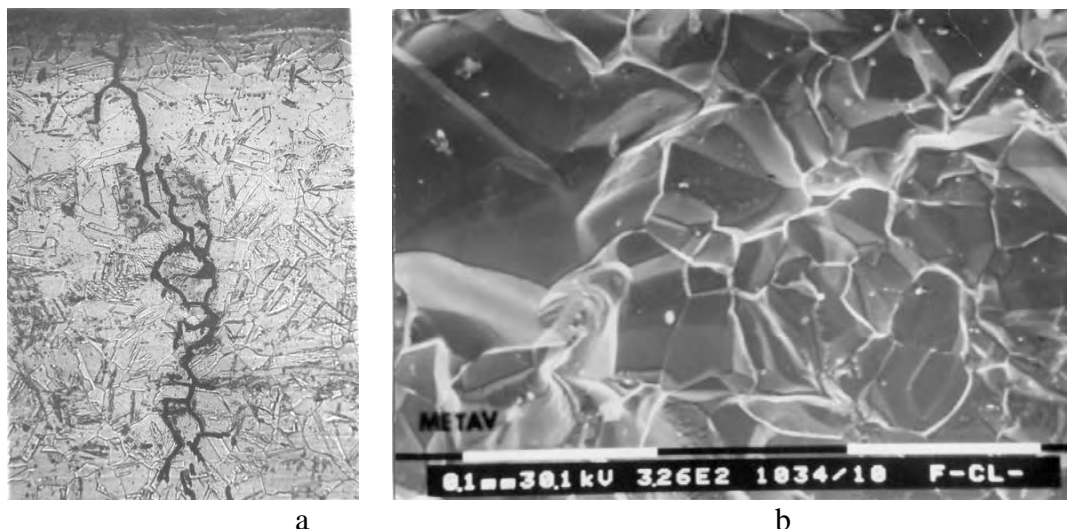


Fig 5. Microstructural aspects of the stress corrosion surfaces of steel A, after testing in 45% MgCl₂, b.t.: a- optic microscopic analysis (10% electrolytic oxalic attack, x100), b- SEM image (x362)

One may remark that steel A, with no silicon alloying, has no resistance in 45% MgCl₂, fracture may appear after a very short period of time, depending on the stress value. In cross section cracks have a transcrystalline aspect (figure 5a) and also a cleavage aspect, with a brittle feature (figure 5b). In silicon experimental steels no cracks may be induced at any value of applied stress, after a period of 1000 hours.

Conclusions

The following conclusions may be drawn from the previous data;

- Silicon content (over 3%) in austenitic stainless steels may increase the corrosion resistance in highly oxidizing media (like concentrated nitric acids: 5NHNO₃ + 1g/ICr⁶⁺);
- Silicon content (over 3%) may decrease the intergranular corrosion resistance in the Huey test, in both annealed and sensitized steels;
- The test in 5N HNO₃ + 1g/ICr⁶⁺ is proper to select stainless steels for after their resistance in oxidizing media (a corrosion rate smaller than 0.3g/m²·h being enough for preventing the intergranular attack).

-Silicon alloying may determine the increasing of passivity characteristics values of sensitized steels and decreasing of current values in passive field in sulfuric acid.

-Silicon may highly increase stress corrosion behavior in 45% MgCl₂, at boiling temperature of the austenitic stainless steels, no cracks being seen after a period of 1000 hours.

References

- [1]. Ghiban B.- Doctoral thesis, UPB, 1995
- [2]. Ghiban B., Coșmeleată G.- "Nitrogen and Silicon Influence on the Intergranular Corrosion Resistance of the Austenitic Stainless Steels", Bulletin des Cercle d'Etudes des Metaux Saint Etienne, may, 1995, pg.8.1-8.10
- [3]. Ghiban B., Cosmeleata G.- Silicon influence on the intergranular corrosion resistance of the austenitic stainless steels by scanning Microscopy, Metalurgia vol.1 (1996), nr.2, 40-42
- [4]. Ghiban B., Cosmeleata G.- Stress Corrosion cracking in chloride solutions of the silicon alloyed austenitic stainless steels, Rev. Metalurgia, vol II, (1997), nr. 2, 23-26
- [5]. Ghiban B., N. Ghiban - "Stability of Austenite in Silicon Austenitic Stainless Steels", Scientific Bulletin, Serie B: Chemistry and Materials Science, vol.62, 2000, nr.1, pag.105-112
- [6]. Ghiban B., N. Ghiban - "Silicon Influence on the Corrosion Behavior of Stainless Steels", Scientific Bulletin, Serie B: Chemistry and Materials Science, vol.62, no.3, 2000, pag.79-86.



RECYCLING POSSIBILITIES OF METALLURGICAL SLAG

¹Maria CIOROI, ^{1,2}Licuta NISTOR(CRISTEA)

¹ "Dunărea de Jos" University of Galati, Faculty of Sciences,

² SC DSU Romania SRL Galati

email: maria.cioroi@ugal.ro, licuta_59@yahoo.com

ABSTRACT

The target of the current metallurgical industry is to recycle and utilize all their by-products. Slags are the important wastes and by-products of metallurgical industry, which have been treated, recycled and used worldwide. The present paper summarizes results obtained from physical and chemical analyses on blast furnace slag. The physical structure and gradation of granulated slag depend on the chemical composition of the slag, its temperature at the time of water quenching, and the method of production. The chemical reaction between blast furnace slag and water is slow, but it is greatly enhanced by the presence of free calcium oxide and free magnesium oxide getting on calcium and magnesium hydroxide. These alkalis can modify the mechanical properties of slag. It is very important to analyze the content of the free calcium oxide and free magnesium oxide. Blast furnace slag is mildly alkaline and exhibits a pH in solution in the range of 10 to 12. Processed slag exhibits favorable mechanical properties for aggregate use including good abrasion resistance, and high bearing strength. By our assessments it was proved that the blast furnace slag from S.C. "Arcelor Mittal Galati" S.A. have comparable properties of granite. This fact will allow utilizing the slag aggregates on the road construction, railway embankments, hydrotechnic constructions.

KEYWORDS: blast furnace slag, mechanical properties, abrasion resistance

1. Introduction

The global warming effect and natural resource saving are the general environmental topics nowadays. In addition, the land filled with the waste materials has become a significant source of pollution of air, water and soil, and further adversely affects the human health, and the growth of plant and vegetation. From the viewpoint of preservation and protection of the global environment, slag recycling has attracted the attention of many scientists in recent years. Boom reviewed the recent research trend on slags and found that there is significant increase in studies on recycling of slags and their environmental problems.

Slag plays an important role in the metallurgical process as it has to ensure the complete separation of the metal from ore. Moreover, it has a refining role – to render soluble the elements which, in general, have to be removed from metal. A refined slag has to render soluble, the more the better, the sulphide so that the sulphur concentration in cast iron and steel should be as small as possible. An important factor in differentiating slag is the treatment applied during cooling which leads to differences in the use of slag.

Metallurgical plant slag is the main source of waste which can be recycled on location. By limiting the capacity of the wasteyards, the disastrous impact on the natural equilibrium and environment is reduced. The study of slag has as a result the valorization and, implicitly, the diminution of the necessary quantity of natural ore extracted from lithosphere, the lessening of environmental degradation by establishing extraction pits. Due to the large slag quantities and the stricter environmental regulations, recycling and utilization of these slags are an attractive alternative in order to reduce and eventually to eliminate the disposal cost, to minimize the related environmental pollution, and to save the resource conservation.

2. Materials and methods

Physico-mechanical analyses

The main physical-mechanical analyses made at SC DSU ROMANIA SRL Galati on the metallurgical slag were:

- Density(g/cm³) SR EN 1097-3/2002 and SR EN 1097-6/2002
- Volume stability SR EN 1744-1/2004



- Compressive strength (%mass losses) and (N/mm²) SR EN 1926/2000
- Impact strength (%mass losses) SR EN 1097-2/2002
- Water absorption(%) SR EN 1097-6/2002 and SR EN 1625/2000
- Polished stone value PSV SR EN 1338/1339/1340-2004
- Wear resistance- Los Angeles (%mass losses) SR EN 1097-1/1998
- Freeze –thaw resistance (%mass losses) SR EN 1367-1/2002; 10 frost-thaw cycles in the temperature range (-20°C /+20°C).
- Granulometry of the mixture of granulometric sorts, SR EN 662/2002 and SR EN 667/2004
- Electrical conductivity(mS) SR EN 1744-1/2004

Chemical analyses

Chemical reagents of type p.a. were used in the chemical analyses. The main reagents acquired and used are: H₂SO₄, HNO₃, HCl, Na₂SO₄, MgSO₄, CaCl₂, BaSO₄, ethylene glycol, acquired from SC Chimopar SA Bucharest, indicators (methylorange, phenolphthalein, tymol blue) from SC Sinteza SA Oradea. Methods adapted to the European standards were used for the analysis of the oxide percentage of slag.

- The determination of free CaO and MgO was carried out in accordance with SR EN 1744-1/2004 through acidimetry, conductometric analysis, as well as through constancy of volume measurement and in the case of the complexonometric method STAS 4605-9/1988 and STAS 4605-10/1980 were used.
- FeO and Fe₂O₃ were determined in accordance with SR ISO 2597-1/2001 and STAS 1574-3/1990.
- SiO₂ determination was made in accordance with SR ISO 2598-1 /1996; S was determined in accordance with SR ISO 4690/2001

• MnO was determined in accordance with SR ISO 1574/1994

• Al₂O₃ was determined in accordance with SR ISO 4687/2001

• CaO and MgO total quantity determination was carried out in accordance with SR 6482/2002 and SR EN 196/2002

The determination of pH was carried out with the OP-264 pH-meter, existent in the laboratory, whose calibration was made with a solution of known pH (pH- 4, 7, and 8) (citric acid solution + Na₂HPO₄)

The resistance to the gelivity test (frost-defrost) was determined from a chemical point of view by treating metallurgical slag with saturated solutions of Na₂SO₄ or MgSO₄ (under the form of ten cycles of immersion-drying). In both processes applied to metallurgical slag, the values obtained with regard to resistance are the same although the substances used have different molecular weight.

3. Results and Discussions

The following mineralogical components resulted from the chemical analysis of metallurgical slag: cristobalite (SiO₂)(1); gelenite (2CaO*Al₂O₃*SiO₂)(2); corundum (Al₂O₃)(3); sillimanite (Al₂O₃*SiO₂)(4); pyrope (3MgO*Al₂O₃*3SiO₂)(5); dicalcium ferrite(6); calcium orthosilicate (7) (*table 1*) Theoretically, steel slag should be chemically inert because of its crystallized minerals content (dicalcium silicate- β and γ polymorph forms, dicalcium ferrite, wüstit, magnetit), minerals that do not react with any fluids usually in contact with in the normal environmental condition(rain water). The main oxides existent in ferrous metallurgical plants are rendered in percents as obtained through the analytical quantitative determinations (*table2*).

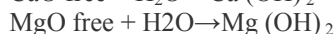
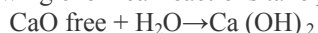
Table 1. The mineralogical composition of metallurgical slag compared to natural rocks

The mineralogical composition	u.m.	Metallurgical slag	Natural rocks
Cristobalite(1)	%	30-36	32-38
Gelenite(2)	%	8-10	10-12
Corundum(3)	%	2,5-5	3-6
Sillimanite(4)	%	4,5-6,5	4-5,5
Pyrope(5)	%	2-4	3-5,5
Dicalcium ferrite(6)	%	1-2,5	0,5-1,5
Calcium orthosilicate(7)	%	1-2	-
Wüstit(8)	%	0,5-1	<0,5

Table 2. The oxidic composition of metallurgical slag

Metallurgical slag	CaO	MgO	SiO ₂	Al ₂ O ₃	S	Fe ₂ O ₃	FeO	MnO	Other oxides
	%								
Blast furnace slag	41	7-8	36	7-9	0,8	0,5-1.5	0,5-0,8	0,2-1	~1,3 (P)
Steel slags	42-44	5-7	30-35	2,5-3,7	-	15-20	2,5-5	3-6	-0,5 (Cr and V)

Apart from the above mentioned oxides in the composition of steel mill slag there are also to be found free oxides such as Ca and Mg oxides, whose percentage presence in the slag composition has to be as small as possible since, in contact with water, the following chemical reactions take place:



which would make the aggregates obtained through slag processing disintegrate (under the above mentioned condition).

The elimination of this problem is effected through controlled cooling of the slag and through its ageing, meaning, the continuous watering of it for approximately 6 months so as to ensure consistency of volume of the aggregates obtained during the mechanical processing of crude slag. Figure 1 represents the comparative graph regarding the constancy of volume of two slag samples which indicates the role that ageing has (that is, eliminating Ca and Mg free oxides).

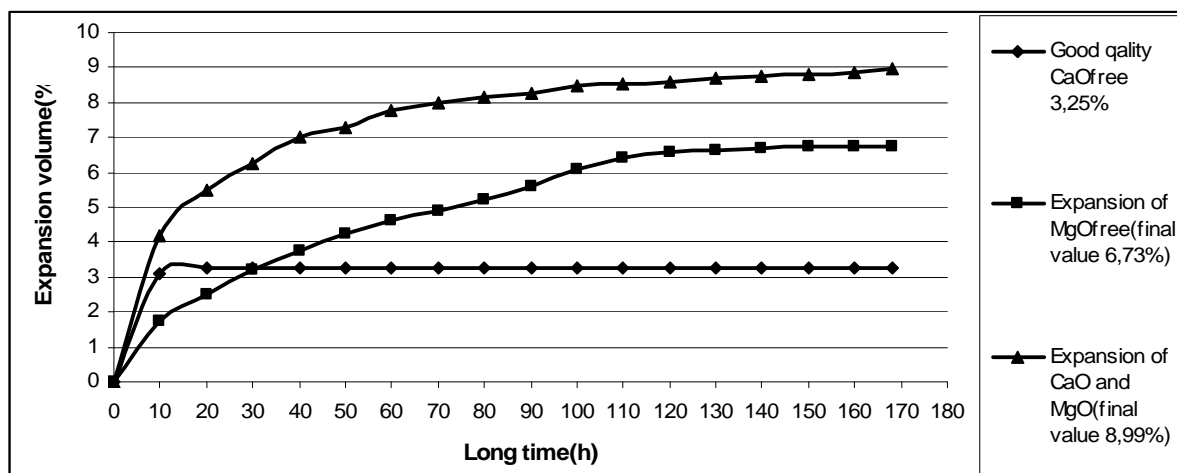


Figure 1: The constancy of volume of metallurgical slag

The presence of Fe (+2) and Fe (+3) → Fe (total) oxides in the metallurgical slag composition makes its gross density be greater thus being possible to compare it to natural rocks.

Table 3 gives the density values obtained through determinations.

Table 3. Metallurgical slag density compared to natural rocks

Physico-mechanical characteristic	Aggregate type		
	Metallurgical slag	Granite	Gravel
Gross density(g/cm ³)	2,600-3,500	2,800	2,600
Refined state density (g/cm ³)	1,650	1,400	1,300



During the determination of the resistance to frost-defrost (chemically and physico-mechanical) very similar values were obtained through both processes due to the slow cooling process of metallurgical slag and implicitly to the formation of its crystalline structure.

The slow cooling process is also essential for obtaining the porosity close to that of natural rocks.

Slow air cooling favours to a great extent crystallization but, at the same time, allows the unfolding of polymorphic transformation reactions of type β calcium silicate into γ calcium silicate in basic slag (*the pH of ferrous metallurgical plant slag varies from 10 to 12*).

Through the same system of slow cooling from the metallurgical slag state of fusion, under atmospheric conditions or through successive watering, these materials are ensured with a high level of homogenous cristallinity, high physico-mechanical resistance, and in general, properties that can be compared to those of aggregates obtained from natural rocks.

Metallurgical slags contain mainly silicates and they are provided by metallic melt solidification. Any

slag has the main role to render soluble as much sulphur gases as it's possible and all other minerals that are not desired into metallic melt (iron and steel). There are two kinds of metallurgical slag: furnace slag resulted on iron works and steel slags. At it turn, there are three kinds of steel slags all depend on the type of furnace atmosphere it is used: Linz-Donawitz converter, where it is produced LD steel slag, electric-arch furnace, where it is produced EAF slag, and ferro-chromium slag produced also into electric- arch furnace. After separation from the melted steel, the liquid slag is discharged into a pit, where the slag start to cool, slowly under natural condition of humidity, for minerals crystallizing and chemical stabilization.

After a period of six month of maturation, the raw slag is crushed and sieved into a special factory equipment, and carried out in a special storage place. Prepared in this way, LD steel slag aggregates have the proper characteristics to be used in road construction field, railway construction, waterway construction and civil engineering as well (table 4).

Table 4. LD steel slag aggregates characteristics comparing with natural aggregates

Characteristics		Type of aggregate			
PROPERTY	U.M.	BOS steel slag	Basalt	Granite (monolithe)	Requested under German norms for road construction
Apparent density	[g/cm ³]	>3,2	~2,95	~2,70	-
Volume increase-steam test	[%]	<1 - <3	-	-	<5 ⁴⁾
Water absorbtion	[%]	0,3-0,9	<0,5	0,3-1,2	<0,5
Impact strength sorts 8/11 mm	[%(m)]	15-20	9-20	12-27	<18 ¹⁾ <22 ²⁾ <34 ³⁾
Compression strength	N/mm ²	>130	>230	>160	-
Bulk density	[g/cm ³]	1,5-1,6			-
PSV	PSV	54-57	45-56	45-58	>43
Thaw- freeze resistance	[%]	< 0,3	< 0,8	0,8-2	< 3,0
Environmental compatibility- pH		10-12	-	-	10-13
Electrical conductivity	mS/m	<300	-	-	<500
Cr ^{IV}	mg/l	<0,01	-	-	<0,02
Wear resistance- Los Angeles	[%]	<18	<20	<12	10-20

The results of the analyses carried out indicate that the slag under study has a composition and properties similar to natural rocks. Hence slag can be mechanically processed (crushed and

granulometrically separated) into aggregates similar to those obtained from natural rocks. Broken stone is obtained in this way with dimensions ranging from 4 to 8 mm; 8-16 mm; 16-25 mm; big broken stone with



granular dimensions ranging from 25 to 63(80) mm; as well as mixtures of granulometric varieties (*broken stone ballast*) the granulosity ranging from 0 to 31,5 mm or 0-63 mm. The granulometry thus resulted (eg. 0-63 mm) falls within the granulometric curbs prescribed by SR EN 662/2002 for the ore used in road construction. Apart from broken stone and mixtures of granulometric varieties, crush sand is also obtained at a granulosity of 0 to 4 mm, being possible to use it instead of natural sand (river sand).

Due to a slow and steady cooling some slag achieve a high level of homogenous cristallinity which give them a very great resistance to compression and breaking (with a loss of only 5 to 6% in weight during the processing), fact which makes it impossible for this slag to be processed (through crushing) resulting in grains of big dimensions such as 45-125 mm;63-180 mm;90-180 mm;45-180 mm; 90-250 mm, dimensions which correspond to natural rocks (coarse aggregates) used in hydro technical constructions or bank protection in accordance with SR EN 13043/2003.

4. Conclusions

Being obtained from crude slag through crushing, aggregates have sharp edges and angles that is, a high roughness and, as a result the adherence to any binders (bitumen or hydraulic binders) is excellent which means that they are ideal in road construction [7].

The presence of SiO₂ in slag composition gives it the properties of a hydraulic binder (that is why blast furnace slag is currently used in the making of cement).

Due to the high resistance to gelivity (frost-defrost), as well as to the high gross density, the aggregates obtained in this way are ideal in hydro technical construction works, these being hard to "wash" by the water currents. [9]

The characteristics regarding the form of the grains (measured with the sliding calipers) and the coarse surfaces of aggregates make it possible to obtain the necessary bearing capacity and even to exceed the values specified in standards for the making of layers resistant to frost or bearing layers of *macadam* type (crushed stone surface, calibrated, of monogranular variety, laid and cylindrated up to clamping first under dry conditions, fastened through colmation by water and aggregation material (crushed sand) and then cylindrated until definitive fastening [3,4].

All the results obtained through chemical and physico-mechanical determinations correspond to the technical quality requirements for aggregates used in road construction and specified in SR EN 13242/2004

Moreover, aggregates from metallurgical slag can be successfully used in the making of railway beds, giving the respective constructions durability and resistance in accordance with SR EN 13450/2000.

The study of ferrous metallurgical plant slag deserves greater attention as what has already been obtained up to the present moment (through laboratory determinations) makes it possible for us to anticipate that slag can be efficiently used instead of the aggregates obtained from natural rocks.

References

- [1]. Boom, R., Mills, K.C., and Riaz, S. 2002, *Recent trends in research on slags*. Proceedings of the Sixth International Conference on Molten Slags, Fluxes and Salts, Stockholm, Sweden-Helsinki, Finland, 12-17
- [2]. Cioroi, Maria, 2005 – *Elemente de Chimie Generala*, Ed. Universitatii Dunarea de Jos din Galati
- [3]. Cioroi, Maria, 2006 – *Chimie analitica. Gravimetrie si volumetrie*, Editura Ars Docenti, Bucuresti
- [4]. Dumitrescu, Cristina – 2006, *Utilizarea agregatelor LIDONIT in Romania* pps, Galati - Lucrari sesiune comunicari stiintifice SC DSU Romania SRL.
- [5]. Drissen, Peter, 2006 – *Istoricul utilizarii zgurilor de furnal si otelarie in lucrari de drumuri* pdf Germania.
- [6]. J. Emery, 1982 – *Slag utilization in pavement construction*. American Society for Testing and Materials.
- [7]. Goanga, Aurel Stefanescu, 1983 – *Incercarile mortarului, betonului si materialelor componente*, Editura Tehnica Bucuresti
- [8]. Gugiuman, Gheorghe – 2006 *Imbracaminti bituminoase subtiri realizate cu LIDONIT* – Iasi.
- [9]. A., Hartopianu, M. Cioroi, O. Mitoseriu, 2002 – *Chimie analitica – separarea si identificarea anionilor*, Editura Ars Docenti, Bucuresti.
- [10]. Joost Michael 2006 – *Utilizarea zgurilor de otelarie in lucrari hidrotehnice* pps- Germania.
- [11]. Niac G., Neacsu H., 1998 – *Chimie ecologica* Editura Dacia Cluj-Napoca
- [12]. M.I.A., Osrouhov, 1970 – *Economia de coals la furnale si zgura de furnal*, Editura tehnica Bucuresti.
- [13]. Ramachandran, V. 1995, *The treatment and minimization of waste*. J. Met, February, pp. 50-51.
- [14]. Ripan, R., Popper, E.; Liteanu, C., 1964 - *Chimie analitica calitativa*, Editura Tehnica Bucuresti
- [15]. N.O. da Silveira, M.V.A.M. e Silva, E.J. Agrizzi, M.F.de Lana, R.L.de Mendoca – *ACERITA – Steel slag with reduced expansion potential* – 2005.
- [16]. D.I.Seracu – *Indreptar de chimie analitica*, Editura Tehnica Bucuresti, 1989.
- [17]. H.Motz, S.Haimi, M.Makikyro-*Slags-Providing Solutions for Global Construction and Other Markets* 20th – 21st June 2005, OULU – FINLAND
- [18]. Tikkakoski, Antti – *Proprietati geotehnice ale amestecurilor de zgura de furnal si Ld pentru drumuri* pps 2006, OULU Finlanda



MODELLING AND PREDICTION IN FAILURE PROCESSES BY MECHANICAL STRESSES IN CORROSIVE ENVIRONMENT

Liviu PALAGHIAN¹, Mioara THOMPSON¹,
Svetlana BĂICEAN¹, Sorin BUCȘĂ²

¹"Dunarea de Jos" University of Galati, ²Linde Gaz Romania SRL
email: liviu.palaghian@ugal.ro

ABSTRACT

The complex interaction effect of mechanical stress- mechanical systems and aggressive environment, leads, at dramatic decreasing of their durability and reliability. The analyze of physical-chemical processes such as: electrode potential evolution, anodic current density evolution, size evolution and growing speed of cracks, allow finding common characteristics of failure due to mechanical stress combined with aggressive environment. Based on the analyze of failure mechanisms by stress cracking corrosion (monotonic mechanical loading), fatigue corrosion (cyclic mechanical loading) and tribocorrosion the paper authors suggest a global model of this kind of failure, based on degradation process of stress cracking corrosion with capability to realize a prediction of damage by these processes

KEYWORDS: corrosion pit, crack, stress cracking corrosion, fatigue corrosion, tribocorrosion.

1. Introduction

Due to permanent presence of corrosive environment in all human activities, the study of its influence on engineering structures mechanical loaded is necessary in order to establish their durability.

In the same time with corrosive environment, on engineering structures act different kind of mechanical stresses. Their action, combined, lead to: stress corrosion, fatigue corrosion, tribocorrosion. The evolution speed of these compound failure processes is higher than each and every situation considered separately, and the effect is not added, but, by overlapping of individual effects, much more complex, there is a synergetic process.

The aim of this paper is to analyze processes that occur at the interface metallic loaded structure-corrosive environment. There will be studied three types of stresses: monotonic stresses, cyclic stresses, wear stresses under relative sliding conditions of metallic surfaces.

Failure under mechanical stresses in corrosive environment is connected mainly by the initiation and growth of cracks which involves the following stages:

- initiation of corrosion pit;
- pit-crack transition;

- crack development under aforementioned stresses: monotonic stress leads to failure by stress corrosion; cyclic stress leads to failure by fatigue corrosion; cyclic stress at low loading and low frequency and close to flow limit leads to failure by tribocorrosion.

2. Initiation of failure processes by corrosion and mechanical stresses

2.1. Modelling of pit corrosion initiation process

According to previous studies, the first stage of failure by mechanical stress in corrosive environment is mainly connected with electrochemical processes that occur during corrosion process, [1], and the result is corrosion nucleation [2].

The number of pit corrosions at a certain moment in time, t , may be described by the distribution function $P(x,t)$, where x is the dimension (usually the pit depth). This way the number of pits with the depth of $x + \delta_x$ with be $P(x,t)\delta_x$.

Depending on environment aggressively pit corrosions will grow in time. It may be assumed that

the growth in time of the pit corrosion can be expressed by the relationship:

$$\frac{dx}{dt} = g(x) \quad (1)$$

where g is a function depending of pit size, which, in its turn, depends of other parameters such as applied stress and temperature [3].

It was shown that the pit depth distribution function evolution $P(x,t)$ is ruled by a differential equation as:

$$\frac{\partial P(x,t)}{\partial t} = -\frac{\partial}{\partial x}[g(x)P(x,t)] + S(x,t), \quad (2)$$

where $g(x)$ is the pit growing speed with depth x , and $S(x,t)$ is the number of pits between x and $x+\delta x$, which trigger at the studied surface within the time δt .

The term $S(x,t)$ means a more general situation, but when a stabile distribution for pit depth is considered, this member may be neglected, and the depth may be described by:

$$x = \alpha \cdot t^\beta, \quad (3)$$

and the growing speed of the crack will be:

$$\frac{dx}{dt} = g(x) = \beta \alpha^{1/\beta} \cdot x^{(1-1/\beta)} \quad (4)$$

β is a constant that must be determined and α is unknown with a normal distribution.

2.2. Pit to crack transition

According to Kondo criterion [6] transition occurs when the crack depth is bigger than a critical depth, which is an opening force threshold for the crack or the growing speed of crack is higher than the growing speed of pit. The depth threshold at which will be triggered the growth of crack depends of applied stress, σ , and the environment conditions. Thus the growing speed of crack can be described by the relationship:

$$\frac{dx}{dt} = c \cdot \sigma^p \cdot x^q, \quad (5)$$

where x is the crack depth.

This relationship has a similar configuration as the one for stress intensity factor [7]:

$$K = Y \sigma \sqrt{\pi l}$$

where Y - dimensional factor, σ - applied stress, l - crack length.

Considering a statistical distribution of pit growing speed, it means that the crack growing speed can also be statistically interpreted. In the equation that gives the grow speed of pit, the factor that can offer this character is parameter C that may be random

determined in a normal distribution.

Finally, the critical depth at which the failure evolution speed is higher than the necessary crack evolution speed is:

$$x_{crt} = \left(\frac{\beta \alpha^{1/\beta}}{e \alpha^p} \right)^{\beta/(1-\beta(q-1))} \quad (6)$$

3. Modelling of failure process by stress cracking corrosion

Anodic failure process at the crack tip depends of anodic dissolution mechanisms and brittleness by hydrogen which combine together or, at some moment one of them may be more important than the other [8]. Processes intensity evaluation at the crack tip may be done, taking in account both mechanisms contribution:

$$\Delta V_c = \Delta V_a + \Delta V_n, \quad (7)$$

where: ΔV_c is the growing evolution speed of crack due to anodic dissolution, and ΔV_n is the growing evolution speed of crack due to brittleness by hydrogen [8], [9].

Knowing that in the case of anodic dissolution the crack tip is anodic and metal surface is cathode [10], the difference in potential between the crack tip (τ_v) and the metal surface (τ_s), $\Delta \tau_s = \tau_v - \tau_s$, will determine the size of anodic dissolution current $I_a(\Delta \tau_a)$ [11]. The size of this current determines the dissolution speed at the crack tip and thus the growing evolution speed of crack due to this process. If the growing evolution speed of crack is controlled only by this process, based on Faraday law, it can be written:

$$\Delta V_a = \frac{i_a}{z \cdot F \cdot \rho}, \quad (8)$$

where: i_a is the anodic dissolution current intensity at the crack tip; M - atomic mass of metal; Z - electrical load of negative ions in the solution; F - Faraday's constant; ρ - metal density.

If the crack is considered like a V cut, with the tip angle α (fig. 1) and if it is assumed that the anodic dissolution happens only on the height h situated at x_1 distance from the crossing point of crack faces and at $x_1 - x_2$ distance from the specimen surface, the anodic dissolution current intensity at the tip of the crack will be:

$$i_a = \frac{\alpha \chi \Delta \phi_a}{h \ln \left(\frac{x_2}{x_1} \right)}, \quad (9)$$

where χ is the electro-conductivity of the electrolyte.

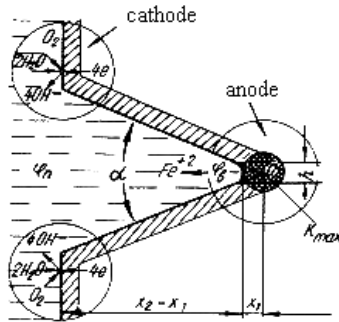


Fig. 1 Electrochemical processes at crack tip.

After replacement:

$$\Delta V_a = \beta_a \Delta \varphi_a, \quad (10)$$

where:

$$\beta_a = \frac{\alpha M \chi}{ZF \rho h \ln \left(\frac{x_2}{x_1} \right)}, \quad (11)$$

For a system metal-watery environment the growth of corrosion crack speed under stress is determined at some point by the jump in potential in the crack. The size of speed growth for crack evolution may be used for quantitative determination of anodic metal dissolution using an average value of S_a parameter.

$$S_a = \frac{\beta_0}{\tau_0} \int_0^{\tau_0} [\Delta \varphi_a(\tau)] d\tau, \quad (12)$$

where τ_0 is the process evolution time.

For cyclic loading this parameter may be determined in a similar way. Thus,

$$S_a = \frac{\beta_0}{N_0} \int_0^{N_0} [\Delta \varphi_a(N)] dN \quad (13)$$

where N_0 is the number of cyclic loading.

Generally speaking, every system material-corrosive environment has its own characteristic failure diagram. Thus, the kinetically diagram for stress corrosion is a curve with three distinct areas between two characteristic values of stress intensity factor (fig. 2): K_{ISCC} , the corresponds to stress intensity factor under which the crack in corrosive environment at monotonic loading doesn't develop; $K_{IC}(K_c)$ - value of stress intensity factor that characterises materials strength at brittle fracture [15], [16], [17].

The threshold value K_{ISCC} is an essential characteristic of cracking process. Depending of the

nature of material-environment system, the value of this factor may vary in a wide range, and for corrosion resistance is close to K_{IC} . Some materials, such as aluminum alloys don't have a physical limit K_{ISCC} . That is why for this value is adopted the value at which the evolution rate of crack on the flat portion of the curve may be considered as a characteristic of stress corrosion failure.

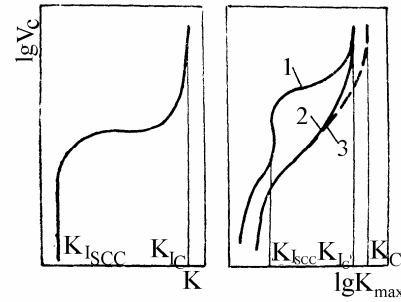


Fig.2.2. Kinetic diagrams of failure in corrosive environment.

For this particular reason, in the case of monotonic loading in corrosive environment it is important finding this type of relationships. These would allow a comparative analyze of experimental data for different types of material-environment couples and would appreciate both qualitative and quantitative influence of various factors on failure kinetic diagram. Besides, with little experimental data, based on analytical relationships, can be established conventional values for K_{ISCC} , values than could be very hard to be found out on experimental ways [18], [19].

In a first approximation the diagram for evolution speed of stress corrosion crack may be described with relationships similar to the ones for fatigue crack evolution:

$$v = v_0 (K_I - K_{ISCC})^n (K_{IC} - K_I)^m, \quad (14)$$

where v_0 , n , m material depending constants.

In this relationship, for K_I values close to K_{ISCC} , evolution rate of crack goes to zero. And for $K_I \rightarrow K_{IC}$, this will grow unlimited. If n and m go to zero, in the mean zone of K_I , the diagram will be merely horizontal.

4. Modelling of failure process by fatigue corrosion

Most of research papers regarding fatigue corrosion suggest a failure process starting from pit-crack transition. After this, failure may continue under several mechanisms: small cracks growth,

transition from short crack to long crack, big cracks growth and their reunion to a main crack.

From rupture mechanics point of view [20] the transition from pit to crack trigger occurs when stress intensity factor reaches the threshold K_{th} necessary to fatigue crack appearance.

$$(\Delta K)_{pit} = (\Delta K)_{th}, \quad (15)$$

where

$$(\Delta K)_{th} = \beta \Delta \sigma \sqrt{a}, \quad (16)$$

and β is a geometric parameter.

The growth speed of small cracks may be described with Paris law:

$$\frac{da}{dN} = C_{sc} (\Delta K)^{m_{sc}}, \quad (17)$$

where C_{sc} and m_{sc} are material parameters.

The transition from small cracks to long ones is modelled by specialists in two ways:

1. surface crack followed by through crack and
2. short crack followed by a long crack [21], [22],[23].

Long crack growth may be described by a Paris relationship as well:

$$\frac{da}{dN} = C_{lc} (\Delta K)^{m_{lc}}, \quad (18)$$

where C_{lc} and m_{lc} are material parameters.

In the case of fatigue stress in corrosive environment it is characteristic that cracks get reunited in a main crack that leads to rupture.

5. Modeling of failure process by tribocorrosion

In tribological contacts that work in corrosive environment, failure appears by removing the material from both surfaces, simultaneously, both by wear processes and corrosion reactions. The two mechanisms interact [24], [25], [26]. Material removing by abrasion lead to the local removal of the passive layer resulted after pure material is exposed to aggressive action of environment, and further acceleration of corrosion process (tribocorrosion) [27]. Usually the term abrasive wear may be interpreted as material loss due to hard particle action. Material removal may be done by several mechanisms, such as micro-ruptures, loss of individual particles, or fatigue mechanism by repeated deformation [28], [29].

If failure by tribocorrosion is analyzed based on material loss, the total loss by tribocorrosion V_{cw} is higher than by cumulating material loss by pure

corrosion V_c and material loss by wear in the absence of corrosion V_w :

$$V_{cw} = V_c + V_w + \Delta V_s \quad (19)$$

where ΔV_s is the corrosion process effect that leads to wear intensification ΔV_w and of wear process that leads to corrosion intensification ΔV_c .

Consequently

$$\Delta V_s = \Delta V_w + \Delta V_c \quad (20)$$

Generally writing

$$W_{cw} = V_{wc} + V_{cc} \quad (21)$$

where

$$W_{cw} = V_w + \Delta V_w \text{ and } V_{cc} = V_c + \Delta V_c, \quad (22)$$

From crack evolution by tribocorrosion point of view, [30], [31], the process is similar to fatigue corrosion process, and may be given by the relationship

$$\left(\frac{da}{dN} \right)_t = \left(\frac{da}{dN} \right)_R + \left(\frac{da}{dN} \right)_{cf} + \left(\frac{da}{dN} \right)_{scc}, \quad (23)$$

where, $\left(\frac{da}{dN} \right)_R$ is pure mechanical fatigue of the

superficial layer contribution; $\left(\frac{da}{dN} \right)_{cf}$ is the

component of crack evolution speed growth as a result of cyclic loading and corrosive environment;

$\left(\frac{da}{dN} \right)_{scc}$ crack evolution speed growth as a result of

static loading under residual stresses and of static stress when crack sides are not in contact, at higher levels of stress intensity factor K_{ISCC} .

It was shown that material loss may be expressed by [32], [33]

$$V_c = \frac{M \cdot t}{ZF \rho} A_a i_p \quad (24)$$

and

$$\Delta V_c = \frac{M \cdot t}{ZF \rho} K_w l \left(\frac{W}{H} \right)^{1/2} (i_0 - i_p) f \tau_0 \left[1 - \exp \left(\frac{-1}{f \tau_0} \right) \right] \quad (25)$$

where A_a - apparent contact area; i_p - passive current intensity through the contact area; t - time; K_w - constant; l - friction trace widening; W - normal load; H - fragility; i_0 - maximum density of the current on the fresh material surface in the begging of the passive process; f - contact frequency between the two surfaces; τ_0 - initial time.

The V_w and ΔV_w components may be written

$$V_w = \frac{\pi D^2 N_c A_a f \cdot t}{6} \left[\left(\frac{da}{dN} \right)_r + \left(\frac{da}{dN} \right)_{cf} + \left(\frac{da}{dN} \right)_{css} \right] \quad (26)$$

and

$$\Delta V_w = \frac{\pi D^2 N_c A_a f \cdot t}{6} \left[\left(\frac{da}{dN} \right)_{cf} + \left(\frac{da}{dN} \right)_{css} \right], \quad (27)$$

where D – worn particle diameter; N_c – number of active zones with micro-cracks.

These relationships show that the main influence of cyclic mechanical stresses on V_w component, and the main influence of chemical factor on V_c component. The analyze of chemical and physical aspects of tribocorrosion processes shows that, at this kind of process as well, there are two essential mechanisms: the cyclic mechanical one- as a result of fatigue process at high level of stress, close to low cycle fatigue, and the electrochemical mechanisms un stress corrosion conditions.

6. Suggested models for failure by mechanical stresses in corrosive environment

In conditions of mechanical stresses in corrosive environment there are several models of failure due to static loading, dynamic loading and tribocorrosion.

The objectives of this project are to set up new models for failure by corrosion fatigue and tribocorrosion based on experimental analyze that govern these processes. In the same time, the project aims the set up of an integrated model of failure by mechanical stresses in corrosive environment where to initial source of failure is the stress corrosion.

6.1. Suggested model for corrosion fatigue

The authors of this project suggest as a model for failure by corrosion fatigue, a model similar to the one that describes fatigue stress, with a static component determined by the mean value of stress, σ_m and a variable component σ_a .

$$\sigma(t) = \sigma_m + \sigma \sin(2\pi ft + \varphi), \quad (28)$$

where $f = 1/T$ is the fundamental frequency.

Extending to cyclic stresses in corrosive environment, the static component may be described by stress corrosion process (SCC) overlapping the cyclic component which may be described with Paris relationship $\Delta K = Y \Delta \sigma_a \sqrt{\pi a}$, where Y – geometric factor and $\Delta \sigma$ – variation of the second term in the loading general equation.

6.2. Suggested model for tribocorrosion

Analyzing the failure process in the superficial layer shows that this is a result of overlapping several simple failure processes and has a evolutionary character.

An elastic plastic surface subjected to alternative movements of sliding, in contact with a hard object, has an elastic cyclic strain with two components:

a cyclic plastic strain where the number of cycles up to the braking moment can be determined with Coffin-Manson relationship [35]:

$$\frac{\Delta \varepsilon_p}{2} \varepsilon'_f (2N_f)^c, \quad (29)$$

where ε'_f – fatigue ductility factor; ε_p – plastic deformation, c – fatigue ductility exponent or Coffin exponent, $2N_f$ – number of total cycles until rupture and a plastic monotonic component. For most of materials ε'_f is identical with breaking elongation, and for many metals has values between 0.5 and 0.7.

When the plastic reversible strain is accompanied by the accumulation of unidirectional plastic strain (ratcheting process) and when this value reaches a critical level ε_c , than the crack is triggered. The number of cycles at breaking moment is

$$N_r = \frac{\varepsilon_c}{\Delta \varepsilon_r}, \quad (30)$$

where $\Delta \varepsilon_r$ is the necessary stain for ratcheting process appearance on a loading cycle.

The two processes compete and as a result material fails either by oligocyclic fatigue or by cumulating plastic excessive flows (ratcheting). According to the two competing processes the failure in corrosive environment continues similarly to fatigue process when the corrosive environment may lead to the increase of number of possible crack triggering areas.

The second mechanism is related with wear debris appearance by weakening the connections between atoms at the crack tip under the influence of active products of corrosive wear.

Knowing the number of cycles under the final break N_f and the correspondent time t_f the speed of generating wear debris v_g may found out:

$$v_g = \frac{N_c}{t_f}, \quad (31)$$

Where N_c is the number of crack starting centers on the surface unit.

When the ratcheting process is dominant in corrosive environment conditions the failure may go on similarly to a stress corrosion process.

6.3. The global model regarding failure by mechanical stress in corrosive environment

Analyzing the failure by mechanical stress in corrosive environment, such as failure by stress

corrosion, by corrosion fatigue and by tribocorrosion, shown a few common characteristics of all these processes.

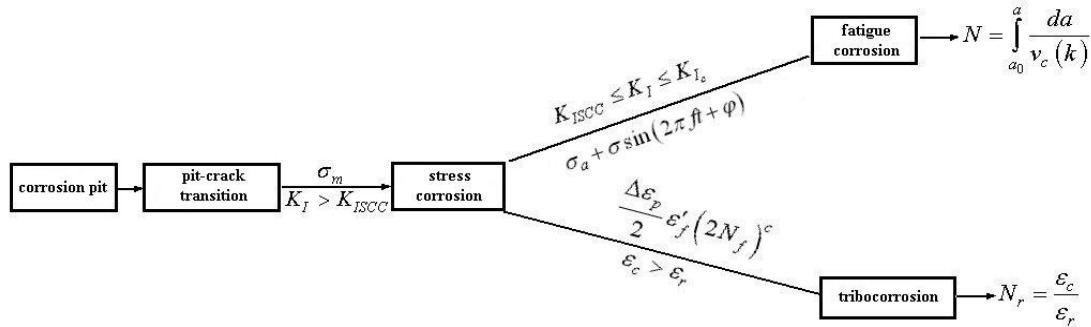


Fig.3. The stress evolution by mechanical damage in corrosive environment

The authors of this paper consider that the central mechanism governing failure by mechanical stress in corrosive environment is the one of stress corrosion by electrochemical processes of anodic dissolution and mechanical processes of oxide layers rupture.

Overlapping a cyclic component of stress over the failure by stress corrosion leads to corrosion fatigue. The stress evolution is described by a Paris like relationship with more intense physical mechanisms than stress corrosion.

Overlapping a cyclic component of low frequency stress close to flow limit leads to tribocorrosion. The speed of stress evolution is described by a Coffin-Manson like relationship or by cyclic plastic strain values (fig. 3).

From the point of view of rupture mechanics, stress corrosion processes appear when stress intensity factor goes above the threshold value $K_I > K_{ISCC}$. Furthermore corrosion fatigue appears when $K_{ISCC} < K < K_c$.

Tribocorrosion appears when the durability is: $N < N_r$ (N_r number of loading cycles at the bound elastic-plastic).

In the same time the number of rupture cycles N_r is determined by rate between critical values of unidirectional plastic strain (ratcheting process) and the plastic strain ϵ_r at which the process starts (fig. 4).

$$N_r = \frac{\epsilon_c}{\epsilon_r}, \quad (32)$$

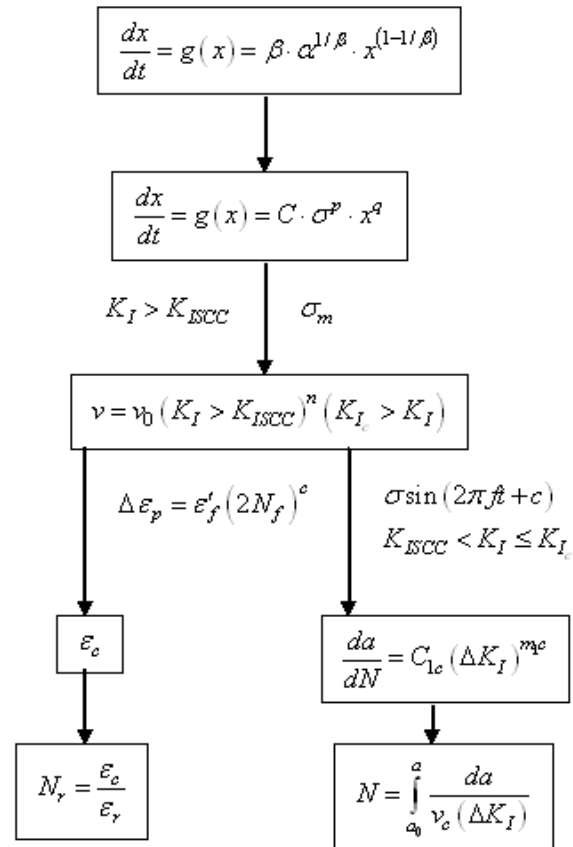


Fig.4. Logical scheme of damage rate by mechanical stresses in corrosive environment.

7. Conclusions

This paper suggests a model for failure due to mechanical stresses in corrosive environment.

Analyzing the failure by mechanical stress in corrosive environment, such as failure by stress



corrosion, by corrosion fatigue and by tribocorrosion, shown a few common characteristics of all these processes like: anodic dissolution, brittleness by hydrogen, oxide layers rupture.

The authors of this paper consider that the central mechanism governing failure by mechanical stress in corrosive environment is the one of stress cracking corrosion and these processes are manifesting by a synergetic mechanism.

Overlapping a cyclic component of stress over the failure by stress corrosion leads to corrosion fatigue. Overlapping a cyclic component of low frequency stress close to yield limit leads to tribocorrosion.

References

- [1]. **Turnbull, A., McCartney, L.N., Zhou, S.**, 2006, Modelling of the evolution of stress corrosion cracks from corrosion pits. *Scripta materialia* 54, pp.575-578.
- [2]. **Tribonod, B.**, 2004, A model for anodic dissolution cell in connection to its dimensions for stress corrosion cracking. *Corrosion Science*, 46, pp. 2715-1741.
- [3]. **Engelhardt, G., Macdonald, D.D., Zhang Y, Dooley, B.**, 2004, *Power Plant Chem.*, 6, pp.647.
- [4]. **Mc. Cartney, L.N.**, 1979, *Int. Jour. Fracture*, 15, 477-479.
- [5]. **Turnbull, A., McCartney, L.N., Zhou, S.** 2006, A model to predict the evolution of pitting corrosion and the pit-to-crack transition incorporating statistically distributed input parameters, *Corrosion Science*, 48, pp.2084-2105.
- [6]. **Kondo, Y.**, 1989, *Corrosion*, 45, pp.7-11.
- [7]. **Gangloff, R.P.**, 2002, Environment Sensitive Fatigue Crack Tip Processes and Propagation in Aerospace Aluminium Alloys, *Fatigue 02, Ed. Engineering Material Advisory Services*, West Midlands, UK, pp. 3401-3433.
- [8]. **Palaghian, L., Bîrsan, I. G.**, 1999, Solicitări mecanice ale oțelurilor în medii corosive, *Ed. Tehnică, București*.
- [9]. **Petrov, L.N.**, 1990, O mehanizme korrozionogo etapa razvitiya trescin, *Fiziko-himicashia mehanica materialov*, No.4, pp.308-309.
- [10]. **Bristoll, P., Roeleveld, J.A.**, 1978, Fatigue offshore structures: effect of sea water on crack propagation in structural steel. *Proc. European Offshore Steel Research Seminar*, Cambridge, P. VI/28-1-VI/18-10.
- [11]. **Ford, F.P.**, 1992, Environmental assisted cracking of low alloy steels, EPRI NP-7473-L.
- [12]. **Norton, F.L.**, 1962, *Hydrogen in steel*, Pergamon Press, Oxford.
- [13]. **Cracknell, A.**, 1976, The effect of hydrogen on steel. *Chem. Eng. (Gr. Brit)* No.306, pp.92-94.
- [14]. **Peng, Q. J., Know, J., Shoji, T.**, 2004, Development of a fundamental crack tip strain rate equation and its application to quantitative prediction of stress corrosion cracking of stainless in high temperature oxygenated water, *Journal of Nuclear Materials*, 324, pp.52-61.
- [15]. **Speidel, M.O.**, 1979, Stress Corrosion Research, *H. Arup and R.N. Parkins, Eds. Sijthoff & Noordhoff, Alphen den Rijn*, Netherlands, pp.117-183.
- [16]. **Wei, R.P., Landes, J.D.**, 1969, *Materials Research and Standards*, vol.9, pp.25-28.
- [17]. **Bucci, R.J.**, 1970, Environment Enhanced Fatigue and Stress Corrosion Cracking of a Titanium Alloy Plus a Simple Model for the Assessment of Environmental Influence on Fatigue Behaviour, *Ph. D. dissertation*, Lehigh University, Bethlehem, P.A..
- [18]. **Chu, H.P.**, 1974, Fatigue crack propagation in a 5456-H117 aluminium alloy in air and sea water. *Trans ASME Ser.D*, No.4, pp.261-267.
- [19]. **Cizelj, L., Mavko, B., Opperman H.R., Brücker-Foit**, 1995, Propagation of stress corrosion crack in steam generator tubes, *Int. J. Pres, Ves, Piping*, 62, pp.1-9.
- [20]. **Shi, P., Mahadevan, S.**, 2003, Corrosion fatigue and multiple site damage reliability analysis, *International Journal of Fatigue*, 25, pp.457-469.
- [21]. **Dolley, E.J., Wei, R.P.**, 1998, Importance chemically short-crack-growth on fatigue life, *Proceedings of the Second Joint NASA/FAA/DoD Conference on Aging Aircraft*, Williamsburg, VA, pp.679-687.
- [22]. **Kaynak, C., Ankara, A., Boker, T.J.**, 1996, Effects of short cracks on fatigue life calculations. *Int. J. Fatigue*, 18(1), pp.25-31.
- [23]. **Shi, P., Mahadevan, S.**, 2001, Damage tolerance approach for probabilistic pitting corrosion fatigue life prediction. *Eng. Fract. Mech.*, 68 (13), pp.1493-1507.
- [24]. **Celis, Ponthiaux, P., Wenger, F.**, 2006, Tribo-corrosion of materials: Interplay between chemical, electrochemical and mechanical reactivity of surfaces, *Wear*, 261, pp.939-946.
- [25]. **Palaghian L., Bucșă, M.**, 2002, Aspect regarding material failure due to tribocorrosion, *The Annals of University, "Dunarea de Jos" of Galati, Fascicle VIII, Tribology*, pp.11-16.
- [26]. **Palaghian, L., Ciortan, S., Bîrsan I.G.**, 2001, About Fatigue and Wear Damage in Corrosive Environment The Annals of Dunărea de Jos University of galati, *Tribology*, pp.3-8.
- [27]. **Kajdas, C., Harvey, SSK, Wilusz, E.**, 1990, Encyclopaedia of Tribology, *Tribology Series*, 15. Amsterdam, Elsevier, 1990, pp.7-76.
- [28]. **Stott, F.H., Kreakell, J.E., Newman, R.C.**, 1990, The corrosion wear of cast iron under potentiostatically-controlled conditions in sulphuric acid solutions. *Corrosion Science*, 30, pp.813-830.
- [29]. **Jiang, X.X., Li, S.Z., Tao, D.D., Yang, J.X.**, Accelerative effect of wear on corrosion of high-alloy stainless steel. *Corrosion*, 49, pp.836-841.
- [30]. **Leis, B.N., Rungta, R., Mayfield, M.E., Beavers, J.A.**, 1983, Corrosion system. *Crooker T.W, Leis BN editors. Corrosion fatigue: mechanics, metallurgy, electrochemistry and engineering*. ASTM STP 801, ASTM, pp.197-228.
- [31]. **Wei, R.P., Shim, G.**, 1983, Fracture mechanics and corrosion fatigue. In: *Crooker TX, Leis BN editors. Corrosion fatigue: mechanics, metallurgy, electrochemistry and engineering*. ASTM STP 801, ASTM, pp.5-25.
- [32]. **Jiang, J., Stack, M.M., Neville, A.**, 2002, Modelling the tribo-corrosion interaction in aqueous sliding conditions, *Tribology International*, 35, pp.669-679.
- [33]. **Jiang, J., Stack, M.M.**, 2006, Modelling sliding wear: From dry to wet environments, *Wear* 261, pp.954-965.
- [34]. **Johnson, K.L.**, 1995, Contact mechanics, and the wear of metals, *Wear*, 190, pp.162-170.
- [35]. **Coffin, L.F.**, A study of the effect of cyclic thermal stresses on a ductile metal, *Transactions of the American Society of Mechanical Engineers*, 96, pp.931-950.



STRUCTURE - PROPERTIES CORELATION IN SINTERED HARD ALLOYS WITH HIGH TOUGHNESS AND STRENGTH

Victor STANCIU

„Gh. Asachi” Technicalal University Iași
email: stanciu.victor@hotmail.ro

ABSTRACT

The researches effectuated until now in the field of sintered hard alloys based on metallic carbides have the aim to improve them properties through modifications of existing technologies and by creating other news ones, like mechanical alloying. The present paper has the purpose to study all influencing factors on the hard alloys properties and his correlation in order to obtain materials with ultra fine structures able to assure superior properties for pieces made from this alloys.

KEYWORDS: sintered metallic carbides, structure, properties.

1. Introduction

Sintered hard alloys based on metallic carbides represent a very important field of powder metallurgy. High hardness combined with a very good wear resistance recommends these alloys for a large number of industrial applications: machining tools, active parts for ball mills, mining tool, tunneling etc. Metallic carbides have low sinter ability, the final product being very fragile, in useful. To increase the toughness of these materials, in the carbide powder is introduced a metal from the iron group, the most utilized being the cobalt, in a proportion of 3-30% like binder. Alloy is sintered at temperatures which is favorising liquid faze apparition. In this way it is possible to obtain a density close to the theoretical ones and a corresponding toughness [1]. All over the world, exist at this time a continuously preoccupation for improving sintered hard alloys' properties. With all progresses, the ways for better properties are still open. The possibility to obtain powders much more finely using more efficient technologies, utilization of special procedures for sintering or by introducing alloying carbides in materials composition it's opening new research directions [2]. The main objective of present paper consists in a study on the relation between sintered hard alloys structure and their properties, in order to improve materials performance. The researches done in this field has demonstrated that hardness and toughness of these materials are very close together with carbide particles dimensions that form the alloy. The values of these properties are increasing when particles

dimensions decrease. The next step is to study the factors that have an influence on the hard alloys structure and their optimization, in order to obtain the best properties in the final product.

2. Influence factors

Resistance, ductility and toughness of samples made form hard alloys based on sintered metallic carbides are depending by matrix proportions, carbide particles dimensions and presence of secondary phases. This secondary phase is formed from other type of carbides, like chromium carbide, vanadium carbide, tantalum carbide and titanium carbide. The cobalt is the most utilized material for matrix in sintered hard materials because it presents a high capacity to wet the hard phase.

Properties of sintered hard alloys depend on many factors, the most important being:

- Chemical composition
- Constituents individual properties
- Size, shape and distribution of hard phase
- Insufficiency or excess of carbon
- Hard phase solubility in matrix
- Composition variation
- Production method

To have optimum properties, a WC-Co alloy has to present a very low porosity, a uniform distribution of carbide particles in matrix and a stoichiometrical content of carbon. Tungsten carbide presents a much-reduced tolerance at carbon content variations (stoichiometrical content 6, 13% C). Small increases of carbon content favors the apparition of graphite separations which reduce bending strength and

hardness. On the other side, carbon content lower than 6,13 %, caused by decarburizing at sintering or by a carbon deficiency in carbide powder, lead to

apparition of W_2C phase, a compound hard and very brittle, which decrease alloy toughness and ductility.

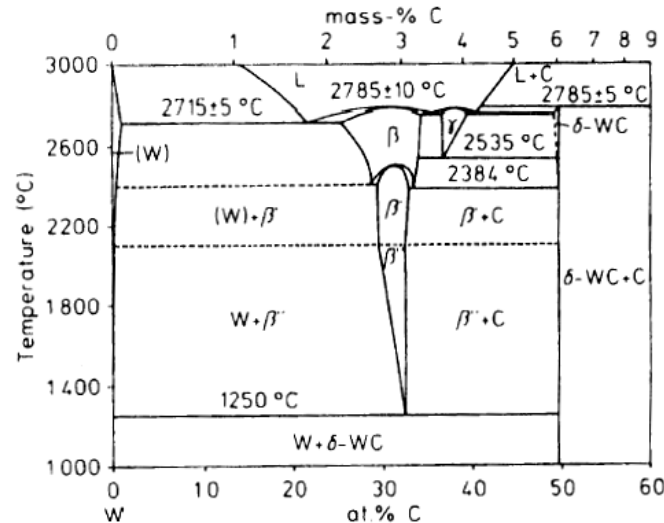
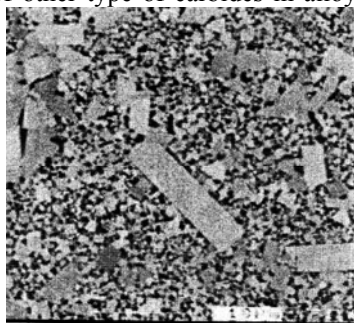


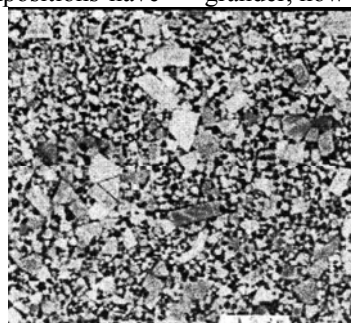
Fig. 1. W-C phase diagram [2].

This compound reacts with matrix metal forming complex carbides by type $W_xCo_yC_z$ (η phase). The presence of η phase determines a coarse and unregulated microstructure. This type of structure makes the material very brittle by reducing proportions of matrix material. [3] The introductions of other type of carbides in alloy compositions have

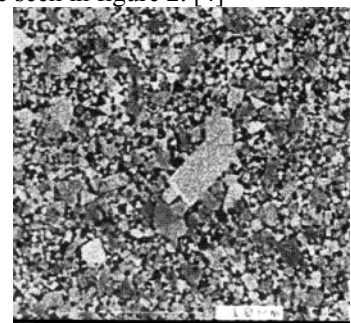
as purpose to avoid grain growth at sintering, to increase hardness, toughness, wear resistance and to improve corrosion resistance. The utilization of tungsten carbide powder without grain growth inhibitors is not recommended. How much finer is the start powder, for that grain growth at sintering will be grander, how can be seen in figure 2. [4]



0,6 μm, 6% Co, X3000

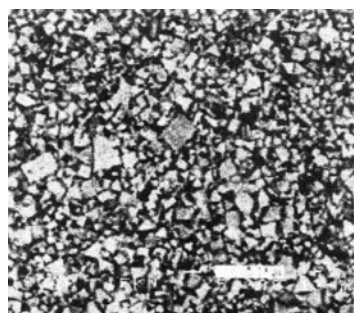


0,8 μm, 6% Co, X3000

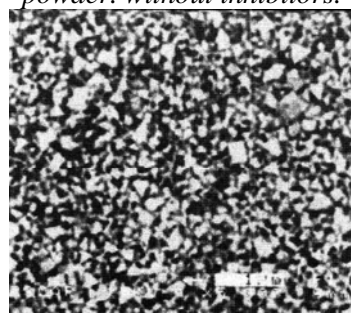


1 μm, 6% Co, X3000

Fig. 2. The growth of carbide grains after sintering in alloys with different dimensions of initial powder. without inhibitors.



0,6 μm, 10% Co, 0,3% Cr_3C_2



0,6 μm, 10% Co, 0,5% Cr_3C_2



0,6 μm, 10 % Co, 1,35% Cr_3C_2

Fig.3. The effect of inhibitors (Cr_3C_2) addition on the microstructure of WC-Co alloys.

Chromium carbide (Cr_3C_2) and vanadium carbide (VC) is the most utilized crystalline grain growth inhibitors. In alloys composition the inhibitors are present in a proportion of maximum 1.5 %, as functions of binder content and his solubility in binder. A higher content of inhibitors lead to apparition of γ phases. At sintering temperature, the inhibitor is dissolved in cobalt, limiting the solubility of tungsten carbide in the binder. At cooling, VC precipitate like nano particles of complex carbide (V,W)C and chromium carbide remains in solution, presenting the tendencies to diffuse on grain boundaries [5]. A corresponding wetting of hard phase by the binder leads to improved mechanical and technological properties. A thick layer of tough binder who separates the carbide particles will stop the crack propagation. Next figures show the effect of binder proportions on the hardness and toughness of sintered hard alloys.

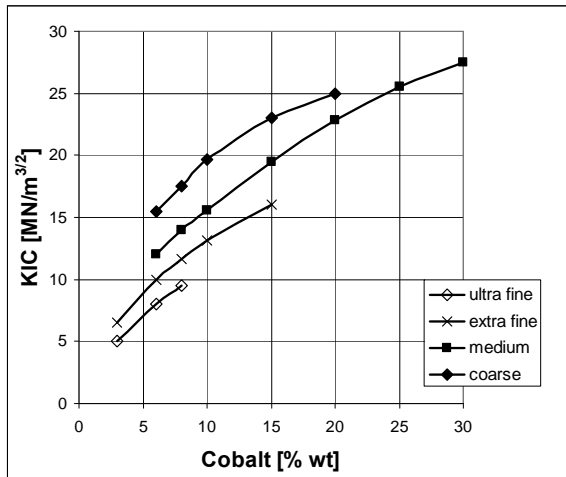


Fig.4. Toughness of WC-Co as function of cobalt content and carbide size.

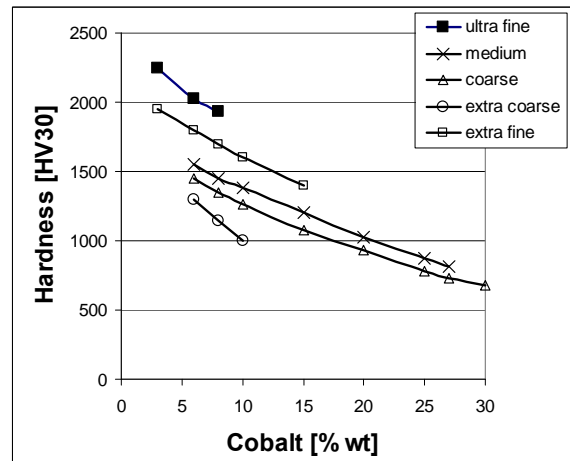


Fig.5. Hardness of WC-Co as function of cobalt content and carbide size

3. Structure – properties correlation

The design of hard alloys has to be donning, every time when possible, keeping account by the working conditions of the final product. Interaction between components, maximum temperature and maintaining time at maximum temperature are factors that have a decisive importance in sintered products structure evolutions. Particle dimensions and granulometric distribution of tungsten carbide are very important factors in sintered hard alloy structure determination. WC-Co alloys with a coarse structure are more ductile than that finer. On the other hand, the alloys with a finer structure present higher hardness, toughness and wear resistance. Carbide particles complete separation with an intermediate layer of cobalt with a 0.4-0.6 μm thickness permit to obtain an optimum resistance for sintered hard alloys, this fact being presented in figure 6.

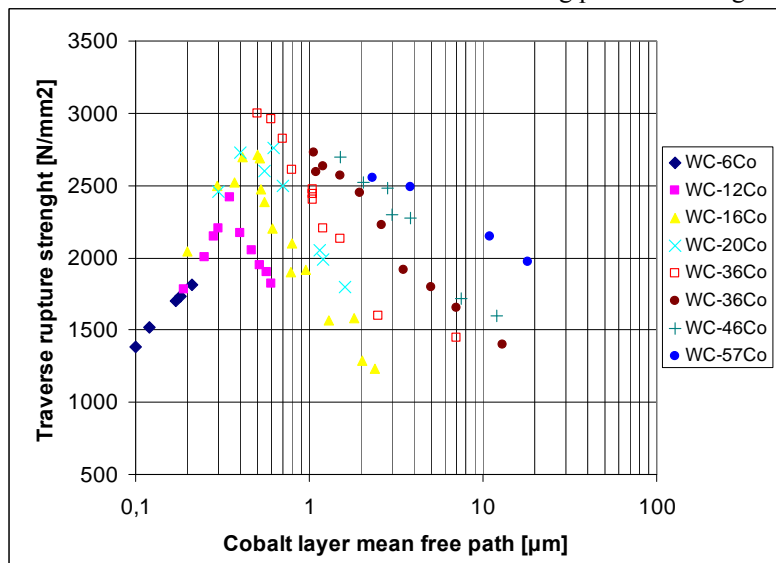


Fig.6. Traverse rupture strenght of WC-Co as function of binder mean free path [1].



The contact apparition between carbide particles lead to a structure type "skeleton" which must be maintained at low level is possible because the alloy toughness decreases [6].

For increase properties of sintered hard alloys, the classical hard alloy, WC-Co, is modified with an amount of other carbides like titanium carbide, tantalum carbide and niobium carbide. Titanium carbide is less soluble in cobalt comparative with tungsten carbide. Present at lower diffusivity and, for this reason, have a higher wear resistance at high temperatures and low tendencies to adhere to the chip. This property recommends WC-TiC-Co grades for machining tools in steel industry at great work speed where pear high temperatures on chip – tool interface. Instead, TiC reduces the strength of sintered hard alloys and his associated properties: edge resistance, toughness and compression resistance.

Additions of Ta/NbC have improved as results of wear resistance and hardness at high temperatures. Ta/NbC reduce strength alloy less than TiC. With hardness exception, WC-Ta/NbC-Co alloys have superior properties than WC-TiC-Co grades. [6]

4. Conclusions

Hard phase-binder rapport determines hardness and toughness values; increased binder proportions will improve toughness and decrease hardness.

At the same rapport between hard phase and binder, dimensions of carbide particles determine alloys properties. The alloys with more fine structure present increased values for hardness and toughness.

The utilization of ultra fine carbide powders make possible to rise binder content without affecting hardness values.

The fine structures is maintained by introduction of small amount of crystalline grain growth inhibitors in alloys composition, the most utilized being VC and Cr₃C₂. Vanadium carbide assure a high hardness and small dimensions of carbide particles and chromium carbide improve alloy toughness.

References

- [1]. *** - *Powder metallurgy of Hard metals: Course Lectures*, European Powder Metallurgy Association, Shrewsbury, 1995
- [2]. *** - *ASM Handbook*, vol. 7, *Powder Metallurgy*, ASM Eight Ed., Ohio, 1991
- [3]. J.F. Shackelford – *introduction to materials science for engineers*, Practice & Hall, New-York, 1998.
- [4]. T.Taniuchi, K. Okada, T. Tanase – *Sintering behaviour of VC dopped micro-grained cemented carbide*, 14th Plansee Seminar '97, Plansee Proceedings, v. 2, Cemented Carbides and Hard Materials, 1997.
- [5]. S. Luckyx, M.Z. Alli – *Comparison between V₈C₇ and Cr₃C₂ as grain refiners for WC-Co*, Materials and Design, nr. 22/2001.
- [6]. V. Stanciu – *Perspective and actual methods for sintered hard alloys properties improving*, Buletinul institutului politehnic din Iasi, Tomul I (liv), fasc. 1, 2004.



TWO - WAY SHAPE MEMORY EFFECT IN A Cu-13wt. %Al-4 wt.%Ni SHAPE MEMORY ALLOY BY THE THERMO -MECHANICAL CYCLING METHOD

Carmela GURAU, Gheorghe GURAU,
Petrică ALEXANDRU, Nicolae CĂNĂNĂU

"Dunărea de Jos" University of Galati

email: carmela.gurau@ugal.ro

ABSTARCT

A Cu - 13 % wt Al 4% wt Ni polycrystalline shape memory alloy has studied with a thermo mechanical cycling method. The two – way shape memory effect (TWSME) was obtained bending the alloy around a cylinder mold and by using a constrained heating – cooling technique. This alloy elaborated by a classic melting method was extruded in wires with 4 mm diameter and was hot rolled in sheets with thickness.

KEYWORDS: Cu-13wt. %Al-4 wt. %Ni shape memory alloy, Two way shape memory effect, Cu based shape memory alloy, Thermal cycling, Martensite transformation

1. Introduction

Shape memory alloys (SMA) obtained under classic technology benefit by a low price engineering applications like sensors and actuators. Cu Al Ni SMAs can be used for higher working temperatures required (200^oC) excellent conductivity. Also those alloys are more resistant to degradation of functional properties due undesired aging effects than Cu Zn Al SMAs [1]. In Cu Al Ni SMAs with DO3 parent phase order thermoelastic transformation can be generate the two way shape memory effect (TWSME) not only shape memory effect (SME) like in reversible non thermoelastic martensite

TWSME is none an intrinsic property of shape memory alloys, it can be obtained only by training methods.

In parent phase is induced an internal tension by several methods:

- Thermo mechanical training under load heating;
- Excess deformation;
- Constrained aging treatment.

After training for obtain two-way shape memory effect, the material can alternate between two distinct shapes as it undergoes a thermal cycle. The origin of this particular property of SMA`s is still not completely understood but it has been proposed few different explanations:

- The effect of internal stress fields due to the complex dislocations introduced during training that produce selected martensitic variants;

- The presents of stress induced martensite inhibits the nucleation of self accommodating martensite plates.

The second mechanism has been reported to be the most plausible for TWSME [3].

In Cu-Al-Ni Alloys the types of martensite phases formed β'_1 (18R) or γ' (2H) can also play a role in have been considered that TWSME is. It is clear that TWSME corresponds to the preferential creation of certain variants of martensite that are energetically more stabile. Although there have been reports on the induction of TWSME by banding alloy samples around cylindrical shaped structures but only in Cu-Al-Zn alloys. The Cu-Ni alloy with 13% Al weight is a hard deformable SMA are less to the stabilization process then Cu Zn Al, and only few results exists on this training method for this alloys and that more for single crystals.

2. Experimental

The elaboration of Cu 13 Al 4 Ni alloy was made in the tilting induction furnace using pure metals copper nickel and aluminum plates. The cast ingot after remelting was turned in cylindrical shapes and was extruded from 35mm to 4 mm diameter in

two steps. The specimens after extrusion were solubilised at 850 °C for 30 minutes and immediately in ace water quenched. The transformation temperatures measured by DSC (Differential Scanning Calorimetry) and calculated for 1 % austenite and martensite start and 99% austenite and martensite finish were $M_s = 70$ °C, $M_f = 109$ °C, $A_s = 102$ °C, and $A_f = 159$ °C. Finally the hot extruded wires were hot rolled in fourteen successive passes into strips with 0.32 mm x 8 mm x 140 mm.



Fig. 1. Trained TWSME strip specimen

The specimens obtained after hot rolled were in martensite state. The transformation temperatures after measured by DSC calculated for 1 % austenite and martensite start and 99% austenite and martensite finish were $M_s = 44$ °C, $M_f = 91$ °C, $A_s = 60$ °C, and $A_f = 109$ °C.

In the first step the strip shaped specimens were bent around a cylinder mould of 50 mm diameter in R at room temperature in a circular arc shape. The second step consists in an unconstrained immersing in boiled water at 100°C when the strips recovered the straight shape.

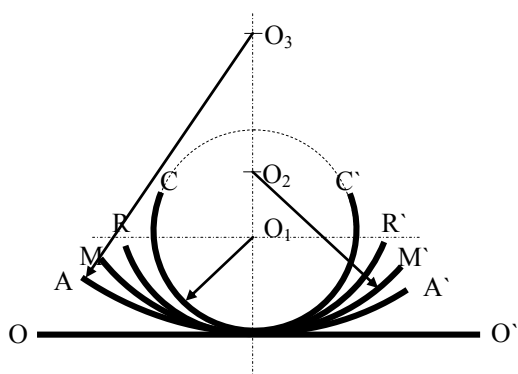


Fig. 2. Measurements TWSME scheme

The qualitative TWSME was assessed by cycling the samples between the temperature below M_f and above A_f . This routine was repeated for 50

cycles in the same bending direction. A good SME was obtained after 20 cycles.

Measurements were carried out in the manner indicates in figure 2, in which the distance OO' , AA' , MM' , RR' and CC' were measured at both ends of the sample. The curve MM' represents the cold states while curve AA' represents the hot state shape after training treatment. OO' represents the original shape of the sample, RR' remanent shape after eliminated constrain in cold state and CC' the deformation of imposed shape during the treatment.

TWSME was assessed using the following equation:

$$\text{strength of TWSME} = \frac{AA' - MM'}{CC'} \cdot 100 [\%] \quad [5]$$

Times between two consecutive cycles are 10 to 15 seconds.

For DSC measurement was used small pieces weighting less than 0.100g. The calorimetric experiments were performed by means of SETARAM 92 instrument in air at a heating and cooling rate of 15°C/min, between -50°C and 250°C. The cooling treatments were acted by using liquid nitrogen. Endothermic and exothermic peaks on DSC profiles were taken from two sets of experiments:

- one thermal cycle were performed for hot rolled strip
- one thermal cycle were performed for sample trained.

3. Results and discussions

In table 1 is shown the variation of strength of two way memory effect in Cu13Al4Ni alloy as a result of varying the number of training cycles in the cold water constrained bend and unconstrained heating bend at 100°C.

Table 1

Number of cycles	10	20	30	40	50
TWSME [%]	28.95	34	76.3	76.3	76.3

The strength of TWSME are about 28.95% after 10 training cycles and 76.3 after 30 training cycles indicating that TWSME increases continuously at least up to 30 cycles and it is maintained until 50 training cycles (fig.3.)

The transformation temperatures were obtained by DSC and calculated for 1 % austenite and martensite start and 99% austenite and martensite finish. In figure 4 is shown the subtracted DSC peaks for hot rolled samples and trained for TWSME samples.

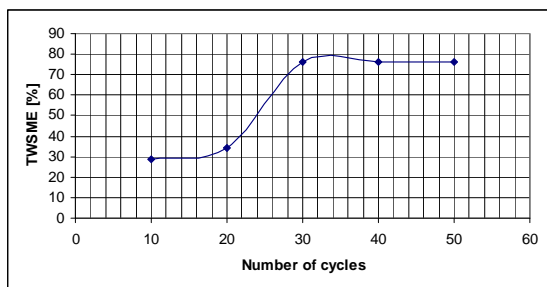


Fig.3. TWSME variation with number of cycles.

When the critical points for hot rolled specimens were: $M_s = 70^\circ\text{C}$, $M_f = 109^\circ\text{C}$, $A_s = 102^\circ\text{C}$, and $A_f = 159^\circ\text{C}$ and for trained specimens were $M_s = 44^\circ\text{C}$, $M_f = 91^\circ\text{C}$, $A_s = 60^\circ\text{C}$, and $A_f = 109^\circ\text{C}$.

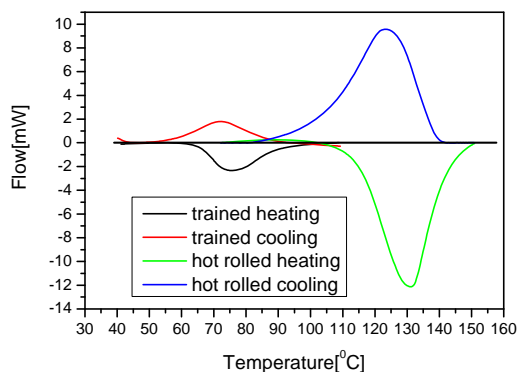


Fig. 4. Subtracted DSC curves

Thermo mechanical cycling, by which one forward and reverse transformation is completed it is known that produces a large number of dislocations, especially in parent phases of shape memory alloys. In this system alloy M_s temperature decreases markedly with increasing number of thermo mechanical cycle in the same time with A_f temperature.

That means equilibrium temperature between parent and martensite is decreasing. It is considered that the density of dislocations accumulated by thermo mechanical cycling also depends on transformation mode. The amount of dislocations produced by repetition of parent phase to 18R transformations is larger than to 2H transformations.

In figure 5 is shown the comparative transformation temperature between specimens after hot rolled and trained strip shaped. After training process for obtain TWSME all the critical points decreases.

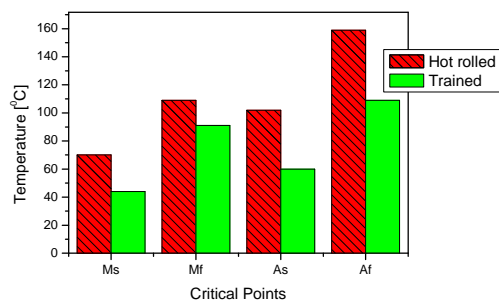


Fig.5. Critical martensitic transformation points in hot rolled state and trained state.

4. Conclusions

The two way shape memory effect in Cu13Al14Ni alloy was induced by a training method with cycles of constrained cooling and unconstrained heating.

The thermomechanical cycling treatment was achieved with constraining in ice water and unconstrained training at 100°C in as- quenched state. After hot rolling, samples are in the martensite state without quenching treatment.

The mechanical straitening of the alloy was performed by bending around a cylinder mould.

The strength of TWSME tends to increase with increasing number of thermomechanical cycles until almost 30 cycles and tense to maintain for 20 cycles more.

5. Acknowledgements

The authors would like to acknowledge the support from CENIMAT FCT/UNL Caparica Portugal, especially Mister Professor F.M.Braz Fernandez and his team and Mister V Dia from Mittal Steel Iasi.

References

- [1]. G. Logen, I. Anzel, A. Krizman, E. Unterweger, Z.B. Kosec, M. Bizjak, *Microstructure of rapidly solidified Cu-Al-Ni shape memory alloy ribbons*, Mater.Proc.Tech, 162/163 (2005)220
- [2]. H. W. Kim, *A study of the two-way shape memory effect in Cu-Zn-Al alloys by thermomechanical cycling method*, Mater.Proc.Tech, 146(2004)326-329
- [3]. C. Picornell, R. Rapacioli, J. Pons, E. Cesari, *Two way shape memory effect in Cu-Al-Ni single crystals*, Mat. Science and Engineering A273-275 (1999) 605-609
- [4]. C. Lexcelent, S. Leclercq, B. Gagry, G. Bourbon, *The two way shape memory effect of shape memory alloys: an experimental study and a phenomenological model*, International Journal of plasticity 16(2000) 1155-1168
- [5]. J. X. Zhang, Y. X. Liu, W. Cai, L.C. Zhao, *The mechanism of the two-way shape memory effect in Cu-Zn-Al alloy*, Materials Letters, 33(1997)211-214
- [6]. Z. Li, Z. Y. Pan, N. Tang, Y. B. Jiang, N. Fang, F. Zheng, *Cu-Al-Ni-Mn shape memory alloy processed by mechanical alloying and powder metallurgy* Materials Science and Engineering A 417 (2006) 225-229



A STUDY OF ELECTRIC PROPERTIES OF FIBER FABRIC BASED FILLED EPOXY COMPOSITES

**Gabriel ANDREI, Adrian CÎRCIUMARU,
Iulian-Gabriel BÎRSAN, Dumitru DIMA**

"Dunărea de Jos" University of Galați
email: adrian.circiumaru@ugal.ro

ABSTRACT

Electric and magnetic properties of laminate carbon fiber fabric based epoxy composites are investigated through experimental techniques. Various concentrations of powder fillers were used in order to change the basic properties of standard composite. Also effects of an electric or a magnetic external field over the mentioned properties are investigated. Electric conductivity is evaluated across and along reinforcement and at the surface of the samples.

KEYWORDS: Laminate Composite, Ferrite, CNT, Electric Properties, External Electric and Magnetic Fields.

1. Introduction

In recent years there are more and more researches about the electric and magnetic properties of composite materials based on the need of metal replacement in aircraft and spacecraft industries. There are many researches and also many results published in various journals covering a range of interests from physics to engineering. In the majority of the cases the approach is connected to a certain problem, for a certain application. There are also many papers concerning the modeling of electric properties of composites in order to ensure the design of composites [1]. However it is considered that such an approach is just a partial one because the design has to take into account not only those properties but also the mechanical and thermal properties. Obviously this is a very difficult approach and it can be found an extensive study over its complexity [2]. One of the cheapest and most convenient method is to fill the polymer with various powders (metal powders, CNT, carbon black, clay, ferrites etc.) [3]. The cited paper is an excellent review of actual orientations and results in the domain of filled polymer composites and emphasizes the importance of filler dimensions and shapes bringing in attention the importance of interface. One of the most important assessments in last years is the highly contribution of interfaces at the macroscopic properties of composites [4]. A composite material is made up of at least two components. The electric and magnetic properties of the finite material depend

essentially on the same properties on the components but also of external conditions of composite forming. Taking into account a woven fabric reinforced composite with filled polymer matrix the problem becomes more complex. As we mentioned above there are many papers concerning modeling of electric properties of composites but they are often limited to a particular structure of a bi-composite [5], [6]. It is not our intention to develop, at this very moment, a model for multi-composites but we consider that it is important to know, even just qualitative, the influence of various fillers over electric properties of a composite with a certain reinforcement, in various external conditions. This study is based on the idea that using different fillers in different concentrations for the same reinforcement we might establish the macroscopic properties of multi-composites. However electric magnetic properties of composites, as manifestations at the external changes, have to be averaged manifestations of the components. As it was mentioned already it is not the intention of the research, at this point, to test one model or other or to build up a new model. This is just a "trial and error" approach viewed as a starting point both for further studies and decision making in forming a composite with certain properties. It is extremely difficult to mathematically describe a four component composite even if there are various models for bi-component composites. The aim of this study, based on intuition, is to present some empirical results in order to help the manufacturers in decision making of forming a special composite.

2. Samples

Plates of four components composites with a 4 mm thickness and 120 mm x 250 mm as planar dimensions were formed, in glass moulds using polyvinyl alcohol 20% as un moulding agent. As basic matrix for composite was used the bi-component epoxy resin EPIPHEN 4020 and it was used in order to obtain the reference samples for two types of reinforcements. Both reinforcements are realized from carbon fiber fabric with an arrangement of alternate 0 and 45 degrees sheets. For the magnetic field samples had been used 15 sheets of reinforcements while the electric field samples containing 13 sheets of reinforcements.

The orientation of reinforcement sheets is been given relatively to the sample's edges: 0 degrees means that the yarn and the fill of the fabric are parallel to the length and the width of the sample and 45 degrees means that the yarn and the fill of the fabric are oriented at 45 degrees relatively to the same dimensions of the sample. In the case of the electric field samples it had been used a simple type fabric while in the case of magnetic field samples a satin type fabric had been used. Both fabrics were prepared for cutting in order to avoid the tear. In order to obtain the filled resin certain quantities of ferrite and CNT were dispersed in the A-component of the resin using a mixer at a temperature of 85 Celsius. For the sample realization amounts of filled A-component were mixed with specified quantities of B-component and the mixture was used in 15 minutes, 10 minutes after the mixture was made.

The forming of samples were made using a combined method, first a "layer-by-layer" adding of resin imbued sheets of reinforcement. After the mould was closed the excess of resin was extracted through application of a mechanical effort, then the mould was introduced in a rubber bag.

The air and other gases from the bag were removed using a small vacuum pump in order to avoid the gas intrusions in the sample. One hour after the described above technique the moulds were introduced in electric or magnetic field and kept there for 12 hours. One of the goals of this experiment was to investigate the influence of external fields over the electric properties of composite.

The idea is not new but it is possible to improve such properties using electric and magnetic fields or their superposition [4]. The electrostatic field was obtained using a plan-parallel plates capacitor. The magnetostatic field was obtained inside of a tubular wrapping of coils. After the extraction the samples were prepared for electric measurements.

First the edges were rectified by abrasion in order to ensure the contact of electric plungers, then they were cleaned using alcohol.

3. Measurements

Measurements were performed in order to determine the electric conductivity. In this case because of sample's anisotropy, we have to make distinction between transversal conductivity (measured between the large faces of the sample) and longitudinal conductivity (measured along the yarn or the fill of the external sheets of reinforcement). It is expected a high anisotropy for electric properties of the material because both the presence of reinforcement and the action of external fields [7]. It is obvious that the ferrite particles will be aligned along the magnetic field (for example). Those orientations have to have effects in electric properties magnitude [8], [9], [10].

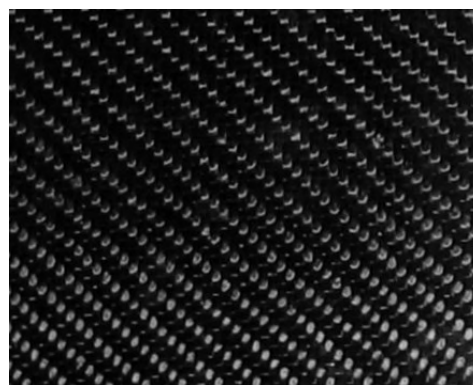


Fig. 1. Image of sample's surface after extraction and preparation

The resistivity measurement techniques are described in [11] and [12]. In [11] is described the van der Pauw technique in order to determine the resistivity which had been used for the longitudinal resistivity by measuring voltages and intensity for dc.

Figure 2 shows the experimental setup for the van der Pauw technique.



Fig. 2. The experimental arrangement for van der Pauw Technique

For the others measurements it had been used the same experimental setup, described for two distinct applications [12]. It is about the volume

resistivity of plates and, also about surface resistivity of plates. Both methods are based on the use of a measuring cell (three electrodes) and an apparatus able to measure electric resistance. For this purpose it had been used a *RLC-meter* at 1kHz . In order to perform those measurements a measuring cell was realized according to [12]. Figure 3 shows the main characteristics of measuring cell as they are described in [11]. In order to respect all the geometric conditions (imposed by the sample thickness) the cell was designed in accordance to [11].

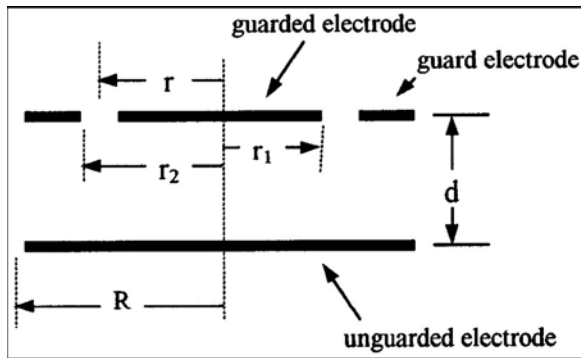


Fig. 3. Geometric characteristics of the measurement cell

The cell is of next dimensions: $R = 47.85\text{mm}$, $r_2 = 34.5\text{mm}$, $r_1 = 32.45\text{mm}$.

The value of r is given in [11] and is $r = r_1 + \Delta$ where

$$\Delta = \frac{1}{2}(r_2 - r_1) - \frac{2d}{\pi} \ln \left(\cosh \frac{\pi(r_2 - r_1)}{2d} \right) = \frac{1}{2}(r_2 - r_1) - 1,4659d \ln \left(\cosh 0,7854 \frac{r_2 - r_1}{d} \right).$$

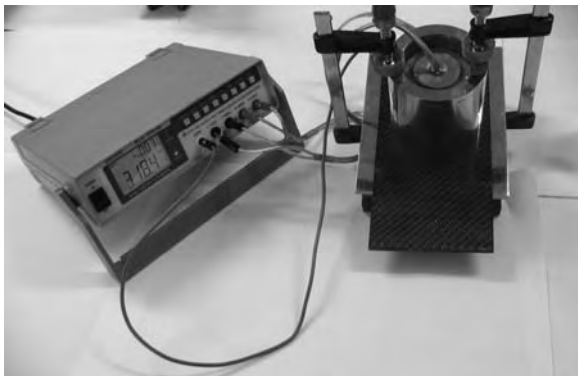


Fig. 4. The experimental arrangement for standard method for determination of ρ_V and ρ_S

With those we have: $\rho_V = \frac{RS}{d}$ where R is the read value of resistance. $S = \pi r^2$ and d is the

sample's thickness (all the dimensions are according the I.S.). Figure 4 shows the experimental setup of the cell method.

4. Results

The epoxy resin, as well as all the polymers, is a dielectric so its resistivity has high value and, of course, its conductivity has a small value.

On the other hand we used as reinforcement sheets of carbon fiber fabric which is an excellent conductor so, the standard plate (a laminate composite) looks like a sandwich of alternate conductor and dielectric layers. To improve the electric conductivity of such a material we may spread in dielectric a powder with high value of conductivity, this is the case of CNT used as filler.

In such conditions the composite's resistivity along the reinforcement has to be smaller than the across one.

There are not reasons to consider that the matrix (filled epoxy) is influencing the natural conductivity of carbon fiber increasing or decreasing its resistivity. In fact, the yarn and the fill will act as insulated conductors.

Adding fillers to the resin we can improve its conductivity and, as an effect, we can have an improvement of composite's conductivity as a consequence of superposition principle.

Figure 5 shows the across resistivity $\rho_V [\Omega m]$, surface resistivity $\rho_S [\Omega]$, along resistivity $\rho_L [\Omega m]$ for standard sample and CNT filled epoxy composite (electric type sample).

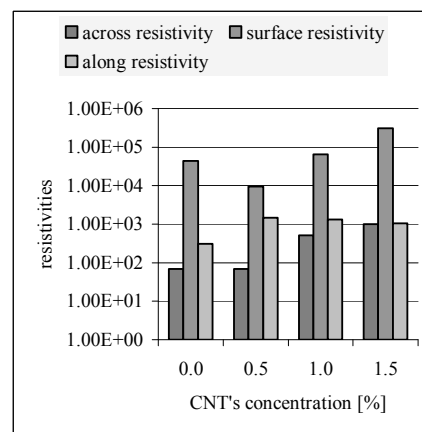


Fig. 5. Influence of CNT's concentration on samples' resistivities (13 sheets of reinforcement)

Figure 6 shows the $\rho_V [\Omega m]$, $\rho_S [\Omega]$, $\rho_L [\Omega m]$ for standard sample and CNT filled epoxy composite (magnetic type samples).

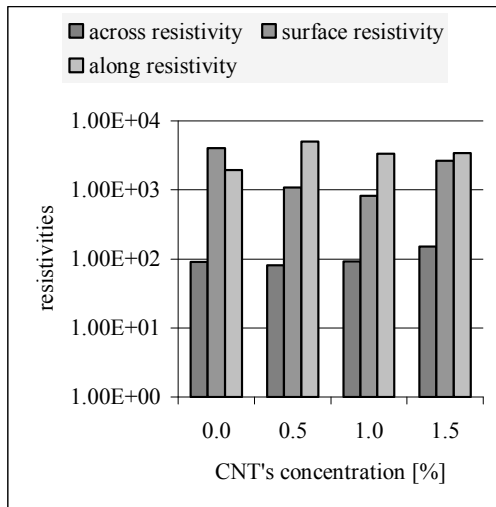


Fig. 6. Influence of CNT's concentration on samples' resistivities (15 sheets of reinforcement)

Comparing the two diagrams above it can be noticed also the influence of reinforcement over the resistivity of the samples.

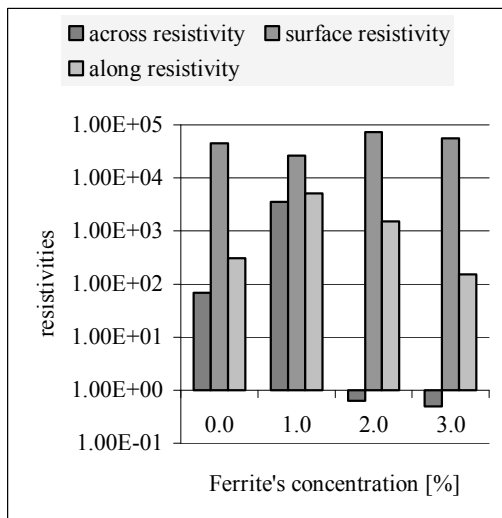


Fig. 7. Influence of ferrite's concentration on samples' resistivities (13 sheets of reinforcement)

There are small values for the 15 sheets of reinforcement samples than the 13 sheets ones. We can also notice that only small amounts of CNT can bring benefits in terms of resistivity. A soft decreasing of the value of bulk resistivity in both cases for 0.5% concentration of CNT can be noticed.

Figure 7 and 8 shows the influence of ferrite over the samples' resistivities.

When a composite material is formed with filled polymer it is expected that it is sensitive to external electric or magnetic field. Under these fields actions there is possible that small particles of fillers to suffer an alignment so some kind of order may be installed

in the polymer structure.

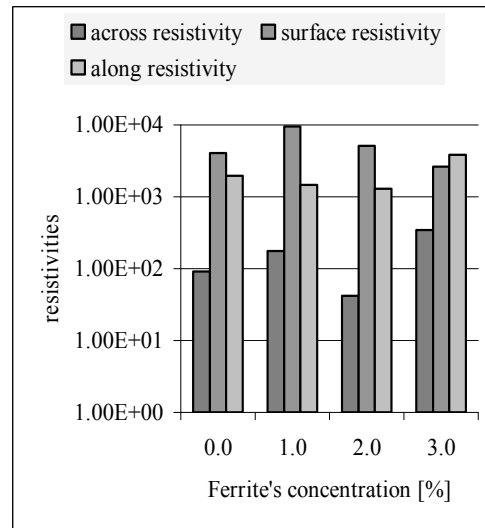


Fig. 8. Influence of ferrite's concentration on samples' resistivities (15 sheets of reinforcement)

The electric and the magnetic fields were parallel to the reinforcement so it is expected that the across resistivity to increase and also the surface resistivity in the case of CNT used as filler.

In the case of the magnetic field the ferrite particles are expected to be aligned along the magnetic field lines. Figure 9 shows the variations of samples' permittivities with the intensity of the electric field for the 0.5 % CNT filled epoxy matrix.

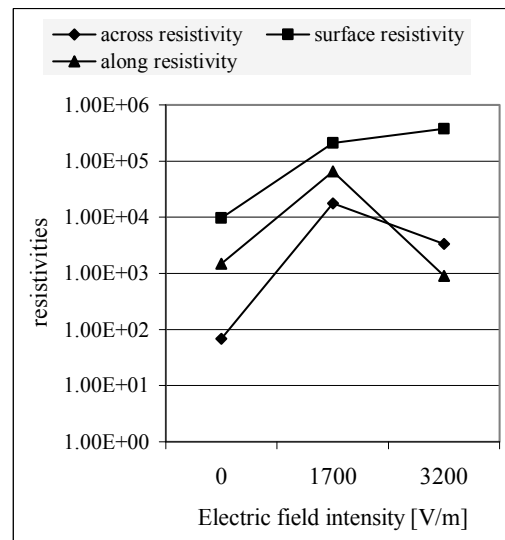


Fig. 9. Resistivities' variations with electric field intensity (CNT 0.5%)

Figure 10 present the variations of permittivities in electric field for the 1% ferrite filled epoxy matrix.

Next section is about the magnetic field effects over resistivities of samples and we will present just the results for 0.5 % CNT and 1 % ferrite filled epoxy matrix composites.

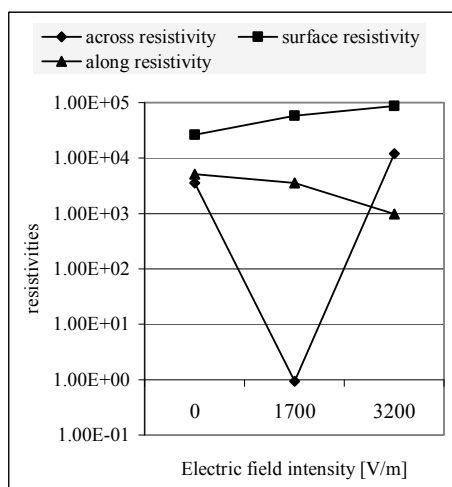


Fig. 10. Resistivities' variations with electric field intensity (ferrite 1%)

Figure 11 present the variations resistivities for 0.5% CNT filled epoxy composite with 15 reinforcement sheets in external magnetic field and the figure 12 for 1 % ferrite filled epoxy matrix, 15 reinforcement sheets of carbon fiber fabric.

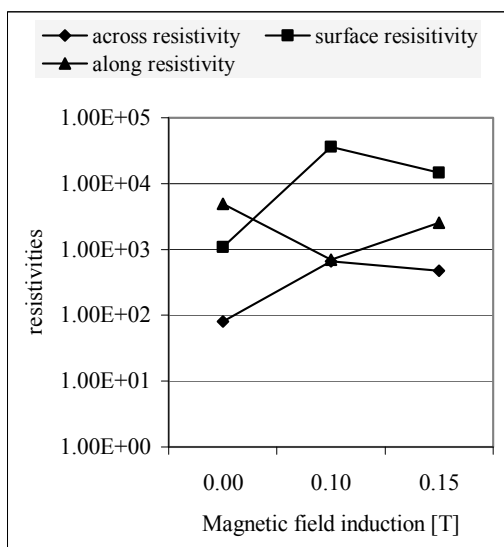


Fig. 11. Resistivities' variations with magnetic field induction (CNT 0.5%)

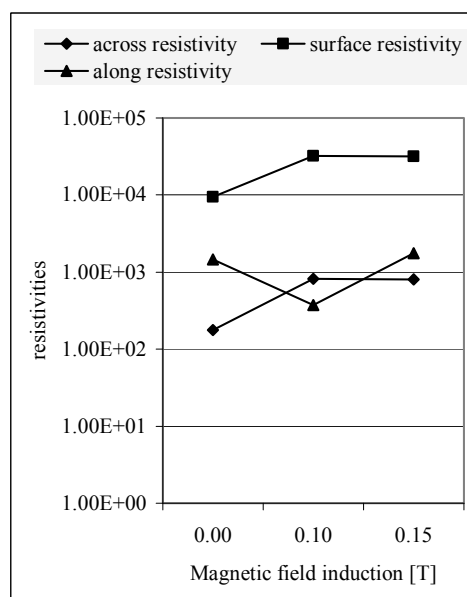


Fig. 12. Resistivities' variations with magnetic field induction (Ferrite 1%)

5. Conclusions

Based on above presented results - it is possible to design a fiber fabric based filled polymer composite with certain values of surface resistivity and across resistivity in order to avoid the electric charging.

The above presented results allow the conclusion that it is possible to form a composite based on a certain geometry of reinforcement (fiber fabric) using various types of filled polymers. It is clear that these results are just a part of an exhaustive characterization of samples. Mechanical, thermal and thermomechanical analysis are necessary.

Another aspect to be taken into account is the fact that because of the fillers and of the reinforcement such a composite material is frequency sensitive *i.e.* the electric and electromagnetic properties depend on the frequency of measuring signal.

The study of mechanical and thermal properties will allow manufacturers to make the right decision about the best reinforcement, best geometry of the reinforcement, best fillers' concentrations for a given application. Based on these results it is possible to start verifying some models regarding electric and electromagnetic properties of complex composites.

Acknowledgments

The research was carried out inside the CNCSIS type A Grant, code 514 /theme 1/ 2006.



References

- [1]. Torquato, S., Hyun, S., Donev, A., *Optimal design of manufacturable three-dimensional composites with multifunctional characteristics*, *Journal of Applied Physics*, 94, 2003.
- [2]. Kalamarkov, A. L., Kolopakov, A. G., *Analysis, Design and Optimization of Composite Structures*, John Wiley&Sons, 1997.
- [3]. Winey, I. Karen, Vaia, A. R. (ed), *Polymer Nanocomposites*, *MRS Bulletin*, Vol. 32, April 2007.
- [4]. Jong-Kyo Kim, Yin-Wing Mai, *Engineered Interfaces in Fiber Reinforced Composites*, Elsevier, 1998.
- [5]. Roberts, A. P., Knackstedt, M. A., *Structure-property correlations in model composite materials*, *Physical Review E*, 54, 1996.
- [6]. Torquato, S., *Modeling of physical properties of composite materials*, *International Journal of Solids and Structures*, 37, 2000.
- [7]. Donglu Shi, Peng He, Jie Lian, Chaud, X., Bud'ko, S. L., Beaugnon, E., Wang, L. M., Ewing, R. C., Tournier, R., *Magnetic alignment of carbon nanofibers in polymer composites and anisotropy of mechanical properties*, *Journal of Applied Physics*, 97, 2005.
- [8]. Liu, L., Matitsine, S. M., Gan, B. Y., Rozanov, K. N., *Effective permittivity of planar composites with randomly or periodically distributed conducting fibers*, *Journal of Applied Physics*, 98, 2005.
- [9]. Makhnovskiy, D. P., Panina, L. V., *Field dependent permittivity of composite materials containing ferromagnetic wires*, *Journal of Applied Physics*, 93, 2003.
- [10]. Kim, B., Lee, J., Yu, I., *Electrical properties of single-wall carbon nanotube and epoxy composites*, *Journal of Applied Physics*, 94, 2003.
- [11]. Webster, J. G. (ed), *Measurements, Instrumentations, and Sensors*, CRC Press, 1999; Heaney, M. B., *Electrical conductivity and resistivity*, 43 and Misra, D. K., *Permittivity measurement*, 46.



A STUDY OF ELECTROMAGNETIC PROPERTIES OF FIBER FABRIC BASED FILLED EPOXY COMPOSITES

**Adrian CÎRCIUMARU, Iulian-Gabriel BÎRSAN,
Gabriel ANDREI, Dumitru DIMA**

Dunărea de Jos University, Galați, România
email adrian.circiumaru@ugal.ro

ABSTRACT

Electric and magnetic properties of laminate carbon fiber fabric based epoxy composites are investigated through experimental techniques. Various concentrations of powder fillers were used in order to change the basic properties of standard composite. Also effects of an electric or a magnetic external field over the mentioned properties are investigated. Characterizing the reaction of the sample to an electromagnetic wave the electric capacitance and the electric inductance of samples are investigated both across the reinforcement and at the surfaces of samples.

KEYWORDS: Laminate Composite, Ferrite, CNT, Electromagnetic Properties, Resonance Frequency.

1. Introduction

Assuming that a composite material is a complex structure it is obvious that it is hard to describe all its properties in terms of its parts properties. The electromagnetic properties of the composite depend not only on the electromagnetic properties of the components but on the quality and nature of the interface between the components and its electromagnetic properties [1]. There are many researches about the interdependencies between components and there are also many purposed models which describe the macroscopic electromagnetic properties of composites in terms of constituents' properties. A new field of development was opened regarding the controlled electromagnetic properties. One question is, for example, if it is possible that a composite material can be, at the same time, a metamaterial [2]. Powders are used as fillers in order to obtain bi-components composites. There is no structural order in such a filled composite, the most important aim being the uniform distribution of particles in matrix. The powders can be dielectric as talc, clay or ferrites, can be magnetic active as ferrite, can be electric active as CNT or carbon nano-fibers. All these powders have effects over the electromagnetic properties of the composite [3].

There exist many models regarding the mathematic description of electromagnetic properties of the bi-component composites [4], [5]. Also there are studies regarding the bounds of models [6].

Obviously the electromagnetic properties of the filled polymer composite are depending on the arrangement of the filler's particles in the polymer structure. If there is no structural order then there is no anisotropy of electromagnetic properties. Anisotropy is present if the filler's particles are arranged in polymer's structure [7], [8], [9].

The design problem of a composite with given electromagnetic properties is of high complexity [10]. Taking into account that not only the electromagnetic properties are important but also the mechanical and thermal properties the problem becomes almost impossible. The aim of this research is to analyze the electromagnetic effects of the powders presence in the polymeric matrix of a composite.

2. Samples

Samples used for this study were described already in the first part of this research [11]. There are two types of samples, one filled with magnetic active powder (ferrites) the other one filled with electric active powder (CNT).

3. Measurements

Measurements were performed in order to determine the electric capacitance and the electric impedance both across the reinforcement and at the surface of the plates.

For these measurements it had been used an experimental setup described by [12]. This arrangement is made in order to determine the electric capacitance and, subsequently the electric permittivity. The method is based on the use of a measuring cell (three electrodes) and an apparatus able to measure electric capacitance and electric inductance. The measuring cell is also described in [11]. Using a *RLC-meter* it is possible to record also the quality factor and the dielectric loss. With those

we have: $\varepsilon = \frac{C_V d}{S}$ where C_V is the read value of capacitance, $S = \pi r^2$ and d is the sample's thickness (all the dimensions are according the I.S.). Also the L_V value of electric inductance was recorded. Based on the observation that the standard method allows the determination of surface resistivity as it was recorded, also, C_S and L_S characterizing from the electromagnetic point of view the surface of the sample [13]. All the values of above mentioned parameters are results of an average of over 20 measured values. It is necessary to mention that electric capacitance and the electric inductance are for a cylinder with sample's thickness as height and a circular disk of r radius as base, L_S and C_S correspond to a circular sector between r_1 and r_2 [11]. It was also tested a method for magnetic permeability determination based on a theoretical application [14]. Unfortunately the method's efficiency is restricted to low frequencies of measurement.

4. Results

In the last period there are more and more interests in tailoring the composites in order to satisfy various electromagnetic requirements (shielding, electromagnetic response to electromagnetic waves action). In the next section we present the results of electric permittivity measurements [15].

It is expected a decrease of electric permittivity of CNT filled epoxy with the concentration of CNT because they have high electric conductance. At macroscopic level it is present in a decrease of electric capacitance, C_V [16]. Filling the epoxy with ferrites it is expected that L_V will increase. The samples used for this study are not only of filled polymer but also they are reinforced with parallel sheets of carbon fiber fabric and the presence of reinforcement has its effects on measured C_V and L_V . It can be said that C_V and L_V are characterizing a four component composite [11] while C_S and L_S are characterizing a bi-component composite (filled epoxy). Because their electric or magnetic sensitivity it is expected that values of C_V , L_V , C_S , L_S to be

dependent on external fields applied during the formation of samples. Figure 1 present the variations of electric permittivity, in F/m , of the carbon fiber fabric based CNT filled epoxy matrix laminate composites and its variation with external electric field and the figure 2 the variations of the electric permittivity, in F/m , of the same structure with ferrite filled epoxy.

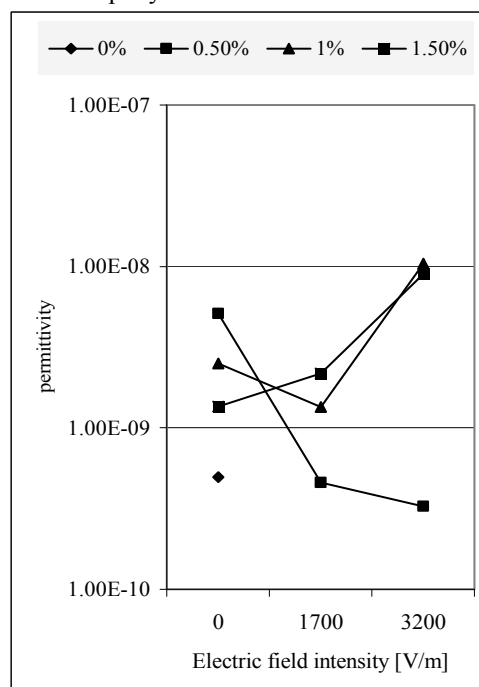


Fig. 1. Electric permittivity of samples CNT filled epoxy in external electric field.

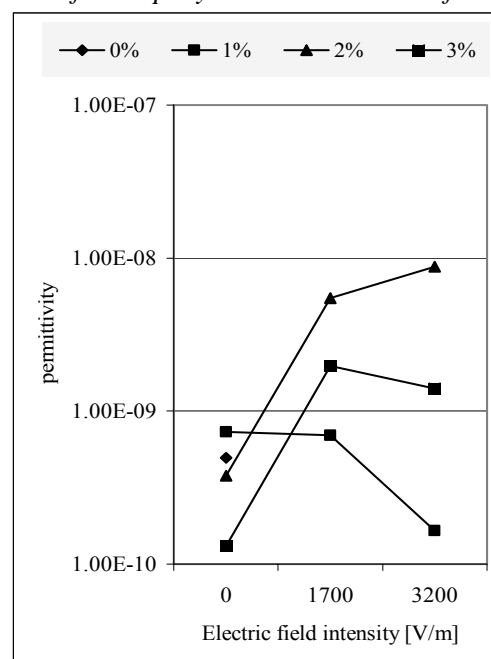


Fig. 2. Electric permittivity of samples Ferrite filled epoxy in external electric field.

The figure 3 present the variations of electric permittivity, in F/m , of the carbon fiber fabric based CNT filled epoxy matrix laminate composites and its variation with external magnetic field and the figure 4 the electric permittivity, in F/m , of the same structure with ferrite filled epoxy.

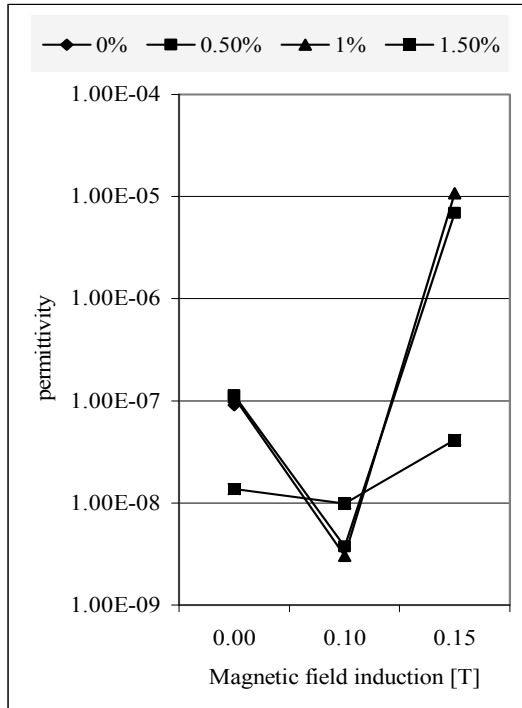


Fig. 3. Electric permittivity of samples CNT filled epoxy in external magnetic field.

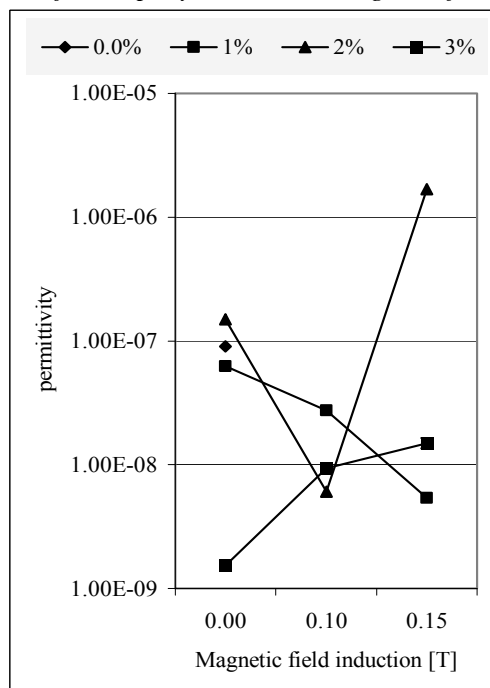


Fig. 4. Electric permittivity of samples Ferrite filled epoxy in external magnetic field.

The last aspect we want to emphasis is about the resonance frequency of the composite. This parameter is hard to model even for simple composites such as random distributed fiber composites or powder filled composites [17], [18]. There is a model (extremely simple to use) the mixed rule. In this section we will present calculated resonance frequencies based on L_V and C_V measurement through the cell method. The frequency, in rad/s is given by the simple relation: $f_0 = 1/\sqrt{LC}$.

Perhaps, the best way to characterize the samples from the electromagnetic point of view is to show the electric permittivity and the magnetic permeability of each sample. Figure 5 presents the resonance frequencies for CNT filled epoxy matrix laminate with 13 sheets of reinforcement in electric field. It can be noticed that there is a strong influence of the external electric field over the resonance frequency. This may be explained through the filler's alignment. In our opinion the triple point in the right part of diagram is very important because it can be used as starting point for a concentration-electric field equivalence in order to optimize the forming of such composites. From the future experiences point of view we also present the resonance frequencies for ferrite filled epoxy matrix composites. Figure 6 presents the resonance frequencies for Ferrite filled epoxy matrix laminate with 13 sheets of reinforcement in electric field.

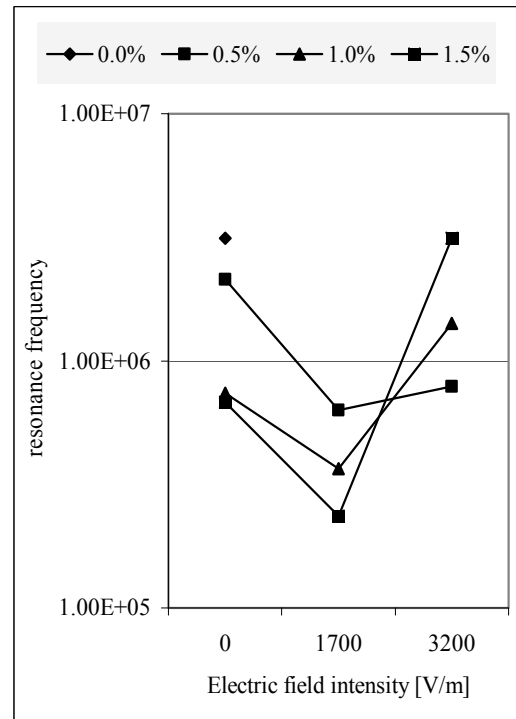


Fig. 5. Resonance frequencies of the CNT filled epoxy samples formed in external electric field.

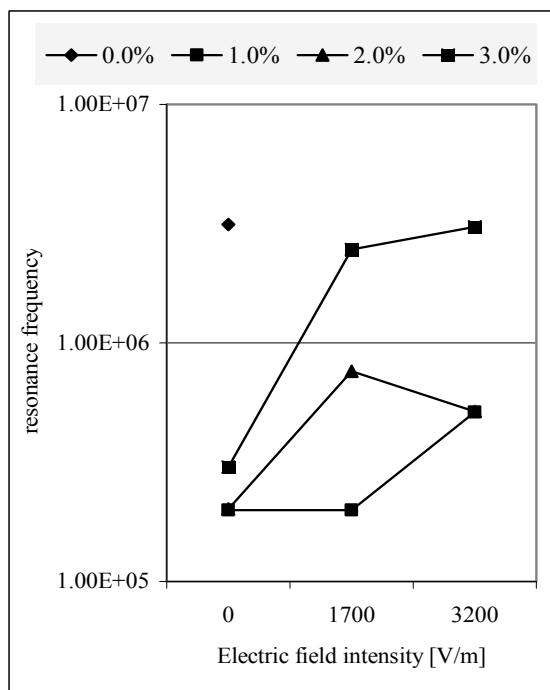


Fig. 6. Resonance frequencies of the Ferrite filled epoxy samples formed in external electric field.

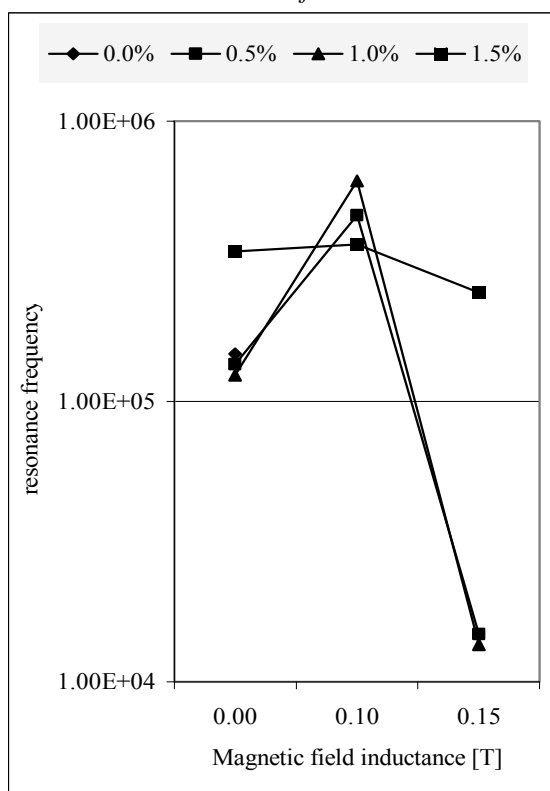


Fig. 7. Resonance frequencies of the CNT filled epoxy samples formed in external magnetic field.

Figure 7 - the resonance frequencies for CNT filled epoxy matrix laminate with 15 sheets of reinforcement in magnetic field and the figure 8 the resonance frequencies for Ferrite filled epoxy matrix laminate with 15 sheets of reinforcement in magnetic field.

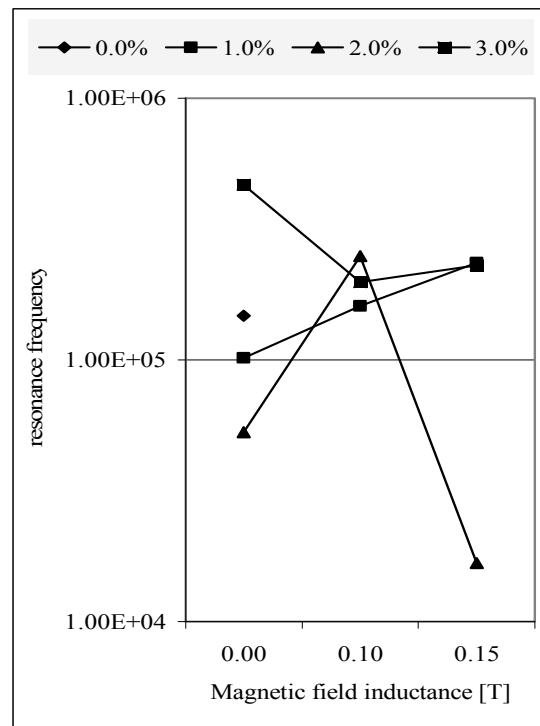


Fig. 8. Resonance frequencies of the Ferrite filled epoxy samples formed in external magnetic field.

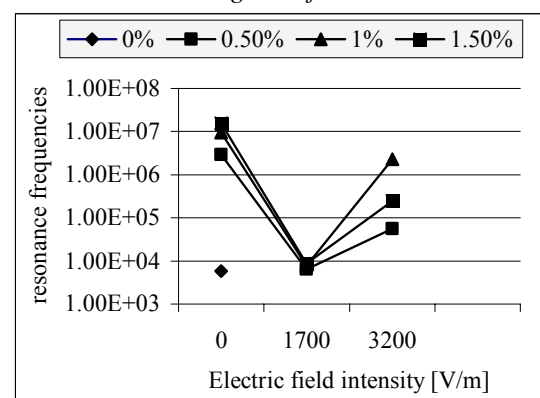


Fig. 9. Resonance frequencies of the CNT filled epoxy samples formed in external electric field – surface.

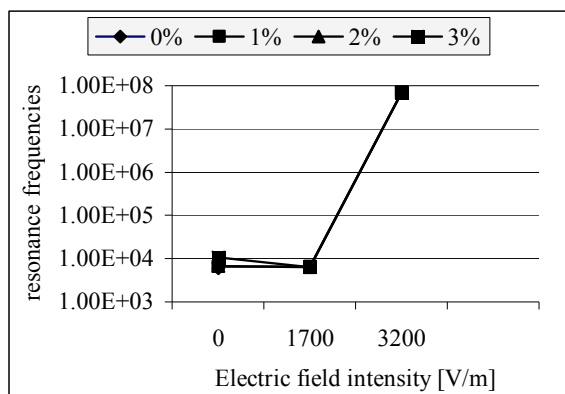


Fig. 10. Resonance frequencies of the Ferrite filled epoxy samples formed in external electric field – surface.

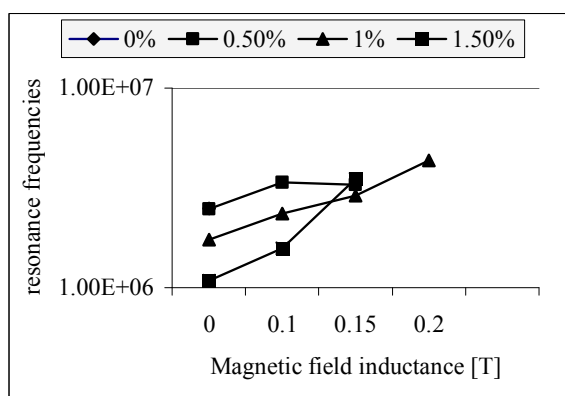


Fig. 11. Resonance frequencies of the CNT filled epoxy samples formed in external magnetic field – surface.

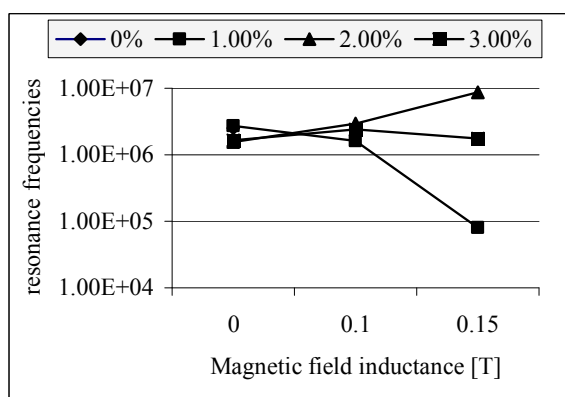


Fig. 12. Resonance frequencies of the Ferrite filled epoxy samples formed in external magnetic field – surface.

Figures 9, 10, 11 and 12 are respectively corresponding to figures 5, 6, 7, and 8 but show the resonance frequencies for the surfaces of the samples.

5. Conclusions

The above presented results allow the consideration that it is possible to form a composite based on a certain geometry of reinforcement (fiber fabric) using various types of filled polymers. It is clear that presented results are just a part of an exhaustive characterization of samples. Mechanical, thermal and thermomechanical analysis are necessary.

Another aspect to be taken into account is the fact that because of the fillers and of the reinforcement such a composite material is frequency sensitive *i.e.* the electric and electromagnetic properties depend on the frequency of measuring signal. More, it is necessary to determine the above parameters through other methods, including electromagnetic waves based methods.

The study of mechanical and thermal properties will allow us to make the right decision about the best reinforcement, best geometry of the reinforcement, best fillers' concentrations for a given application. Based on our results we intend to start verifying some models regarding electric and electromagnetic properties of complex composites.

It is possible to design the electromagnetic properties of reinforced composites by using filled polymers as matrix. This design is useful regarding the response of the material under the action of a certain electromagnetic wave. This could be the starting point of a study regarding multi-component composites as metamaterials.

Acknowledgments

The research was carried out inside the CNCSIS type A Grant, code 514 /theme 1/ 2006.

References

- [1]. Jong-Kyo Kim, Yin-Wing Mai, *Engineered Interfaces in Fiber Reinforced Composites*, Elsevier, 1998.
- [2]. Caloz, C., Itoh, T., *Electromagnetic Metamaterials: Transmission Line Theory and Microwave Applications – An Engineering Approach*, Wiley-Interscience Publications, 2006.
- [3]. Winey, I. Karen, Vaia, A. R. (ed), *Polymer Nanocomposites*, *MRS Bulletin*, Vol. 32, April 2007.
- [4]. Torquato, S., Hyun, S., Donev, A., *Optimal design of manufacturable three-dimensional composites with multifunctional characteristics*, *Journal of Applied Physics*, 94, 2003.
- [5]. Torquato, S., *Modeling of physical properties of composite materials*, *International Journal of Solids and Structures*, 37, 2000.
- [6]. Milton, G. W., *Bounds on the Electromagnetic, Elastic, and Other Properties of Two-Component Composite*, *Physical Review Letters*, 46, 1981.
- [7]. Roberts, A. P., Knackstedt, M. A., *Structure-property correlations in model composite materials*, *Physical Review E*, 54, 1996.
- [8]. Liu, L., Matitsine, S. M., Gan, B. Y., Rozanov, K. N., *Effective permittivity of planar composites with randomly or*



periodically distributed conducting fibers, *Journal of Applied Physics*, 98, 2005.

[9]. Lagarkov, A. N., Matytsin, S. M., Rozanov, K. N., Sarychev, A. K., *Dielectric properties of fiber-filled composites*, *Journal of Applied Physics*, 84, 1998.

[10]. Kalamarkov, A. L., Kolopakov, A. G., *Analysis, Design and Optimization of Composite Structures*, John Wiley&Sons, 1997.

[11]. Andrei, G., Circiumaru, A., Birsan, I. G., Dima, D., *A study of electric and magnetic properties of fiber fabric based filled epoxy composites – I*.

[12]. Webster, J. G. (ed), *Measurements, Instrumentations, and Sensors*, CRC Press, 1999; Heaney, M. B., *Electrical conductivity and resistivity*, 43.

[13]. ***, STAS 6108/71, *Rezistenta placilor*.

[14]. Jackson, John David, *Classical Electro-dynamics*, Academic Press, New York, 1999.

[15]. Brosseau, C., Qu  ff  lec, P., Talbot, P., *Microwave characterization of filled polymers*, *Jornal of Applied Physics*, 89, 2001.

[16]. Kim, B., Lee, J., Yu, I., *Electrical properties of single-wall carbon nanotube and epoxy composites*, *Journal of Applied Physics*, 94, 2003.

[17]. Donglu Shi, Peng He, Jie Lian, Chaud, X., Bud'ko, S. L., Beaugnon, E., Wang, L. M., Ewing, R. C., Tournier, R., *Magnetic alignment of carbon nanofibers in polymer composites and anisotropy of mechanical properties*, *Journal of Applied Physics*, 97, 2005.

[18]. Makhnovskiy, D. P., Panina, L. V., *Field dependent permittivity of composite materials containing ferromagnetic wires*, *Journal of Applied Physics*, 93, 2003.

VIBRATION DIAGNOSIS SYSTEMS FOR A COLD ROLLING MILL MACHINE

Stefan DRAGOMIR, Silviu MĂCUTĂ, Constantin SPÂNU

"Dunărea de Jos" University of Galati
email: silviu.macuta@ugal.ro

ABSTRACT

In this work is shown the importance to use a monitoring by vibration system for a cold rolling mill machine. The using of this monitoring vibration system reduce maintenance costs, minimize the impact on operation because is monitoring the rolls, the backup rolls, the coupling shaft, the gears from power system. Another advantage is to preventing damage occurring by detecting signs of abnormalities. The accurate prediction of works parameters is essential for a product quality. Currently, a mathematical model is used. It is important to directly predict the roll force and the other parameters, to compute a corrective coefficient Using a mathematical model, we grove up the possibility to obtain a new quality for laminates strip.

KEYWORDS: Cold rolling mill, Strip, Vibration, Prediction, Undulation

1. Introduction

A rolling mill process for obtain cold thin strip, consists in four stands where the force, the speed and the intermediate thickness tension between each pair of stands is continuous monitoring.

The roll gap is the distance between two working rolls, most important variable to affect the actual output thickness of the strip. The set parameter values are dynamically adjusted as the strip thickness and tension who are measured during milling process.

The initial setting produced by the mathematical model can give errors that can usually be compensated by the real – time controller, but large errors lead to quality decline and cost increase. The installed system produced, the initial settings on the tension roll the strip speed and the force prediction values with the settings from the mathematical model.

Using a mathematical model, the mill settings are determined before a strip enters in the mill, like the work load, the roll gap for each stand is calculated, the speed in each stand (from the first stand to the five stand).

It is known that milling process is a function of many variables, with an exception – the presetting roll force-. It is essential to predict the roll force as accurately as possible. The roll force is calculated using mathematical formula based on the metallurgical and mechanical knowledge like:

$$F_m = f(H_i, H_o, T_b, R_{p0,2}, \mu, v_e, n_r) \quad (1)$$

where F_m - the roll force produced by the mathematical model.

The roll forces are influenced by deformation resistance ($R_{p0,2}$), thickness (H_i and H_o), backward and forward tension (T_b and T_f), friction coefficient (μ), and other constants. The first four factors (thickness and tension) are constant and impose.

The rolling stands press a strip of steel using upper/lower rolls to a desired thickness.

The gap between upper/ lower rolls determines how much pressure or force is applied. Force, thickness, speed and tension is measured while the strip is processed, and then for real – time control like in the fig. 1.

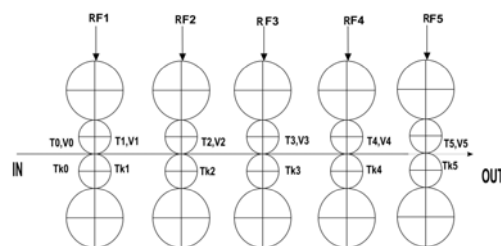


Fig. 1. Control of cold rolling mill process, with presetting in recalculation, which is related to thickness control.

The mathematical model does not take all the factors into account. The friction coefficient is known to be affected by working roll parameters such as the rolling speed, the roll surface, the oil used, etc. However, the mathematical model employs only the rolling speed in calculating the friction coefficient. The mathematical model's prediction values (F_m), against the target values (F) are selected in the time of coil processed.

The mathematical model, by definition, can employ only the factors whose exactly physical relations are understood. The parameters predictions involve many other factors whose exact relations are not well understood and the mathematical model is far from perfect.

Recent studies about the roll force tension and coil width prediction were made in two directions, first in improving the mathematical model and second in employing the neural network.

The neural networks were used to calculate the roll force with the improved prediction accuracy in cold rolling process.

- Use of neural networks improves the accuracy of roll force prediction.
- Many factors not considered in the mathematical model can easily be incorporated in neural networks.

The rolls forces, the coil tension, the coil width and the speed sheet were measured with specifically tools and than we draw the next curves by a mathematical model prediction.

The models of roll force prediction are given in fig. 2. The exception was stand (cage) no. 5, where the mathematical model made very good predictions.

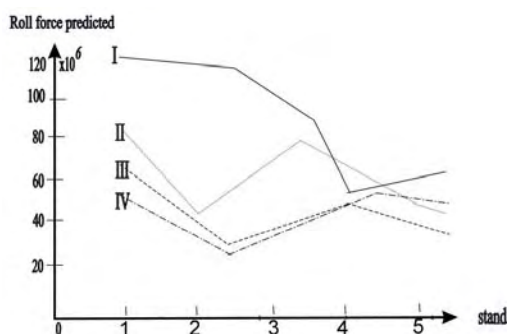


Fig. 2. The predicted values of roll force.

Those models that we show are a test pattern and are not likely to make a reliable prediction. The deviant domain approach proposed in [1] tries to identify the part of input space where the prediction accuracy of model is not expected to be good. For each input variable, we analyzed the correlation with the prediction error in order to identify the default domain (force, tension, width, speed, acceleration).

Another way for controlled the good functionary at the cold rolling mill for strip is to do a monitoring by vibration for the moving parts of mill machine.

2. Experiments on monitoring system by vibration

The configuration of the system used for measuring and recording of vibration parameter (displacement, velocity, acceleration, and frequency) is shown in fig. 3.

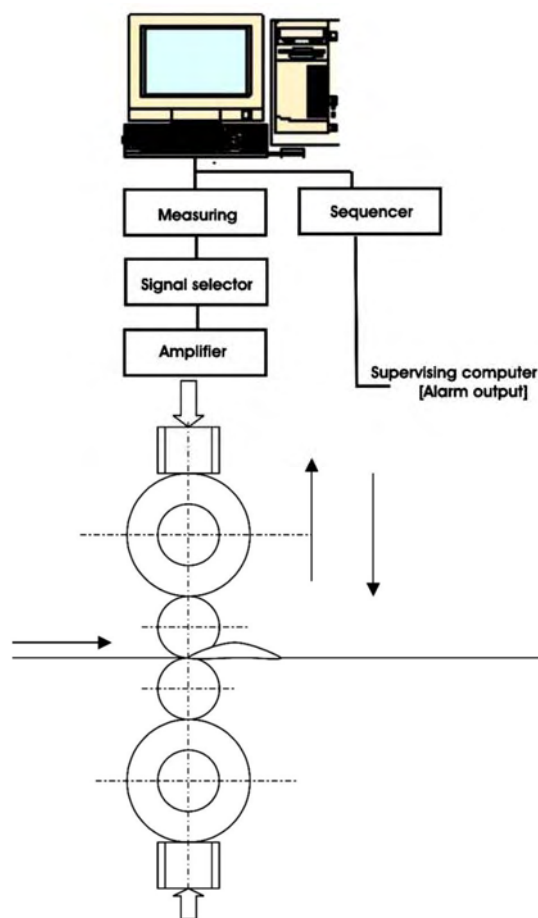


Fig. 3. The configuration of vibration monitoring system.

This system work like an alarm which automatically determines the incident who has occurred on basis of measured values and notifies the operator accordingly, a diagnostic function to estimate check times from past measurement data, and a database of apparatus repair times.

The system, displays this information graphically on a screen. Example of screens recording are shown in fig. 4.

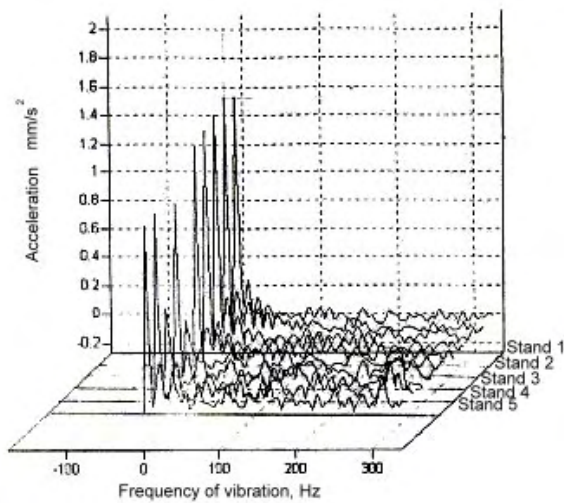


Fig. 4. Running time transition and power spectrum for five stand cold rolling mill.

In fig. 5, 6 we show (partially) the recordings by comparing the parameters of vibrations at the beginning of work period and after six month in function. Because the wear who appears in bearings, box gear, bar of coupling, the amplitude of vibration increase and determine the “out” of initially work parameters for the cold rolling mill machine. The model directly predicts all work parameters, while the corrective model produces a correct coefficient, which is then multiplied to the mathematical models prediction. Additional variables which were not used in the mathematical model were found to be necessary for the substitutive model only. The networks of parameters (forces, tensions between stands (cages), speed, can be easily retrained if necessary as all the data from the processed coils are automatically saved in a workstation located next to the process computer. The retraining period does not have to be fixed such as monthly or yearly. It will be more proper to determine it dynamically by monitoring the trend of prediction error [2].

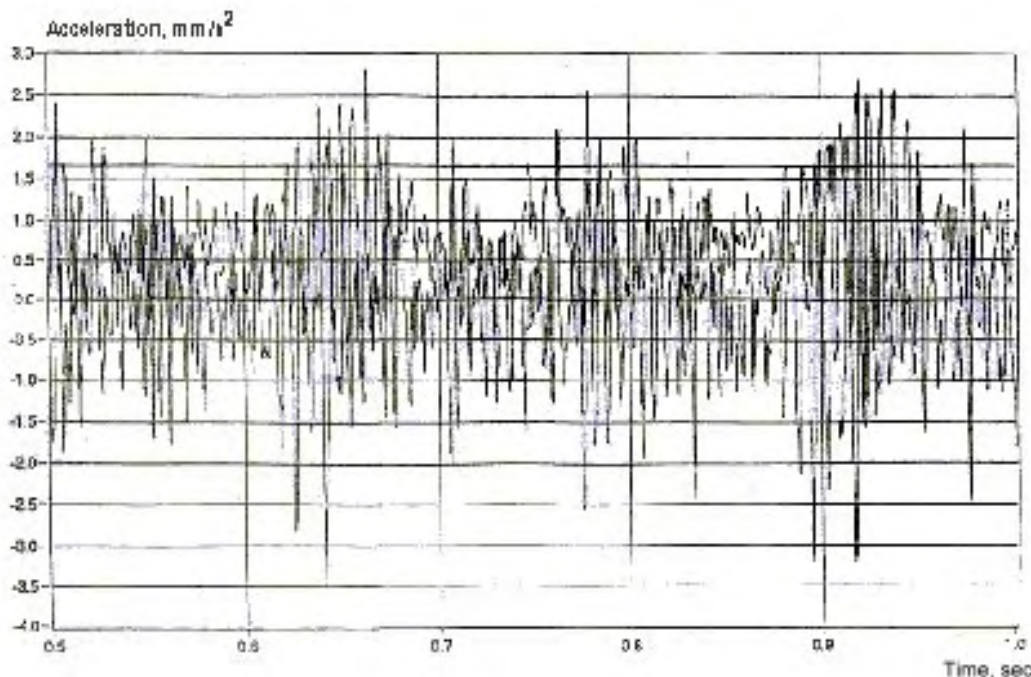


Fig. 5. The acceleration spectrum measured on the backup roll support in while of vibration (side machine).

The-network models are planned to be used in daily operation. One difficulty is to estimate the monetary savings resulting from the improved quality and decreased off-gauge [7].

Using the network of parameters-based roll force – prediction models show that the prediction

errors of the currently used mathematical model reduced by 30-50%. The substitutive model directly predicts the roll force, while the corrective model produces a correct coefficient, which is then multiplied to the mathematical models prediction.

The networks can be easily retrained if necessary as all the data from the processed coils are automatically saved in a workstation located next to the process computer. The retraining period does not have to be fixed such as monthly or yearly. It will be more proper to determine it dynamically by monitoring the trend of prediction error.

The -network of parameters models are planned to be used in daily operation. One difficulty is to estimate the monetary savings resulting from the improved quality and decreased off-gauge.

The networks of parameters (milling process force, tension between cages (stands) have a potential to improve the accuracy of the computation by substituting or correcting the mathematical model [8].

From the effectuated experiments it can conclude the fact that, the highest values for displacement, velocity, acceleration and power

spectrum (on the direction of the action system) have been recorded at the 3, 4 and 5th cages of the rolling mill machine (the causes that determinate these important values for the measured made are great tension into the strip between mill cages; high speed of strip while the milling process or the variation of those; abrupt change for the rolling mill work parameters; types or different quality for the emulsions used in work; the decrease of reduced number when the strip pass between the work rolls; unpredictability for one of work parameters.

At rolling mill's speed between 600 – 1250 m/min and frequencies of vibration measured that do not excel hadn't recorded of marks, undulations and abrupt variations of the strip thickness after milling process.

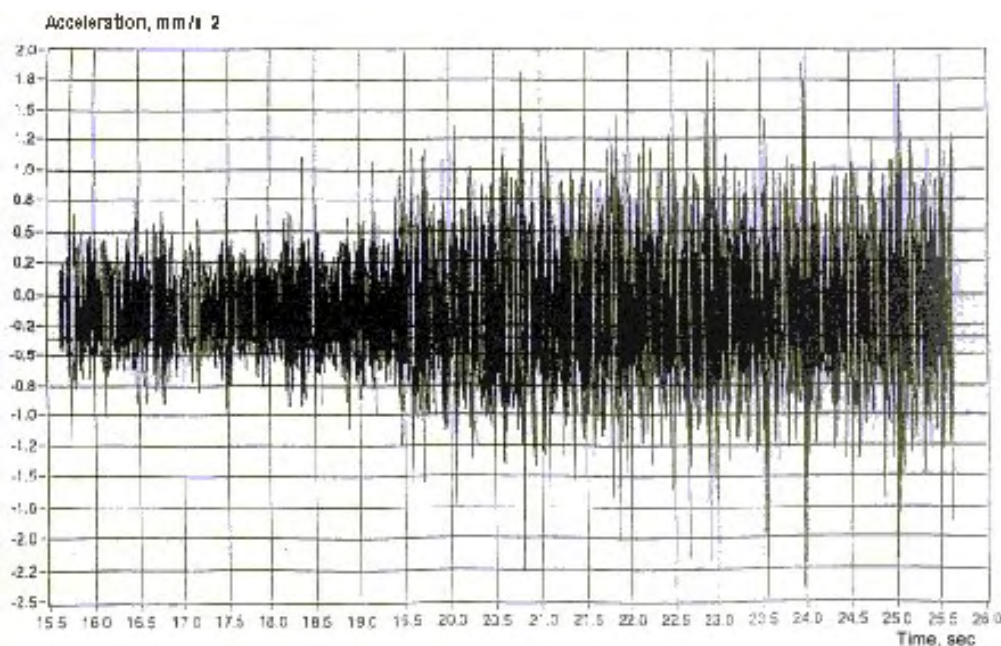


Fig. 6. Accelerations spectrum (side operator) measured in function of rolling mill.

At vibration's frequencies between 450 – 1150 Hz, we observed undulation at strip's surface with the gap between 2- 40 mm, big wear of shell of work rolls and into the bearings of work rolls.

4. Conclusions and results

The problem studied is very important for:

- the quality of surface and geometry of cold rolling strip;
- the correct command of milling process ;
- the prominence of causes and the oscillation's effects, vibrations, shocks etc. – owing the own system of rolling mill cages and the parts of kinematics action fluxes;

- the fix measures for control, decreasing, command ;

- the increase of productivity, the reduce of costs;

The vibrations are present in equipments and installations of cold rolling mill by different type. By an ample study and perform experiments – with modern gear – it result a series of aspects.

From the effectuated experiments between 2004-2005 at a number of over 200 coils of cold milling strip, which in fact were measures and vibration's analyses, the have been established the following series of characteristics frequencies:

- vibrations in series of frequency between 5-90 Hz, for coupling, couplings bars, gear boxes with defects into their bearings;



- vibrations in series of frequency between 125-300 Hz for the strip which is being milling, for the gaps of positioning system, the wears into the backup and work roll bearings, lubricant used;

- vibrations in series of frequency between 500-980 Hz, wear's afferents accentuated backup and work rolls shell of these encampments, determination the appearance of hallmark and undulation on the surface of strip.

The experiments in the functionality for rolling mill machine show the tendency of vibrations amplitude at the increase of milling speed. We record a increase of milling speed with 50% at each cages of the rolling mill, the vibration's amplitude record a increase 35 % at each cage) by the other way, at strip with small breadth and with high toughness is manifested the same tendency of increasing of vibrations amplitude, but on the other hand the strip with a big breadth and thickness, where the effect of amortization of vibration is considerable highest.

From the all experiments done it results haw actual is at the problem of science analyze by functional conditions of rolling mill machine, the

identification and the quantification of disturb factors and, finally, the modern projection, in the scope of resistance and reliability increase and diminutions of consumptions, insurance of continuing technological process and the quality of the final product.

References

- [1]. **Sungzoon Cho, Yongjung Cho, Sungchul Yoon**, *Reliable Roll Force Prediction in Cold Mill Using Multiple Neural Network*, IEE Transactions On Neural Network, 1977, Vol 8, Nr 4.
- [2]. **Bishop C.**, *Neural Networks for Pattern Recognition*. Oxford, 1995, U.K:Oxford Univ. Press,
- [3]. **Cohn D., Atlas L., Ladner R.**, *Improving generalization with active learning*, Machine Learning, 1994, vol.15 no.2, pp.201-221.
- [4]. **Pohang Iron and Steel Company Tech.Rep.**, 2nd Cold Mill Contr. Equipment (PCM part), POSCO, 1989, Korea,.
- [5]. **Lee W.**, , *Improvement of set-up model for tandem cold rolling mill*, Tech. Rep. POSCO, 1994, Res.Inst.Sci.Technol.
- [6]. **Pican N, Alexandre F. and Bresson P.**, *Artificial neural networks for the presetting of a steel temper mill*, IEEE Expert, 1996, vol.11, no1. 22-27.
- [7]. **Portman N.**, *Application of neural networks in rolling mill automation*, Iron and Steel Eng., 1995, vol.72, no.2, pp.33-36.
- [8]. **Rosen B.**, *Ensemble learning using decorrelated neural networks*, Connections Sci1996, vol.8, pp.373-384.



X-RAY DIFFRACTION RESIDUAL STRESS MEASUREMENTS FOR QUALITY CONTROL TESTING

**Constantin GHEORGHIEȘ, Alina-Mihaela CANTARAGIU,
Iuliana Valentina STASI**

"Dunarea de Jos" University of Galati
email: cgheorg@ugal.ro

ABSTRACT

This paper presents the primary difficulties which are associated with the obtaining and interpreting surface X-ray diffraction residual stress results: the surface stresses may be identical for the shot peening, nitriding and grinding parameters; many machining and grinding metal removal processes can generate local fluctuations in the surface residual stress; for many material removal and surface treatment processes the depth of penetration of the X-ray beam is quite shallow and can cause experimental error in the measurement of the surface stress. The stress distributions by conventional and abusive grinding of 4340 steel, the surface residual stresses for 5160 steel leaf springs shot peened may prohibit the use of non-destructive surface stress measurements.

KEYWORDS: XRD, Surface Residual Stress, Grinding, Machining and Shot Peening Processes

1. Introduction

X-ray diffraction (XRD) is a non-destructive and efficient analytical technique which reveals information about the crystallographic structure, chemical composition, and physical properties of materials and thin films. X-ray diffraction (XRD) methods of residual stress measurement have been widely used for forty years, particularly in automotive and aerospace applications, and interest in the use of XRD stress measurement for quality control testing is increasing. Specifications now exist requiring that minimum levels of compression be achieved by shot peening, and limiting the tensile stresses allowed on EDM'd and ground surfaces. Because of subsurface stress gradient appears difficulties in measuring and interpreting XRD surface residual stress results and limit the usefulness of surface data. The most common problems encountered in using XRD methods of residual stress measurement are related to the high precision required for measurement of the diffraction angles. XRD methods are applicable only to relatively fine-grained materials, and often cannot be applied to coarse-grained castings. The shallow depth of penetration of the X-ray beam can be a disadvantage when trying to characterize a subsurface stress distribution with only surface measurements. This paper describes the assumptions, theory and

limitations of XRD residual stress measurement as applied to the study of residual stress distributions produced by such processes as machining, grinding and shot peening. It exists three addressing the difficulties encountered in obtaining and interpretation of surface residual stress results: **I.** The surface residual stresses present on the samples are not representative of the processes which produced them; **II.** The stress (machining and grinding) practices produce variations in the plane of the sample surface; **III.** Material removal and surface treatment processes produce errors in measurement caused by the penetration of the X-ray beam.

2. Materials and methods

I. The shot peening and grinding processes produce surface residual stresses by variation of processing parameters. The stress distributions will be useful for quality control testing.

II. The metal removal processes which involving chip formations such as machining and grinding can generate pronounced local fluctuations in the surface residual stress. The deformed layer variation in the depth and magnitude and the heat input near the surface during chip formation can result in large differences in the resulting surface residual stresses. The apparent surface residual stress

measured by X-ray diffraction will be dependent upon the size and the positioning of the irradiated area. If a small irradiated area is used, the assumption of uniform stress within the irradiated area may be satisfied, and the stress variation at the sample surface will be revealed. The surface stress variation can be so pronounced as to render non-destructive measurement useless for process control. The irradiated area may be made large enough to provide a useful average surface stress; but then the assumption of uniform stress in the irradiated area may be violated. The surface stress measured will be the arithmetic average within the diffracted volume, and will depend upon the details of technique used, such as the rotation angle Ψ and the diffraction angle 2θ , irradiated area.

III. For most materials of practical interest and the X-ray used for residual stress measurement, the effective depth of penetration of the X-ray beam is quite shallow. 50% of the diffracted radiation originates from a depth of less than 10 μm . The X-ray beam is attenuated exponentially as a function of depth. The rate of attenuation is governed by linear absorption coefficient which depends upon the composition and density of the specimen and the radiation used. Any "surface" measurement is an exponentially weighted average of the stress at the surface and in the layers immediately beneath it. In developing the relationship between the observed strain in the crystal lattice and the stress at the sample surface, the assumption was made that the residual stress is constant throughout the depth of penetration of the X-ray beam. Unfortunately, for many samples of practical interest, the stress varies rapidly with depth beneath the surface, and the assumption of constant stress is violated. The result can be errors as large as 600 MPa. The sign and magnitude of the potential error is dependent upon the subsurface stress gradient; i.e., the direction and rate of change of stress with depth into the sample surface. Because the depth of penetration of the X-ray beam also varies with the rotation angle Ψ and the diffraction angle 2θ , the apparent surface residual stress will depend upon the details of the technique chosen, specifically the radiation and angles selected, if a significant subsurface stress gradient exists.

3. Results

I. In the case of shot peening, where X-ray diffraction is usually applied, the surface residual stresses are independent of the peening parameters including shot size and Almen intensity. **Figure 1** shows the similar surface results of the stress distributions produced by shot peening Inconel 718 to 6-8 A and 5-7 C intensities.

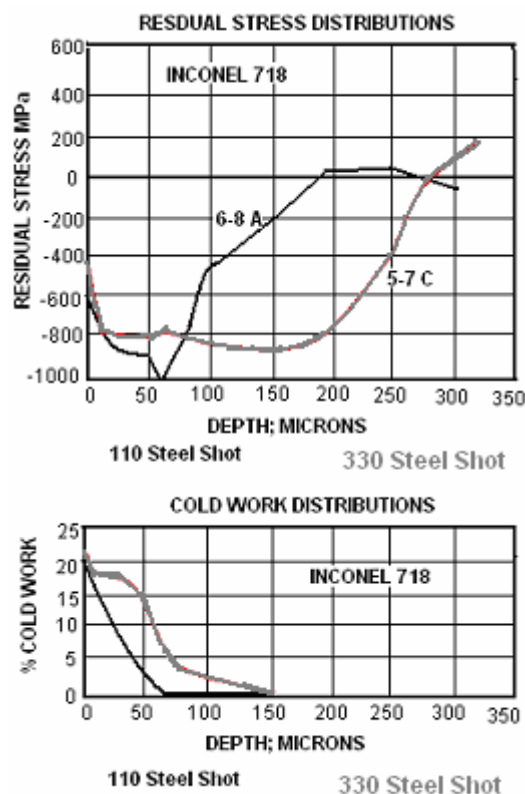


Fig. 1. Variation of the Stress Distributions with the Depth Produced in Shot Peened Inconel 718⁽⁵⁾.

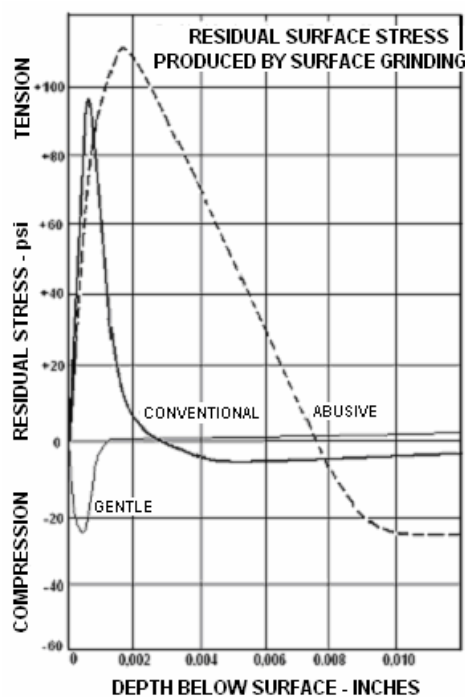


Fig. 2. Surface Stress Distributions Produced by Gentle, Conventional and Abusive Grinding Conditions in 4340 Steel.

The results indicate a pronounced variation in the depth of the compressive layers.

Grindings processes produce the surface stress independent of the grinding parameters. **Figure 2** shows the representations of 4340 steel of three kinds of grinding.

Grinding and shot peening produce comparable surface residual stresses in 8620 steel to an 18 A intensity (**Fig. 3**). It was observed that the non-destructive surface residual stress measurement cannot be used to distinguish the part which was in the ground or shot peened condition. That is why are used other cold abrasive processes such as grit blasting, wire brushing and polishing for to produce surface residual stresses indistinguishable.

A given level of surface residual stress is necessary to indicate that a critical component may have been correctly processed ^(1, 10).

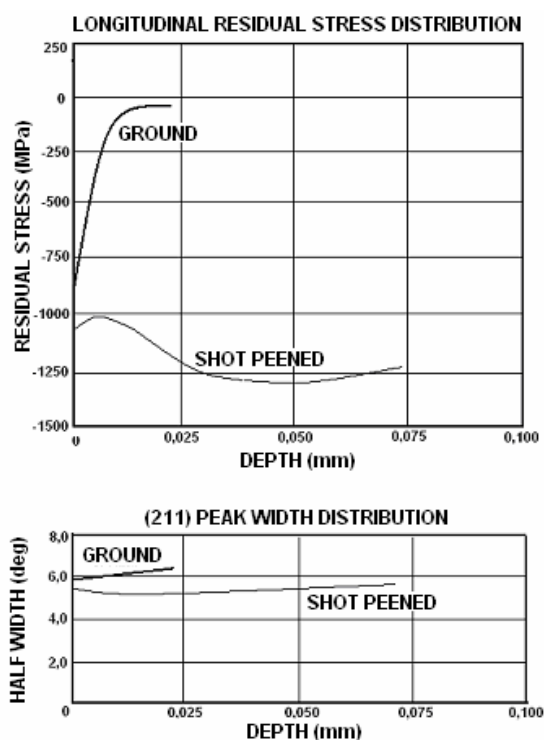


Fig. 3. Residual Stress Distributions Produced by Shot Peening and Grinding of 8620 Steel.

II. **Figure 4** shows the surface residual stress measured using an irradiated area of 12mm x 0.5mm across a 19mm wide surface of a ground 4340 steel sample. The surface stresses vary by nearly 600 MPa from a region of maximum compression near one edge of the sample to maximum tension in a burned area. The use of a larger irradiated area, plotted as a horizontal line with a length equal to that of the irradiated area, yields the arithmetic mean, as expected.

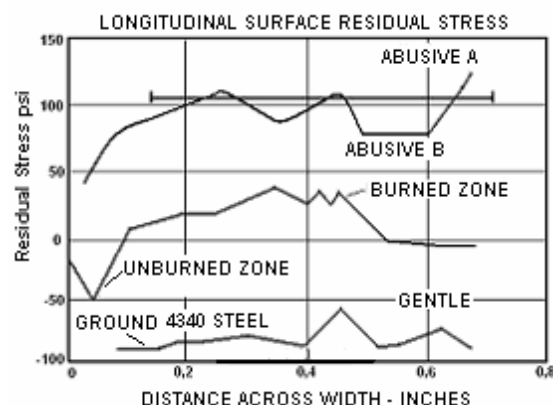


Fig.4. Surface Residual Stress Variation in Surface of Ground 4340 Steel.

Comparable variations in the surface residual stress are seen in **Fig. 5** for milled Inconel 718. Work hardening alloys often exhibit local areas of highly worked material at the sample surface.

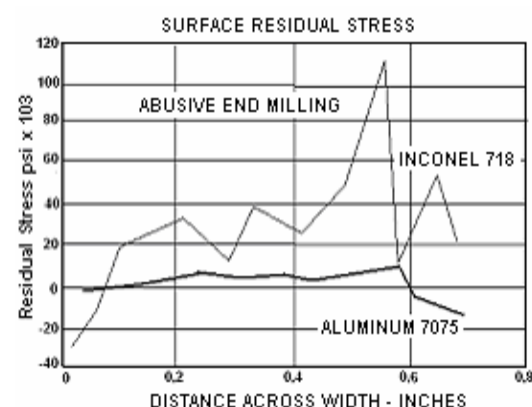


Fig. 5. Surface Stress Variation in Milling of Inconel 718 and Aluminium ⁽³⁾.

III. **Figure 6** shows examples of large subsurface stress gradients produced by two different methods of nitriding 52100 steel. **Figure 1** shows a pronounced gradient in the "hook" commonly seen at the surface of shot peening stress distributions.

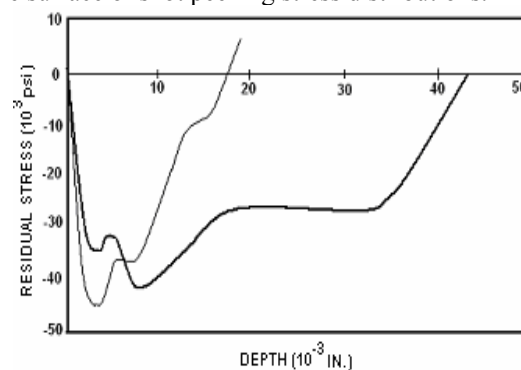


Fig. 6. Subsurface Stress Distributions Produced by Nitriding 52100 Steel ^(4, 8).

It is possible to correct for the errors caused by the penetration of the X-ray beam into the stress gradient, provided subsurface measurements are made by electro polishing to remove layers with sufficient depth resolution to accurately establish the stress gradient⁽⁹⁾. Koistinen and Marburger⁽⁶⁾ developed a method of calculating the true residual stress by unfolding the exponential weighting caused by penetration of the X-ray beam. Their often cited example of agreement between X-ray diffraction and mechanical methods of residual stress measurement in ground steel, reproduced in Fig. 7, shows agreement only because the correction was applied.

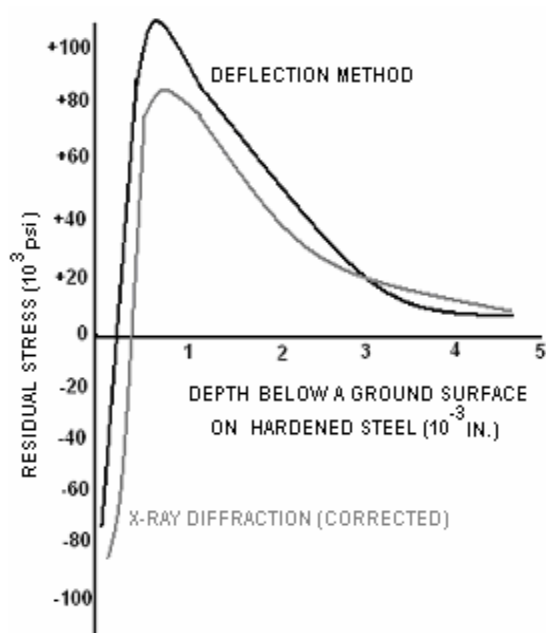


Fig. 7. Subsurface Stress Distribution in Ground Steel Measured by Mechanical and X-ray Diffraction Methods with Correction⁽¹⁾.

4. Conclusions

The limitations in the use of surface X-ray diffraction residual stress measurements have been shown to result in three areas of concern which must be considered before non-destructive surface results may be used reliably.

I. The surface residual stress measured non-destructively by X-ray diffraction is not correlated with the method of process control testing which produced the stress distribution. Subsurface stress differs significantly from the surface results.

II. Extreme local variation of the surface stress, frequently encountered on machined and ground samples, may prohibit the use of non-destructive surface X-ray diffraction residual stress measurement for quality control testing. The variability of the local surface stresses and the dependence of the results upon the measurement technique should be investigated before attempting to use surface measurements.

III. Non-destructive surface residual stress measurements cannot be corrected for errors caused by penetration of the X-ray beam into a varying stress field. The true surface stress frequently cannot be accurately determined by surface measurement alone.

References

- [1]. Gheorghies, C. , 1990, *Controlul structurii fine a materialelor cu radiatii X*, Ed. Tehnica, Bucuresti
- [2]. M. Rîpă, C. Gheorghies, L. Deleanu, I. Crudu, 2004, *X-ray Diffractometry Analysis in Rolling-Sliding Wear Tests*, Bul. Inst. Pol. Iași, Tom L(LIV), Fasc. 6A, pp.267-72
- [3]. Fitzpatrick, M.E., Fry, A.T., Kandil, F.A., Shackleton, J., 2002, NPL Good Practice Guide No. 52: Determination of Residual Stresses by X-Ray Diffraction.
- [4]. Prevey, P.S., 1987, *The measurement of Subsurface Residual Stress and Cold Work Distributions in Nickel Base Alloys*, *Residual Stress in Design*, Process and Materials Selection, ASM International, p. 11-19.
- [5]. Fry, A.T., 2002, *Evaluation of the Repetability of Residual Stress Measurements Using X-Ray Diffraction*, Measurement Note MATC (MN) 019.
- [6]. Fry, A.T., Kandil, F.A., 2002, *A Study of Parameters Affecting the Quality of Residual Stress Measurements using XRD*, ECRS 6 Paper, Coimbra, Portugal.
- [7]. Kandil, F.A. et al., 2000, *Manual of Codes of Practice for the Determination of Uncertainties in Mechanical Tests on Metallic Materials*, Project UNCERT, Standards Measurement and Testing Programme.
- [8]. C.-P. Papadatu, I. Stefanescu, C. Gheorghies, 2005, *Experimental Study of Behaviour of Some Non-Conventional Treated Steels During Friction Process*, The Annals of Dunarea de Jos University of Galati, Fascicle VIII, Tribology, ISSN 1221-4590, p. 58-64.
- [9]. C. Gheorghies, D. Scarpete, 2001, *A fast method for tribological characterisation of bearing steels*, Proc. of the Tribology-Conference, 25-26 oct.2001, Sofia, Bulgaria, p. 3-7;
- [10]. C. Spanu, C. Gheorghies, 1999, *Structural Changes in Superficial Layer During Passing from Elastic to Elasto-Plastic Deformation*, Proc. of The 3-rd International Conference of Tribology, Balkantrib'99, Sinaia, Vol I, p. 165-172;

NEW WELDING TECHNOLOGY – THE COLD WELDING ON COGGED SURFACES

Bogdan GEORGESCU, Valeriu GEORGESCU

Dunarea de Jos University of Galati, Romania

email: valeriu.georgescu@ugal.ro

ABSTRACT

Welding by cold pressing on coggled surfaces, produces the joint of a component made from an easy deformable metal by pressing on the coggled surface of a harder metal component. Different welds between aluminium (the easy deformable component) and copper, brass, steel, stainless steel (harder component, coggled on the contact surface) can be obtained. The weld is obtained only by deforming the aluminium component at a deformation rate of 20...30%. The weld tensile strength is up to 10% of aluminium ultimate tensile strength, better results being obtained for the shearing strength. The weld contact electric resistance is negligible, recommending the process for producing dissimilar elements used in electrotechnics.

KEYWORDS: Cold Pressure Welding, Aluminum Joints.

1. Introduction

Cold welding on coggled surfaces is a technology developed by researchers from Robotics and Welding Department, Dunarea de Jos University of Galati [1]. Easy deformable samples, having plane surfaces, are pressed on coggled surfaces of harder samples (Fig. 1). Of importance for joint achievement is the deformation rate of the easy deformable material.

The practical advantage of the cold welding on coggled surfaces is due to the fact that the joint is obtained only by deforming the easy deformable

sample, at lower deformation rates than in the case of classical cold welding. This aspect is illustrated in Fig. 2. At the same deformation rate, the weld was achieved only in case of pressed samples on coggled surfaces, the pressed plane samples couldn't be joined [2].

Cold welding on coggled surfaces can be achieved in the following variants:

- ⇒ direct, between two samples with different plasticity;
- ⇒ indirect, between two samples with the same plasticity, using an intermediate easy deformable material.

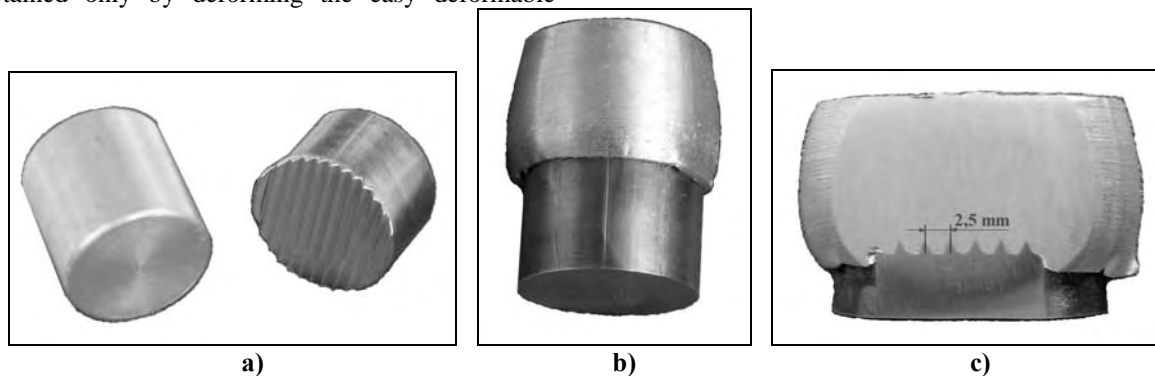


Fig. 1. Specimens' components: a) before up-setting; b) welded specimen; c) the brass cogs imprint the aluminum.

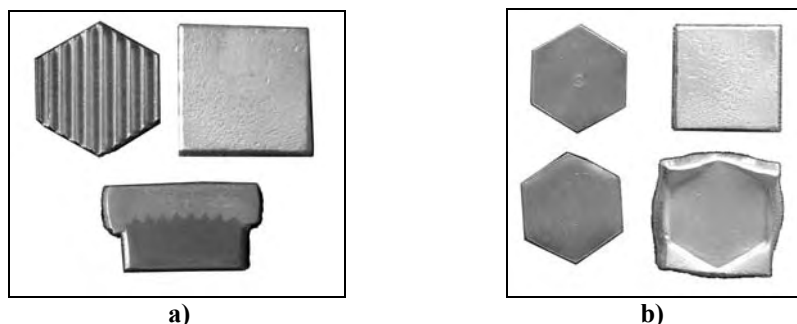


Fig. 2. Al-Cu pressed samples at the same deformation rate:
a) weld on cogged surface; b) un-weld samples on plane surfaces.

2. Direct welding

Through direct welding by cold pressing on cogged surfaces an easy deformable material is joined with the cogged surfaces of a harder metal. Were used cylindrical samples with 30 mm diameter and highs of 20...40 mm. The contact surfaces were firstly mechanically cleaned with a rotating steel-wire brush, at a rotating speed of 2800 rot/min. Immediate after the samples' cleaning, a hydraulic press was used for samples up-setting [3]. Different welded joints were achieved between aluminum (easy deformable sample) and copper, brass, steel and stainless steel (harder, cogged sample). Based on the mechanical test results, several conclusions about the characteristics of the cold welded on cogged surfaces joints were drawn.

Deformation rate. The weld was achieved only by deforming the aluminum sample, at a deformation rate of 20-30%. Higher deformation rates aren't

recommended [4]. Insufficient pressings with reduced degrees of deformation have resulted in an incomplete filling of the space between the cogs, and consequently, in a reduced mechanical resistance. This inconvenience may easily be eye-noticed. The smaller discrete unfilled spaces may be seen with the microscope or by means of penetrating liquids. Moreover, exaggerated pressings result in the deformation of cogs or in cracks. The practice has proved that the peripheral cog frequently modifies its position towards the exterior as a result of the influence of the deformed aluminum on it. Exaggerated pressing is signaled by the flaring of the components.

The cogs geometry must be correlated with the dimensions of the welding samples. In small samples case, the cog angle must be up to 45° for a pitch over 2.5 mm (Fig. 3 and 4). The double cogged joints resisted better of the simple cogged joints (Fig. 5).

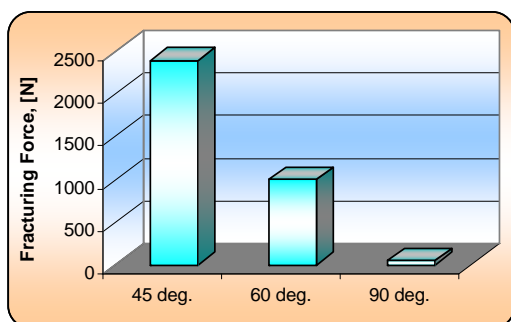


Fig. 3. The ultimate strength by the stretching of cogs with different angles.

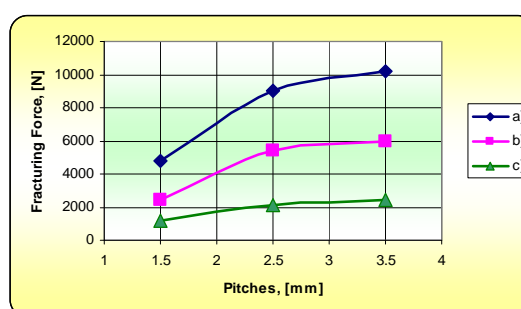


Fig. 4. The ultimate strength at different pitches:
a) by cross shearing; b) by longitudinal shearing;
c) by stretching.

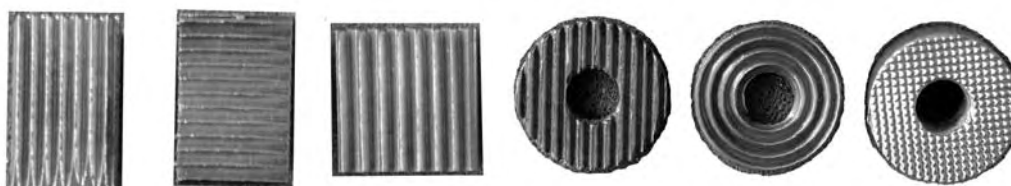


Fig. 5. Different cogging.

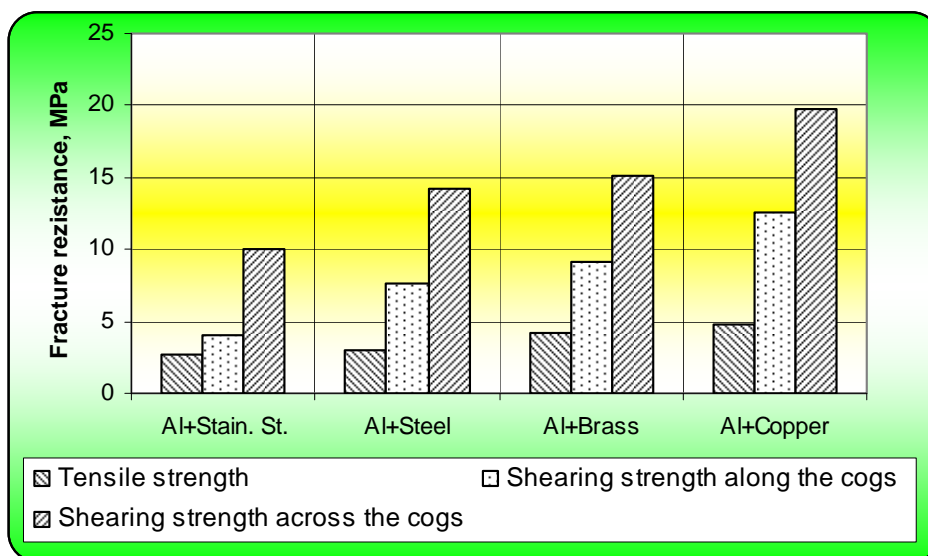


Fig. 6. The fracture resistance for different cold-welded samples on cogged surfaces [5].

The joint mechanical characteristics are: the tensile strength is up to 10% of aluminum ultimate tensile strength (50...80 MPa), double values were registered in case of the shearing strength (Fig. 6).

Thermal treatments. Components of aluminum and copper, on the one hand, and of aluminum and carbon steel, on the other, were welded by using a degree of deformation of 30 % applicable to the aluminum component only.

The lack of homogeneity in the joints (made up of materials with very different dilatation – contraction coefficients) may result in the shearing of the joint during the warming- cooling of the samples. In order to avoid such situations, a pre-compression device has been used (see Fig. 6). It is represented by

a U 120 profile with plane-parallel processed internal facets and holes, which allow the free passing of the screws threaded in the samples.

The pre-compressing is obtained by means of the screwed nut. The dimensions of the support have been chosen so as to allow its placing in the thermal-treatment furnace. The heating was performed in an electrical laboratory furnace.

The mechanical characteristics can be improved through thermal treatments; up to a 3 times increase can be obtained by joints' 30 minutes heating at 500 °C, at normal atmosphere [6].

The heating by favoring the diffusion processes lead to a constant increase in the traction resistance of the joints welded on cogged surfaces , as it may be seen in the graph under figure 8.



Fig. 7. The compression device for the welded samples and the electrical furnace.

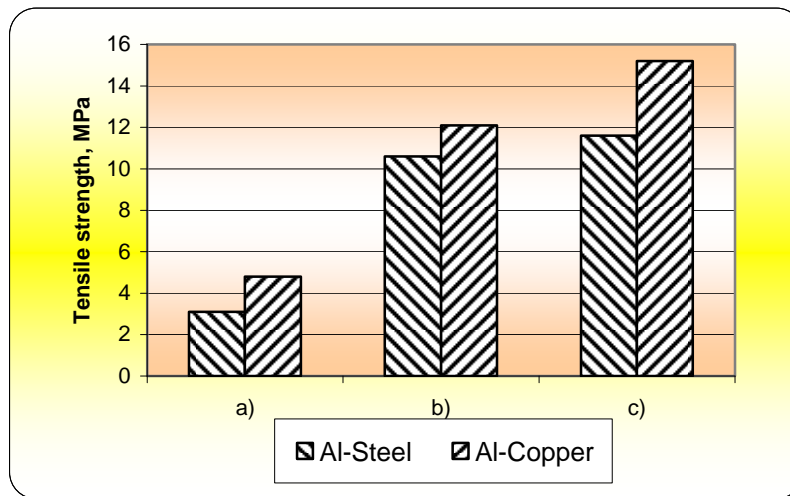


Fig. 8. The influence of the thermal treatment on the resistance of the joint: a)-without thermal treatment; b)-with free thermal treatment; c)- with pre-compressed thermal treatment.

The contact electric resistance measurements made with a CA 10 Microhmeter on the cold welded samples on cogged surfaces (Fig. 9) indicates negligible values: $1 \mu\Omega$ for Al+Copper and $6 \mu\Omega$ for Al+Steel. These values are constant for different pressing force.

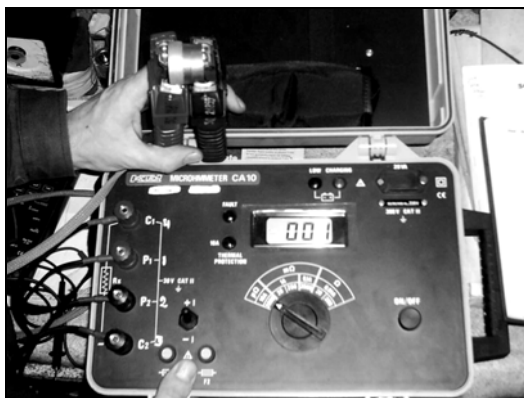


Fig. 9. Contact electric resistance measurements.

3. Indirect welding

At indirect welding, the intermediate metal must be weld with each sample, according to their plasticity. Depending on their plasticity, it can be discussed about:

- ⇒ cold welding on cogged surfaces with an intermediate easy deformable layer;
- ⇒ cold welding on cogged surfaces with an intermediate hard metal layer.

It must be underlined that the plasticity characteristic is relative, comparing with the steel, the copper is easy deformable and the steel is harder than the aluminum or lead [7].

Indirect welding with an intermediate easy deformable layer of aluminum or lead was used for dissimilar hard metals (having cogged contact surfaces) joints as copper+Al+stainless steel, brass-Al-steel etc. Figure 10 presents the brass+Al+brass joint and the copper+lead+copper joint.

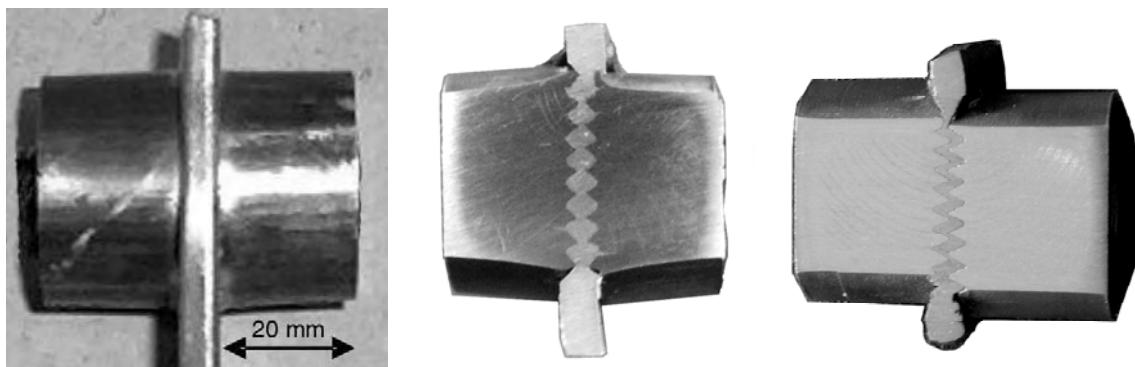


Fig. 10. Cold welding samples with Al and Pb intermediate layer.

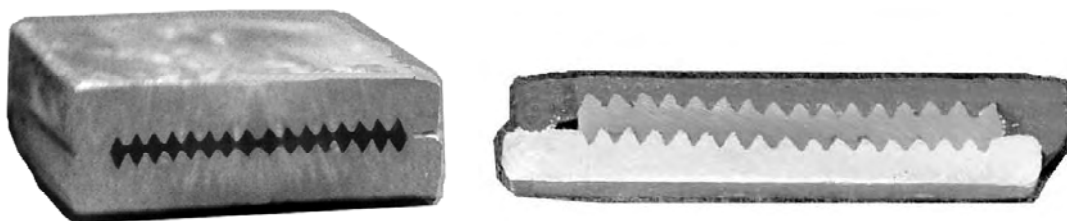


Fig. 11. Cold welded samples with intermediate cogged layer.

Indirect welding with hard metal intermediate layer. Easy deformable samples with plane contact surfaces are welded through a cogged intermediate layer of a hard metal. The intermediate sample, adapted to the easy deformable samples shape, can be obtained by chipping, forming, drawing or bending. Figure 11 presents aluminum + copper + aluminum and lead + copper + aluminum cold welded samples.

4. Conclusions

- Cold pressed welding on cogged surfaces can be obtained at lower deformation rates of the aluminum component, up to 20... 30%.
- Bi-metallic or multi-layer components can be produced by cold welding on cogged surfaces between materials with different plasticity properties.
- The joints' tensile strength can be improved by thermal treatment, with or without pressing, stimulating the diffusion process of the peripheral atoms of the two materials.
- The contact electric resistance of the cold welded samples on cogged surfaces is negligible, recommending this type of joints for the electrical engineering applications.

References

- [1]. Georgescu, V., Iordachescu, M., Georgescu, B., *Practica sudarii prin presiune la rece*. ISBN 973-31-1558-4, Editura Tehnica Bucuresti, 2001.
- [2]. Georgescu, B., *Sudarea prin presiune la rece intre suprafete zimtate (Pressure cold welding on cogged surfaces)*, Teza de Doctorat, Universitatea Dunarea de Jos din Galati, 2006.
- [3]. Georgescu, B., *Sudarea prin presare la rece pe suprafete zimtate*, Cerere de brevet de inventie nr. 2006 00639 / 10.08.2006.
- [4]. Georgescu, B., Constantin, E., Georgescu, V., *Gradul minim de deformare necesar sudarii la rece pe suprafete zimtate*. Revista Asociatiei de Sudura din Romania "SUDURA", ISSN 1453-0384, Nr 3 / 2005, pag. 23-26.
- [5]. Georgescu, B., Iordachescu, M., Georgescu, V., *Characteristic of the cold welded joints on cogged surfaces*. Intern. Institute of Welding (IIW), Proc. Intern. Conf., Prague – Czech Republic, ISSN 0043-2288, 2005, pag. 435-442.
- [6]. Georgescu, B., Iordachescu, M., Georgescu, V., *Several aspects concerning cold welding of cogged parts*. The Annals of "Dunarea de Jos" University of Galati, Fascicle XII, Year XVI, ISSN 1221-4639, 2005, pag. 5-12.
- [7]. Georgescu, B., Constantin E., Georgescu V., *Sudarea la rece pe suprafete zimtate cu material de adaos intermediar*. Revista Asociatiei de Sudura din Romania "SUDURA", ISSN 1453-0384, Nr 1 / 2006, pag. 5-10.
- [8]. Georgescu, B., *Sudarea prin presiune la rece pe suprafete zimtate*, Editura EUROPLUS Galati, ISBN (10) 973-7845-49-8 si ISBN (13) 978-973-7845-49-8, 2007.
- [9]. Georgescu, B., Iordachescu, M., Georgescu, V., *Varieties of cold welding on cogged surfaces*, The Annals of "Dunarea de Jos" University of Galati, Fascicle XII, Year XVII, ISSN 1221-4639, 2006, pag. 25-29.

EXPERIMENTAL AND THEORETICAL INVESTIGATIONS ON MODE I CRACK PROPAGATION IN NOTCHES UNDER CYCLIC LOADING

**Alexander SAVAIDIS¹, Georgios TSAMASPHYROS¹,
Dimitrios KARAGIANNIS², Georgios SAVAIDIS³**

¹ National Technical University of Athens, Department of Mechanics, Greece

² Integrated Aerospace Sciences Corporation, R&D-Department, Athens, Greece

³ Aristotle University Thessaloniki, Department of Mechanical Engineering, Greece

email: asavaidis@the.forthnet.gr

ABSTRACT

Research works regarding crack opening stresses covering various types of Mode I cracks initiated and growing in notches under cyclic loading are shown. A large number of parameters influence the crack opening behavior, i.e. material, crack length, notch geometry, and load amplitude. The experimental results indicate uniform relationships cracks in notches and build the basis for developing improved formulae and algorithms to describe Mode I crack opening behavior. Theoretical calculations of crack opening stresses based on Newman's equations have been found out to be in good agreement with corresponding experimental data determined from thin, notched specimens subjected to fatigue loading with constant amplitudes.

KEYWORDS: Fatigue, notches, crack opening stresses, fracture mechanics

1. Introduction

Classical fatigue analyses discriminate between the phase of technical crack initiation, i.e. the lifetime till to the initiation of crack lengths of about 1mm, and the phase of crack propagation. The phase of technical crack initiation, however, is itself dominated by the growth of short fatigue cracks.

Since the work of Elber [3], it is confirmed that crack opening and closure are significant parameters controlling the growth behavior of cracks. Nowadays, various analytical models have been developed to calculate opening stresses for cracks growing in unnotched and notched material specimens [1,2], [4-7], [10, 12], [15]. A first discussion and assessment of the accuracy of the most favoured relationships to describe crack opening stresses in notches has been carried out in [8]. Though the experimental database used was not sufficiently large, from the statistical point of view, the assessment revealed and quantified certain prediction inaccuracies of the analytical formulae. The present paper deals with experimental and theoretical results regarding the opening and closure behavior of cracks growing in non-uniformly stressed fields of notched specimens. For this,

experimental crack opening stress data determined from two specimen types with different notch geometries have been taken into account. The specimens were made of two materials, a fine-grained construction steel and an aluminum alloy. They were subjected to fatigue loading with constant amplitudes. In addition, theoretical results determined with Newman's crack opening stress equations [7] for unnotched specimens combined with the description of notch stress distributions according to the Theory of Elasticity are compared to the experimental ones.

2. Specimen geometry and load configuration

Two specimen types providing two different notch shapes and made of two materials have been considered in the present investigation. Figure 1 shows the geometry and the load configuration of the specimens used for the investigation.

The plates made of ductile steel FeE460 provide a central hole with a radius of $\rho=12\text{mm}$. The corresponding notch stress concentration factor

amounts to $K_t=2.5$. The plates made of steel Al5083 provide a central, quasi-elliptical notch with a radius of $\rho=4\text{mm}$ yielding a notch stress concentration factor of $K_t=3.4$. The notch surfaces were mechanically polished to avoid roughness-influencing effects on the crack initiation.

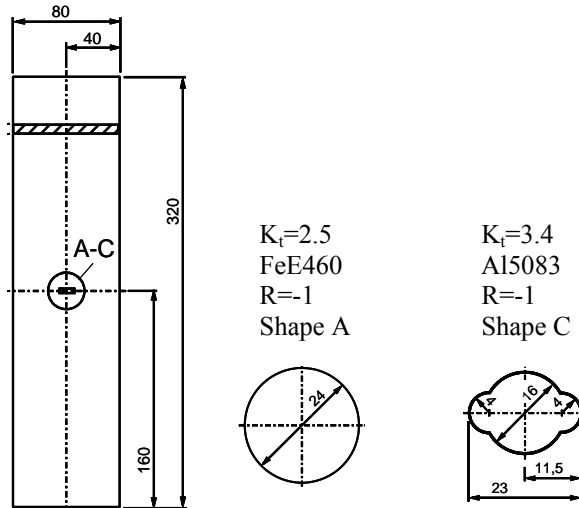


Fig. 1. Specimen's geometry and load configuration, dimensions in [mm].

The specimens were subjected to uniaxial, fully reversed cyclic loading (load ratio $R=-1$). The cracks were initiated as surface cracks at the very notch root of the specimens. They turned into corner and later into through-thickness cracks during the loading sequence.

Figure 2 illustrates the various crack types schematically. "2c" (surface cracks) or "c" (corner cracks) corresponds to the length of the crack lip at the very notch root surface, while "a" stands for the length of the crack lip at the specimen's face side.

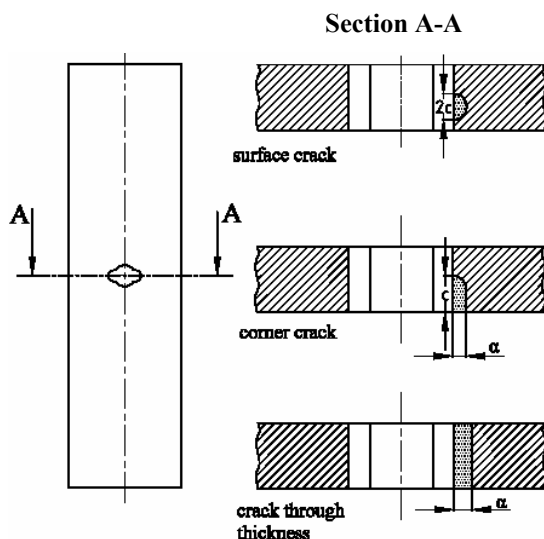


Fig. 2. Definition of the various crack types.

3. Crack opening behaviour

3.1. Measurement technique

Crack initiation can reliably be detected optically at lengths of about 0.2mm using a microscope. The measurement procedure suggested in [15, 9] was carried out to determine crack opening stresses. Figure 3 illustrates the measurement procedure.

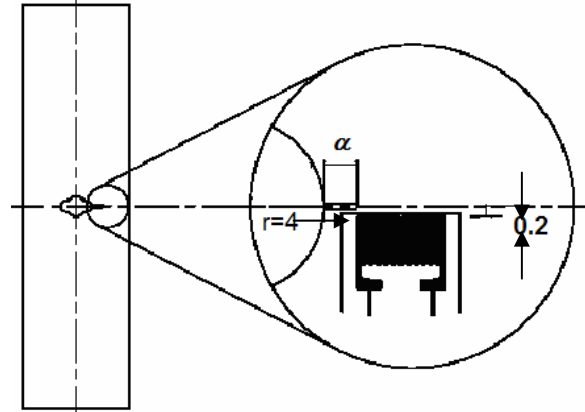


Fig. 3. Measurement technique for crack opening and closure levels.

Small strain gages with lengths of 0.6mm to 3mm were applied very close to the crack lips. The distance between the crack path and the grating of the strain gage did not exceed 0.2mm. The strain gage on the specimen surface is mounted so that the beginning of its grating is positioned directly under the crack tip.

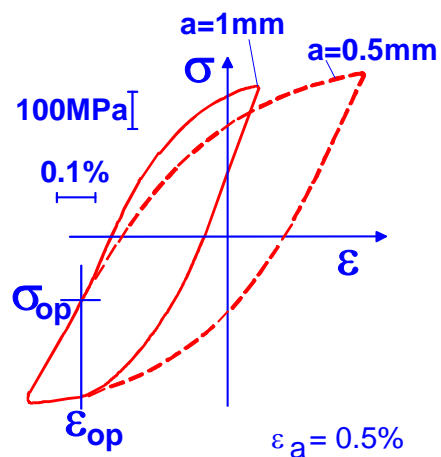


Fig. 4. Stress-strain (σ - ϵ) paths measured under cyclic loading by means of strain gages.

To illustrate the determination of crack opening stresses and strains, fig. 4 shows exemplary stress-strain paths measured during cyclic loading at crack

lengths of $\approx 0.5\text{mm}$ and 1mm at a cracked smooth specimen made of FeE460 subjected to a fully-reversed total strain amplitude $\epsilon_a=0.5\%$ [14].

When the crack is closed, its surface is able to carry stresses. Specific stress-strain behaviour is settled that obeys the Masing behaviour [5]. When the crack opens, the stresses get diverted around the crack tip, so that the local stiffness in front of the crack tip changes significantly. The change of the local stiffness reveals the crack opening point in the stress-strain diagram. The crack opening point is defined as the value, where the last contact of the crack surfaces at the crack tip vanishes. This definition is identical with the one of Newman [7], McClung and Sehitoglu [6], Vormwald [15] and Taylor [13].

It is essential that crack opening and closure occurs at the same strain level. Further experimental evidence for this behaviour is given in [9].

3.2 Crack opening stress results

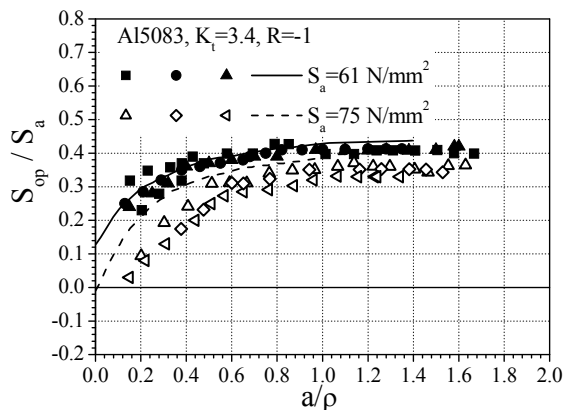


Fig. 5. Calculated and measured crack opening nominal stresses in the notch area of thin plates made of Al5083.

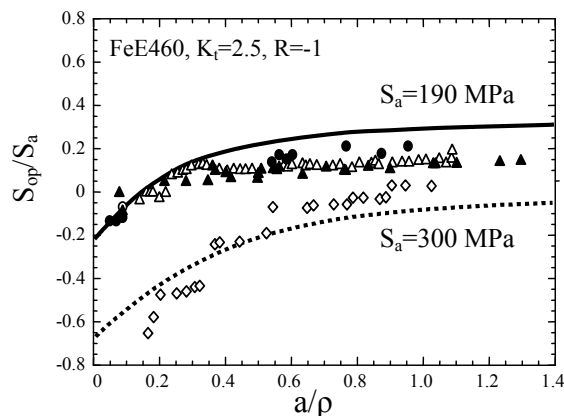


Fig. 6. Calculated and measured crack opening nominal stresses in the notch area of thin plates made of FeE460.

In fig. 5 and 6 measured nominal opening stress values S_{op} normalized by the applied nominal stress amplitude S_a are plotted versus the crack length a normalized by the notch radius ρ using marker symbols for both material/notch configurations, respectively.

The symbols in fig. 5 and 6 represent test results measured during cyclic loading at the various nominal stress amplitudes. Thereby, the results of two nominal stress amplitudes are shown for each material and notch case investigated. These figures contain results measured at the face side of the specimens, i.e. from corner and through-thickness cracks.

In the case of the quasi-elliptical, sharp notch (specimens made of Al5083), the black symbols stand for test results at $S_a=61\text{ MPa}$. The hollow symbols represent test results at $S_a=75\text{ MPa}$.

In the case of the mild notch (specimens made of FeE460), the hollow rhombs correspond to $S_a=300\text{ MPa}$, while the black symbols and the hollow triangles stand for the results at $S_a=160\text{ MPa}$.

In each case, the low S_a -level is slightly higher than the endurance limit of the corresponding specimen, where the notch strains are mainly elastic. The high S_a -level yields significant plastic strains at the notch leading to fatigue lives within the Low Cycle Fatigue regime of the corresponding specimen.

The experimental results derived from both specimen types show a clear tendency of decreasing S_{op}/S_a -values with increasing nominal stress amplitudes for particular crack lengths. This is due to the increase of the plastic deformation with increasing S_a .

In addition, the test results confirm that there is no influence of the crack type (corner, through-thickness) on the measured crack opening stresses.

Furthermore, for a particular nominal stress amplitude S_a , the S_{op}/S_a -values increase as the ratio a/ρ increases. This is due to the descending distribution of the local stress and, therewith, the decreasing plastic deformation with increasing distance from the notch root. Thereby, the crack front grows out of the highly stressed notch root into material areas with mainly elastic deformations. No significant changes of the S_{op}/S_a -values can be determined as the crack tip grows completely out of the notch area. At $a/\rho \approx 1$ a quasi stabilisation of the S_{op}/S_a -values can be observed. For higher values of a/ρ , the mechanisms controlling the crack propagation behaviour follow well-known propagation laws of long through-thickness cracks in materials under uniform stress distribution.

The solid and dashed lines in fig. 5 and 6 represent calculation results corresponding to the investigated nominal stress amplitudes for both specimens. These curves have been determined

combining the Theory of Elasticity for the calculation of the elastic stress distribution along the notch section, Seeger's and Beste's [11] approximation formulae for the calculation of elastic-plastic stresses, and the well-known crack opening stress equations of Newman [7] as slightly modified by Savaidis et al. [8] to account for the notch influencing effect.

In general, the calculation results are in satisfactory agreement with the measured ones for both notch geometries and all load levels, especially for the high ones yielding significant plastic deformations at the notch areas. This confirms the accuracy of the modified Newman's equations [7, 8] for predicting crack opening behavior in notched components. More detailed discussion of the calculation procedure and its verification is presented in [8].

4. Conclusions

The present paper deals with experimental and theoretical results regarding the opening and closure behavior of cracks growing in non-uniformly stressed fields of notched specimens. Two notch geometries and two materials have been considered in this investigation.

The test results show a similar crack opening behaviour between corner and through-thickness cracks in both notch types.

S_{op}/S_a increases with increasing crack length at a constant nominal stress amplitude S_a . It stabilizes when the crack propagates out of the notch area, i.e. at $a/p \geq 1$.

S_{op}/S_a decreases with increasing nominal stress amplitude S_a for a certain crack length a .

Newman's crack opening equations developed for un-notched specimens combined with the Theory of Elasticity and Seeger's and Beste's elastic-plastic notch approximation formulae in notches have been found out to evaluate crack opening load values successfully for both notch cases and all load values investigated.

Acknowledgement

The research activities have been co-financed by E.U.-European Social Fund (75%) and the Greek Ministry of Development-GSRT (25%).

References

- [1]. DeKoning A.U., 1981, *A simple crack closure model for prediction of fatigue crack growth rates under variable loading*, Fracture Mechanics 13th Symposium, ASTM STP 743, pp. 63-85.
- [2]. DuQuesnay D.L., Topper T.H., Yu M.T., Pompetzki, M.A., 1992, *The effective stress range as mean stress parameter*, Int. J. Fatigue, 1, pp. 45-50.
- [3]. Elber W., 1971, *The significance of fatigue crack closure*, Damage Tolerance in Aircraft Structures, ASTM STP 486, pp. 230-242.
- [4]. Ibrahim F.K., 1989, *The effect of stress ratio, compressive peak stress and maximum stress level on fatigue behaviour of 2024-T3 aluminium alloy*, Fatigue & Fracture Engng Mat. Struct., 12, pp. 9-18.
- [5]. Masing G., 1926, *Eigenspannungen und Verfestigung beim Messing*, Proc. 2nd Int. Congress Appl. Mech., pp. 332-335.
- [6]. McClung R.C., Sehitoglu, H., 1992, *Closure and growth of fatigue cracks at notches*, J. Engng Mat. Techn., 114, pp. 1-7.
- [7]. NEWMAN jr J.C., 1984, *A crack opening stress equation for fatigue crack growth*, Int. J. Fatigue, 24, pp. R131-R135.
- [8]. Savaidis G., Dankert M., Seeger T., 1995, *An analytical procedure for predicting opening loads of cracks at notches*, Fatigue & Fracture Engng Mat. Struct., 18, pp. 425-442.
- [9]. Savaidis G., Seeger T., 1994, *An experimental study on the opening and closure behaviour of fatigue surface, corner and through-thickness cracks at notches*, Fatigue & Fracture Engng Mat. Struct., 17, pp. 1343-1356.
- [10]. Schivje J., 1981, *Some formulae for the opening stress level*, Eng. Fract. Mech., 14, pp. 461-465.
- [11]. Seeger T., Beste A., 1977, *Zur Weiterentwicklung von Näherungsformeln für die Berechnung von Kerbspannungen im elastisch-plastischen Bereich*, Kerben und Bruch, VDI-Fortschritt Berichte series 18, No. 2.
- [12]. Sun W., 1991, *Finite element simulations of fatigue crack closure*, Report 159, University of Illinois at Urbana-Champaign.
- [13]. Taylor D., 1992, *The definition and measurement of crack closure*, Eng. Fract. Mech., 16, pp. 109-115.
- [14]. Vormwald M., Seeger T., 1991, *The consequences of short crack closure on fatigue crack growth under variable amplitude loading*, Fatigue & Fracture Engng Mat. Struct., 14, pp. 205-225.
- [15]. Vormwald M., Hertel O., Savaidis G., 2007, *Modelling fatigue crack growth in the elastic-plastic regime*, Bruchmechanik und Bauteilsicherheit, DVM, Dresden.



THE ANALYSIS OF THE BREAKING SUSCEPTIBILITY OF SOME FERRITIC STAINLESS STEEL

**Marian BORDEI, Aurel CIUREA,
Ştefan DRAGOMIR**

Dunarea de Jos "University" of Galati
email: mbordei@ugal.ro

ABSTRACT

The growth of the world stainless steel consumption was the result of some new domains development, of some demands and special conditions undercooling not only the adaptability of this alloy but also the remarkable range of some important properties. It has a high resistance – weight proportion, is extremely resistant at corrosion, usage and heating and it can be, relatively, easily malleable or welded.

The stainless steel are, also, excellent materials from point a view of the environment protection. The special characteristics of the stainless steel create sometimes during the working process some difficulties that can lead to the rise of the working costs. In this paper it is made an analysis of the causes of breakage of the strip made of ferritic stainless steel during the preparing operation for cold rolling and solutions are suggested for eliminating the deficiency.

KEYWORDS: cold rolling, breaking susceptibility, ferritic stainless steel

1. Introduction

The stainless steel is successful used in the products used in the chemical industry, in the alimentary industry, in construction domain, machine construction industry, medical domain, environment and transport.

The stainless steel tends to replace, in a series of products, the carbon steels, aluminum, brass or bronze. The success of the stainless steel has following major advantage: the chrome, which is part of the steel composition has a good affinity with the oxygen, forming in its presence, protection film of chrome oxide.

All the alloyed elements which form the stainless steel, especially the nickel, contribute to the significant growth of the mechanical resistance and hardness values.

The stainless steel is superior to the carbon steels from many point of view and it is preferable in manufacturing of the finishing profiles, in the first place, owing to its superior resistance to corrosion, the aesthetic qualities of this material are not neglectable – satinized or shiny, particularly elegant.

Under the conditions when the maintenance costs are low, the life span is comprised between 10 and 20 years and the influence over the environment is not harmful, the stainless steel market has an

increasing trend. If we take into account the total costs along the life span of the material, the stainless steel proves sometimes to be the most convenient as a price.

Therefore an object made of stainless steel can be bought with 25% cheaper than a chrome plated one, but with a bigger life span, to the prejudice of a cheaper chrome plated object, but with smaller life span.

2. Experiments

During the preparation for the cold rolling process of the strip coils made of ferritic stainless steel X6Cr17 (according to EN), respectively, W4016, with 0.06 %C and 17% Cr, it was remarked a high breakage susceptibility in various states (at the pickling, before the thermal treatment process, during the rolling process).

That is way, the results obtained in various states, in industrial conditions were analysed; the results are compared with those obtained in laboratory conditions (table 1).

The coils, after thermal treatment were analysed made in industrial conditions:

- a. annealing treatment: maintaining 2 hours at 810°C, furnace cooling;
- b. annealing treatment: maintaining 1 hour at 840°C, furnace cooling

Tabel 1. The coils of hot rolling strips with cold breakage susceptibility

Nr. crt.	Coil No.	The state in which cold breakage susceptibility was noticed
1	265.065	while pickling
2	273.555	while pickling
3	228.290	before the thermal treatment
4	215.664	while pickling
5	265.058	while pickling
6	321.667	before the thermal treatment

The chemical composition of the ferritic stainless steel 10Cr170, show that the analyzed coils is placed in the limits of the prescribed chemical composition through standards for this steel mark.

The values of the hardness for the analyzed coils are presented in table 2 and the chemical composition in table 3. Measurements on groups of three coils were made for each coil. In the table being presented the medium values of three measurements made on every coil.

Table 2. The hardness of the analysed coils

Coil No.	Hardness, HV		
	Initial state	After the thermal treatment type A	After the thermal treatment type B
265065	375; 386; 388	213; 216; 216	215; 216; 218
273555	264; 255; 256	172; 172; 170	172; 173; 170
228290	394; 407; 388	158; 180; 184	179; 178; 150
215664	390; 247; 322	184; 184; 184	133; 144; 143
265058	295; 265; 288	173; 165; 164	184; 177; 175
321667	277; 267; 284	171; 168; 167	180; 188; 189

2.1. Bending behaviour

The bending was made on punch of 10mm at an angle of 90° (fig.1), on coil under thermal treatment in laboratory furnace at the temperatures and maintenance period previously presented. The results of bending test are presented in table 2.

Fig.1. Aspects of breakage at the bending stress for the tests prelevated from coils without thermal treatment; (the punch diameter– 10mm).



Tabel 3. Chemical composition

Coil no.	State	C	Mn	Si	S	P	Ni	Cr	Mo
265065	lich.	0,05	0,50	0,15	0,015	0,025	0,34	17,40	-
	prod.	0,07	0,82	0,24	0,015	0,027	0,70	17,10	-
273555	lich.	0,06	0,93	0,55	0,013	0,023	-	16,60	-
	prod.	0,08	0,77	0,36	0,017	0,024	0,26	17,00	0,110
228290	lich.	0,04	0,85	0,27	0,014	0,022	-	17,00	-
	prod.	0,08	0,87	0,30	0,016	0,024	0,33	13,95	0,011
321667	lich.	0,07	0,33	0,46	0,016	0,023	0,10	16,25	-
	prod.	0,07	0,67	0,74	0,016	0,027	0,24	16,80	-
215664	lich.	0,04	0,56	0,81	0,013	0,022	-	16,88	-
	prod.	0,07	0,76	0,36	0,017	0,023	0,27	17,10	0,11
265058	lich.	0,07	0,50	0,33	0,012	0,024	-	17,75	-
	prod.	0,08	0,76	0,36	0,017	0,023	0,27	16,80	0,4

From the analysis of the data presented in table 3, we have drawn the following conclusions:

a. in initial state the coils present an accentuated susceptibility at bending only coil 2 being unbroken from three tests;

b. after annealing at 840^oC (with maintenance of 1-12 hours) or at 810^oC (for 2-12

hours) the tests from all the 6 coils analysed have not presented sensibility of the breakage of the bending test;

c. after annealing at 810^oC with maintenance period of 4 or 8 hours – three coils presented a greater susceptibility by a rise of the hardness (table 4).

Table 4. The hardness variation function of annealing thermal treatment parameters

Coil no.	The value of the hardness after the annealing effectuated in mentioned conditions [HB]							
	810 ^o C 2h	810 ^o C 4h	810 ^o C 8h	810 ^o C 12h	840 ^o C 1h	840 ^o C 4h	840 ^o C 8h	840 ^o C 12h
265.065	216	333	376	287	218	-	234	244
273.555	171	166	184	204	173	-	165	166
228.290	176	184	246	200	173	164	187	193
215.664	184	180	173	166	156	159	167	183
265.058	167	167	165	166	181	-	172	169
321.667	169	165	167	178	189	-	-	169

2.2. Metallographic analysis

1. The coils in the thermal treatment in industrial furnace state

The coils from the coils in rolling state, respectively, 228290 coil no. and 231667 coil no present a great quantity of ferite with scale pitted, resulting from the austenite transformation at the cooling of the strip during the rolling process or after quantity of ferite with smooth surface (fig. 2 - 228290 coil no. and fig. 2 - 231667 coil no.).



Fig.2. Microstructure 228290 coil no. (rolling state).

Attack: oxalic acid 10% magnify: 500:1.

The carbure quantity is relatively small in 228290 coil no. (fig. 2), fact that proves on the one hand heating for the rolling process at temperature high enough for the dissolving of the carbide (1050^oC-1100^oC) and, on the other hand, at the cooling process, the crossing with a high rate of the temperatures domain where the carbides precipitate intensely. In 231667 coil no. (fig. 3) the quantity of precipitated carbides is bigger, fact that shows that in case of this coil, the cooling rate during and after rolling was smaller.



Fig.3. Microstructure 231667 coil no. (rolling state).

Attack: oxalic acid 10%; magnify: 500:1.

2. The coils in the thermal treatment in laboratory furnace state

a. The coils 3 and 6 have, after annealing at 810^oC or 840^oC with maintaining period for 2-12

hours, presents, also, a microstructure with elongated and very fine grains (size 10-11) and a great quantity of precipitated carbides, both on the grain limit, and in side them (fig.4 – 228290 coil no.) and fig. 5.a, b –

231667 coil no.). But, it has been found that inside the ferrite grains with smooth surface (initial ferrite not turned into austenite during the heating for the rolling process) the quantity of precipitated carbide is smaller in ferrite grains with scale-pitted surface (ferrite resulted from the transformation of the austenite during the cooling process) explainable by the fact that the austenite, at the heating temperature for the rolling process (1050-1100°C) has dissolved in

itself a much more content of carbon (about 0.12%) than the ferrite not turned into austenite (about 0.12%). In this case, substantial structural modifications were not found, at the same time with the variation of the annealing temperature from 810 to 840°C or at the same time with the growth of the maintenance period from 2 hours to 12 hours (comparatively, fig.4.a and 4.b).



Fig.4. Microstructure 228290, coil no. (laboratory thermal treated: annealing 2 hours at 810°C).
Attack: oxalic acid 10%, magnify: 500:1.

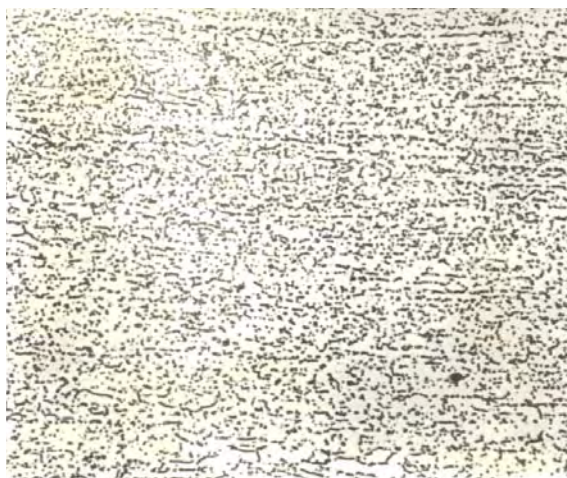


Fig.5. Microstructure 231667 coil no. (laboratory thermal treated):
a. annealing 2 hours at 810°C, **b.** annealing 12 hours at 810°C.
Attack: oxalic acid 10%, magnify: 500:1.

3. Results and discussions

The analysis of the test results correlated with some data from the specialised literature concerning the phase transformations at the heating and cooling processes of the ferrite stainless steels with 17%Cr, allow to be made the following findings regarding the causes that provoke the increased breakage susceptibility of the hot rolled strips during the preparation operations for the cold rolling:

3.1. The high hardness of the rolled state steels (320-420 HB), determined by the high hardness of the ferrite obtained from the austenite transformed during the cooling process (about 480 HV, compared with about 260-280 HV on the ferrite not turned into austenite at the heating for the rolling process).

Connected with these things, the following aspects are mentioned:

a. The quantity of austenite obtained at the heating for the rolling depends on the content in alloying elements (Cr, Si) and gamma-generators (Ni, C, N,



Mn) and the heating temperature. At the heating temperature, at which the maximum quantity of austenite (cca. 1100°C) is obtained, the austenite quantity can vary, for the ferrite steels with 17%Cr, between about 30% (the case of maximum content in alfacene elements Cr and Si) and about 60% (the case of minimum content in gamagene elements C și Mn). In the case of the coils analysed, the echivalent content in Cr is, as a rule, over 17%, fact that ensures the premise of forming of a maximum 30-40% austenite at the heating for the rolling process. With the exception of 228290 coil no., where, the content of Cr echivalent of only 14.40% determined the appearance in the microstructure of a quantity of about 90-95% austenite formed at the heating for the rolling process varies relatively with the variation of the temperature between 1000-1150°C, in such a way that there is no practical possibility of decreasing the quantity of austenite through the variation of this technological parametre. It follows that, in order to obtain a smaller quantity of austenite at heating (with unfavourable consequences by the harness of the cold rolling stip) the steel must be elaborated with content in Cr of 17-17,5% and in Si of 0,40-0,60% and, respectively, C of 0,04-0,07% and in Mn of 0,4-0,6%, reducing at the same time the content in N at minimum possible.

b. The austenite obtained at the heating from the rolling process is transformed at the cooling during the rolling process and after cooling in scale-pitted ferrite with massive precipitation of carbides and the formation of eutectoid. But if the cooling during the rolling process and after the rolling process is achieved with high speed (intense spraying with water during the rolling process finishing the rolling process at the low temperature, tranformed partially in ferrite and partially in martensite, the respectiv steel belonging to the ferrito-martensite steel class (diagrama Schaeffer). The fact that at the hot rolling strip process of the steel with 17% Cr the partially transformation of the austenite in martensite is produced, this fact is demonstated by the big hardness of the so called „scale-pitted“ ferrite; the ferrit had micro-hardness of 48HV. The high rate of hot rolling strip is proved, supplimentary, by the absence of the precipitated carbides in big quantity (fig.1), and by the fact that the ferrite grains remain strongly lengthened (unrecrystallised) and size 10-11 (very fine). Technologically, it is necessary to finish the rolling process at a high temperature, in the limits recomanded for this class (730-770°C), the rolling process at a higher temperature (1100°C) can, also, start taking into account that in the specialised reference materials for similar steel (AISI 340) it is prescribed as an interval for deformation temperature 1125-815°C. At the same time it is necessary to avoid the cooling of the strip during the rolling process

diminishing as much is possible the water flow capacity for cooling the rolls and, respectively, of the unscaling.

c. Fact that, in the hot rolling strip practice it is possible to obtain some strips with relatovelly low hardness (240-260 HB, in comparison with the hardness of 320-420 HB of analised rolling strips) and with smallsensibility at the strip breakage during at uncoiling process, fact that was stated at the analysis of the rolled strips (without annealing treatment).

3.2. *The very fine grained (size 10-11)* and the absence, in majority of cases, of the recrystallisation, and the precipitated carbures show that the final rolling temperature it too low and the cooling rate during the rolling process and after coiling is relatively high. It results that from this point of view it is necessary previously mentioned in order to avoid the partial transformation of the austenite in martensite (higher temperature of begining of rolling and final rolling temperature, lower cooling rate).

3.3. *The inadequate behaviour of the bending test* of the coils drawn from some coils thermal treated in the industrial furnaces as well as strip breakage during their uncoiling in the technological operation are determined by the incomplete efectuation of the annealing process in addition to some technological aspects (mentioned at the 3.1. and 3.2. points). This fact was aproved by diminishing hardness from about 260-420 HB, on coils from the coils industrially, thermal treated to 165-220HB on coil.s thermal treated in laboratory furnaces (table 2 – annealig 2 hours at 810°C). Efectuation of annealing process in laboratory furnaces at 810-840°C, for a maintance period of 2 hours, ensured a sensible diminishing of the hardness and an inadequate behaviour at bending test fact that leads to the adoption of necessary measures for achieving a full annealing in the industrial furnaces.

References

- [1]. Adrian, M., *Tehnologia laminării*-Editura Tehnică, București, 1977
- [2]. Geru, N., *Metallurgie fizică*, Ed. didactică și pedagogică, București, 1981
- [3]. Geru, N., *Teoria structurală a proprietăților metalelor*, Ed. didactică și pedagogică, București, 980
- [4]. Geru, N., *Materiale metalice. Structură, proprietăți, utilizări*-Editura Tehnică, București, 1985
- [5]. Kaspar, R., The Influence of Thermo mechanical Treatment on the Transformation Behaviour of Steels, *Steel Research*, 6/1994, pag. 242-247
- [6]. Kulika, V., Zitka, A., *Aplicarea metodelor moderne de calcul pentru calculele termice in produsele laminate*, Rutnicke listy, R.S.Cehoslovakia, nr.6/1981, pag. 386-390
- [7]. Slesar, M., *Aspecte microstructurale ale proceselor de deformare și de rupere*, Neue Hütte, 12/1989, pag. 450-453
- [8]. Trușculescu, M., Ieremia, A., *Oțeluri inoxidabile și refractare*-Editura Facla, Timișoara, 1982
- [9]. Ursache, M., Chircă, D., *Proprietățile metalelor*-Editura Didactică și Pedagogică, București, 1982.

REDUCTION RATE OF REMANENT STRESS IN THERMAL SPRAYING DEPOSITIONS BY SHOT PEENING

Leonard TEODORU, Valentin MIHAILESCU

Fundatia "Prof. Constantin Popovici" Bucharest
email: lteodoru@gmail.com

ABSTRACT

Thermal electric-arc spraying coatings are widely utilized both to get new parts and to repair the used ones. Just like with the other thermal spraying procedures, the thickness of these coatings is limited by the level of the internal stresses developed in the depositions. The paper presents an indirect method of measuring these internal stresses consisting in metal spraying the surface of a steel strip and then measuring the deflection of the respective strip curvature. The second part of the paper shows a method of reducing remanent stresses by making use of spherical steel shot peening.

KEYWORDS: Remanent stress, Shot peening, Thermal spraying

1. Measurement of remanent stress in the depositions carried out by thermal spraying

Remanent stress is stress existing in a solid body in absence of exterior stress [1] [2]. As a rule, remanent stress is generated in three ways: thermal stress (as a result of non-uniform extension or contraction because of differences in temperature, cross section and volume); structural stress (produced by suppressing volume changes specific to heating or cooling transformations); operational stress (introduced as a result of mechanical action during casting, deformation, welding, cutting).

Remanent stress falls under three categories: macroscopic, microscopic and submicroscopic or reticular

The coating technology by thermal electric-arc spraying is now widely utilized to repair the used parts or to become preventively coated the new parts in order to increase their reliability. Just like with other thermal spraying procedures, the deposit thickness is limited to the level of the internal stresses developed in the deposition.

It is well-known that the most defects emerging at the parts coated by thermal spraying appear when exceeding the accepted values of the deposit remanent stresses during the spraying process, mechanical working or exploitation.

A simple method for determining the remanent stress, method which might be used in any thermal spraying workshop, is that consisting in performing a

deposition on a steel strip and then measuring the amount of deflection of the respective strip.

The condition that the sample must meet is to be elastic so as not to appear remanent deformations which could distort the results of the measurements, and concerning its section and length, respectively, the elasticity is needed to allow elastic deformations measurable by ordinary control means (micrometer, comparator).

Knowing the relation existing between stress (σ) and deformation (ε), $\sigma = E\varepsilon$, and between specific deformation (y) and radius of curvature (ρ), we may write [3]:

$$\varepsilon = \frac{y}{\rho}$$

$$\text{where: } \sigma = E \frac{y}{\rho}; \rho = \frac{l^2 + 4f^2}{8f}; y = \frac{g}{2}$$

$$\text{That leads to: } \sigma = 4E \frac{\rho f}{l^2 + 4f^2}.$$

Simplifying and admitting an error of less than 1%, the formula becomes [4]:

$$\sigma = 133,75 f \left[N / mm^2 \right].$$

The spraying parameters conditioning the heat amount of the melt particles influence directly the remanent stresses [6] [7]. Therefore, the small particles will lose more heat during flying and thus, the heat transfer at the base surface level will be less.

The diminution of transferred heat amount entails the reduction of stresses in the layer.

The increase of the air pressure enhances the fineness of the particles what leads to decrease the remanent stress. The increase of the voltage determines the increase of the particle temperature and consequently, this leads to high stresses. The spraying distance is inversely proportional to the temperature at which the particles reach the work piece, and therefore also to the stresses induced in the layer.

In addition to the remanent stresses developed during the thermal spraying, as a result of the reasons presented above, there are also another category of stresses induced due to the phase changes during the solidification and cooling of the deposition.

The volume modifications associated to the phase transformations which occur at high temperature, tend to be equilibrated by tensions causing plastic deformations.

The present method is exact and efficient, being able to be applied in any specialized metal spraying workshop, and allows, when the spraying conditions are different from those under which the tests were made, to perform spraying tests and determine optimum working parameters. It is also possible to use for spraying some other materials that have not been tested or have uncertain composition.

First, the initial deflection was measured by means of a comparator device, and then the first deposit was sprayed up to 0.1 mm in thickness. The amount of deflection was measured again and then other depositions of 0.1 mm in thickness were performed, always making measurements of deflection for each one. The data obtained were used to trace diagrams and to determine the calculation formula for the function $\sigma=ks$.

The temperatures of the work pieces were measured making use of a precision pyrometer – HPA Carl Zeiss Yena type ranging from 0°C to 900°C and owning a measurement precision of 1 %.

Each test was made on there samples sprayed under identical conditions with a TEROSPRAY-E3 metal spraying plant.

Till now, there were tested the following categories of materials: carbon steel, alloy steel, mild non-ferrous materials (aluminium, copper, brass), hard non-ferrous materials (bronze, Cu-Ni alloys). It was analyzed the influence of the following factors on the amount of the remanent stresses existing in the deposits: voltage (V), air pressure (bar), spraying distance (mm), work piece temperature (°C).

The curve charted after performing the measurements on strip-type samples, while the deposit thickness increases, presents a straight line with a high slope for the first 0.1 mm deposits followed by another straight line of smaller slope for

the deposits of up to a 0.8...1.0 mm thickness. It found that the remanent stresses increase uniformly together with the increase of the deposit thickness (fig.1).

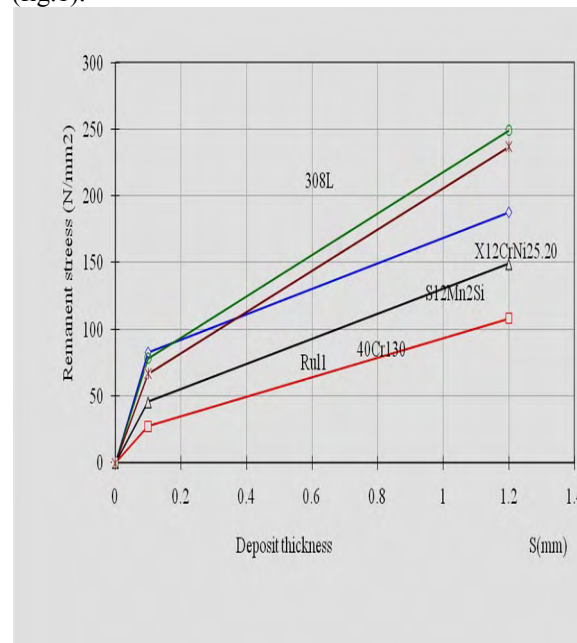


Fig.1. Diagram of remanent stress at the base of deposition –deposit thickness obtained by electric arc for the tested materials.

2. Reduction of remenent stresses in the depositions carried out by thermal spraying

Depending on the material and the deposit thickness, the methodology establishes the technological parameters of shot peening hardening so as to make sure the reproducibility of the testing results and the diminution of the remanent stresses of 30 %, at least.

To reduce the remanent stresses in the coatings obtained by thermal spraying it was used the stress relieving method by shot peening.

Shot peening is a superficial hardening procedure applied to metallic workpiece surface.

This is performed by bumping spherical metallic shots upon work piece surface, these shots being highly speed ejected by some turbo blades or an air-compressed jet.

After performing the depositions by metallizing for the materials indicated above, there were measured for each sample the initial and final deflections, the total deposition thickness as well as the tension stress at the base of the deposition according the final deflection.

The duration of hardening between two measurements is chosen depending on the material,

respectively on its capability to accumulate compressive stresses during shot bumping.

Based on those measurements the diagrams σ - t_a , meaning the variation of remanent stress in relation to hardening duration were charted (fig.2).

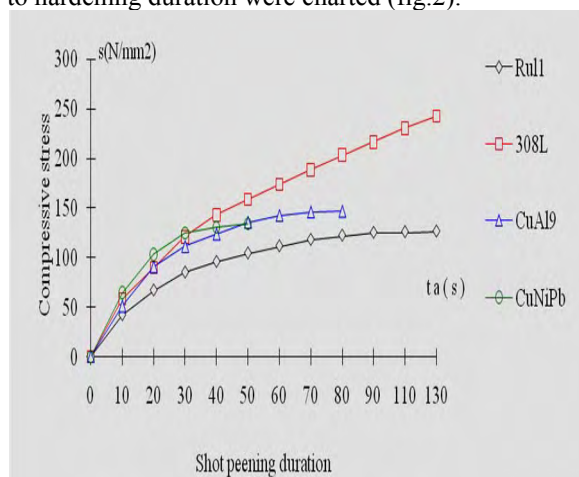


Fig. 2. The variation of remanent stress in relation to hardening duration.

The shot peened surfaces improve their appearance becoming smoother, this feature being very important for these surfaces which are not going to be machined after that.

It was also determined the diagram depicting the deposit thickness reduction according to the shot peening duration (fig.3); in this diagram can be noticed the time when the saturation phenomenon appears (continuing to bump shots on surface doesn't produce significant compressing stresses in the deposit anymore).

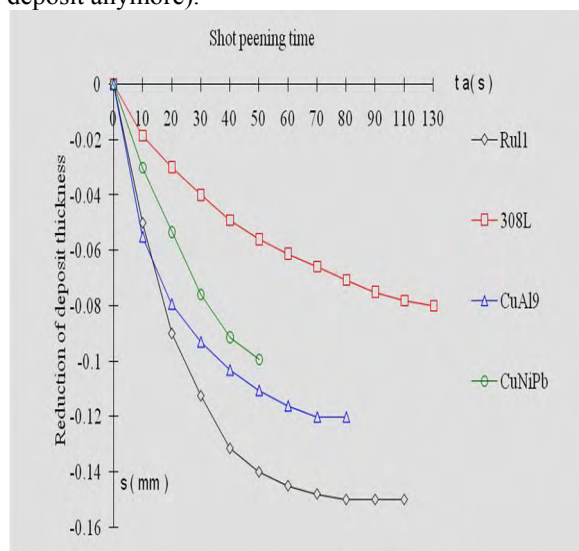


Fig.3. The diagram depicting the deposit thickness reduction according to the peening duration.

There were also determined the specific shot peening durations (t_a) what represents the shot peening duration per surface unit (cm^2). This unit is needed to make comparison among different materials and to apply stress relieving by hardening to real workpieces.

3. Reduction rate of remanent stress and compaction rate of thermally sprayed deposit

The mechanical treatment of hardening by shot peening of the metallic depositions surfaces obtained by thermal spraying entails the modification of some of their physical-mechanical properties, such as: porosity reduction, mass density increase, remanent stress reduction by inducing compressive stresses. These changes have as effect the following: increase of corrosion resistance of the coatings (stainless steels and non-ferrous materials) due to the decrease of permeability, mass density increase, deposition hardness increase, fatigue strength increase.

Logically, these modifications influence the tribological properties of the antifriction materials applied by metal spraying.

The values of stress relieving duration and of remanent stress were determined for each tested material.

These values were used to chart two diagrams.

The first diagram represents the variation of the shot peening duration for tested materials in relation to the stress relieving percentage (fig.4).

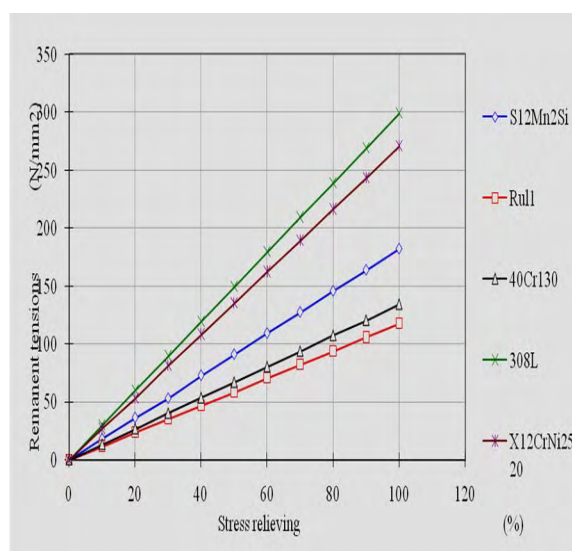


Fig.4. Variation of remanent stress to stress relieving percentage.

The second diagram depicts the variation of the remanent stress for each tested material in relation to the stress relieving percentage (fig.5).

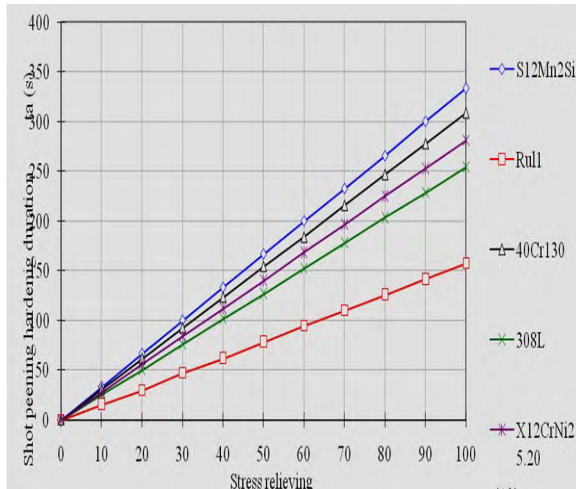


Fig.5. Variation of shot peening hardening duration to stress relieving percentage.

In the two diagrams, the variation of the shot peening duration and of the remanent stress to stress relieving percentage is linear, the differentiation being made by the chart slope given by the hardening level of the depositions. The two diagrams are useful when, for a coating material, we need to know exactly the shot peening duration required to reach a certain stress relieving degree.

From the analysis of the diagrams [4], $\sigma = f_1(t_a)$ and $S = f_2(t_a)$, we can define the parameters K_1 and K_2 [5] for the two zones of proportionality, where:

K_1 - reduction rate of remanent stress in the deposit coated by electric-arc spraying (N/mm²s);

K_2 – reduction rate of deposit thickness coated by electric-arc spraying (N/mm);

S_d – deposit thickness (mm);

S_{rg} - thickness reduction (mm);

t_d – coating duration (s);

t_e - shot peening hardening duration (s);

p_d - stress relieving percentage (%).

$$tg\alpha = K_1 = \frac{\sigma_t}{t_d}$$

$$tg\beta = K_2 = \frac{S_{rg}}{t_d}$$

$$tg\gamma = K_3 = \frac{\sigma_t}{S_d}$$

4. Conclusions

Concluding, we may say that for these coating materials the shot peening represents a technological possibility to increase the operating durability of the depositions performed by electric-arc spraying.

The researches undertaken so far entitle us to extend the investigations, both by lab experiments and on real operating equipment, to another pseudo-alloys and alloys coated by thermal spraying, too.

References

- [1].Mocanu, D. R., et al., 1977, *Analiza experimentală a tensiunilor*, vol.I, II, Editura Tehnică, București.
- [2].Mocanu, D. R., et al., 1982, *Testarea materialelor*, vol. I, Editura Tehnică, București.
- [3].Minca, I., Atanasiu, C., Sandu, A., Sandu, M., 1998, *Rezistența materialelor*, Editura Tehnică, București.
- [4].Stănculescu, N., Teodoru, L., 1997, *Metodă de diminuare a tensiunilor remanente în depunerile realizate prin pulverizare termică (metalizare)*, Tehnologii, calitate, masini, materiale, Vol. 32, Editura Tehnică, București.
- [5].Stănculescu, N., Teodoru, L., 1997, *Metodă de măsurare a tensiunilor remanente în depunerile realizate prin pulverizare termică (metalizare)*, Tehnologii, calitate, masini, materiale, Vol. 32, Editura Tehnică, București.
- [6].Metal Finishing News, 2004, Vol.5, p.26-28.
- [7].Sauer, J. P., Sahoo, P., 2001, *HVOF Process Control Using Almen and Temperature Measurement*, Proc. International Thermal Spray Conference – ITSC.
- [8].Metal Finishing News, 2005, Vol.6, p.26-28.

GRANULARLY UNBIND MATERIALS FOR CASTING COMPOSITE MOULDS

**Ioan MARGINEAN, Mihai TARCOLEA,
Vasile MIREA, Sorin-Adrian COCOLAS**
University "Politehnica" Bucharest

ABSTRACT

This paper present some partial result based on this idea (of pollution prevention) the domain of making composite-casting moulds (in time of casting, solidifying, and alloy cooling). Casting process impose temporary or permanent moulds in classical approach, capable to assure the liquid alloy flow and cooling. The moulds made by bound mixtures are considerer the most dangerous sources in foundries. Initially the mould is made only by gasified model and dry siliceous sand, the casting of the alloy concomitant with the thermo-destruction of the model and decomposing the products of thermo-destruction , filtering through the mould wall it makes possible realization the mould composite- siliceous- graphite, favorable the process of interface metal-mould. The elimination of the binder and of the separation plane, the raising of thermal conductivity of the mould and even the retention of thermo-destruction products in inter-granular spaces could be a solution to minimize the contamination in foundry

KEYWORDS: pollution prevention, composite, casting moulds

1. Structure of a composite mould at casting with gasified model

The principle of casting technologies that use gasifiable models is simple and consists in model obtaining from an expanded synthesis material, covered with a refractory material (in a container) and the refractory material consolidation (Figure 1).

There are peculiar problems at gasifiable model casting, comparing with casting in chills or classical one. In this case the gating has to assure two essential conditions:

- correct filling of the mould cavity with liquid alloy;
- optimum gasification of the model and quick evacuation of the gases resulted by thermal-destruction of the model.

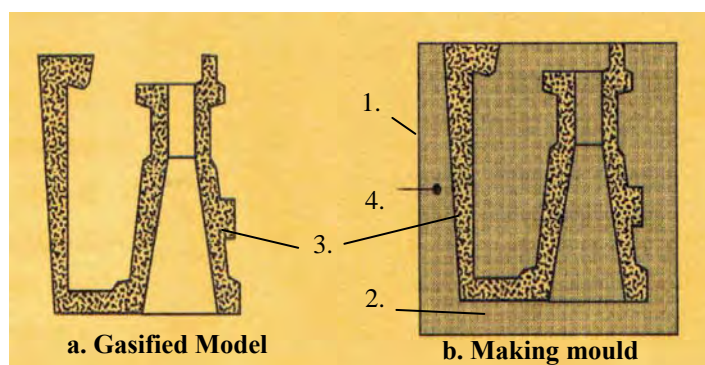


Fig.1. Making a full mould with gasified model. 1. Forming tank; 2. Sand bed; 3. Gasified model; 4. Consolidation sand.

Thermo-destruction of casting mould lead to the appearance of the graphite flake with alongside with granularly unbind sand, making the composite of the casting mould.

2. Method theoretical fundamentation

Duration of the model thermal-destruction phenomenon is about few seconds, depending on melted alloy temperature, and size and model density. The importance of this phenomenon optimization is

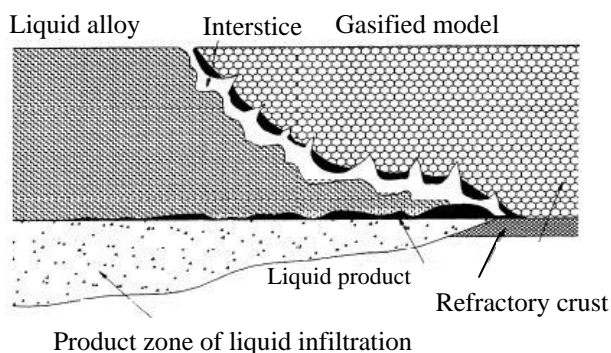


Fig. 2. Thermo-destruction of model and filtering the gaseous product in mould

Determination of the volume of gases resulted by materials models thermal-destruction can be done with equation 1:

$$Q = a \cdot S \cdot t_{\text{top}}^m \quad (1)$$

where: **Q** is the volume of thermal-destruction gases; **a** is the coefficient of gasification process, proportional to the irradiation surface of model and the irradiation duration, in m³/m²×sm; it's values are in the range (17.2...37.6)×10⁻²m³/m²×sm depending on the (calculated) velocity of cavity filling with alloy, in the range 4.00...17.30×10²m/s; **m** is a coefficient that takes into account the gasifiable polystyrene characteristics; it is dimensionless and has values in the range 0.824...0.553.

It is necessary to know the permeability level of the granular material columns that form the mould with gasifiable model, because this must be correlated with the volume of the resulted gases from thermal-destruction.

Permeability determination can be done with classical apparatus (with few accessories) existing in usual laboratories for molding sand analyses.

The permeability value can be calculated with:

$$P = \frac{V \cdot h}{A_o \cdot p \cdot t} \quad (2)$$

where: **P** is the permeability value; **V** is the air

decisive with implication on quality part and specific fabrication. In figure 2 is presented the manner where the liquid alloy act over the gasified model in time of thermo-degradation and in figure 3 is sketch the filtering of the thermo-destruction products through form wall. Here is presented the variation mode of the main parameters, depending on the metal alloy flow velocity. Practically this principle stays at base "filling" of full mould, being the critical stage in obtaining of a quality piece.

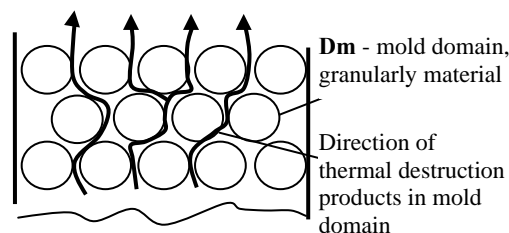


Fig. 3. Flowing itinerary of thermal destruction products

volume that passed through sample, in cm³ (usually 2000 cm³), **h** is the sample height, in cm (usually 5 cm), **A_o** is the surface area of sand sample, in cm² (usually 19.66 cm²), **p** is the pressure difference between the two plane surfaces after **t** time, in cm (water column height) – can be read from manometer, **t** is the necessary time for air volume crossing through sample, in minutes.

3. Interface process at casting with gasified models

Technological elements can be classified in some domains: the mould domain, **D_m** – sand, the gasifiable model domain, **D_{gm}** – cellular polystyrene, liquid alloy domain, **D_a** – aluminum alloy (see Figures 4, 5, 6). The model domain and the alloy domain modifies in time, from the moment of pouring to the moment of complete filling and solidifying of the part, the liquid alloy taking the place of the model that is gasified. The interfaces and the domains are variable in time.

The gasifying process duration is short and directly depending on the model size, density and thermo-physical properties.

The interstice may vary between 5-8 mm and consist in a mixture of polystyrene de-polymerization products.

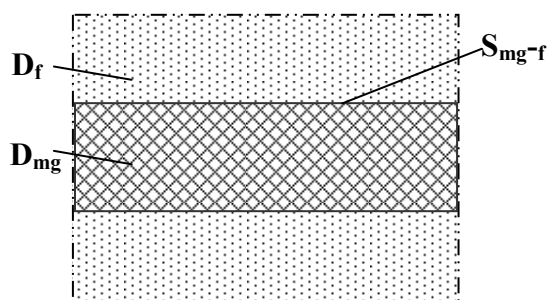


Fig. 4. Technological element that participate, before pouring (in which S_{mg-f} is the surface or frontier among model and sand)

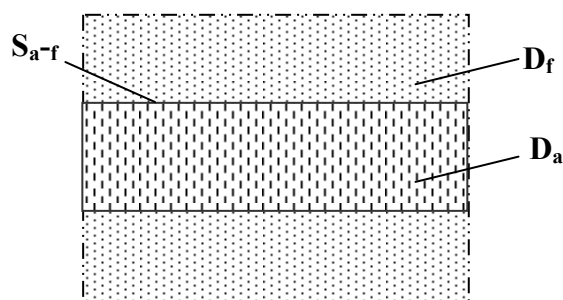


Fig. 5. Technological element that participate, at complete filling of the form (in which S_{a-f} is surface or frontier among alloy and sand)

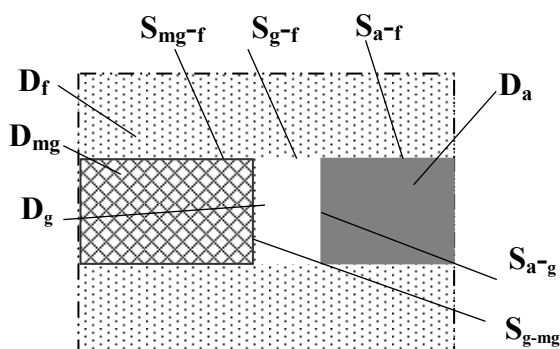


Figure 6. The variation of technological elements that participate at the process of gasification models to the contact with liquid alloy

Symbols:

S_{a-g} = liquid alloy – gas interface,
 S_g = gas – gasifiable model interface;
 S_{mg-f} = gasifiable model – mould interface;
 S_{g-f} = gas – mould interface;
 S_{a-f} = liquid alloy – mould interface;
 D_g = interstice domain.

Their state of aggregation is different:

Solid – brown-russet pyrolysis carbon in flakes or ashes;

Liquid – brown-russet;

Gas – identified in the working environment.



Fig. 7. Thermal-destruction products in sand around the cast part

4. Experimental result

In order to reveal the pyrolysis graphite resulted from polystyrene thermal-destruction, we used an experimental installation (fig. 8). Pyrolysis graphite was collected on a metallic support (fig. 9). There was obtained a crust of from pyrolysis graphite on the metallic support. In the case of casting moulds, the resulted pyrolysis graphite by thermal-destruction of the model will depose on sand granules. Pyrolysis

graphite retaining on sand granules (fig. 7), during casting process accordingly with the thermal destruction of gasifiable model determines the realization of a composite layer at the interface metal/mould, composed by sand granules sand and pyrolysis graphite flakes. This phenomenon favors a behavior specific to filled moulds made of granularly unbind material. So, during casting it is accomplished a reducing atmosphere in mould cavity and also changes mould behavior to thermal flux transfer.



Fig. 8. Experimental installation for pyrolysis graphite revealing as a result of gasifiable model thermal destruction: a) equipment for process parameters control; b) detail of experimental installation.



Figure 9. Pyrolysis graphite layer resulted from thermal destruction of polystyrene: a) aspect of the pyrolysis graphite layer resulted from thermal destruction of polystyrene; b) aspect of the deposit of pyrolysis graphite on holde; 1- holder for pyrolysis graphite collection; 2- aspect of the pyrolysis graphite deposit

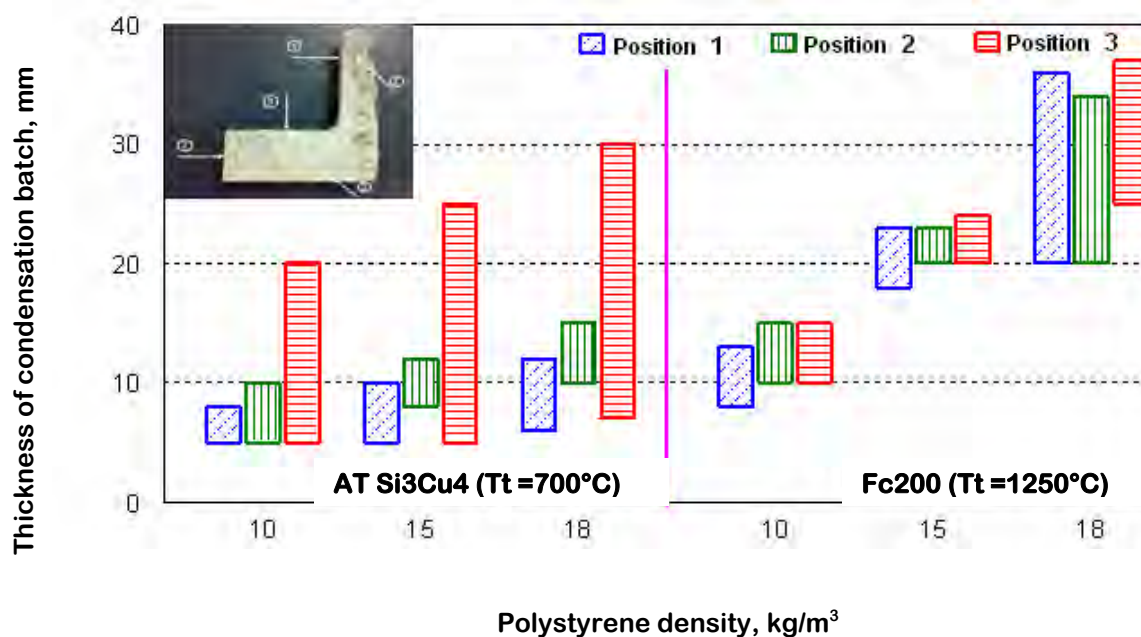


Fig. 10. Casting temperature influence on polystyrene density.

Laboratory experiments has followed the putting in evidence the composite thickness batch from full mould utilized at casting and the dependence of this by different agents, as casting temperature (nature of casted alloy), duration of

mould cooling after casting, the position of the wall form regarding the front filtering gases. In figures 10, 11 are presented experimental laboratory result in this domain.

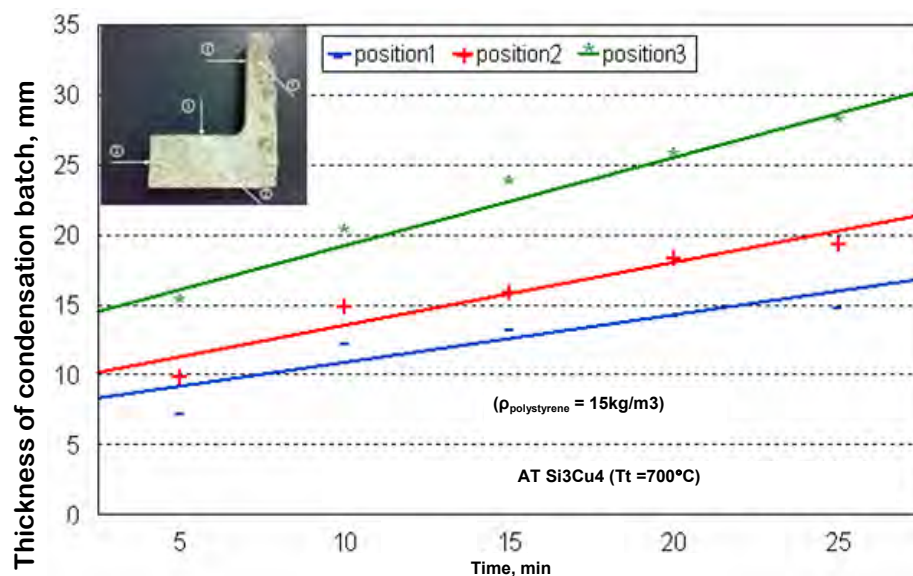


Fig. 11 Influence of cast part cooling time on condensation batch thickness (different positions in mold: 1-beside the horn gate, 2-beside the part, 3-above the part).

In table 1 and 2 are presented values of polystyrene density and position in mould. composite batch thickness in situation of changing

Table 1. Values of composite batch thickness at casting aluminum (700°C) and grey cast iron (1250°C) for various density of model.










						
Position	(position 1)	(position 2)	(position 3)	(position 1)	(position 2)	(position 3)
ρ , kg/m ³	Batch thickness, (aluminum), mm			Batch thickness, (grey cast iron), mm		
0	5-8 / 6.5	5-10 / 7.5	5-20 / 12.5	8-13 / 10.5	10-15 / 12.5	10-15 / 12.5
15	5-10 / 7.5	8-12 / 10	5-25 / 15	18-23 / 20.5	20-23 / 21.5	20-24 / 22
18	6-12 / 9	10-15 / 12.5	7-30 / 18.5	20-26 / 23	20-34 / 27	25-36 / 30.5
22	10-15 / 12.5	10-18 / 14	10-35 / 22.5	-	-	-

Table 2. Values of composite batch thickness at casting aluminum (700°C) for various intervals of time for cooling the piece in mould.

Position			
	(position 1)	(position 2)	(position 3)
Time, min	Batch thickness, (aluminum), mm ($\rho=15$ Kg/m ³)		
5	5-10 / 7.5	8-12 / 10	5-25 / 15
10	10-15 / 12.5	10-20 / 15	10-30 / 20
15	10-17 / 13.5	10-22 / 16	15-32 / 23.5
20	10-19 / 14.5	12-25 / 18.5	17-34 / 25.5
25	10-20 / 15	12-27 / 19.5	20-36 / 28



5. Conclusion

Experimental observations revealed that the mould walls retain the condensed thermal-destruction products, resulting the composite mould.

The technological behavior of such mould at the alloy-mold interface and the reducing atmosphere that forms into the cavity of the mold confirm the composite mold status, with a reducing atmosphere during casting.

The experimental research revealed enough thickness for the impregnated layers with thermal destruction products, those layers thickness was about 5...30mm. Such a thick layer is capable to assure a behavior very similar to metallic molds (high cooling rates), an overpressure of the alloy during solidification, and a very good protection against

oxidation,

The presence of pyro-graphite at interface metal-mould modified the humectation angle in way of diminution the capillary effect due to mould porosity.

References

- [1]. **Marginean Ioan.** "Researches concerning increasing toughness and improvement quality parts casted" Doctoral dissertation 1995, Politehnica University of Bucharest.
- [2]. **Simona Avram.** „Studies and researches regarding at casting aluminum alloy in moulds with gasified models" Doctoral dissertation 2005, University Tehnica Cluj-Napoca
- [3]. **Marginean Ioan, etc.** "Experimental model for determination of the expanding condition and dimensioning of the horn gates utilized in method of obtaining the metallic piece through precision casting", Project INVENT 195/2006.

VALUES OF THE SOLUTAL MARANGONI NUMBER IN VERY DILUTE Fe-C-O SOLUTIONS AT 1873K

Petre Stelian NITA

"Dunarea de Jos" University of Galati

email: pnita@ugal.ro

ABSTRACT

Low carbon, aluminum killed steels are well represented by the adequate part of the Fe-C-O system, where are available useful experimental data, regarding the surface tension and viscosity. The reference dynamic characteristic scale, of about 1-2 μ m at which local chemical inhomogeneities were experimentally observed in some particular conditions is possible to be extended at around 10 μ m and even more, according to basic relations. A characteristic concentration of 0.0001%mass oxygen was taken into account at 1873K. At oxygen contents up to 0.0020%mass and at low contents of carbon(0.05-0.15%mass), the values of the Marangoni solutal number (Ma_s) always were found to be higher than the critical values($Ma_s^c = 50$) especially due to the reduction of the viscosity with the oxygen content. When the dynamic characteristic length is 6 μ m, $Ma_s=379$ and the parameter $\varepsilon=6.58$, permitting the development of hybrid convection roll cells. Even at such high dilutions, in Fe-C-O solutions at 1873K, the convection due to the solutal effect is present. At a concentration of 0.0017%massO(soluble) takes place a change of the relations between viscosities and between the value of Marangoni numbers. It is suggested that the finally induced dynamics in liquid steels are responsible for some decreasing of the steel cleanliness.

KEYWORDS: surface tension, characteristic length scale, viscosity, Marangoni number

1.Introduction

Advanced refining and controlled solidification, in normal and low gravity conditions lead to materials of higher purity and controlled structure. In systems with specific reactions, affecting the surface tension and viscosity, like in low carbon, aluminium killed steels, the evaluations of aspects regarding the local dynamics of layers at micro and nanoscale could contribute to the quality increasing. Fe-C-O system, at low dilutions is closed to this class of steels grades. Traditionally, only sensible higher contents of soluble oxygen are considered to exert an influence on the surface tension of the steels, also on the interfacial tension. In real conditions, liquid steels are processes for different purposes, including for advanced refining, in an advanced state of deoxidization, when soluble oxygen content is of order of several ppm. In this paper are analysed the values of the Marangoni numbers at very low dilutions of oxygen in the

system Fe-C-O. The oxygen content must be understood as being totally in solution.

2. Local effects of surface tension variations

The quantitative aspects of local convection in the limit layer (100-10 μ m), usually are analysed under many simplified premises. It is generally accepted that the thermal Marangoni effect in liquid steels is small when compared with the solutal and electrical Marangoni effects[2].

In ref. [1] it is suggested that interfacial chemical reactions induce Marangoni and natural convection at slag-metal interface, leading to interfacial waves, due to Kelvin-Helmholtz instability, causing the waves to become unstable and lead to emulsification of slag in steel and of steel in slag, affecting the quality of steels at high aluminum and/or titanium contents.

In ref. [2], at the interface, it was found that solutocapillarity contributed only with 15% to the maximum interfacial depression. Aspects of the interface dynamics argue that at higher initial rates of interface reactions, the interfacial area becomes even higher due to the droplet emulsification [1][2]. A length scale of inhomogeneity of 1-2 μ m was established based on the presence of pockets of fluid of the same dimensions [2], with different oxygen contents, moving about within the bulk. Protuberances of the near the interface, during the early stages of the involved reaction [1]. same size were observed on the droplet surface [2]. These dimensions of the local instability are more realistic compared to those reported in the ref. [1]. In principle, it is mentioned [1] that both thermal and chemical variations at interface give rise to Marangoni flow along the interface and since the viscosity of metal and of slag largely differs, the velocity of the motion of each phase, parallel to the interface, will be different. A reference scale length in the systems of liquids (density ρ_l) in equilibrium with their vapors (density ρ_g) is the capillary length expressed in forms given by rel. (1)[3] or rel (2)[4]:

$$l_c = \sqrt{\gamma / g\rho} \quad (1)$$

$$l_c = 2\gamma / g(\rho_l - \rho_g) \quad (2)$$

Rel.(1) dictates the curvature of the interface far away from the contact line with a solid substrate[3], rel.(2) governs the propagation of the capillary waves[4]. The variation of the length scale, as effects of the local variations of the surface tension γ could be considered as a dynamic characteristic length scale (l_c'), having similar forms:

$$l_c' = \sqrt{\Delta\gamma / g\rho}, \quad \Delta\gamma(c) = \gamma(c_1) - \gamma(c_2) \quad (3)$$

$$l_c' = \sqrt{\frac{\partial\gamma(c)}{\partial c} c_0 / g\rho} \quad (4)$$

The solutal Marangoni number (Ma_s) is given in the following forms:

$$Ma_s = \left(-\frac{\partial\gamma}{\partial c} \right) c_0 L / \mu D \quad (5)$$

The term between brackets is the coefficient of dependence of the surface tension (γ) upon concentration (c) of the surface active element, the sign (-) being taken when to avoid negative values of the Ma number; c_0 - is a characteristic concentration; L - is a characteristic length, m; μ - dynamic viscosity, Ns/m²; D - diffusivity of the surface active element, m²/s.

Frequently are used modified forms of Ma_s as $\Delta C = c_s - c_b$, between surface (c_s) and bulk (c_b)

concentrations, also for L could be considered one of proposed forms in rel. (3) or (4)

3. Results

Following data for Fe-C-O system containing up to 0.0020% mass O and up to 0.15% mass C, were used:

1. Surface tension dependence upon mass percentage content of oxygen, at $T=1873$ K[5]; according to experimental data from [6], up to carbon contents of 0.5% mass, there is not an influence on surface tension:

$$\gamma = 1.903 - 0.28 \ln(1 + 170[\%O]) \quad \text{N/m} \quad (6)$$

2. Kinematic viscosity (ν) dependences upon mass percentage content of oxygen, are obtained from base relation established in [7], in 10⁻⁷ m²/s:

$$\begin{aligned} &\text{-at } C=0.05\% \text{ mass} \\ &\nu = 9.453 - 2072.527[\%O] - 31107.5[\%O]^2 - 1.42 \times 10^7 [\%O]^3 \end{aligned} \quad (7)$$

$$\begin{aligned} &\text{-at } C=0.10\% \text{ mass} \\ &\nu = 8.632 - 1473.113[\%O] - 94290[\%O]^2 - 1.42 \times 10^7 [\%O]^3 \end{aligned} \quad (8)$$

$$\begin{aligned} &\text{-at } C=0.15\% \text{ mass} \\ &\nu = 7.881 - 955.269[\%O] - 149227.5[\%O]^2 - 1.42 \times 10^7 [\%O]^3 \end{aligned} \quad (9)$$

$$\mu = \nu \cdot \rho \quad \text{Ns/m}^2 \quad (10)$$

3. At 1873K, diffusivity of oxygen in iron is $D_O = 11.7 \times 10^{-9}$ m²/s and density of liquid iron is taken $\rho = 7038$ Kg/m³ [8].

The value of the characteristic length scale taken into account is 1 μ m in normal gravity, being of the same magnitude with the experimentally found inhomogeneity domain extend (1-2 μ m)[2].

The characteristic concentration ($\Delta c = c_\theta = 0.0001\%$ mass oxygen).

In fig.1 are presented corresponding values of the Ma_s , resulting values $Ma_s > Ma_s^c (=50)$ on all range of considered contents of oxygen.

As an example, at values of $l_c' = 6\mu$ m and $c_\theta = 0.0001\%$ O mass, in an alloy containing 0.05%C and 0.0005%O, when Navier and Biot numbers are zero, the parameter describing the distance from the threshold of the instability, ε [8] is:

$$\varepsilon = (Ma_s - Ma_s^c) / Ma_s^c = (379 - 50) / 50 = 6.58 \quad (11)$$

At values $\varepsilon > 6.3$ convection rolls, hybrid cells are formed[9].

In fig.1 at a value of about 0.0017% mass oxygen a the relations between the viscosities of Fe-C-O predicted based on the relations (7)-(9) change and because of this situation, also the relations between the viscosities.

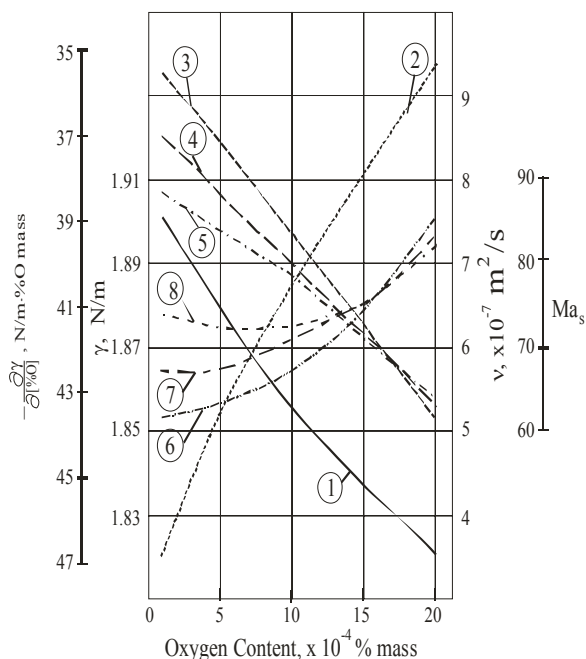


Fig. 1. Values of Marangoni numbers in Fe-C-O system at low contents of solutes and the evolution of some related quantities, at 1873K, in normal condition of gravity. 1- surface tension γ ; 2-concentration coefficient of the surface tension, $\partial\gamma/\partial[\%O]$; 3,4,5-kinematic viscosity ν at 0.05%C, 0.10%C, 0.15%C, respectively; 6,7,8- Marangoni solutal numbers at 0.05%C, 0.10%C, 0.15%C, respectively.

4. Conclusions

In dilute Fe-C-O systems, at 1873K, corresponding to some classes of steel grades, even small variations of solutes are able to promote a local pattern of flow due to the Marangoni effect.

Values of $Ma_s > Ma_s^c (=50)$ are obtained for local characteristic concentrations or variations of 0.0001% mass O, when $C=0.05-0.15\%$ mass, at

microscale corresponding to an experimentally determined inhomogeneity of 1 μ m.

Increasing of the oxygen content leads to increasing of Ma_s values, due to their effect in decreasing the viscosity and in a lower decreasing of the absolute values of concentration coefficient of the surface tension. At higher values of the involved parameters variations, higher values of Ma_s are obtained.

A value of the soluble oxygen content of 0.0017% mass appeared as being a particular point where the relations between viscosities and the values of the Marangoni numbers change and on this account it would be possible that the quality in some industrial steel grades to be affected.

Based on the aspects mentioned in this paper it could be better explained some unexplained cases when some indicators of quality in steel, like cleanliness in non-metallic inclusions decrease in the final stage of processing in liquid state.

References

- [1] Chung, Y., Cramb, A.W., Metall.Mater.Trans.B, 31B (2000) 957-971
- [2] M.A.Rahmdani, K.S.Coley, "Analysis of the source of dynamic phenomena during reaction between metal droplets and slag" Metall. Trans. B.vol.36B., 591-604 (2005).
- [3] J.Eggers, H.A.Stones, "Characteristic length at moving contact lines for a perfectly wetting fluid: the influence of speed on the dynamic contact angle" J.Fluid Mech.vol. 505, 309-321,(2004).
- [4] J.S. Rowlinson, "Thermodynamics of inhomogeneous systems" Pure & Appl. Chem.vol 65, no.5, 873-882, ((1993).
- [5] D.R.Poirier, H.Yin, M.Suzuki, "Interfacial properties of dilute Fe-O-S melts on alumina substrates, ISIJ, Vol38, no.3,229-238 (1998).
- [6] Van Tszin-tan, R.A.Karasev, A.M.Samarin, "Russ. Metall. Fuels", vol.1, 21-27(1960).
- [7] B.A.Baum, M.N.Kushnir, H.E.Bodakin, G.V.Tiagunov, "Viazkost' jidkih splavov sistemi Fe-C-O" Chernaia Metallurgija, no.6, 21-23, (1976).
- [8] T.Iida, R.I.L. Guthrie The Physical Properties of Liquid Metals, Claredon Press- Oxford,England, p. 220 (1993).
- [9] J. Bragard, S.G.Slavtchev, G.Lebon, J.Colloid and Interface Sci.,168, 402- 413, (1994).

MANUSCRISELE, CĂRȚILE ȘI REVISTELE PENTRU SCHIMB, PRECUM ȘI ORICE
CORESPONDENȚE SE VOR TRIMITE PE ADRESA:

MANUSCRIPTS, REVIEWS AND BOOKS FOR EXCHANGE COOPERATION, AS WELL
AS ANY CORRESPONDANCE WILL BE MAILED TO:

LES MANUSCRIPTS, LES REVUES ET LES LIVRES POUR L'ECHANGE, TOUT AUSSI
QUE LA CORRESPONDANCE SERONT ENVOYES A L'ADRESSE:

MANUSKRIPTEN, ZIETSCHRIFTEN UND BUCHER FUR AUSTAUCH SOWIE DIE
KORRESPONDENZ SIND AN FOLGENDE ANSCHRIFT ZU SEDEN:

UNIVERSITATEA "DUNĂREA DE JOS" DIN GALAȚI
REDACȚIA ANALELOR

Str. Domnească nr. 47 – 800036 Galați, ROMÂNIA

E-mail: marian.bordei@ugal.ro

AFFILIATED WITH:

- *ROMANIAN SOCIETY FOR METALLURGY*
- *ROMANIAN SOCIETY FOR CHEMISTRY*
- *ROMANIAN SOCIETY FOR BIOMATERIALS*
- *ROMANIAN TECHNICAL FOUNDRY SOCIETY*
- *THE MATERIALS INFORMATION SOCIETY*
(ASM INTERNATIONAL)

Annual subscription (2 issues per year)

**Edited under the care of
Faculty of
METALLURGY AND MATERIALS SCIENCE
and Research Center
QUALITY OF MATERIALS AND ENVIRONMENT**

Edited date: 15.05.2007

Issues number: 200

Printed by

Galati University Press

accredited CNCSIS

47 Domneasca Street, 800036 Galati,
Romania